Surfaces of Complex Metallic Alloys and Their Adsorption Properties

Thesis submitted in accordance with the requirements of
the University of Liverpool for the degree of Doctor in Philosophy
By

Amnah Musaed Alofi

May 2023

Abstract

Quasicrystals are a novel phase of solids that were first reported in 1982. Quasicrystals display aperiodic long-range order but lack translational symmetry. Furthermore, quasicrystals often exhibit classically forbidden rotational symmetries such as five-fold and ten-fold. Surfaces of icosahedral (*i*)–Ag–In–Yb quasicrystals and their approximants have been a subject of extensive research recently. Approximants are periodic metallic compounds with large unit cells that share similar chemical composition and atomic structure to their related quasicrystals. The basic building block of *i*–Ag–In–Yb quasicrystals and approximants are rhombic triacontahedral(RTH) clusters, which are formed by five successive atomic shells.

Surface studies carried out in this thesis are: the growth of pentacene (Pn) films on the two-fold and three-fold surfaces of *i*–Ag–In–Yb quasicrystals, the study of (110) surface of Au-Al-Gd 1/1 approximant and the (010) surface of Ga_3Ni_2 crystal. To understand the surface structure, scanning tunneling microscopy (STM) and low energy electron diffraction (LEED) tools were employed.

Pn molecules on the two-fold surface were found to be arranged in rows and aligned predominantly along the high-symmetry five-fold and two-fold axes of the surface. The row separation perpendicular to the five-fold symmetry axes is either short S = 0.79 ± 0.03 nm or long L = 1.24 ± 0.02 nm. The ratio between them is close to the golden mean ($\tau = 1.618..$) and the row separations generate Fibonacci sequence segments, indicating that deposited Pn molecules have quasicrystaline order. The Fast Fourier-Transform (FFT) of the images produced by (STM) also reveals a two-fold quasicrystalline long-range order. Pn molecules are adsorbed on Yb sites because the distance between two sites is close to the length of Pn molecules. This is consistent with previous work on five-fold surface *i*–Ag–In–Yb where molecules were found to adsorb on Yb.

Similarly, Pn molecules deposited on the three-fold surface of *i*–Ag–In–Yb formed quasicrystalline monolayers on the surface. The FFT and the autocorrelation of high-resolution images show a three-fold pattern with maxima located at τ-scaling distances, confirming the quasicrystalline order of molecules. Rod and triangle motifs were the two types features observed in STM. Adsorbed molecules aligned along three-fold axes form the triangular motif. Rods shape were formed by molecules located at three-fold axes and rotated 30° with respect to the three-fold axes. These STM features can be understand if Pn molecules selectively adsorb on Yb. The behaviour of selective adsorption can be understood in terms of the geometry of the Yb sites in the surface substrate. The Yb–Yb separations are close to the C–C or H–H distances in a Pn molecule, indicating that Pn adsorbed on Yb sites.

The surface study of the (110) surface of the Au-Al-Gd 1/1 approximant showed the (110) orientation is predominant, but different other orientations were also identified. The comparison of observed step heights and high resolution STM images with the bulk structure model reveal that terraces form on planes that break the icosahedron, the third shell of the RTH cluster, which is the building block of the system.

STM and LEED from the Ga_3Ni_2(010) surface reveal four different structures, depending on annealing temperature. These structures are (4×2), c(2×2), (2×1), and (1×1) observed at increasing annealing temperatures from 360 °C to 500 °C. In addition, the annealing time for transfer between different structures is identified.

Contents

Glossary of Terms and Acronyms

Quasicrystals (QCs) are predominantly intermetallic compounds that exhibit long-range order without periodicity and frequently possess rotational symmetries that are classically forbidden, such as five-fold and ten-fold.
Approximants are periodic metallic compounds whose chemical composition and atomic structure are similar to those of their related quasicrystals, and whose unit cells are typically large.
RTH: The rhombic triacontahedral cluster is the fundamental constituent of Ag-In-RE quasicrystals and approximant. It consists of five atomic shells in succession.
Golden Mean (τ)is an irrational number characteristic of quasicrystalline order ($\tau = 1.618....$)
ACs: approximant crystals
RE: Rare Earth Elements
UHV: Ultra High Vacuum
STM: Scanning Tunneling Microscopy
LEED: Low Energy Electron Diffraction
FFT: Fast Fourier Transform
i: Icosahedral
d: Dodecahedral

Acknowledgements

I would like to express my deepest gratitude to Albaha University for providing financial support and the opportunity to do my PhD in The University of Liverpool. I am also greatly indebted to both my supervisors, Prof. Ronan McGrath and Dr. Hem Raj Sharma for their continuous guidance and advice during my thesis, always pointing me in the right direction and helping me to focus on the relevant points.

I would also like to thank Dr Sam Haq, and my lab-mate, Dominic Burnie, for their help during my experiments. Also, thanks to Dr Sam Coates for providing the Au-Al-Gd 1/1 approximant. As a result, I was able to obtain STM data for the final chapter of results.

Last but not least, I would like to thank my family: my parents and my sisters, especially Huda and Smaherh, for supporting me spiritually throughout all four years of my Ph.D.

Chapter 1

Introduction

Quasicrystals (QCs) were first discovered in the 1980's by Dan Shechtman, which resulted in a Nobel Prize being awarded to him in 2011 [1]. Quasicrystals are characterised as a different type of solids from crystals and amorphous. They are initially defined as intermetallic compounds that have long range order but they lack periodicity and often they show the symmetries that are forbidden in conventional crystals such as five-fold and ten-fold rotational symmetries [2]. Quasicrystals are not solely observed in intermetallics; they also have been observed in colloidal systems and soft matter [3, 1]. An approximant crystal (ACs) is a periodic crystal with a large unit cell and a chemical composition that closely resembles that of a quasicrystal. Additionally, it contains atomic clusters that are nearly identical to those in the quasicrystal, resulting in physical properties that are comparable to those of the quasicrystal. Therefore, the existence of approximant crystals is necessary for both calculating the physical properties of quasicrystal and determining their atomic structure.

The study of surface properties which is known as surface science include the study of interface interactions, for example gas-solid interactions and the study of epitaxial phenomena. The study of surface science ensures a better understanding of the surface properties of quasicrystals, which include structural properties such as the non-sticking, low friction coefficient, and catalysis, as well as the industrial applications of quasicrystals being closely related to these novel properties. In addition to this, an understanding of electronic properties of these surfaces can aid in getting an insight into how the molecules interact on the surface of quasicrystals [4].

In general, both atoms and molecules are able to form films on the surface of quasicrystals. Firstly, the formation of artificial quasicrystals from a single element which can result in the reduction of the chemical complexity and give a better understanding of their structure in relation to the bulk QC [5].

An *i*–Ag–In–Yb quasicrystal and an Au-Al-Gd 1/1 approximant sample have been used for surface studies in this thesis. Two- and three-fold surfaces have been used as templates to grow Pn films [6]. The purpose for using two- and three-fold surfaces of *i*–Ag–In–Yb quasicrystals to grow the Pn molecules is to compare to the growth of Pn on the five-fold *i*–Ag–In–Yb surface [7]. The Pn films grown on both templates have produced quasicrystalline films. In addition, it is found that Pn molecules are adsorbed on Yb sites on both templates. These results are consistent with those previously published [7].

Also investigated is the structure of Au–Al–Gd approximant surfaces. Studying the structure of these surfaces and comparing their surface terminations to those of similar quasicrystals and approximants helps to understand their surfaces and may provide insight into the magnetic order in Au-based approximants. Recently, an antiferromagnetic Au–Al–Tb 1/1 approximant with a whirling spin order oriented along the [111] direction was discovered [8], with antiferromagnetic order evident in increasingly complex approximants [9, 10, 11]. The Au–Al–RE approximants belong to the group of complex intermetallics defined as Tsai-type [12]. The Au-Al-RE approximant and *i*–Ag–In–Yb quasicrystal share this building block, and it is anticipating that understanding antiferromagnetic order in approximants will lead to the synthesis of quasicrystals with long-range magnetic order.

This thesis also describes a detailed characterization of the atomic properties of the (010) surface of Ga_3Ni_2 single crystal using LEED and STM. Intermetallic compounds could be potential alternatives to pure and alloyed metals as catalyst materials in heterogeneous catalysis due to their enhanced selectivity enhanced long-term stability for specific reactions [13]. It is found that Ga_3Ni_2 active catalyst in hydrogenation of carbon dioxide into methane. LEED and STM results showed that there were four surface structures obtained at a specific annealing temperature. Four structures are three superstructures are c(2×2), (4×2), (2×1), and (1×1).

The thesis has been organised as follows: The second chapter provides an introduction to quasicrystals, approximant, and their structures. The third chapter is a review of the literature on adsorption studies on quasicrystals and approximant. Chapter four describes the experimental methods used in this thesis. Ultra-high vacuum (UHV) technology is introduced, and surface techniques including scanning tunnelling microscopy (STM) and low energy electron diffraction (LEED) are discussed. Chapter five presents STM images of the clean and Pn dosed two-fold and three-fold *i*–Ag–In–Yb surfaces. Chapter six presents a structural study of the (110) surface of the Au-Al-Gd 1/1 approximant using STM. In Chapter seven, we give LEED and STM images of the (010) surface of Ga_3Ni_2 crystal. Chapter eight provides a brief summary and conclusions of the work of the thesis. Also, future work will be proposed on a project to study the effect of oxidation on the Ga_3Ni_2 surface. This investigation will be an expansion of the Ga_3Ni_2 surface study.

Chapter 2

Quasicrystals and Approximants

2.1 Introduction

This chapter provides a brief introduction to the quasicrystals and their approximants. The binary icosahedral-Cd-Yb quasicrystal which is a parent of the icosahedral Ag-In-Yb quasicrystal is discussed in detail as its two and three-fold surfaces have been used as a template to grow quasicrystalline organic molecular films. The structure of Au-Al-R (R = Tb, and Gd) 1/1 approximants also described as their surfaces are investigated in this thesis.

2.2 Quasicrystals

A quasicrystal is a material that has a long-range aperiodic structure but does not have translational symmetry. Quasicrystals often shows five-fold or ten-fold symmetries [14]. It is common for such materials to have `"unusual"` rotational symmetry orders. In this case, the term unusual denotes an order of symmetry that is not compatible to the Bravais lattice or periodic systems. The most common and studied quasicrystalline systems are the intermetallic alloys exhibiting such structures [1, 2].

Shechtman, Blech, Gratias and Cahn [1] reported the first quasicrystal in 1984. In their work, they provided details on the diffraction pattern resulting from the rapid quenching of molten Al–Mn, which showed aperiodic order with icosahedral symmetry, including five–fold rotational axes. This resulted in the discovery of a completely new category of solid-state structural order. This work was awarded the Nobel Prize in Chemistry (2011) to Shechtman.

Apart from the five and ten-fold specifies [15, 16], other quasicrystalline materials have been discovered, including eight-fold [17, 18] and twelve-fold [19, 20]. Around 80 % of discovered thermodynamically stable quasicrystals are composed of Al along with two or more other elements. Some well-studied families include the icosahedral phases, Al-Pd-RE (RE—Rare Earth) and Al-Cu-Fe, and the decagonal phase, Al-Ni-Co and Al-Co-Cu [21]. These quasicrystals are good candidates for study due to the ability to grow these materials as single grains of satisfactory size, and because of their stability in vacuum condition. The alloy containing exhibits a high vapor pressure makes its preparation in such an environment problematic.

Quasicrystals come in two main forms. The first comprises the intermetallic (hard QC). These can be synthesized through the ternary or pseudo-binary phases, and their structures are icosahedral or decagonal. The second group of quasicrystals are called soft quasicrystals [22].

The Fibonacci sequence and Penrose tilings are often associated with the structure of quasicrystals, and are described below.

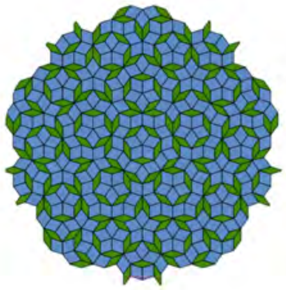

Figure 2.1: Penrose tiling made with two types tiles of rhombus, showing five-fold symmetry.

2.3 Fibonacci Sequence and the Golden Mean

The Fibonacci sequence represents an excellent example of a 1D quasi-periodic structure displaying aperiodic long-range order. The sequence comprises of two basic elements `'L'` (large) and `'S'` (short). The substitution rule can be used to generate the sequence using S → L and L → LS. Starting from S, a series of sequences can be obtained, as follows
S (1)
L (1)
LS (2)
LSL (3)
LSLLS (5)
LSLLSLSL (8)
LSLLSLSLLSLLS (13)
LSLLSLSLLSLLSLSLLSLSL (21)

The total for the L and S will be 1, 1, 2, 3, 5, 8, 13, 21, 34, 55, 89, creating the Fibonacci sequence. We can also guarantee that segment vertex points on a line conforming to the Fibonacci sequence have no translational symmetry because the ratio L/S is an irrational number. The golden ratio, given as $\tau = (1+\sqrt{5})/2 = 1.618..$, is a conventional irrational number related with the ratio between successive terms of the numerical Fibonacci sequence [5]. The golden ratio is mentioned here because it is useful to confirm quasicrystalline order in structural studies.

2.4 Penrose Tiling

In 1970, Roger Penrose discovered several tiles to produce infinite, non-periodic tiling [23]. The Penrose tiling is a perfect example of the 2 D quasi-periodic order. When quasicrystals were discovered[24], the importance of Penrose tiling in solid state physics was realised because the diffraction pattern of a Penrose tiling shows five-fold and ten-fold symmetries that are very similar to the diffraction pattern of quasicrystals [25]. Penrose tiling can thus be used to model the structure of quasicrystals [5]. Penrose used more than one shape to tile a plane aperiodically as it is impossible to make such a tiling with a single shape. There are three different types of Penrose tiling: P1, P2 and P3. The first pattern to be constructed is known as the P1 tiling shown in Figure 2.2(a). This pattern involves 4 different tiles; boat, star, pentagon and rhomb. To construct an aperiodic arrangement that stretches to infinity while keeping the aperiodicity without any spaces or overlaps, matching rules must be applied. The P2 tiling consists of two different shapes of tiles kites and darts [23]. The P3 tiling, is constructed using just two shapes; the fat and skinny rhombs, as shown in Figure 2.2(b). These rhombs, with internal angles of 108° and 72°, and 114° and 36°, can again be tiled to infinity to form a five-fold a periodic structure when the correct matching rules are used.

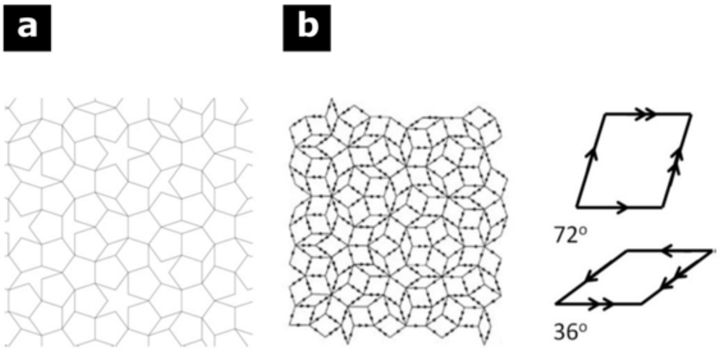

Figure 2.2: The two famous Penrose tiling patterns. (a) Demonstrates a P1 tiling, consisting of 4 tiles; rhomb, star, boat and pentagon. (b) Shows a P3 tiling, with appropriate matching rules [26].

2.5 Icosahedral Quasicrystals

Icosahedral quasicrystals are quasiperiodic in three dimensions without any directional periodicity. These structures have been extensively studied, particularly Al-based quasicrystals. Surface studies are usually limited to the five-fold surface. However, studies have also been performed on other surfaces including three-fold and two-fold surfaces [27]. It is difficult to obtain atomic resolution of these two surfaces. This makes it harder to compare to the bulk atomic structure [28]. Icosahedral quasicrystals can be categorized into different groups based on elements that quasicrystals are made from. There are three types of icosahedral systems: Mackay (Al-based, with Mn and Si), Bergman clusters (Zn-based) and rhombic triacontahedral (RTH) Cd-based alloys. Usually, Al-based QCs such as icosahedral–Al–Cu–Fe ((i)–Al–Cu–Fe) and icosahedral Al-Pd-Mn ((i)–Al–Pd–Mn) can be labelled as Mackay-type, and Zn-based i–QCs such as i–Zn-Mg–RE (RE = rare earth elements) labelled as the Bergman-type. i–Ag–In–Yb, used in this thesis is formed by rhombic triacontahedral clusters.

2.6 Mackay and Bergman Clusters

The Mackay type is considered to have 54 atoms which are responsible for the formation of three shells, defined as icosahedron, icosidodecahedron and larger icosahedron of the transition metal [29], which is illustrated in Figure 2.3(a). The valence electron concentration of Al-Pd-(Mn, Re) and Al-Cu-(Fe, Ru, Os) is a = 1.75 [30]. The Bergman type structure, constituted of 104 atoms, results in the formation of four shells, icosahedron, dodecahedron, larger icosahedron, and truncated icosahedron. The values of the valence-electron concentration for these structures are a = 2.1. These formulas are a derivative of the face-centred type

(F-type) exhibits τ-scaling rule (τ : golden mean), which is clearly illustrated in Figure 2.3(b) [31].

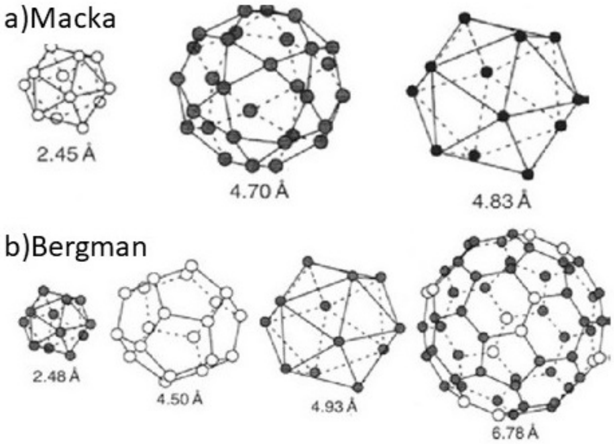

Figure 2.3: Icosahedral atomic clusters. (a) Mackay-type in Al-Mn-Si approximant and (b) Bergman-type in Zn-Mg-Al approximant [31].

2.7 Rhombic Triacontrahedral (RTH) Clusters

The Rhombic Triacontrahedral (RTH) cluster is the main building block of *i*–Cd–Yb type quasicrystals and approximants. It consists of five successive shells of atoms, the first of four shell is called Tsai-type cluster (65) atoms. The last shell being the rhombic triacontahedron. The 1^{st} shell contains a tetrahedron which is composed of four atoms, the 2^{nd} shell is a dodecahedron which is made up of 20 Cd atoms; the icosahedron which is the 3^{rd} shell consists of 12 Yb atoms; the icosidodecahedron which is the 4^{th} shell contains 30 Cd atoms, and finally the 5^{th} shell is a rhombic triacontahedron (RTH) which is made up of 92 Cd atoms [30], [32], as shown in Figure 2.4.

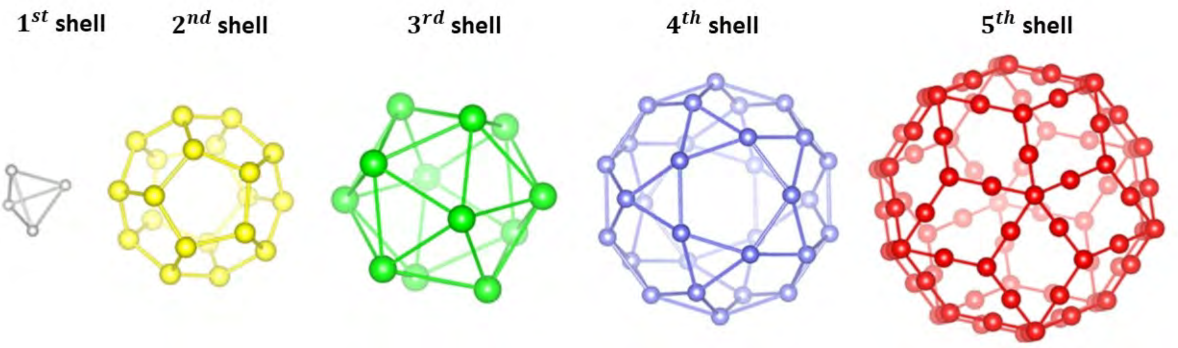

Figure 2.4: Rhombic triacontrahedron (RTH) cluster which is defined by five successive atomic shells [6, 12].

2.8 Discovery of the *i*–Cd–Yb Quasicrystal

Tsai *et al.* produced a Cd-Mg-RE quasicrystalline (where RE is a rare earth) alloy [33]. This family of quasicrystals was discovered by replacing the Zn in Zn-Mg-RE with Cd.

The structure of this quasicrystal adheres to the Hume-Rothery electron compound rules with a definite valence concentration (valence electron to atom ratio or e/a) of roughly 2 [26]. The e/a ratio may be calculated by;

$$\frac{e}{a} = Z_A(1 - C_B) + C_B \tag{2.1}$$

Where Z is the valency of species A and B and C_B is the concentration of species B. The e/a ratio is an important determinant of crystal structures due to its indication of how full the Brillouin zones are. If a Brillouin zone is filled but more electrons are present, it is energetically favorable to change the shape of the Brillouin zone to accommodate more (resulting in a structure change), then to promote electrons across the band gap to the next empty or partially filled Brillouin zone.

This makes it possible to predict what compounds may make quasicrystals when swapping constituents from existing quasicrystals to make new materials. Stable Al-transition metal quasicrystals have an e/a of around 1.75, while the *i*–Zn-Mg-RE quasicrystal has an e/a ratio of around 2.15. The second condition to construct a stable quasicrystal includes the size of the constituent atoms [26]. The difference in size of atomic species present in a material may be calculated by;

$$\delta = \frac{(r_A - r_B)}{r_A} \tag{2.2}$$

where r is the atomic radius of species A and B. If the size of the constituent species differs by more than 15%, even at low concentrations, a quasicrystalline structure is unstable.

By reducing the amount of Mg, a new quasicrystalline $Cd_{5.7}$-Yb was obtained. Both Cd and Yb are divalent, with the e/a of the quasicrystal being 2.0, adhering to the valence concentration condition. Also, the difference in size of the two species is 2%, so the size condition is also adhered to.

The surface study of the Cd-Yb system is however hindered by the high vapur pressure of Cd. The study of this material in an Ultra High Vacuum (UHV) environment is problematic, as upon heat treatment the Cd component of the material evaporates from the surface.

2.9 Icosahedral Ag-In-Yb Quasicrystal

The Cd's high vapor pressure made the new $Cd_{5.7}$-Yb quasicrystal unsuitable for UHV studies. To deal with this challenge, Guo *et al.* substituted the Cd component with equivalent amounts of Ag and In [34]. This created a new quasicrystal: *i*–Ag–In–Yb. The valence of Indium and Silver is different, with the latter element being trivalent and the former being monovalent. This implies that in the two parts, there are two electrons for every atom. The atomic sizes are also different, namely d_{Cd}= 0.314 nm, d_{Ag} = 0.290 nm and d_{In} = 0.332 nm, with $d_{0.5Ag+0.5In}$ = 0.311 nm, so that the overall difference in size between the original constituent and its substitutes is 1%. The Yb% remained the same. This changed the total composition of the system, which can be written as $Ag_{42}In_{42}Yb_{16}$ [34].

The system described above is an excellent candidate for researching the single grain QCs and ACs. Firstly, the structure is icosahedral, making it isostructural to *i*–Cd–Yb ($Cd_{5.7}Yb$), which has the most detailed structural model of an *i*–QC achieved to date. Secondly, two types of periodic AC exist: 1/1 $Ag_{40}In_{64}Yb_{14}$ and the 2/1 $Ag_{41}In_{44}Yb_{15}$ cubic ACs. They have a close chemical composition and similar structural units to their parents. The new system is easy to handle in experiments. As it was mentioned, this material does not contain elements with high vapor pressure or toxicity [35]. The system is stable under ultra-high vacuum, and it can be annealed at high temperatures. This is very important for the surface studies under UHV conditions [35].

2.10 Approximants

A special class of intermetallics are approximant crystals (ACs) which have similar structure and chemical composition to QCs. Since the discovery of the binary icosahedral quasicrystal $Cd_{5.7}Yb$ in 2000 [36, 37], the presence of the crystalline analogue Cd_6Yb, the so-called Tsai-type 1/1 cubic approximant, in a nearby composition has been recognised [22, 38], and much attention has been paid to its structural and physical properties. Periodic crystals that are closely related to quasicrystalline phases were discovered while investigating the structural similarity between known crystalline phases and related quasicrystalline phases. Therefore, the approximant is a periodic structure consisting of a similar local structural unit, or cluster. The arrangement of atoms in the local structural unit of the approximant closely approximates the local atomic structures of the quasicrystals. They possess a complex atomic structure, which can be explained in terms of clusters of atoms decorating a periodic lattice. They have large unit cells, sometimes containing several hundred atoms. As a result of this similarity, the approximants play a crucial role in understanding the formation, stability, physical properties, and atomic scale structure of quasicrystals [39].

Approximants are periodic structures projected from the same higher-dimensional lattice but with a rational tangent. The cut and project method is explained to understand a rational tangent. The Fibonacci sequence can be utilised as a model structure for an aperiodic but perfectly ordered one-dimensional quasicrystal. A quasicrystal in one dimension can be derived from a periodic lattice in two dimensions using the cut and project method. A two-dimensional system consisting of physical space X|| and orthogonal space X⊥ is rotated by an angle of α degrees in the two-dimensional hyper lattice (h$_x$ and h$_y$). Until the tan $(\alpha) = \tau$, the rotation will continue. The X|| axis cuts the hyper lattice h$_x$ and h$_y$ axes, which are decorated by an object (\) parallel to the X⊥ axis, as a result of rotation [5]. As depicted in Figure 2.5 [5], the atomic positions are the points where (\) intersects the X|| axis, and these points are labelled with L and S. In quasicrystals, the formation of approximant phases is caused by phason strain. Suppose that phason strain rotates the physical space such that the slope approximates the initial slope $1/\tau$. The slope could be 1/1, 1/2, 2/3, or 5/8 , are highlighted with red arrows in Figure 2.5. At these slopes, physical space intersects atomic surfaces and generates periodic sequences, LSLSLSLSLSLSLS..., LSLLSLLSLLSL..., LSLLSLSLLSLSLLS..., and LSLLSLLSLLSLSL..., respectively. These sequences with repeating unit cells LS, LSL, LSLLS, and LSLLSLSL produce approximants of 1/1, 2/1, 3/2, and 5/3 respectively. Higher order approximants resemble the corresponding quasicrystals even more closely [40, 38]. The lowest-order approximant is the 1/1, and successively higher order approximants such as 2/1, 3/2, 5/3, ... more closely approach the quasicrystalline structure.

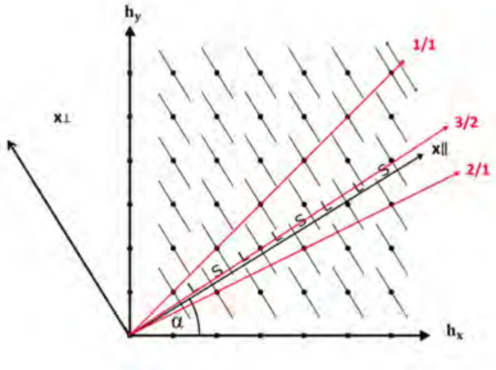

Figure 2.5: The transition from quasicrystalline to approximant phases is caused by phason strain [41].

2.11 Description of Structure of 1/1 Approximant Au-Al-Yb

When Cd atoms were replaced by an average atom $Au_{57.6}$ $Al_{42.4}$, a new quasicrystal Au-Al-Yb was produced [42]. This study represented the result of structural analysis of the quasicrystal and 1/1 approximant in the Au-Al-Yb alloy. Following that, new approximants are created by replacing M in the Au-M-R system with equal amounts of (Ga [43, 44], In[45], Si [46, 47], Ge[46, 48], and Sn [49, 50]) where R = Tb [8] and Gd.

The 1/1 approximant $Au_{49}Al_{36.2}Yb_{15}$ was identified using electron diffraction patterns, as shown in Figure 2.6. It revealed that the Laue class is $m\bar{3}$ and the cubic lattice is a body-centred (bcc) type with the lattice parameter a = 1.45 nm. These observations agree with the known properties of a 1/1 Tsai-type cubic approximant [42].

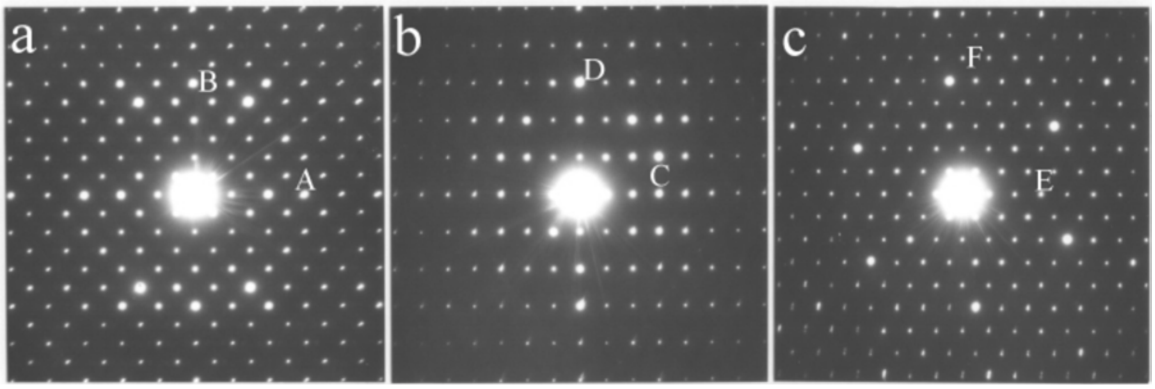

Figure 2.6: Electron diffraction pattern of $Au_{49}Al_{36.2}Yb_{15}$ 1/1 approximant showing three orientations: (a) [001], (b) [101] and (c) [111] [42].

The characteristic feature of the model is the chemical ordering between Au and Al beside the ordering of Yb that forms an icosahedron in Figure 2.7 (c). Other sites are occupied by mixed atoms of Au and Al except for the site named M8. The site M8 is occupied by Al with the occupancy 92% without Au. The mixed sites are classified into three groups; sites containing Au more than 72 %, sites containing Al more than 97 % and sites intermediate between them. Hereafter they will be referred to as Au-site, Al-site and mixed site, respectively. The unit cell includes 89.6 Au, 61.8 Al and 24.0 Yb, and thus 175.4 atoms in total. The composition of the model is $Au_{51.1}Al_{35.2}Yb_{13.7}$ that agrees with the composition $Au_{51}Al_{35}Yb_{14}$ analyzed by means of electron probe micro-analysis (EPMA) as well as the nominal one $Au_{49}Al_{36}Yb_{15}$. The small reduction of Yb in the analyzed compositions from the nominal one suggests evaporation of Yb during the sample preparation.

The approximants belong to a family of complex intermetallics known as Tsai-types, so called for their building block in the bulk, the Tsai-type cluster [12]. Tsai-type approximants and quasicrystals share this same essential component. The unit cell of the Au-Al-Yb 1\1 approximant is depicted in Figure 2.7(f). It is a body-centred (bcc) crystals (space group $Im\bar{3}$) with 168 atoms in a unit cell, which can be thought of as a bcc packing of Tsai-type clusters.

The structure of the 1/1 approximant can be construed as a periodic arrangement of chemically ordered Tsai-type clusters. It is constructed of a system of five hierarchical shells [22, 38], as shown in Figure 2.7(a) to (e). At the centre of the cluster, four atoms are included, which belong to M7 (mixed site) with an occupancy of 16.7%. This complicated shape reflects an average of variously-oriented 1^{st} shell (tetrahedrons) as discussed by Gómez and Lidin [38]. The 2^{nd} shell of Tsai-type cluster is a dodecahedron composed of M2 (mixed site) and M4 (Au-site) shown in Figure 2.7(b). The 3^{rd} shell is an icosahedron of Yb. The 4^{th} shell is an icosidodecahedron composed of M1 (Au-site) and M6 (mixed site) presented in Figure 2.7(d). Figure 2.7(e) presents a part of 5^{th} shell is triacontahedron on which atoms M5 (Al-site) and M3 (Au-site) are arranged alternatively. The arrangement of this polyhedron forms a cage network with holes both at the origin and the body-centre. The ordering scheme, namely preferential occupation by atoms, is very similar to that in $Au_{50.5}Ga_{35.9}Ca_{13.6}$ approximant reported by Lin and Corbett [51].

Eight years after the discovering of the binary (antiferromagnetic) approximants Cd_6R, the occurrence of antiferromagnetism (AFM) was demonstrated in ternary approximants Au-Al-R (R = Gd and Tb) after fine tuning of the composition inside the single-phase domain. The Au-Al-Gd polycrystalline alloy composition is $Au_{73}Al_{13}Gd_{14}$. The condition for the occurrence of the AFM order in the Au-Al-Gd approximant, is expressed in terms of the average electron-per-atom (e/a) ratio, assuming that Au is monovalent and both Al and Gd are trivalent [10]. It was found that e/a ∼1.54–1.56 [11].

The Au-Al-Gd 1/1 approximant is a body-centred-cubic packing of rhombic triacontahedral (RTH) clusters. The lattice constant is (Au-Al-Gd) is slightly similar (Au-Al-Tb: a = 1.475 nm, and Au-Al-Gd: 1.48 nm) [11], as shown in Figure 2.8(a). The structure of the (110) surface is bcc with two lattice constants, a = 1.48 nm and b = 2.05 nm, as shown in Figure 2.8(b). Figure 2.8(c) depicts the perpendicular plane along the [110] direction. The inner plane $d_{(110)}$ is 1.05 nm which corresponds to 0.5 z. As a result,the layers at $z \geq d_{(110)}$ are mirror planes of the layers at $z \leq d_{(110)}$.

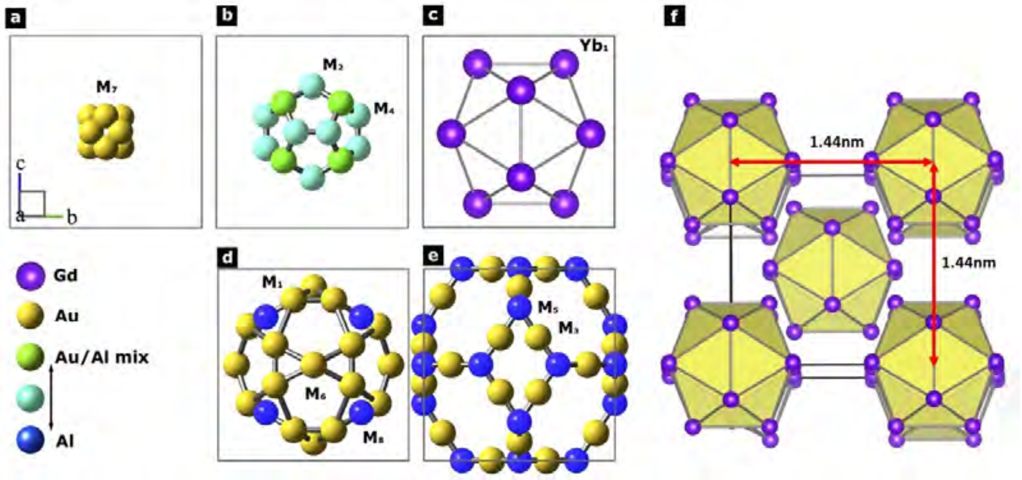

Figure 2.7: Tsai-type cluster's concentric shell structure in the Au-Al-Gd. A unit cell is displayed by a square frame. (a) Au atoms are arranged in an orientationally disordered tetrahedron at the M_7 site. (b) A dodecahedron's 2^{nd} shell constituted of mixed Au/Al atoms at the M_2 and M_4 sites. (c) An icosahedron's 3^{rd}shell consisting of Gd atoms (Yb1 site). (d) An icosidodecahedron's 4^{th} shell consisting of Al atoms and Au atoms (M_1 and M_6 sites) (M_8 site). (e) 5^{th} shell of a triacontahedron constructed of Al atoms and Au atoms (M3 site) (M5 site). (f) A Gd Body-centred cubic arrangement of the icosahedron in the Au–Al–Yb AC.

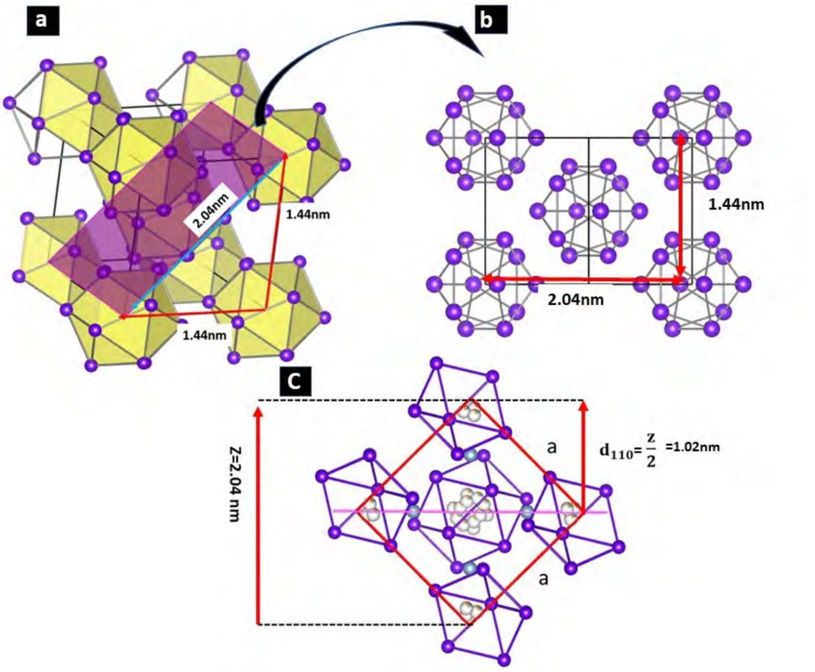

Figure 2.8: (a) structure of the Au-Al-Gd 1/1 approximant. The icosahedral clusters of the Tsai type form a bcc lattice. For clarity, only the Gd atoms are shown. (b) The structure of (110) plane shown, with only Gd icosahedral clusters. (c) A side view of an Au-Al-Gd 1/1 approximant unit cell with z = 2.04 nm shows the (110) plane perpendicular to [110], indicated by a pink line.

Chapter 3

Literature Review on Adsorption Studies

3.1 Introduction

This chapter will provide a brief summary of previous work on the clean of two and three–fold *i*–Ag–In–Yb quasicrystal surfaces, and Au-Al-Tb (111) 1/1 approximant surfaces. Furthermore, the growth of molecular thin films on quasicrystal surfaces will be reviewed.

3.2 Structure of the Two and Three-fold Surface of *i*–Ag–In–Yb Quasicrystal

Following the discovery of *i*–Ag–In–Yb quasicrystals, all high symmetry surfaces of this QC (five–fold [52], three-fold [28]and two-fold [53]) were investigated. All surfaces were found to form on a bulk plane intersecting the centre of the RTH cluster [54]. RTH clusters constitute the bulk structure of these quasicrystals. This section provides details of previous studies on two-fold and three- fold surface structures as they have been used in this study.

The first study of the structure of two-fold surfaces of *i*–Ag–In–Yb quasicrystals was by Cui *et al.* [53] using LEED and STM. This study described the surface of this quasicrystal as a bulk truncation of the Cd-Yb model. The LEED pattern shown in Figure 3.1(a) confirms the two-fold symmetry [53]. In STM, two step heights were discovered: S = 0.27 ± 0.03 nm and L = τ S = 0.45 ± 0.04 nm, which is consistent with the distribution of the cluster centre planes in the Cd-Yb model. Thus, the surface structure is expected to be described by the dense atomic planes intersecting the Cd-Yb cluster centres. However, STM does not achieve atomic resolution of two-fold the surface. [52, 28, 53].

The STM images taken at positive bias V = +1 V revealed rows separated by

1.57 nm. Figure 3.1(b) shows a section of the surface observed by STM from [53]. Figure 3.1(c) shows a clear row structure that corresponds to the distribution of the 5^{th} shell in the Cd-Yb cluster. In addition to the rows, isolated protrusions are also observed, separated by τ–scaled distances along the direction parallel to the row structure.

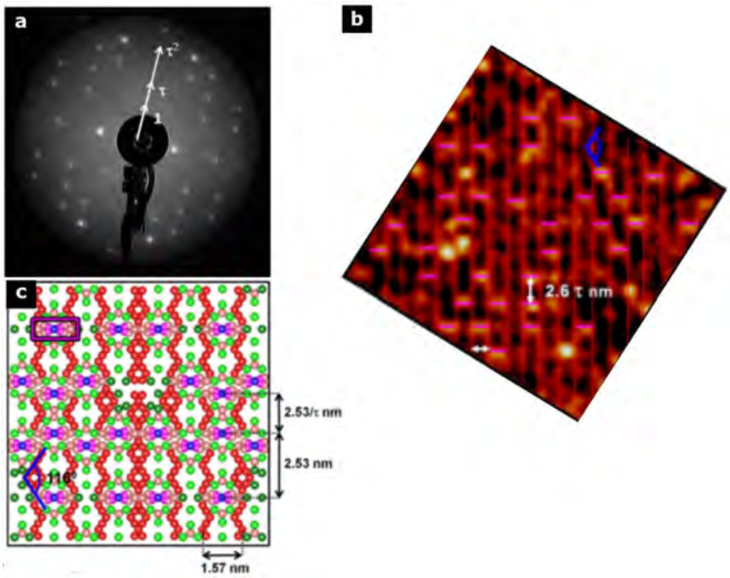

Figure 3.1: (a) LEED pattern of the two-fold *i*–Ag–In–Yb surface measured at an electron energy of 20 eV.(b) A high resolution STM image of the clean two-fold surface displaying a row-like structure. The image is enhanced by Fourier pass filtering (V_b = +1.1 V, 75 nm × 35 nm). (c) An atomic plane intersecting the RTH cluster centres in the *i*–Cd—Yb structure model used to explain the surface ; blue: RTH cluster centre, light green: Yb atoms, dark green: glue Yb atoms, red: Cd atoms in 5^{th} shell, light pink: Cd atoms in 4^{th} and 2^{nd} shells [53].

A recent study by Burnie *et al.* has demonstrated that the atomic resolution of two-fold surface of *i*–Ag–In–Yb depends on the bias voltage [55]. High-resolution STM images of terraces were found to be bias-voltage dependent. Figure 3.2(a) and (b) are STM images taken from the same surface with the same tip condition at positive and negative bias. The STM image taken under a positive bias (+2 V) shows bright protrusions aligned along the twofold and five-fold axes. This leads to the formation of large diamond features. The average small and large diagonals of the diamonds are 2.57 ± 0.08 nm and 4.19 ± 0.02 nm, respectively. The ratio of these two values is $\sim \tau$ (= 1.618..., the golden ratio). STM images taken at -0.8 V negative bias show the same diamond features as at positive bias, but with reduced size (highlighted in Figure 3.2(b)). The protrusions are again at the vertices. In addition, new protrusions of comparable size and contrast appear on the edges of the diamond. This results in a more pronounced alignment of the protrusions in the five-fold direction.

The STM images were compared with the bulk structural model of the *i*-Cd-Yb quasicrystal. Figure 3.2(c) is the in-plane structure (20 nm × 20 nm) of the plane cutting the centre of the RTH cluster (marked with black arrows). The diamond feature was found to consist of two motifs; triangles of three 3^{rd} shell of Yb atoms surrounding the 4^{th} shell of Ag/In and squares of four Yb atoms surrounding the 4^{th} dimer, as shown the inset right Figure 3.2. The vertices of the diamond feature are on one type of motif. Their size and geometry correspond to the diamonds appearing under positive bias. This supports the suggestion that the vertices of the solid black diamond are located at Yb-rich sites, resulting in the large bright protrusions observed at a positive bias. At the negative bias, the contribution to tunnelling current from the Ag/In sites is increased while the contribution from the Yb sites is suppressed. This results in smaller protrusions at the vertices of solid black tiles, as well as additional protrusions along the edges of the diamond (i.e., at the vertices of dashed tiles).

.

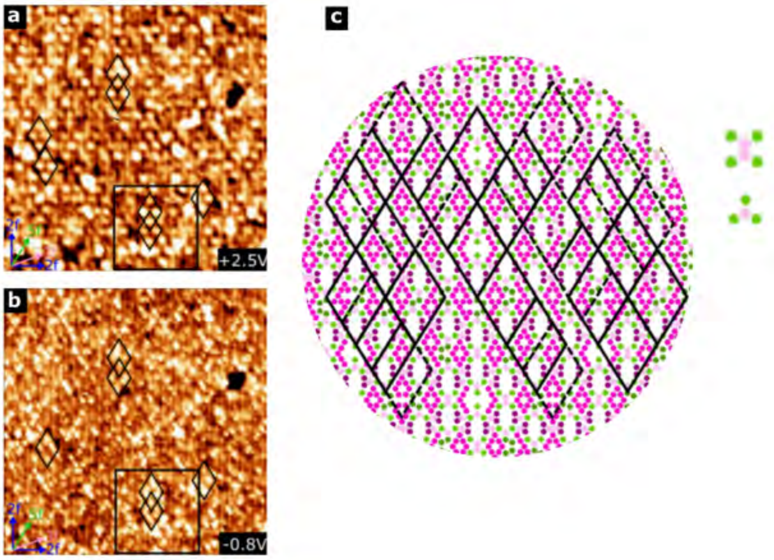

Figure 3.2: (a) and (b) STM images of the two–fold *i*–Ag–In–Yb surface at V_b= +2.5 V and -0.8 V, respectively (50 nm × 50 nm). (c) A model atomic plane intersecting the cluster centres (light green: 3^{rd} shell Yb, dark green: glue Yb, purple: 2^{nd} shell Ag/In, light pink: 4^{th} shell Ag/In and dark pink: 5^{th} shell Ag/In) [55].

The study of the three-fold surface structure of the *i*–Ag–In–Yb quasicrystal was reported by Cui *et al.* using STM and LEED [28]. Figure 3.3(a) depicts the LEED patterns of the three–fold *i*–Ag–In–Yb surface, which show a discrete three-fold symmetric diffraction pattern, with τ-scale points [28]. The STM images revealed terraces, which were separated by steps of different heights. The observed step heights in STM were found to be small (S = 0.12 ± 0.02 nm) and large (L = 0.43 ± 0.02 nm), as shown in Figure 3.3 (b).

High-resolution STM images of terraces were obtained only at positive voltages. The Ag/In positions are not resolved [52]. Figure 3.4(a) is the STM image showing the terraces at positive bias. The STM images show different motifs, small triangular, hexagons, and twisted hexagons. These features are marked in Figure 3.4(b) and shown enlarged in Figure 3.4(c). The edges of the large triangle and `"distorted"` hexagon are 1.61 ± 0.07 nm, 0.68 ± 0.07 nm, and 0.93 ± 0.07 nm, respectively. All triangles and twisted hexagons in the STM image have the same orientation.

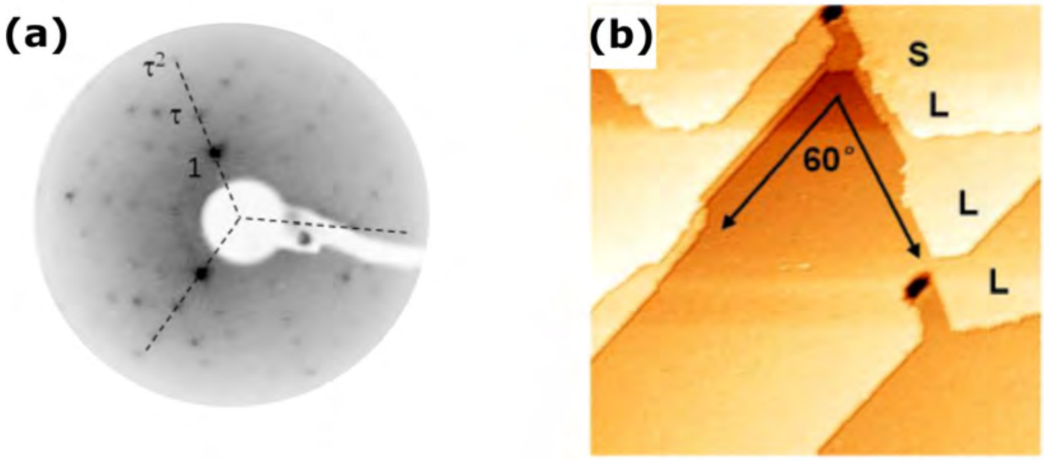

Figure 3.3: (a)LEED pattern taken from the three–fold *i*–Ag–In–Yb surface at energy of 20 eV. (b) Large-scale STM images of the three–fold *i*–Ag–In–Yb surface (300 nm × 300 nm) [28].

The motifs observed by STM were compared with the bulk structure model of the *i*–Cd–Yb quasicrystal. The motifs observed by STM are compared with the atomic structures of those planes that intersect the RTH cluster centres, as shown in Figure 3.4(e). Here, a series of triangles, hexagons, and `"distorted"` hexagons are associated with the Yb arrangement in the cluster centre plane. As demonstrated by a previous study on the five–fold surface of *i*–Cd–Yb, STM can only detect Yb sites under positive bias. Therefore, the Yb atoms are highlighted with large green circles in Figure 3.4(e). The distribution of Yb atoms in the model exhibits the same characteristics as those observed by STM in terms of size, orientation, and their assembly. These features are marked in Figure 3.4(e).

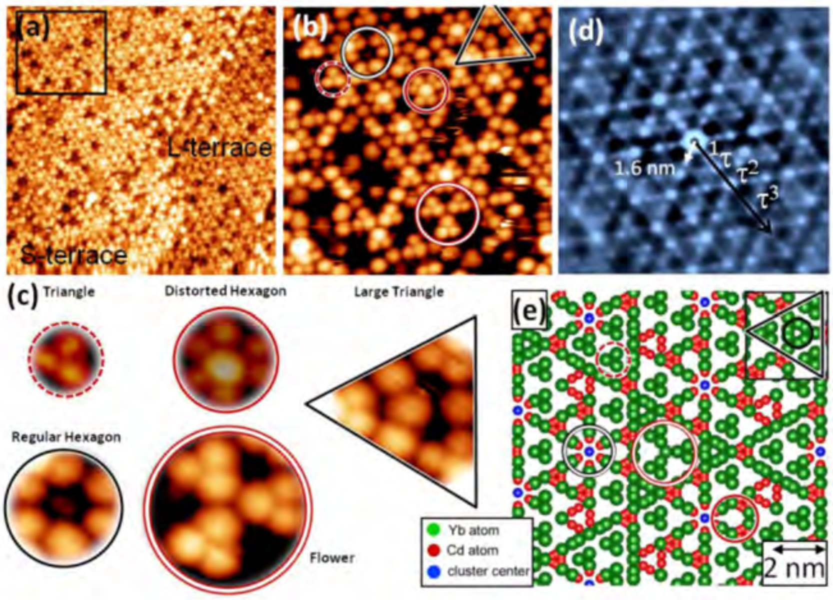

Figure 3.4: a) 50 nm × 50 nm STM image of two step heights S and L terrace made from a three–fold surface of *i*–Ag–In–Yb at a large scale (V_b = +1.1 V, I_t = 0.30 nA). (b) Enlarged view of the section highlighted in (a) (20 nm × 20 nm). Several motifs from this image are displayed and labelled in this (c). (c) Magnified views of triangles, distorted hexagons, large triangles, regular hexagons, and flower motifs are highlighted in (b). (d) An autocorrelation function of section of image (a), (15 nm × 15 nm). τ–scaled locations have been identified. (e) The surface's model plane. The motifs from (c) are highlighted: red and black circle is a distorted and regular hexagon, large red circle is flower motif, black triangle is a large triangle [28].

A recent study by Coates *et al.* [56] has confirmed that atoms are resolved at only positive bias. It was found that the surface is characterised by triangles, a distorted hexagon, and a `"flower"` feature. Highlighted with a white shield tile and triangle in Figure 3.5(a).

Figure 3.5(d) shows a partial model of three-fold of *i*–Ag–In–Yb quasicrystal, Yb atom is highlighted with a green dot. The Yb atoms are distributed in a small triangle with two orientations: up-triangle and down-triangle in the bulk model. The 4^{th} shell hexagons are surrounded by up and down Yb triangles. The motifs observed by STM were compared with the plane model of atomic structure of three-fold of the *i*–Ag–In–Yb quasicrystal. It was found that the distorted hexagon feature corresponds to the Yb triangle of three Yb small triangles, highlighted with a green triangle.

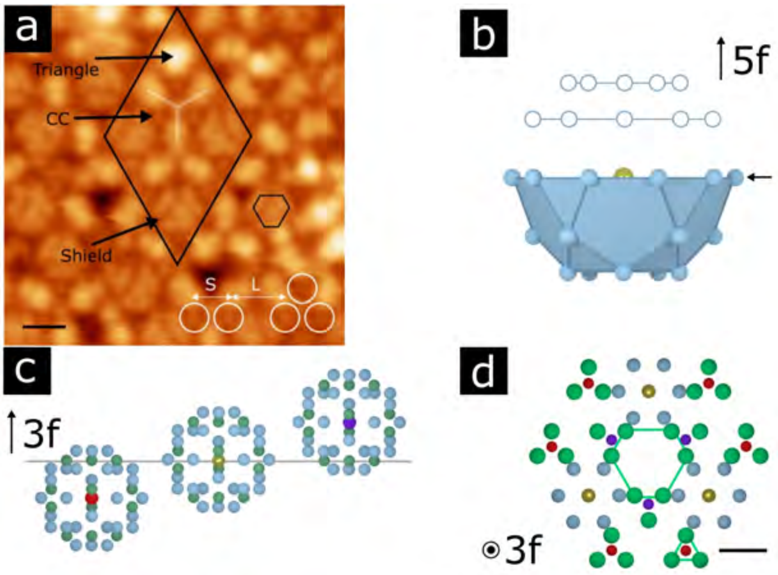

Figure 3.5: (a) STM image (V_b = 3.079 V, I_t = 0.119 nA) of the clean three–fold *i*–Ag–In–Yb surface. Marked are motifs previously observed in [28]. Surface cluster centres are also marked, either by an arrow (C C), or by white circles. (b) Side view of the fourth shell of a truncated cluster, oriented along its five–fold direction. The five–fold surface is marked with an arrow. The cluster centre is shown as a golden atom. Also shown are planes of atoms from the fourth shell if the structure were continued "above" the surface. (c) Side view of how truncated clusters contribute to the threefold surface. Horizontal scale is arbitrary. (d) Arrangement of truncated bulk clusters as observed on the surface. A distorted hexagon and a triangle are marked to compare to STM images. The scale bar is 1 nm.Reproduced from [56].

3.3 Structure of the (111) Surface 1/1 Au-Al-Tb Approximant

The surface of 1/1 approximant in Au-Al-Tb alloy was reported by Coates *et al.* using STM [8]. Large-scale STM images revealed a surface with flat terraces and a step-terrace morphology. A terrace kink angle with value of 119° ± 2°, is labelled with α in Figure 3.6(a). It corresponds to the three–fold symmetry expected from the bulk model structure. The step heights were measured using a histogram taken from an STM image, with the most frequent step height being 1.22 ± 0.04 nm, as shown in Figure 3.6(b).

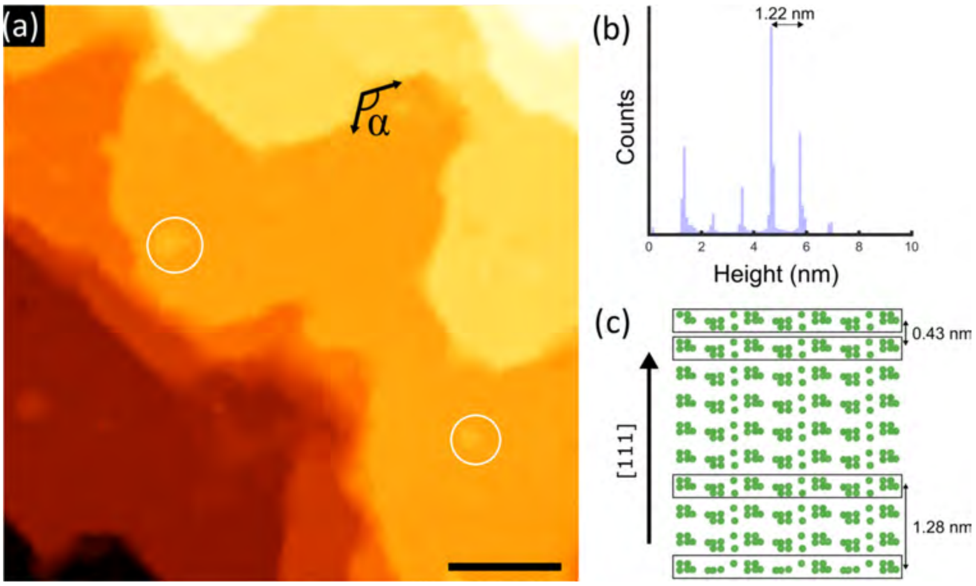

Figure 3.6: (a) STM image of the (111) surface's step terrace structure ((V_b = 2 V, I_t = 172 pA). The terrace kink angle is indicated here. Islands are denoted by white circles. The scale bar is 30 nm. (b) A histogram of the step height distribution derived from (a). The average step height is marked. (c) Tb planes arranged along the [111] direction in a bulk model. The distance between groups of three planes is 0.43 nm, as depicted. There are also groups of planes that correlate to the measured step height [8].

STM can be used to resolve the structure on these terraces, depending on the type of voltage bias used. The surface was decorated with a set of dimer-like bright protrusions arranged in a rhombohedral surface unit cell with lattice parameters a = 2.12 ± 0.07 nm, b = 2.10 ± 0.04 nm, and α = 58 ± 2° where highlighted vectors intersect the centre point of the dimers at positive bias, as shown in Figure 3.7(a). An ellipse demonstrates adjacent protrusions in dimers with a separation of 1.23 ± 0.03 nm. The dimers can potentially be seen as hexagons that enclose a dark contrast area, which is marked with a black hexagon.

Figure 3.7(b) depicts a different area of the surface observed at the same bias value as in Figure 3.7(a). The apparent change in morphology, where the dark centres of the hexagons in Figure 3.7(a) are resolved as low-intensity protrusions, may arise from a change in tip/tunneling conditions. A rhombohedral cell which includes the below-plane protrusion in the hexagon has the parameters c = 1.23 ± 0.07 nm, d = 1.24 ± 0.08 nm and β = 61 ± 2°.

The STM images taken at negative bias revealed the surface has a row structure, as shown in Figure 3.8 (a). It was found that 1.06 ± 0.09 nm is the distance between adjacent rows. A V-shaped protrusion was observed in the row structure, which is highlighted by a black circle. A V-shaped protrusion forms a marked rhombohedral unit cell between the bright rows, with the parameters a = 2.09 ±

0.06 nm and b = 2.15 ± 0.04 nm, i.e., the same unit cell dimensions (111). It was found that two-fold row structure is considered a missing-row structure in which several atoms of the unit cell in the topmost plane are removed.

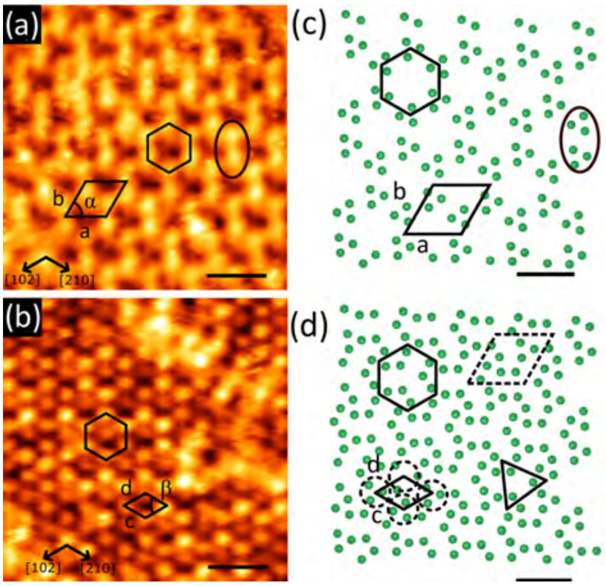

Figure 3.7: (a) STM image of surface showing the atomic structure of (111) facet of Au-Al-Gd (V_b = -1.9 V, I_t = 175 pA). A rhombohedral unit cell or hexagonal structure is formed by bright dimerlike protrusions (highlighted by an oval). The crystallographic axis is highlighted. The scale bar measures 3 nm. (b) STM image of surface showing additional features which appear dependent on tip condition (V_b = -19 mV, I_t = 175 pA). Rhombohedral and hexagonal cells are labelled once again. The crystallographic axis is highlighted. The scale bar measures 3 nm. (c) Model diagram of Tb atoms forming the structure in (a), marked with green circle,the features that correspond to each other (oval, rhombohedron, and hexagon) are highlighted. The scale bar measures 3 nm. (d) The model structure that was employed to explain the additional features in (b) [8].

.

The STM results were compared to the bulk model to explain the observed motifs on the surface. Firstly, the step heights, or terrace separations, are considered in terms of planes of atoms in the bulk model. The Tb slabs used to explain the step heights consist of three closely separated Tb planes. A side view of the Tb planes in the bulk, arranged perpendicular to the [111] direction, as shown in Figure 3.6(c). Three Tb planes form what we will refer to as Tb surface slabs, examples of which are bounded by black boxes. The distance between centres of these slabs is 0.43 nm. Therefore, the measured step height, 1.28 nm, can be considered as the separation between four slabs, as shown at the bottom of Figure 3.6(c). This number, along with the reported step height (1.22 nm), is 1.5 times larger than the spacing between adjacent lattice planes in the bulk, which is 0.8521 nm (where a = 1.4758 nm) [11].

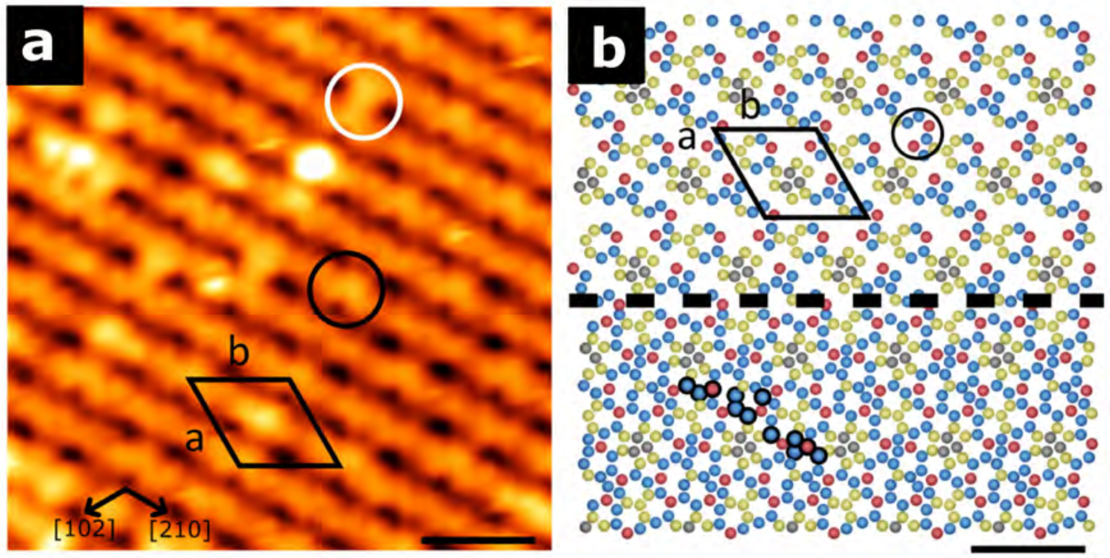

Figure 3.8: (a) STM image of terrace morphology (V_b = 1000 mV and I_t = 140 pA). V-shaped protrusions and a rhombohedral unit cell are highlighted by a black and rhombohedral shape. The scale bar is 3 nm. (b) structural model of (a). The positions of 1^{st}, 2^{nd}, 4^{th}, and 5^{th} shell Au/Al are depicted by the gray, yellow, blue, and red circles, respectively. Below the dashed lines is the truncated version of the complete model. The atoms that will be lost during the reconstruction process are highlighted by a black circle. Rhombohedral unit cell and V-shaped protrusion are highlighted above the dashed line in (a). (3 nm bar for scale) [8].

$$d_{(hkl)} = \frac{a}{\sqrt{h^2 + k^2 + l^2}} \tag{3.1}$$

The centre of these three planes can be used to understand the structure displayed in Figure 3.7(a). Figure 3.7(c) depicts a model of this plane composed of sets of Tb atoms arranged in triangles with 0.55 nm edge lengths and rotated 60° in relation to one another. These triangles are canted by around 7 degrees with respect to the surface vectors. Each bright protrusion detected corresponds to an individual triangle in Figure 3.7(c), which highlights the rhombohedral and hexagonal cells indicated in Figure 3.7(a). The experimental value of a = b = 2.09 nm was well matched by the model rhombohedral unit cell.

The tip tunnelling to the slab's lowest Tb plane explains the alternate positive-bias structure shown in Figure 3.7(b). This plane is displayed in addition to the middle Tb plane in Figure 3.7(d), where examples of the larger triangles are highlighted. It is formed of larger edge length Tb triangles (0.9 nm) with just one orientation. A dashed rhombohedron indicates the projected bulk unit cell. Dashed circles indicate the protrusions measured by STM.

As shown, the combination of these triangles results in a small rhombohedral cell with dimensions that match the experimental values of c = d = 1.21 nm. This study concluded that the surface terminates at the middle Tb plane because the structures in Figures 3.7(a) and (b) can be explained using just the bottom two planes of a Tb slab.

In addition, the STM data with negative bias were compared to the slab structure mode. Figure 3.8(b) shows the surface model considering all non-Tb positions. The 1^{st}, 2^{nd}, 4^{th}, and 5^{th} shell positions of Au/Al atoms are marked with gray, yellow, blue, and red. Black circles indicate the locations of 12 atoms, which are those that were removed from the surface unit cell to create the surface reconstruction. In STM images, this set of atoms appears as a V-shaped protrusion. Four of these groups are joined by the designated unit cell, with a = b = 2.09 nm, which again matches the experimental results.

3.4 Growth of Molecular Thin Film on Quasicrystal Surfaces

In recent years, there has been an increase in literature around quasi-crystalline epitaxial single-element films growth on quasicrystals. The most widely studied are the five-fold surfaces of Al-based quasicrystals, although there have also been studies of the five-fold surface of *i*–Ag–In–Yb and the tenfold surface of d-Al-Co. The most common molecules used to grow films on a quasicrystal are C_{60}, pentacene (Pn), benzene(C_6H_6), and corannulene ($C_{20}H_{10}$). Table 1 shows previous studies of molecular thin films.

Studies of quasicrystalline surfaces as deposition site for molecules are of greater interest. With the quasicrystalline surface, many varieties of atoms can be studied and investigated; surface characteristics and structure can be changed and manipulated in different ways. In addition, the surface reactivity can also be modified by depositing molecules. There are many open questions, particularly in relation to the formation of epitaxial systems.

Table 3.1: Previous studies of molecular thin film.

Molecular	Substrate	Growth temperature	Ref	Result
	five-fold i-Al-Pd-Mn	300K	[57]	disorder
C_{60}	five-fold i-Al-Pd-Mn	623K-673K	[58]	QCS film
	five-fold i-Al-Cu-Fe	773K	[7]	QCS film
	d-Al-Ni-Co	623K-673K	[58]	QCS film
	d-Al-Cu-Co	623K-673K	[58]	QCS film
	Pb/d-Al-Ni-Co	500-520K	[59]	ordered hexgonal islands
	two-fold i-Al-Pd-Mn	600K	[60]	QCS film
	Pb/five-fold i-Ag-In-Yb	300K	[61]	disorder
	five-fold i-Ag-In-Yb	300K	[62]	disorder
Pn	five-fold i-Ag-In-Yb	300K	[7]	QCS film
C_{20} H_{10}	five-fold i-Ag-In-Yb	423K	[63]	QCS film
C_{60}	Cu/five-fold i-Al-Pd-Mn	300K	[64]	periodic film
CO	d-Al-Ni-Co	300K	[65]	molecular adsorption bandvisible
C_6H_6	Al-Pd-Mn	100K	[66]	multilayer formation

Carbon-60 (C_{60})

Buckminster fullerene is a fullerene molecule consisting of 60 C atoms and takes the shape of a closed cage. The carbon atoms are bonded in a spherical, truncated icosahedron shape of regular pentagons and hexagons as shown in Figure 3.9. C_{60} is the smallest fullerene with a van der Waals diameter of 1.01 nm [67]. In most cases, C_{60} forms a covalent bond with surfaces. Carbon-60 is a good starting point for surface studies for two reasons: it is essentially isotropic (behavior similar to a giant atom) and has the same internal symmetries as an icosahedron [61].

Figure 3.9: Atomic model of C_{60} molecule.

Pentacene (Pn)

The pentacene molecule ($C_{22}H_{14}$) is a member of the family of organic compounds, and is composed of 5 fused benzene rings. A simple, atomic model for the pentacene molecule with dimensions 1.421 nm × 0.504 nm, is shown in Figure 3.10, where the C-C bond distance is on average 0.14 nm [68]. Pn molecules adsorbed on the surface can be imaged with a bias voltage either below the highest occupied molecular orbital (HOMO) or above the lowest unoccupied molecular orbital (LUMO). The shape of the orbitals will affect the apparent shape of the molecules in STM [69, 70].

Pentacene molecules have a tendency to form flat, complete layers on metallic substrates. This is due to the anisotropic shape of this planar oligomer and weak, intermolecular van der Waals interactions [71]. The orientation of adsorbed pentacene strongly depends on the electronic structure of the substrate. The organic/inorganic interfaces between the organic semiconductor and the gate dielectric as well as the contacting electrodes play a crucial role for the performance of organic electronic devices [72].

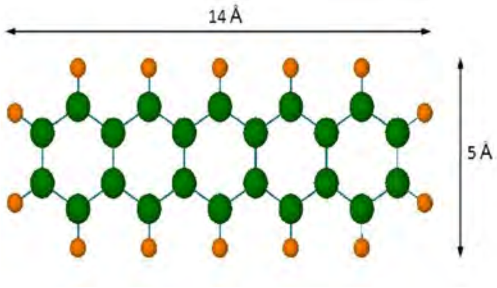

Figure 3.10: Atomic model of a pentacene molecule.

Growth of C_{60} on the Quasicrystal Surface

The first report of growth of C_{60} on QC has been made by Ledieu and Muryn *et al.* [57]. They showed that C_{60} growth on five-fold surface of *i*–Al–Pd–Mn at room temperature adsorption does not produce QC order. The scanning tunnelling microscopy (STM) images show the molecules adsorbed randomly on the surface, and the molecules appear with three different heights above the surface. However local τ-scaling relationships between molecules were identified with bonding of these molecules in five–fold hollow sites [57].

However, the first successful adsorbed C_{60} molecular quasicrystal on Al-based quasicrystals was achieved by Smerdon *et al.* [7]. They found that C_{60} molecules on five-fold surface of *i*–Al–Cu–Fe yield quasicrystalline order. The reason for successful growth was the growth temperature. The depositions of C_{60} were conducted on *i*–Al–Cu–Fe with the substrate temperature ranging from 773 K to 973 K. The autocorrelation pattern of molecular distribution shows ten-fold symmetry with long-range order, as shown in Figure 3.11(b). The STM image shows two types of molecules: bright (B) and dim (D). The B molecules are adsorbed on Fe atoms surface, and form a pentagon lattice with a = 1.2 nm. The D molecules are adsorbed atop subsurface Fe atoms, and form a pentagonal lattice with a = 1.9 nm. D molecules are lower than B molecules and their height is around 0.14 nm, as shown in Figure 3.11(a). These results confirm that the location of quasicrystal molecules depends on the distribution of the least abundant constituent element, which is reasonably well-evidenced for all five–fold quasicrystalline adlayers [7].

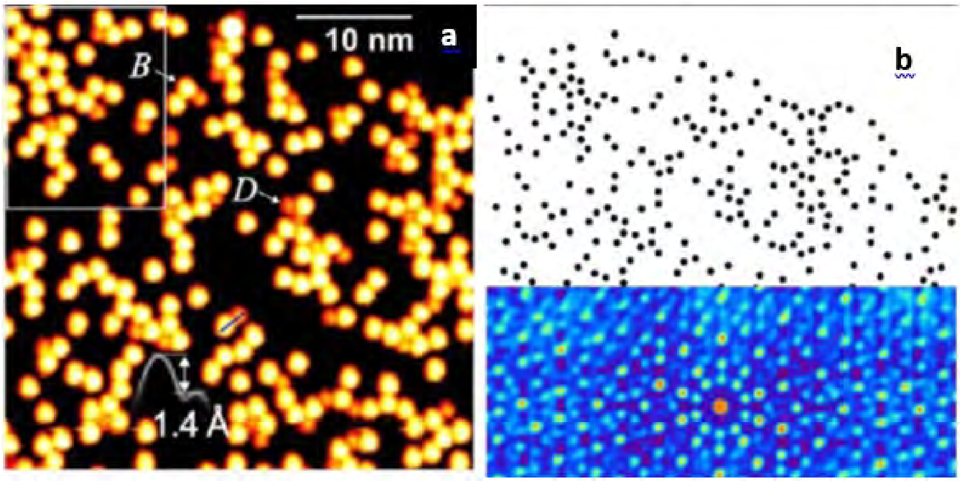

Figure 3.11: Quasicrystalline C_{60} layer on icosahedral Al-Cu-Fe. (a) STM image of C_{60} molecules deposited on *i*–Al–Cu–Fe surface. (b) Autocorrelation pattern shows ten-fold symmetry of the layer [7].

There have been reports on adsorption of C_{60} molecules on another type of Al-based quasicrystal. A study by Fournee *et al.* (2014) found that C_{60} molecules deposited on *i*–Al–Pd–Mn and *i*–Al–Cu–Fe exhibit quasicrystalline structures. The substrate temperatures used in this experiment were from 623 K to 673 K. The low-energy electron diffraction (LEED) pattern of deposition C_{60} on *i*–Al–Pd–Mn or *i*–Al–Cu–Fe confirms that the C_{60} molecules are five-fold quasicrystalline structure, as evidenced by diffraction spot positions with τ-scaling relationships. In addition, STM images at negative bias show two types of molecules: bright and dim molecules due to the height difference between them. D molecules are lower than B molecules, and the difference in their heights is equal to 0.1 nm, as in the case of the five-fold Al-Cu-Fe surface. They have pentagonl form with edge length of 1.26 nm, (Figure 3.12). Furthermore, this finding encouraged applying adsorbed C_{60} on decagonal quasicrystal surfaces such as decagonal (d)-Al-Cu-Co and the (d)-Al-Ni-Co. LEED pattern confirms ten-fold long-range quasiperiodic order of the film (Figure 3.13(b). The autocorrelation of the STM image shows the nearest-neighbor (NN) distance is 1.01 ± 0.01 nm. These molecules form pentagonal tiles of 2 nm length. The tiles are usually included by smaller pentagon length of 1.2 nm and take similar orientations (Figure 3.13(c)) [58].

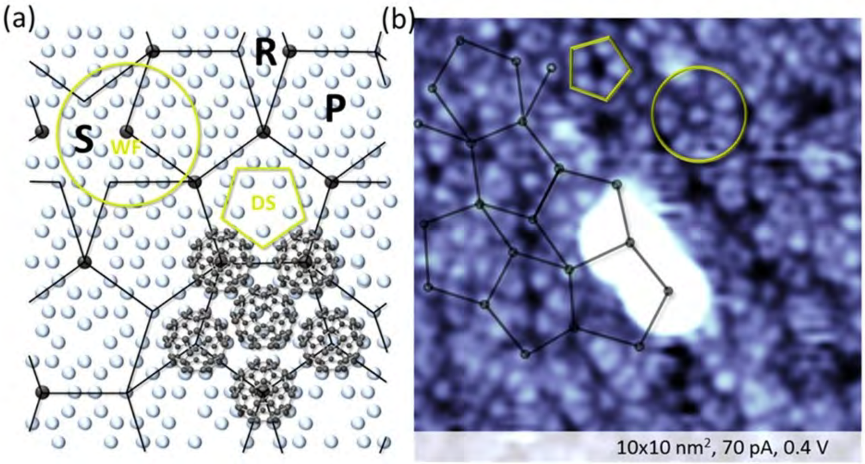

Figure 3.12: (a) Model structure of the five-fold surface of the Al-Pd-Mn QC. (b) STM image of the five-fold surface of the Al-Pd-Mn icosahedral quasicrystal. The white flower(circle) and dark star (pentagon) [58].

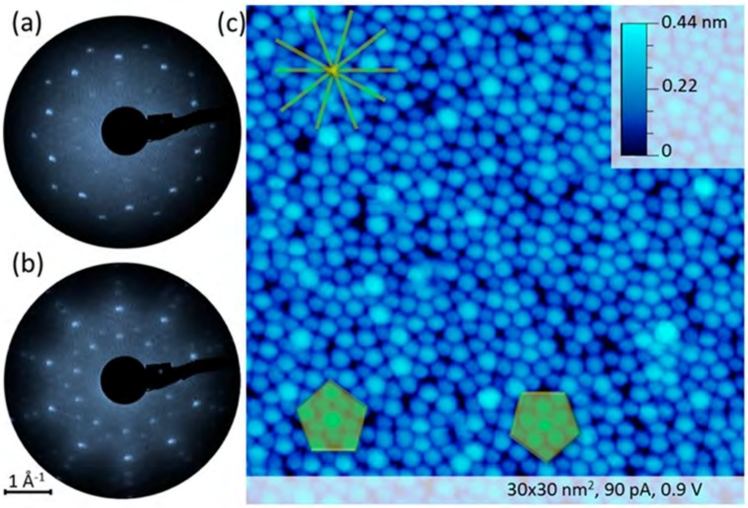

Figure 3.13: (a) LEED patterns of the clean ten-fold surface of the Al-Ni-Co decagonal phase. (b) of the C_{60} film formed on that surface. (c) STM image of the C_{60} monolayer formed on the ten-fold surface of the d- Al-Cu-Co decagonal phase [58].

An attempt to form a quasiperiodic C_{60} network on *i*–Ag–In–Yb substrates was unsuccessful. In 2011, Nugent and co-workers investigated the adsorption of C_{60} on five-fold *i*–Ag–In–Yb with a focus on step-terrace morphology. C_{60} was deposited on the sample at room temperature. They did not obtain any result from LEED or Fast-Fourier transform (FFT). The C_{60} molecules form a random distribution on the surface. The C_{60} molecules stick on surface due to formation of strong bond. Also, C_{60} molecules were unsuccessfully deposited at high temperature; the reason for this may be the energy of adsorption is smaller for C_{60} on Ag-In-Yb [62]. There are two types of molecules which successfully grew quasicrystal molecular films on the five-fold surface of i–Ag–In–Yb: Pentacene (Pn) and corannulene ($C_{20}H_{10}$).

Growth of Pentacene on the Quasicrystal Surface

In 2014, Smerdon *et al.* demonstrated pentacene (Pn) adsorption on i–Ag–In–Yb and formed a quasicrystalline structure. The substrate temperatures during deposition were 300 K. Figure 3.14(a) is an STM image of the five-fold surface after Pn was deposited. Single Pn molecules are shown by the rod shapes. That was the first demonstration of quasicrystalline molecular ordering on a template by the use of a molecule other than C_{60}.

As illustrated in Figure 3.14(b), the autocorrelation function of the distribution of Pn molecules exhibits maxima with ten–fold symmetry. The spots are positioned at τ-scaling distances (where τ is the golden mean), indicating that the molecules are ordered in a quasicrystalline film. Moreover, the autocorrelation functions show the quality of the quasicrystalline ordering is better when the orientation of the Pn molecules is included, as shown in Figure 3.14. This report demonstrates that orientation is important to enhancing the shape of patterns [7]. Also, the STM image shows Pn in a four-lobe pattern and this is not observed in any other STM studies of Pn on metal surfaces.

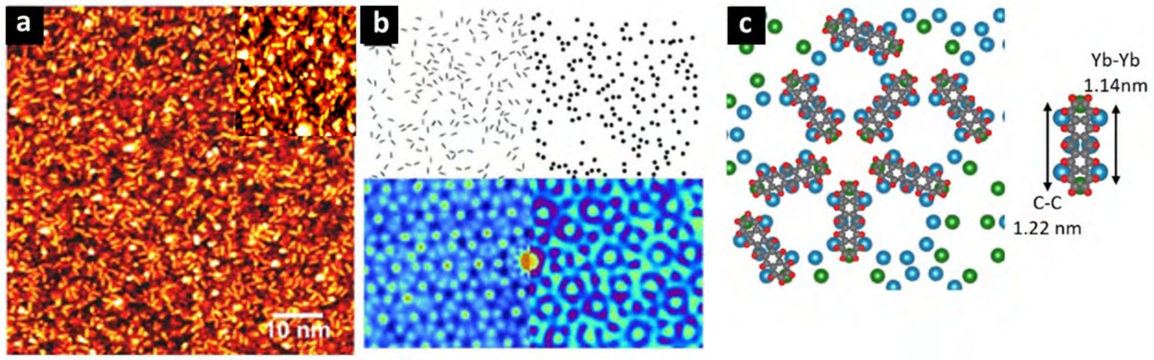

Figure 3.14: (a) High-resolution STM scans of Pn layer on five-fold i–Ag–In–Yb quasicrystal surface (V_b = 2 V, I_t = 0.2 nA). (b) The autocorrelation functions show the molecular positions extracted and plotted with (left) and without (right) orientation [7]. (c) The model diagram shows the adsorption sites of Pn on a five-fold i–Ag–In–Yb surface. Green: 3^{rd} shell Yb and blue: 4^{th} Ag/In shell. Red and gray are the H and C atoms of the Pn molecules [6].

The orientation and separation between molecules were compared with the atomic structure of the intersecting RTH cluster centre. Figure 3.14(c) is the in-plane structure of the plane which cuts the centre of the RTH cluster. Yb atoms are presented, marked with green dots. The distance between Yb atoms corresponds to the size of Pn. It was found that the arrangement of Pn matches Yb sites.

Recently, the (111) surface of the 1/1 Au-Al-Tb approximant crystal was used as a template to grow a Pn film [73]. STM images were obtained at low and high coverages of Pn on the surface. Figure 3.15(b) shows an STM image at coverage approximate 0.3 ML. Some locations and orientations of molecules appear to be more preferential than others. Molecules oriented in the [011] direction, i.e., perpendicular to the Au/Al row direction, were found to be more popular. A number of examples are highlighted by black circles. Furthermore, the STM images revealed the most stable adsorption sites were those that produced Pn orientations that were roughly perpendicular to the row direction of the substrate (0°). Conversely, the perpendicular two-fold orientation (90°) was relatively unstable, with a large proportion of these molecules diffusing. The autocorrelation function taken from only the molecules confirmed the rhombohedral pattern, with lattice constant are a = 1.26 ± 0.08 nm, b = 1.28 ± 0.05 nm as shown in the of right Figure 3.15(b).

All molecules aligned in the [011] direction occupy two triangular sublattices, which together form a honeycomb structure. Figure 3.15(b) shows some examples marked with black hexagons and red/blue circles. A fully occupied unit cell of the red distribution is also highlighted, with c = 2.23 ± 0.06 nm, d = 2.35 ± 0.07 nm, which is twice the size of the lattice as measured from the autocorrelation function.

It was found that the dimension of the rhombohedral lattice of the autocorrelation function and the orientation and position of Pn in STM images correspond to the Tb triangle distribution throughout the surface. The sublattice/honeycomb structure labelled with the red/blue sites matches up with the distribution of small Tb triangles at the surface, as shown in Figure 3.15(a). It depicts a section of model Tb atoms at the surface [8], illustrating this relationship. Blue and red circles surround two small triangles at the bottom, which are each distributed on rhombohedral lattices of c = d = 2.09 nm across the surface. These triangles are canted = 7° in the direction of [011], and they can also be linked by a black hexagon, with the triangles' centres highlighted with either red or blue dots.

Therefore, the Pn molecules appear to adsorb at Tb atomic sites, similar to Pn adsorption on *i*–Ag–In–Yb surfaces with a strong rare-earth atom/molecule interaction. The model adsorption sites were identified in this study. It was suggested that at least one benzene ring is pinned between two Tb atoms, or that at least one benzene ring is directly on top of a Tb atom (or both). Furthermore, the higher Pn coverage of approximately 0.7 Ml was investigated at ambient temperature. The STM image revealed a saturation of feasible adsorption sites, resulting in a film with structural order but rotational or orientation disorder, as shown in Figure 3.15(c). The effect of post annealing this film to 600K was exhibited in the study, as illustrated in Figure 3.15(c). The majority of the Pn molecules were perpendicular or parallel to the Au/Al row direction, i.e., vertically or horizontally.

The adsorption sites of the molecules were indicated by coloured arrows or bars, with eight potential sites identified. The Pn molecules are highlighted as blue and red motifs in the structure model in Figure 3.15(d). The colours of the Pn motifs correspond to the vertical sites. The extra adsorption positions were observed, indicating that post-deposition annealing creates new adsorption sites.

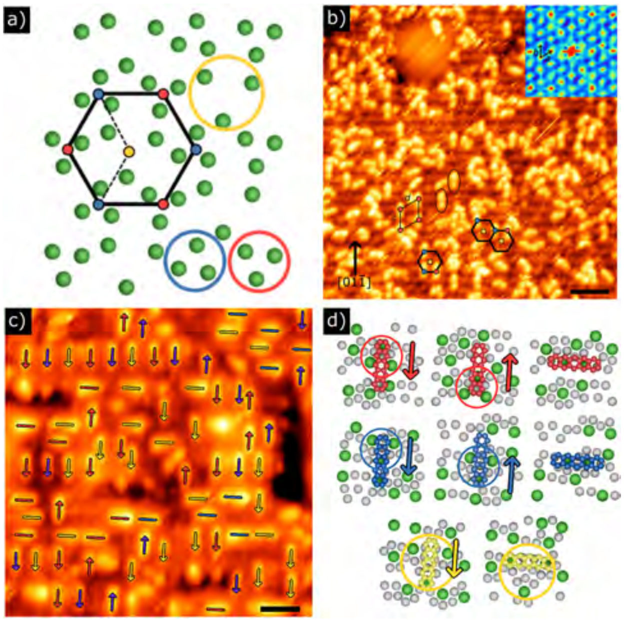

Figure 3.15: (a) Model structure of the (111) surface of the 1/1 Au–Al–Tb approximant. The first shell and 2^{nd} shell, the 3^{rd} shell, 4^{th} shell and 5^{th} shell are highlighted with gray, yellow, green, blue, and red dots, respectively. The triangular adsorption sites are highlighted. (b) After deposition of Pn, STM image of the Au–Al–Tb(111) surface (coverage = 0.3 ML, V_b = 1.9 V,I_t= 0.3 nA, the image size is 40 nm × 40 nm). An autocorrelation function of the molecule centres is shown in the inset, along with unit cell vectors. (c) STM image of the same surface following deposition of 0.7 ML coverage of Pn at room temperature and annealing at 600 K (V_b = 1:8 V, I_t = 0.3 nA, 12 nm × 12 nm). The adsorption sites of molecules are indicated by coloured arrows and bars. A total of eight potential locations have been identified. (d) A representation of the substrate's structure showing Pn adsorption sites. The Tb shell and Au/Al shell are marked with green and gray circles [73].

.

Growth of Corannulene ($C_{20}H_{10}$) on the Quasicrystal Surface

Kalashnyk *et al.* studied the growth of a five-fold symmetric corannulene ($C_{20}H_{10}$) molecular quasicrystal which was grown on five–fold *i*—Ag-In-Yb. The molecules were studied at 423 K. The analysis was carried out using STM and LEED. The LEED pattern proved the molecular film adopt a long-range quasiperiodic order as shown in Figure 3.16(b). This pattern shows ten-fold symmetry. STM characterisation shows the formation of a complete monolayer of corannulene on the substrate. Also, the size of the single feature corresponds to the size of free corannulene. Furthermore, a close-up STM image shows the bowl-shape corannulene molecules can be positioned in the site above the Yb atoms, which leads to the formation of a ten-fold symmetric feature, as shown in Figure 3.16(c). The radius of the corannulene ring is 2.12 nm, which matches with the bulk model. The autocorrelation image demonstrates the short, $S = 1.6 \pm 0.1$ nm and long, $L = 2.5 \pm 0.1$ nm distance between spots. The ratio of L to S corresponds to the golden mean $= 1.618$ and follows the Fibonacci series. The success of the growth of a ($C_{20}H_{10}$) molecular film is because the molecular a has which pentagonal ring surrounded by five benzene rings and is bowl-shaped, may approach the symmetry of the surface, the presence of hydrogen at its rim might enhance the adsorbate-substrate interaction [63].

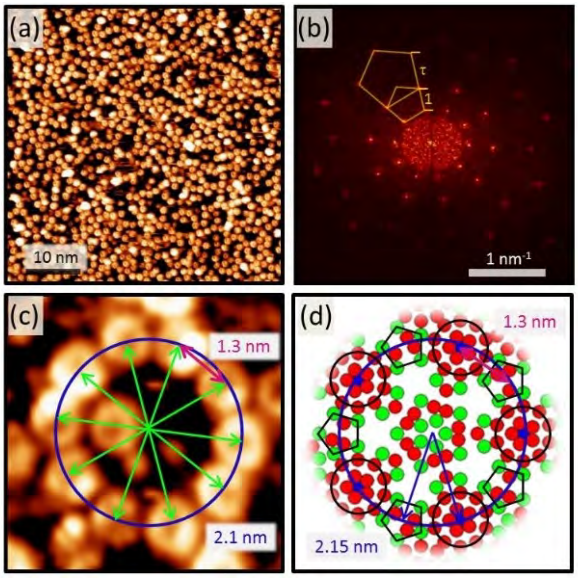

Figure 3.16: (a) STM image of corannulene monolayer grown on the five-fold *i*–Ag–In–Yb surface. (b) LEED pattern from the molecular film. (c) Close-up STM image of a molecular ring composed of 10 corannulene molecules. (d) Corresponding model illustrating the preferential corannulene adsorption on Yb-and (Ag, In)-based sites [63].

A few studies have been done at temperatures below room temperature. For example, Benzene (C_6H_6) was found to adsorb in a disordered manner at the surface of Al-Pd-Mn at 100 K, and completely adsorbed from the surface at 150 K. The adsorption molecules were detected by a mass spectrometer [66]. Also, carbon monoxide deposited at room temperature on the ten-fold surface of d-Al-Ni-Co was found to cause the complete disappearance of the LEED pattern from the clean surface after a 20 L exposure, indicating disordered adsorption [65].

Growth of C_{60} on Single-Element Quasicrystals Surface

Single-element quasicrystals can act as templates for molecules to deposit and align in a structural, ordered arrangement. C_{60} molecules were grown on a quasiperiodic Pb film which was adsorbed on the ten-fold surface of d-Al-Ni-Co. The molecules tended to form ordered hexagonal islands. This close-packed structure indicates that the C_{60}-C_{60} interaction dominates and the substrate potential corrugation is too shallow to trap the C_{60} molecules in a quasiperiodic array [59].

In 2008, Smerdon *et al.* studied the adsorption of C_{60} on Cu/five-fold Al–Pd–Mn. Adsorption occurs at room temperature (300 K). The adsorption behaviour of C_{60} on the aperiodic film appeared different as compared to deposition on single crystal Cu surfaces. Room temperature led to decreased mobility of molecules, and causing them of stick where they impinged on the surface rather than to form islands. At higher coverage (above 0.5ML C_{60}), there are some suggestions for reconstruction of the underlying Cu film in the observed different heights of adjacent rows of aligned C_{60} molecules [64].

There have been studies in adsorption of C_{60} on the Pb/five-fold *i*–Ag–In–Yb surface. The growth of both Pb and C_{60} was carried out at room temperature. The Pb first forms quasicrystalline layers and then periodic islands are formed atop. Adsorption behavior of C_{60} depends on the type of Pb allotrope. C_{60} molecules adsorb at edges of islands although the tops of island are uncovered. C_{60} form hexagonal close packed (hcp) islands between a step or island edges. In contrast, C_{60} molecules grows randomly on the quasicrystalline Pb layer. This may be because of a far greater barrier to diffusion of C_{60} presented by the sparse quasicrystalline Pb film on *i*–Ag–In–Yb [61].

Chapter 4

Experimental Methods

4.1 Introduction

This chapter provides a description of the equipment used during the project. The reasons surface experiments must be conducted in an ultra high vacuum (UHV) system are explained. Finally, sample preparation procedures and surface analysis techniques, including low energy electron diffraction (LEED) and scanning tunnelling microscopy (STM) are explained.

.

4.1.1 Importance of UHV for Using in Study Surface Properties

A crystal's surface properties can only be studied when the surface is clean. The presence of molecules in the UHV chamber has a significant effect on the surface, which can also affect the accuracy of the results obtained. These molecules can be absorbed on the surface by physisorption or chemisorption. In addition, contamination can affect the aperiodic arrangement of the atoms on the surface of the quasicrystals, which have been used as templates for the growth of single-element films with aperiodic arrangements. To avoid this, experiments are carried out using a vacuum technique, which has proven to be successful [74].

4.1.2 Ultra-High Vacuum

To maintain the clean surface clean and free of undesired gases, all quasicrystal investigations must be carried out in ultra-high vacuum (UHV). The Ultra high vacuum also helps to avoid unwanted particle interference, such as electrons and ions, when employing techniques such as LEED.

An ultra–high vacuum chamber is constructed of solid, corrosion resistant, low outgassing materials, such as stainless steel or mu-metal. Substances with a high vapor pressure should not be used since they will evaporate, raising the ambient gas pressure inside the chamber. While the chamber is at atmospheric pressure, gases such as water vapour and carbon monoxide are absorbed into the inside walls, lengthening the period for out-gassing. A bake out process is required to achieve UHV. The temperature is raised to 400-500 K for 1-2 days while under vacuum. The bake out removes water vapour and any other remaining gases absorbed on the UHV chamber's internal surfaces. After bake-out is complete and the chamber is cooled to ambient temperature and then individual components are degassed further by being heating up individually to ensure gases are desorbed. All of the available pumps are used to achieve a pressure of roughly 10^{-10} mbar.

Ultra High Vacuum (UHV) is defined as pressures which are in the range between 10^{-5} and 10^{-12} mbar (atmospheric pressure is 1000 mbar). This pressure is taken as standard for surface experiments. The UHV chamber used in this project consists of three parts: the main chamber, pump, and experimental techniques. Each of the elements is explained in detail below.

4.1.3 UHV Pumping System

The main parts of the UHV system consist of the pumps, valves, and gauges. To achieve the desired pressure of 10^{-10} mbar, several pumps are needed, the four used in the current chamber include: the rotary vane pump, the turbo molecular pump, the titanium sublimation pump (TSP) and the ion pump.

Rotary Vane Pump

The rotary vane pump is used to achieve a pressure of about 10^{-3} mbar, initially starting from atmospheric pressure. A roughing pump must be robust enough to pump a chamber down from atmospheric pressure to a low enough pressure for the turbo molecular pump to start functioning. The cross section of a rotary vane pump is depicted schematically in Figure 4.1(a). The rotary vane pump consists of a rotor that rotates within a stator that is cylindrical in appearance. The rotor has vanes that are compressed against the stator's walls by a spring or centrifugal force. The compressed gases in the inlet side are released through the exhaust valve into the atmosphere [75, 76, 77].

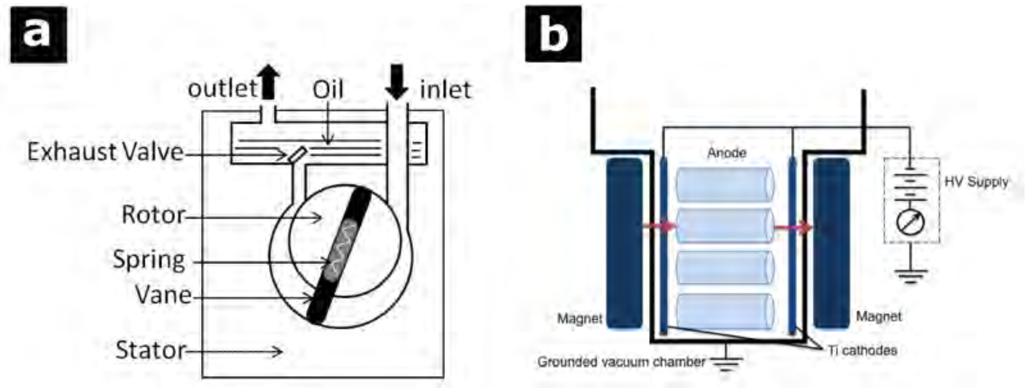

Figure 4.1: A schematic illustration of the types of pumps: (a) rotary vane pump. (b) ion pump [78].

Turbomolecular Pump

The turbomolecular pump uses a high-speed turbine to push gas molecules out of the chamber. The lowered number of molecules in the volume decreases the pressure. The average turbo molecular pump operates in a large range of 10^{-2} - 10^{-10} mbar. This pump removes heavier particles, but other elements are needed for elimination of hydrogen and helium.

Ion Pump

The ion pump belongs to the group of capture pumps due to the gas molecules being trapped inside the pump. It usually operates at a pressure below 10^{-5} mbar, while a pressure of around 10^{-11} mbar can be maintained. Ion pumps are constructed with stainless steel anodes that are mounted between two titanium cathodes. Anodes and cathodes are positioned within a powerful magnetic field that is parallel to the cylindrical axes of the anodes. Approximately 7 kV of high voltage is applied between the electrodes (anode and cathode) [77]. Figure 4.1(b) illustrates the ion pump. An ionisation (ion) pump is used for pressures lower than 10^{-8} mbar. Most gas particles are removed with this pump, however there also remains the risk of residues being left in the system, due to lighter particles being present.

Titanium Sublimation Pump (TSP)

The next pump that is used is the titanium sublimation pump (TSP). This pump requires low pressure in order to be effective. It is a type of `"getter pump"` that removes gases such as CO and O_2. TSPs are very successful when used in conjunction with ion pumps to quickly remove residuals from any sudden degassing of the ion pump.The following describes the operational mechanism of this pump. An electric current flows through a Ti-coated filament, causing the Ti to sublimate. Due to the reaction between the sublimated Ti and residual gases in the chamber, such as oxygen or hydrogen, a non-volatile compound will form on the chamber's walls, reducing the chamber's gas pressure for a period of time.

Ion Gauge

The most common pressure gauge is an ionisation (ion) gauge. The ion gauge, usually works between 10^{-4} mbar and 10^{-10} mbar. The pressure is measured based on the ion current and ionisation rate, because molecules inside the system are ionized.

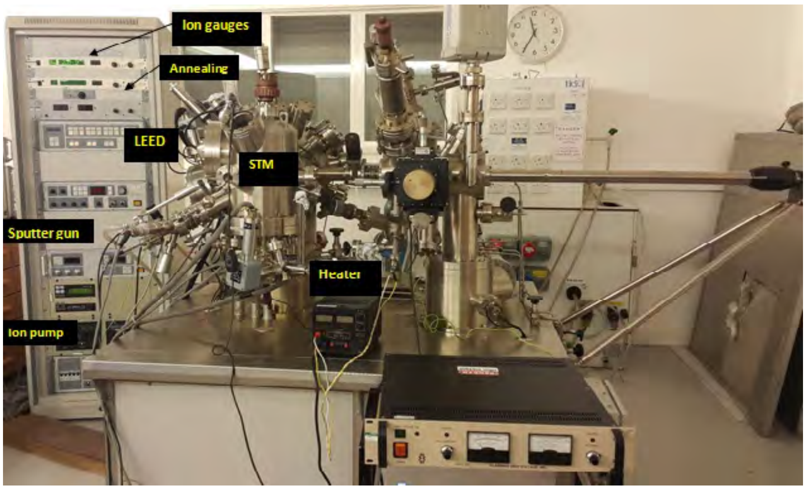

Figure 4.2: Omicron VT-STM UHV system.

4.2 Sample Growth

The samples used in this thesis have been grown with three different methods: the Bridgeman method to grow *i*–Ag–In–Yb quasicrystals, the self flux method to grow both Au-Al-Gd 1/1 approximants [79], and the Czochralski method to grow the Ga_3Ni_2 crystal [80].

Single-grain quasicrystal ingots can be synthesised using normal crystal growth techniques e.g. Bridgman, flux-growth. The most common technique used to grow quasicrystal samples is the Czochralski technique. The Czochralski method [81] uses a 'seed' crystal, typically oriented along a specific direction, which is attached to a 'pull rod'. This seed crystal is inserted into a molten solution of the correct stoichiometry of the desired alloy, which is held in a crucible. The seed is then pulled slowly from the molten mixture, and rotated as it is pulled. As the pulled mixture cools, it crystallises, Figure 4.3. Similarly, the Bridgman method uses a seed crystal inserted into a melt. Here, the molten mixture is cooled gradually from the seed end, either using a heating element with a temperature gradient, or by slowly pulling the crucible through two (high and low) temperature zones [82].

The floating-zone method employs a polycrystalline 'feed' rod of the same composition of the target quasicrystal. Here, a heating coil creates a high temperature zone which melts the polycrystal as it is pulled through. Single-crystal growth occurs by moving this 'floating zone' from the bottom to the top of the feed rod. Finally, the self-flux method relies on the fact that for some QC alloys, the solid QC is in equilibrium with its melt in its phase diagram. Here then, the correct ratio of pure constituents is melted in a crucible or tube, and slowly cooled. For each type of growth method used, a detailed phase diagram for the relevant mixture of constituents is needed for successful growth. Quasicrystal samples are cut along the required crystallographic direction from the ingot grown. The quality of the sample structure is then determined using x-ray or electron diffraction.

The quasicrystal samples were carefully polished to significantly reduce the surface roughness on the macro-scale. The surface was polished with different grades of diamond paste (from 6 to 0.25 μm). After polishing the surface by each grade for 15 minutes, the sample was cleaned of contaminants using an ultra-sonic bath of methanol. The resulting surface is sufficiently flat for many surface science techniques.

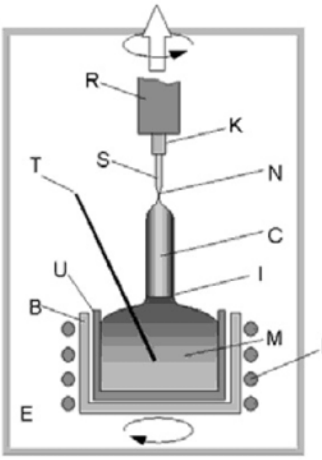

Figure 4.3: Set-up used in the Czochralski crystal growth technique. C: crystal grown M: melt U: protecting envelope E: heater, Z: hot zone, R: pulling rod, N: thin neck, S: seed crystal, K: seed carrier, T: thermocouple, B: susceptor. Reprinted from [83].

4.3 Surface Preparation

4.3.1 Sputtering

Argon ion bombardment was used to remove any surface contamination. These argon ions are produced in the ion gun and accelerated towards the sample. The interaction between positive argon ions and the surface gives enough energy to remove contamination from the surface. Using Ar^+ (2.5-3 keV) at a base pressure of 2.5 × 10 $^{-5}$ mbar, the samples for this thesis were sputtered for 30 minutes, with an average drain current recorded at 7-6.5 μA.

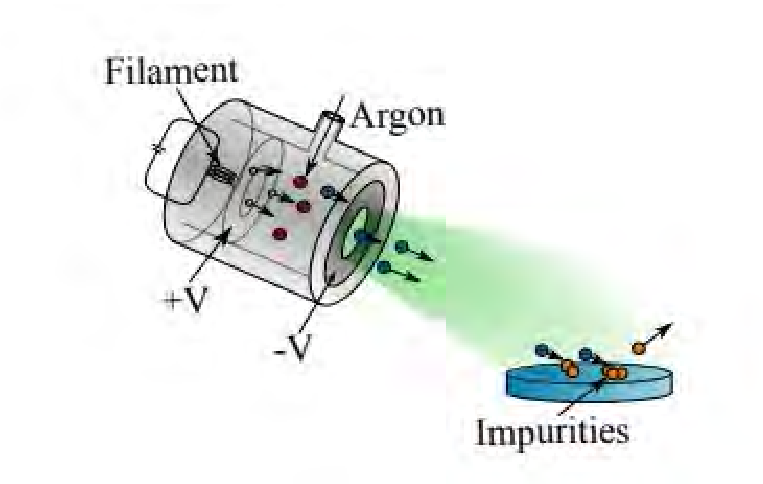

Figure 4.4: Setup of an Ar^{+} ion gun during the sputtering process. Momentum transfer from the incident ions causes the contaminant species in addition to the substrate material to be removed [84].

4.3.2 Annealing

The sputtering process changes the structure of the surface; however, this can be recovered by the subsequent annealing process, through the process of heating to about half of the melting point temperature at a very low pressure. Sufficient energy is given to the surface atoms to allow them to move to their equilibrium positions in order to minimize the total surface energy. Quasicrystal temperature was measured with a pyrometer with an emissivity of 0.35 [85]. The emissivity of a crystal when measured with a pyrometer depends on several factors, including the crystal's composition, surface finish, and temperature. The emissivity of a crystal could be 0, but it was not clear in a pyrometer; for this reason, 0.35 was used.

4.4 Molecular Thin Film Growth

Physical vapour deposition is employed to form thin films in UHV. This method involves the sublimation of a high-purity evaporant source towards the sample surface. Electron beam evaporators (e–beam) are utilised to achieve this. To evaporate the substance from a rod or container, Knudsen cell evaporators use conductive and radiative heating provided by a filament (typically wire). For materials with low melting points, such as noble metals, this type of evaporator is utilised.

Electron–beam evaporators use electron bombardment to locally heat a rod or crucible containing evaporant. Thermally emitted electrons from a filament are attracted towards a positivity biased rod or crucible. Crucibles are normally constructed from alumina, molybdenum or stainless–steel. The evaporant can reach higher temperatures than in the Knudsen cell evaporator and since the electron beam is directed at the evaporant the out-gassing of the surrounding surfaces is reduced during operation.

In this study the evaporator used for molecular deposition was based on the principle of the Knudsen cell, as illustrated in Figure 4.5. It was made from a glass tube surrounded by a wire, which was used to heat Pentacene. Pn powder was put in the glass tube. The was degassed at low temperature in order to remove the adsorbed gases on edge of the tube before starting the molecular deposition.

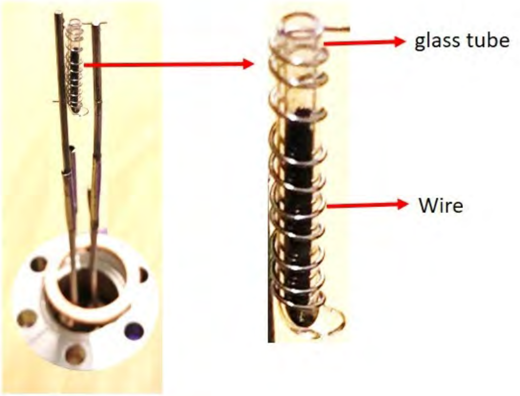

Figure 4.5: Photograph of evaporator used in the experiment for molecular deposition.

4.5 Surface Techniques

4.5.1 Low Energy Electron Diffraction (LEED)

UHV led to the development of several experimental techniques. Low energy electron diffraction (LEED) has become a widely used method to analyse surface structures, providing information on the structure and morphology of surfaces. The main principle of LEED is the elastic scattering of low energy electrons incident normally onto a crystal surface [86]. Electrons in the energy range of 20-200 eV are used.

There are two reasons for the use of electrons in this energy range. The first reason is that the electrons need to have a wavelength (λ) similar or smaller than the lattice parameter (a) ($\lambda \leq$ a) to interfere with the ordered layers at the surface.

The second reason is to obtain data only on the top layers (typically (10–30) A°). If we consider an electron with defined energy, its wavelength is given by the de Broglie relation

$$\lambda \ = \frac{h}{p} = \frac{h}{\sqrt{2mE_k}} \tag{4.1}$$

where ($\hbar$) is Planck's constant, m is the mass of the electron, and E_k is the kinetic energy.

When a beam of electrons strikes the crystal surface, it produces a set of well-defined pattern of diffracted beams that are arranged in a characteristic geometry according to Bragg's law. This mode contains information about the arrangement of atoms in the crystal [87].

Bragg's law geometry for X-ray diffraction from crystal surfaces separated by d_{hkl} is shown in Figure 4.6. An electron beam impinges perpendicularly on a one-dimensional chain of atoms with an interatomic spacing of (a). When electrons from two adjacent atoms are backscattered at a well-defined angle with respect to the surface normal, the radiation must travel a path difference (Δ d) to reach the detector. According to Bragg's law, the path difference must be equal to an integral number of wavelengths for constructive interference to occur when the scattered beams eventually meet and interfere at the detector, which is given by [88]:

$$2d_{hkl} \sin\theta \ = n\lambda \tag{4.2}$$

where d$_{hkl}$ $= \frac{a}{\sqrt{h^2+k^2+l^2}}$ is the inter planar spacing, n is an integer, θ is the angle between the incident beam and crystal plane and λ is the wave length. The above equation is expressed as:

$$\Delta d = a \sin\theta \ = n\lambda \tag{4.3}$$

$$\sin\theta \ = \frac{n\lambda}{a} \tag{4.4}$$

As a result, the following information was obtained:

1. Since sinθ is proportional to 1/a, the diffraction angle decreases as the inter-atomic distance increases, resulting in narrowly spaced scattered beams.
2. Sinθ is inversely proportional to the kinetic energy of incident electrons (E_k in equation 4.1), so the diffraction angle decreases as the energy of the incident electrons increases, resulting in more visible diffraction spots.

The magnitude of the wave vector of the incident electrons is give by [89]:

$$|k| = \frac{2\pi}{\lambda} \tag{4.5}$$

$$|k| = \frac{2\pi}{a} \tag{4.6}$$

The distance between diffraction spots in κ-space is $\frac{2\pi}{a}$=a*, which is identified as the reciprocal lattice vector.

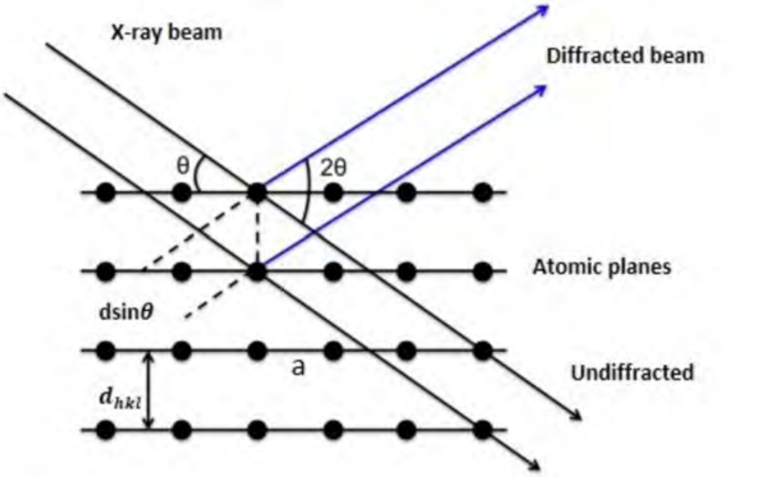

Figure 4.6: Schematic depicting of Bragg's law geometry.

Diffraction can also be explained in terms of Laue's equations. The condition for diffraction is; the incident electron has a wave vector K$_\circ$ and the scattered electron has a wave vector K.

$$K - K_\circ = G_{hkl} \tag{4.7}$$

When both vectors have the same magnitude (elastic scattering), the reciprocal lattice vector (G$_{hkl}$) is given by;

$$G_{hkl} = ha^* + kb^* + lc^* \tag{4.8}$$

where a*, b*, and c* the reciprocal spacing vectors lattice, related to real- space lattice vectors a, b,and c by

$$a^* = \frac{2\pi b \times c}{a.(b \times c)}, b^* = \frac{2\pi c \times a}{b.(c \times a)}, c^* = \frac{2\pi a \times b}{c.(a \times b)} \tag{4.9}$$

Diffraction thus provides quantifiable data about a crystal [77].

4.5.1.1 Ewald Sphere

Laue's law of diffraction can be graphically depicted utilising the Ewald sphere construction. To construct the Ewald sphere, one must first construct the crystal's reciprocal lattice. Draw Ko with an origin selected such that Ko terminate at a reciprocal lattice point. Then, draw a sphere with a radius of (K $= 2\pi/\lambda$) and a centre at the origin of Ko. Find all reciprocal lattice points on the sphere's surface, then connect the scattered wave vector K to these points. Figure 4.7(a) illustrates the construction of the Ewald sphere.

The 2D reciprocal lattice points in the LEED instance are represented by reciprocal lattice rods that are perpendicular to the surface. In a 2D lattice whose periodicity is infinite in the normal direction ($|c| \rightarrow \infty$ thus $|c^*| \rightarrow 0$), which causes the density of reciprocal lattice points to be infinite along the normal direction, these rods are created. In this instance, the scattered wave-vector of diffracted beams can be defined as the intersection locations of reciprocal rods with the Ewald sphere [77]. Figure 4.7(b) depicts the Ewald construction for diffraction on a 2D surface.

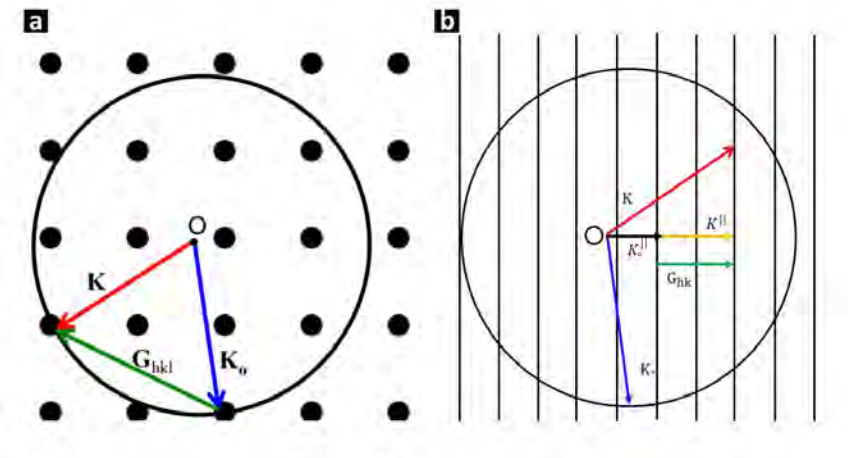

Figure 4.7: Schematic depiction of Ewald sphere construction for diffraction from (a) a three-dimensional lattice and (b) a two-dimensional lattice. .

4.5.1.2 LEED Apparatus

A schematic representation of a LEED set-up is shown in Figure 4.8. The LEED system comprises of an electron gun, a sample holder for the single crystal, and a fluorescent screen to collect the diffracted beam. Variable levels of voltage are used in order for the electrons to be accelerated. After the initial acceleration, the electrons beam is directed to the surface. Electrons are both elastically and inelastically scattered back from the surface. The fluorescent screen follows the last grid, which analyses the diffracted electrons that have been accelerated by a voltage of several kilovolts and these beams produce a pattern of bright spots which appears on the screen.

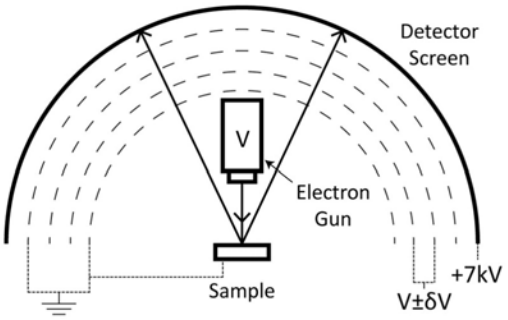

Figure 4.8: Diagram of the low energy electron diffraction (LEED).

4.5.2 Scanning Tunneling Microscopy (STM)

Binnig and Rohrer invented scanning tunnelling microscopy (STM) towards the end of the twentieth century [90]. This technique is widely used to examine quasicrystals, as well as for imaging conductive surfaces in general. The components of an STM system are a sharp conducting tip, usually made of tungsten (W) or platinum-iridium (Pt-Ir), a piezoelectric controlled scanner, feedback electronics for sample-tip separation, a vibration isolation system, a distance control and scanning unit, and finally a computer system to display the data. Figure 4.9 illustrates the main components in a schematic diagram. The interaction between the electron wave functions of a sharp metal tip and a conductive sample surface is the basis of STM. If a voltage is applied between when the two solids are brought into sufficiently close proximity (nearly 1nm), electrons will tunnel across the gap. The tunnel current depend sensitively on the tip–sample separation.

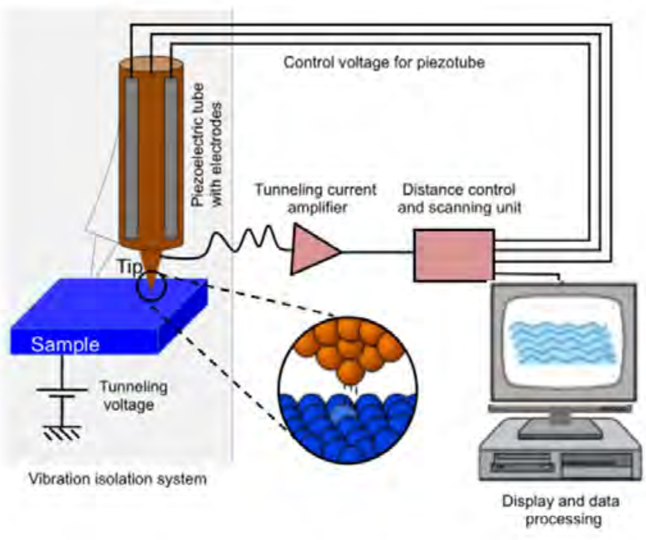

Figure 4.9: Schematic illustration of scanning tunneling microscopy (STM)[78].

STM is based on the quantum tunnelling phenomena, which has been studied by physicists since the 1920s, when quantum mechanics was first introduced [91]. Despite being classically forbidden, quantum tunnelling allows electrons to flow between two potential wells separated by vacuum. If the electron energy is smaller than the barrier height, it is classically reflected. In quantum mechanics, however, there is a small possibility that the electron will not be reflected but will instead tunnel through the barrier. Because electrons have wavelike qualities, tunnelling is a result of this wavelike nature. Within the potential barrier, electron waves do not suddenly terminate at the wall, but instead decay exponentially. Two examples of an electron wave approaching a barrier are shown in Figure 4.10. The barrier is too thick for the wave to pass through to the second section in the first case, thus it decays to zero before reaching the other side. The wave has not decayed to zero by the time it reaches the other side in the second instance, thus there is a small possibility that the electron will be located on the other side of the barrier [92].

The wave function (z) of the electron in quantum mechanics, satisfies the Schrodinger equation

$$\frac{-\hbar^2}{2m}\nabla^2\psi(z) = E\psi(z) - U\psi(z) \tag{4.10}$$

where ∇^2 is $\frac{\partial^2}{\partial z^2}$, m is mass of the electron, $\hbar$ is Planck's constant, E is the total energy of the electron, and U is the height of the barrier (potential energy). The solution to equation 4.10 for a region where E $\geq$ U(z) will be;

$$\psi(z) = \psi(0)e^{(\pm ikz)} \tag{4.11}$$

where κ is the wave vector and is defined by;

$$k = \left(\frac{\sqrt{2m(E-U)}}{h} \right) \tag{4.12}$$

Substituting $\sqrt{-(U-E)} \sim \mathrm{i}\kappa$ (where $\sqrt{1} = \mathrm{i}$) into equation 4.11 for a classically forbidden region (E $\leq$ U(z)).

$$\psi(z) = \psi(0)e^{(\pm iikz)} \tag{4.13}$$

The solution of the Schrodinger equation is given by:

$$\psi(z) = \psi(0)e^{(-kz)} \tag{4.14}$$

In this situation, κ is the decay constant that describes the electron decay state, and it is given as follows:

$$k = \left(\frac{\sqrt{2m(U-E)}}{h} \right) \tag{4.15}$$

When a bias voltage is applied between the tip and the sample in scanning tunnelling microscopy (STM), electrons tunnel through the vacuum and produce a current known as the tunnelling current (I), which depends exponentially on the tip-sample separation (d) and the average work function of the sample and tip (ϕ) [92]. The tunnelling current (I) in STM may be expressed using the equation below.

$$I \propto e^{-kd} \tag{4.16}$$

There is a barrier (work function) at the surface that prevents electrons from leaving the solid and reaching the vacuum level E$_{vac}$ [93]. According to classical mechanics, a barrier that is higher than a particle's energy cannot be penetrated. Particles can pass a region with a barrier higher than their energy in quantum mechanics. The average work function ϕ is defined by;

$$-\phi = (E-U) \tag{4.17}$$

Inserting this into 4.15 results in the following solution of the Schrödinger equation in the region of the potential barrier where κ is given by;

$$k = \left(\frac{\sqrt{2m\phi}}{h} \right) \tag{4.18}$$

Putting equation 4.18 into equation 4.16gives;

$$I = C.e^{-\sqrt{\phi}d} \tag{4.19}$$

where C is constant. Because of the exponential relationship, a very small change in the tip-sample separation results in a relatively substantial change in current. The exponential relationship allows changes that are less than a fraction of the atomic height to be detected.

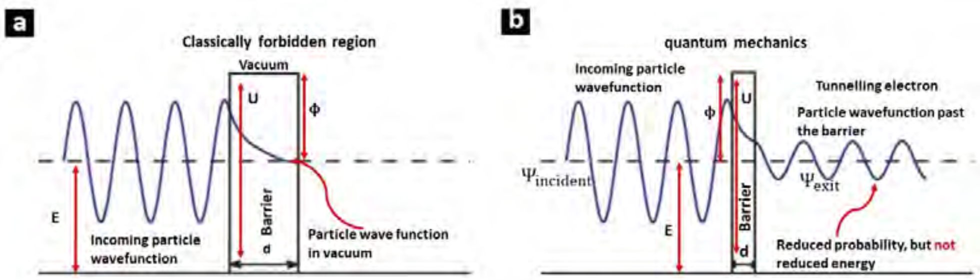

Figure 4.10: Two examples of an electron approaching a barrier. (a) the barrier is too thick and the wave decays to zero before reach the other side of the barrier. (b) The wave can cross through to the other side of the barrier [93].

When scanning metal surfaces, the image is usually considered to be representational of the surface's topography. However, once molecules or compounds that display covalent bonding are scanned, they can become less well related. Covalent bonds might appear brighter than atoms in STM images due to the confined nature of the electrons in them; therefore, attention must be given while analysing STM images. It's also possible that different atoms from various elements in the surface have a significantly higher, or dominant, density of states under the scanning conditions, making them appear significantly brighter than neighboring atoms despite there being no physical difference in height.

As mentioned above,The tip-sample bias is an important factor in cases where scans are not accurate representations of surface topography. Atoms with a highly localised density of states may prefer to tunnel an electron from the tip into their highest occupied molecular orbital (HOMO) or receive an electron from the tip into their lowest unoccupied molecular orbital (LUMO). When scanning molecules on surfaces, this has a significant effect on the intensity of that atom or pixel in the scan image. While scanning pentacene molecules, Repp and Meyer *et al* demonstrated this [80]. The molecule appeared as a rod when the bias was put anywhere in the molecular band gap, but the microscope was able to image the orbitals by setting the bias at or beyond the LUMO (positive V w.r.t. tip) and HOMO (negative V w.r.t. tip).

There are two modes for scanning the tip. The constant current mode that keeps the tunnelling current constant as the tip scans across the surface through the use of a feedback loop. This feedback loop instructs the tip to retract (approach the surface) whenever the current increases (decreases). Thus, the resulting variation in tip height with tip position is recorded as an STM topography image. The alternative mode is constant height.The constant height mode is the second mode. As a tip at a fixed initial height is scanned across the surface, the current is permitted to vary, and the current variation is recorded as the STM image [94]. Constant current is commonly employed for routine STM imaging, whereas the constant height mode is frequently employed on atomically flat substrates to prevent tip collisions during scanning. Notably, the dependence on tunnelling currents requires that STM measurements be conducted only on conducting surfaces. Figure 4.11 depicts a schematic of the STM's operating principle for both constant current mode and height mode.

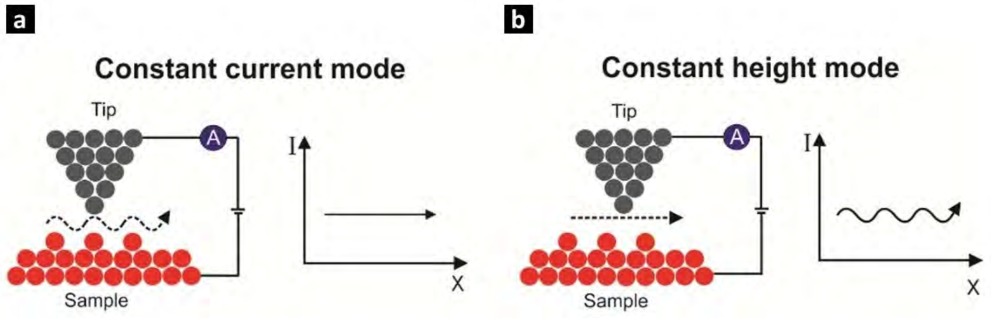

Figure 4.11: The schematic shows the two scanning modes of tip in the STM : the constant current mode (left) and the constant height mode (right) [95].

4.5.3 STM Image and Analysis

In STM imaging of quasicrystals, the real-space image shows the local density of states (LDOS) of the material at the surface. The image analysis in this thesis was carried out using the WSxM and Gwyddion software package [96, 97]. This package includes Fast Fourier transforms and autocorrelations as analytic tools.

The Fast Fourier Transform FFT of the STM image provides a representation of the spatial frequency content of the LDOS, and the inverse FFT can be used to transform this frequency-domain data back into the real-space domain [98, 99, 100]. The FFT pattern of the STM image can be used to determine the arrangement and orientations of the atoms on the surface. If the quasicrystal contains a periodicity that is related to the golden ratio, then the FFT should reveal a visible spot at an arrangement related to the golden ratio (τ). As shown in Figure 4.12. If a high-resolution image is used, it may be possible to observe a pattern similar to the symmetry and long-range order found in LEED patterns.

The quasiperiodic structure of a material can be seen in the real-space representation of the FFT of the STM image of a quasicrystal. The real-space image obtained from selecting specific frequencies in the inverse FFT of the FFT of an STM image of a quasicrystal is a two-dimensional matrix. The overall structure of the image reflects the quasiperiodic structure of the material and can be used to identify the local symmetry and ordering of the atoms.

The two-dimensional autocorrelation function [100] can be used to analyse the periodicity of the diffraction pattern in a quasicrystal, providing evidence of the presence of the golden ratio and Fibonacci sequence. The autocorrelation function shows two distances, long (L) and short (S), between visible spots in the diffraction pattern. As illustrated in Figure 4.12(c) and (d). The ratio between L and S is close to the golden mean (τ). The two distances are arranged following the Fibonacci sequence.

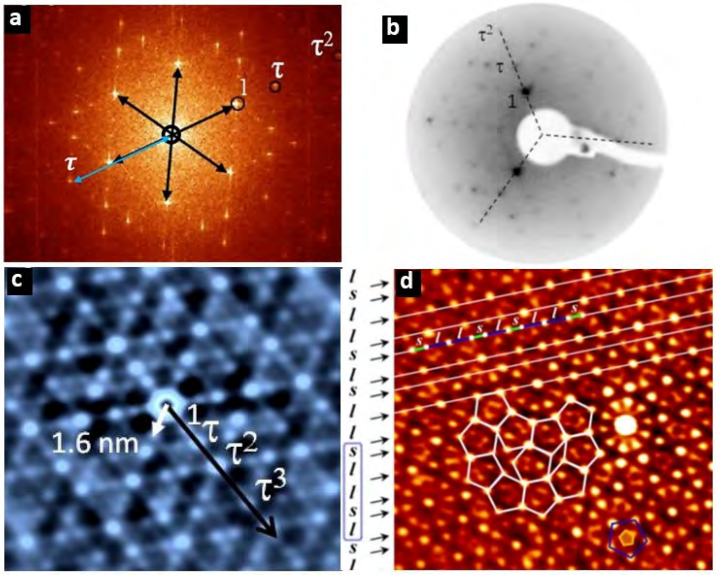

Figure 4.12: (a) FFT pattern of the three-fold i-Ag-In-Yb surface shows six-fold pattern with maxima located at τ-scaling distances. (b) LEED pattern obtained at 20 eV from the three-fold i-Ag-In-Yb surface. (c) Autocorrelation function of the three-fold i-Ag-In-Yb surface showing τ-scaling maxima [28]. (d) Autocorrelation function of corannulene layer growth on the five-fold i-Ag-In-Yb surface shows the spots form a Fibonacci sequence [63].

Chapter 5

Growth of Thin Film of Pentacene on the Surface of the *i*-Ag-In-Yb Quasicrystal

5.1 Introduction

The growth of Pn molecules on the five–fold surface of i–Ag–In–Yb quasicrystal provides the motivation for further investigations to test Pn adsorption on other high-symmetry surfaces of the same quasicrystal [7]. This chapter provides the results of Pn growth on the two- and three-fold surfaces of the i–Ag–In–Yb quasicrystal. Scanning Tunnelling Microscopy (STM) was used to study the growth.

5.2 Experimental Details

Single-grain i–Ag–In–Yb quasicrystal samples were grown using the Bridgman method [34, 101]. After that, the sample was cut perpendicular to the two-fold and three-fold axes. The sample was polished using 6 μm, 1 μm and 0.25 μm grades of diamond paste. After polishing with each diamond paste, the sample was immersed in an ultrasonic bath for 25 minutes to remove any contamination. Once the surface was in ultra-high vacuum, it was sputtered with 2.5 keV Ar^+ ions for 30 minutes, followed by annealing at 430 °C for two hours; this cycle was repeated several times. The pressure during annealing was 2×10^{-9} mbar. A handmade tube evaporator was used to evaporate the Pn molecules, keeping the sample at room temperature. STM images were acquired using the Omicron STM (VT-STM) system.

5.3 Pentacene Growth on the Two-fold Surface

5.3.1 Substrate Structure

To understand the growth of Pn, we first must study the structure of the clean surface. The structure of the two–fold surface was previously described by Cui *et al.* [53] and Burnie *et al.* [55]. STM images of the clean surface show similar features to those previously discussed [55]. The STM bias was set at a voltage between +1.5 V and -1.5 V. Figure 5.1(a) shows atomically resolved STM images of the surface at a positive bias voltage of + 1.5 V. The STM image exhibits two motifs: the center rectangle protrusions and a diamond, which are coloured blue and green, respectively. These features are enlarged and numbered 1 and 2 in Figure 5.1(b). It was found that the edges of the rectangles are aligned along the vertical and horizontal two–fold axes, with average dimensions of 4.07 ± 0.12 nm and 2.51 ± 0.08 nm, while the edges of diamond features are aligned along five–fold axes, with the average length of the large and small diagonals of the diamonds being 4.1 ± 0.17 nm and 2.51 ± 0.15 nm. These values are consistent with the previously reported results [55].

Figure 5.1(b) shows that the structure of these two features is overlapping, and one of the diamond diameters is represented by one of the edge lengths of a centred rectangle. Moreover, the locations of the diamond features relative to the rectangles are variable. Two complete diamonds were observed side to side, as shown in Figure 5.1(b). An Fast Fourier Transform (FFT) of Figure 5.1(a) shows a set of spots which are τ-scaled in five-fold axes, as shown in the inset in Figure 5.1(a).

The autocorrelation function of the STM image of Figure 5.1(a) shown in Figure 5.1(c) displays bright spots arranged along both five–fold axes, with separations of 2.15 ± 0.1 nm and 2.48 ± 0.1 nm. Moreover, these spots are arranged along both horizontal and vertical axes. The two separations along both two–fold directions are marked with blue lines and labelled with L and S as shown in Figure 5.1(c). These separations between spots along the horizontal direction are L = 4.12 ± 0.12 nm and S = 2.53 ± 0.11 nm, and the ratio is 1.69 $\sim \tau$. The separations between bright spots along the vertical direction are L = 4.13 ± 0.1 nm and S = 2.52 ± 0.09 nm, and the ratio is = 1.63 $\sim \tau$. The large and short separations correspond to the edge lengths of the rectangles in the STM image. The ratio between spots along two–fold axes is close to τ which confirms the quasicrystaline two–fold symmetry of the surface. Figure 5.1(c) shows the alignment of bright spots determined via the Fibonacci sequence along two–fold axes, which is highlighted with a blue rectangle. The diamond and square features can also be visible in the autocorrelation function, which is highlighted in green and blue and enlarged on the left side of Figure 5.1(c).

The small and large diagonals of the diamond determined from the autocorrelation function are 2.44 ± 0.08 nm and 3.98 ± 0.13 nm, respectively. The ratio of these two values is 1.63 $\sim \tau$ (close to the golden ratio $\tau \sim 1.618$). The three features including the rectangle and the diamond, shown in the STM image in Figure 5.1(a) are also observed in the autocorrelation function. It can be seen that the diameter of each diamond is the edge of the length of the rectangle or square feature. The square feature was formed by the edge-length S = 2.52 ± 0.09 nm.

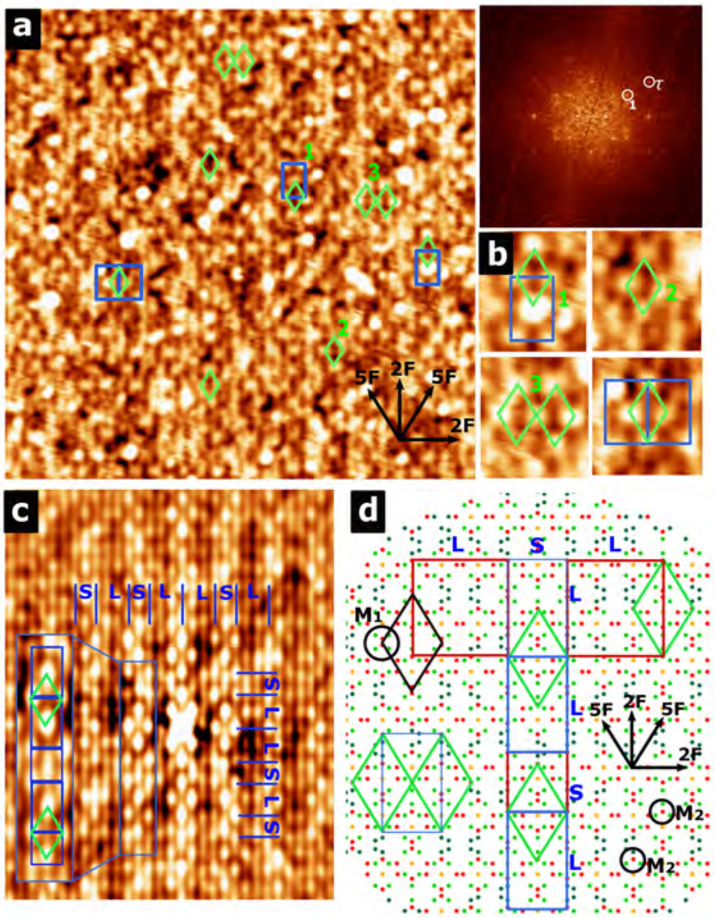

Figure 5.1: (a) 60 nm × 60 nm STM images of the two–fold surface at positive bias $V_b = +1.5$ V, $I_t = 0.19$ nA, showing the rectangle and diamond features. Inset top right is the FFT of (a). (b) An enlarged view of a rectangle and diamond feature of (a). (c) 40 nm × 50 nm autocorrelation function of (a) long and short separations are marked and labelled with blue, L, and S. (d) Two–fold *i*–Ag–In–Yb surface model. The 3^{rd} and 4^{th} shells of the surface plane is used to describe the rectangles and diamond features.

The STM scan of the surface at a negative bias of -1.5 V is shown in Figure 5.2(a). The bright protrusions are aligned along the horizontal and vertical two–fold axes. Two separations were measured along the vertical axis 2.51 ± 0.08 nm and 2.0 ± 0.11 nm. These separations are consistent with those observed by Coates *et al.* [60]. However, the diamonds disappeared at negative voltage, and several new features appeared. These features are highlighted by blue rectangles in Figure 5.2(a), and enlarged in Figure 5.2(b). The two types of centred rectangle observed are large and small rectangles; they are labelled number 1, and 2. The average edge lengths of the large rectangles were 1.53 ± 0.08 nm, 2.51 ± 0.08 nm. The ratio of those values is 1.65, these are similar that reported by Cui *et al.* [53]. The edge lengths of the small centre rectangle are 0.94 ± 0.16 nm, and 1.52 ± 0.0.07 nm, respectively. The ratio of values of edge length for each centre of a rectangle is close to τ. These rectangles are smaller than those observed at positive voltage. The square feature that appeared at the surface, has the edge length of is 1.5 ± 0.05 nm, labelled number 3 in Figure 5.2(a) and (b). The two separations are: the L = 2.51 ± 0.08 nm, and S = 1.5 ± 0.05 nm, and the Fibonacci sequence is marked with blue lines along vertical axes and labelled with L and S, as shown in the inset in Figure 5.2(a). Moreover, features such as complete and incomplete irregular rectangles (trapezoid motif) were also observed. These are highlighted and labelled with green rectangles and labelled 4 and 5 in Figures 5.2(a) and (b). Incomplete irregular rectangles appeared at first looking as a triangle (up triangle and down triangle) with the same sizes. The length side of irregular rectangles is 2.044 ± 0.035 nm, for width 0.914 ± 0.03 nm, and 1.51 ± 0.015 nm. The edge length of the triangle is 0.97 ± 0.07 nm. These triangles may be interpreted as incomplete small rectangles.

The FFT pattern of Figure 5.2(a) is also shown in inset Figure 5.2(c). It shows a rectangle pattern, and the ratio between the two lengths of the two sides is $\sim \tau$, which confirms the quasicrystalline two-fold symmetry of the surface. Figure 5.2(c) shows the autocorrelation function of the STM image displayed in Figure 5.2(a). Rectangles are shown with an average separation on the horizontal and vertical axes spots are 1.32 ± 0.05 nm, and 2.11 ± 0.08 nm. These values were similar to those reported by Burnie *et al.* [55]. However, these values are smaller than the values of the edges length of a large centred rectangle discussed above.

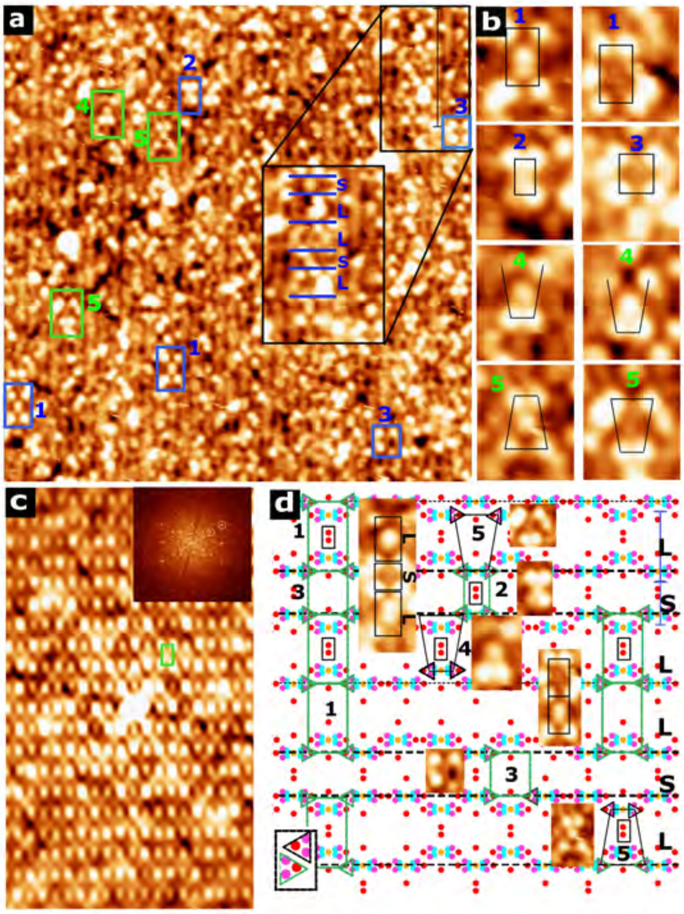

Figure 5.2: (a) 54 nm × 55 nm atomic resolution scan of the two-fold surface at negative bias (V_b = -1.5 V, I_t = 0.19 nA) taken from the two-fold *i*–Ag–In–Yb surface. (b) Several rectangular features from (a). (c) 27 nm × 46 nm autocorrelation function of (a). (d) Model of the atomic structure of a two-fold *i*–Ag–In–Yb plane, showing different types of rectangular motifs, considering 2^{nd} and 4^{th} shell Ag/In sites, highlighted 3^{rd} shell Yb, 2^{nd} and 4^{th} shell Ag/In by light green, light pink and red respectively.

Comparison with the Bulk Structure

Figure 5.1(d) shows a model of a two–fold plane of the *i*–Ag–In–Yb quasicrystal. The 3^{rd} shell Yb atoms, the Yb glue atoms, the 4^{th} shell Ag/In and the cluster centre, are represented by bright green, dark green, red, and yellow dots, respectively. Almost all features observed in the STM data at positive voltage could be explained by Yb atoms and glue Yb atoms in the bulk model of *i*–Ag–In–Yb quasicrystal. Motifs identified in STM can be found in the model.

The first motif is a square of four Yb atoms surrounding two 4^{th} shells Ag/In, and the second motif is a triangle of two 3^{rd} shells Yb and one Yb glue atom, or all the vertices of the triangle are 3^{rd} shell Yb atoms. These motifs are labelled M1 and M2, respectively. M1 and M2 are highlighted with black circles. The motif M1 resides at the vertices of the diamond tile, shown in Figure 5.1(d). The diamond tile was reported by Burnie *et al.* [55]. The separations between two of the M2 along the vertical and horizontal axes (two-fold direction) are 4.1 nm and 2.5 nm, respectively. They are arranged in the Fibonacci sequence and labelled L and S in Figure 5.1(d). These are similar to separations and the alignment of L and S in the autocorrelation functions of STM image (Figure 5.1(c)).

The arrangement of motifs M2 form rectangular and square features with edge lengths of 2.53 nm and 4.1 nm. They are highlighted with blue rectangles in Figure 5.1(d). This feature size is similar to rectangular features observed in STM image (Figure 5.1(a)).

The motifs M2 are also arranged along the five-fold symmetries that form the diamond with large and small diagonals of 4.1 nm and 2.5 nm, respectively. It is highlighted by the green diamond in Figure 5.1(d). This diamond tile has two positions with respect to the rectangles; the first position is within the rectangle (either up or down). The second position is shown in Figure 5.1(d), where two diamonds are located side by side, forming the disordered hexagonal motif. All features observed in the STM image (Figure 5.1(a)) correspond to Yb atoms.

The Ag/In atoms can be resolved at negative bias [52]. The 2^{nd} and 4^{th} shell Ag/In sites could explain the features observed in the STM images at negative bias. The model of the quasicrystal is represented in Figure 5.2(d), consisting of the 2^{nd} and 4^{th} shell Ag/In sites and a cluster centre, which are marked with pink, red and yellow dots, respectively. The Ag/In atoms belong to the outermost shell of the RTH cluster. The cluster centres are aligned along the same level horizontally, with the separation of cluster centres are 1.57 nm and 2.53 mm. Furthermore, cluster centres are also aligned along the vertical axis, the vertical distances between the cluster centres are 2.53 nm and 1.57 nm [53]. The rows follow a Fibonacci sequence, highlighted with black dashed lines with labelled L and S. The 2^{nd} and 4^{th} shell Ag/In atoms form an oval motif that consists of two symmetrical triangles along the five-fold axis, and each triangle belongs to a different cluster centre. The triangles are formed of the two the 2^{nd} shells and one of the 4^{th} shell, marked with a black and green triangles in Figure 5.2(d). The vertices of the large and small rectangles reside at the green triangles, these are highlighted with green rectangles and labelled 1 and 2. The centre of these rectangle motifs is a pair of 4^{th} shell, marked with a small black rectangle. The measurements for the width and length of the large rectangle are 1.57 nm and 2.53 nm, and for the small rectangle, they are 0.96 nm and 1.54 nm. These match up to the two rectangles that are observed in STM images and labelled 1, and 2 in Figure 5.2(b). The motifs of the completed and incomplete squares are also, identified in the model. The vertices of the square motif are located at the triangle of the Ag/In atoms, with an edge length is 1.5 nm which is highlighted in green and labelled with 3. The arrangements of the square and large rectangle motifs are similar to what was observed in the STM image, as shown in Figure 5.2(d). It is clear from the model that not all large rectangles have a pair of 4^{th} shells at their centres, which explains why some rectangle motifs in STM lack a bright protrusion at the centre.

The vertices of the complete irregular rectangles reside on both types of triangles of the Ag/In shell, as highlighted with a black trapezoid motif and labelled 5. The separations between the centre of both triangles (Ag/In shell) along the horizontal axis are 0.96 nm and 1.5 nm and along the vertical axis is 2.1 nm. These separations are similar to the width and length sides of complete irregular rectangles (number 5) in the STM image. Also, some incomplete irregular rectangles are identified in the model, labelled 4. Again, both types of triangles (Ag/In shell) form incomplete irregular rectangles, marked with black triangles. The edge lengths are 0.96 nm and 2.1 nm, which match the edge lengths of incomplete irregular rectangles (number 4) that were observed in the STM. The results of STM at negative bias support the suggestion that one type of triangle of the 4^{th} shell Ag/In represents one protrusion. These results were previously observed and reported [55]. All the observed motifs, their dimensions, and their morphology indicate that part of the 2^{nd} shell has been resolved in the STM image.

A DFT analysis of STM images of the two-fold surface *i*–Ag–In–Yb quasicrystal was reported by Coates *et al.* [102]. It indicates that the 5^{th} shell Ag/In atoms are removed and approximately only the half of the motifs (2^{nd} shell) on the surface are observed at negative bias. It is suggested that the density of Ag has a weak contribution to the surface in the STM images. It was suggested that sputtering removes Ag atoms from surface. It is known for *i*–Ag–In–Yb that the 2^{nd} shell contains 60% Ag and 40% In, and the 4^{th} shell contains 20% Ag and 80% In. The density of Ag atoms in 2^{nd} shell is higher than 4^{th} shell. The 4^{th} shells are resolved whereas not all 2^{nd} shells are resolved [103].

5.3.2 Pentacene Growth

High resolution images of Pn molecules were obtained after deposition for 3.5 minutes. Figure 5.3(a) shows a 76 nm × 76 nm STM image at -2 V. The estimated coverage is 0.37 ML. The substrate is barely visible, and the Pn molecules are visible as bright protrusions. The coverage was estimated by subtracting the area representing the substrate from the image. This high resolution STM image illustrates that the molecules are oriented along the two-fold and five-fold axes, which are marked with black arrows in Figure 5.3(a). It is found that individual Pn molecules are aligned in three different directions with respect to the horizontal axis (which is also one of the two-fold axes of the substrate) 57.0 ± 0.4°, 90.2 ± 0.5°, and 122.1 ± 0.4°. These angles correspond to the directions of the five-fold (58° and 122°) and another two-fold (90°) high–symmetry axes of the surface, which are labelled in black arrows in Figure 5.3(a). The histogram shown in Figure 5.3(b) depicts the distribution of individual orientations of molecules. The orientation of the molecules is calculated from 406 molecules. It is found that the individual orientations of molecules along the five-fold symmetry are more numerous than along the vertical two–fold symmetry.

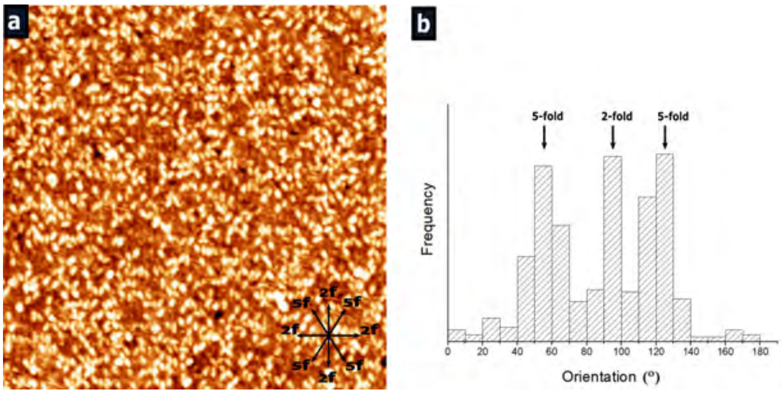

Figure 5.3: (a) An STM image (V_b = -2 V, I_t = 0.11 nA) of Pn on the two-fold *i*–Ag–In–Yb. The two- and three-fold high-symmetry axes of the surface are labelled. (b) Histogram of the orientations of Pn taken from (a).

5.3.2.1 Fast Fourier Transforms (FFT)

To observe the degree of order a fast Fourier transform (FFT) is extracted from Figure 5.3(a) and is shown in Figure 5.4(a). The FFT pattern is calculated after filtering out the contribution from the substrate. The high-symmetry directions of the surface are indicated by white arrows in Figure 5.4(a). The high-intensity spots are marked by coloured circles, the white and green circles indicate the spots that are aligned along the two- and five–fold axes of the surface, respectively. The spots were in turn linked by two rectangles; and the smallest rectangle edge-length is marked as 1. The other edges of both rectangles are related to each other by the golden mean, $\tau \sim 1.618...$ The $\sim \tau$ scaled spots confirm that the Pn thin film is quasicrystalline in nature.

The real space value is calculated using the separation of spots in the FFT, as shown in Figure 5.4(a). The separation along the horizontal and vertical two-fold axes is R_H = 1.31 ± 0.02 nm and R_V = 2.13± 0.03 nm, these are marked with pairs of white circles.

Figure 5.4(b) shows that the centres or ends of Pn molecules are arranged along the horizontal two-fold axis. These have been marked by black dots, and the dashed lines that are joining these dots represent the horizontal two-fold direction of the surface. The Pn molecules are ordered in a row-like structure. The average perpendicular separation of these rows is found to be 2.18 ± 0.07 nm and this is closely matched with the real–space values calculated from the vertical white spots in Figure 5.4(a). Similarly, it was observed that the common separations between the centres of Pn molecules along the rows are 1.22 ± 0.04 nm and 0.82 ± 0.02 nm, respectively. The former value corresponds to the real-space distance between the horizontal white spots in Figure 5.4(a). The spots that corresponded to the smaller distance were presumably too weak to be observed in the FFT.

The real-space separations between the pairs of green-circled along each of the five-fold symmetry axes of Figure 5.4(a) are 0.71 ± 0.03 nm and 1.16 ± 0.02 nm, respectively. These values correspond to the perpendicular separation of rows formed by molecules oriented along one of the five-fold directions of the surface. Figures 5.4(c) and (d) are enlarged sections of Figure 5.3(a), with molecules oriented in one of the five directions. Some of the Pn molecules observed in STM are overlaid with model Pn molecules (Pn molecule motif is highlighted with a dark blue Pn motif), and overlaying lines on the top of molecules confirm the row structure of these molecules. The separations between adjacent rows are either short (S = 0.79 ± 0.03 nm) or long (L = 1.24 ± 0.02 nm), as marked. These rows follow parts of the Fibonacci sequence, as is shown in Figures 5.4(c) and (d).

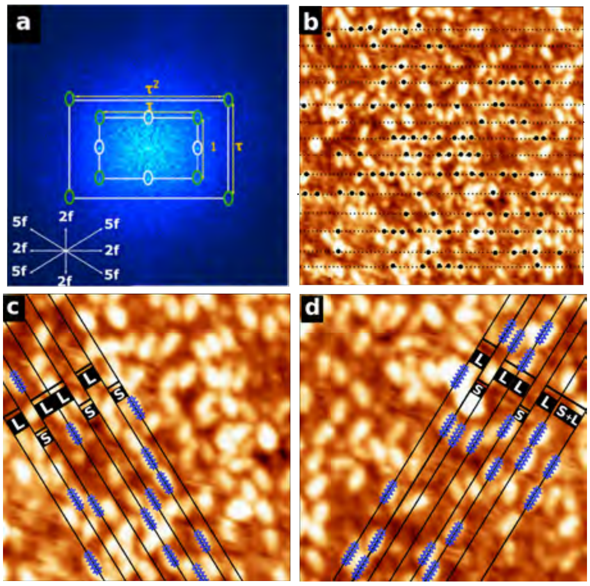

Figure 5.4: (a) The FFT of Figure 5.3(a), taking the Pn contribution only. (b) A section of Figure 5.3(a) where molecular rows formed along one two-fold axis are highlighted by black dots and dashed lines (32 nm × 32 nm). (c), (d) Fibonacci sequences formed from rows of molecules orientated along both of the five-fold axes (20 nm × 20 nm).

5.3.2.2 Autocorrelation Functions

The long–range order of the film in real space can also be characterised by taking the autocorrelation function of the STM data. The autocorrelation function of the STM image is calculated from the sole contribution of the molecules by filtering them from the substrate, as shown in Figure 5.5(a). The two directions symmetry of the Pn molecules is clearly visualised in the autocorrelation of molecule locations. The two separations were measured between the centre of bright spots are $R_H = 1.23 \pm 0.02$ nm and 1.46 ± 0.03 nm, respectively, along the horizontal two–fold axis, while separations measured are $R_V = 2.08 \pm 0.03$ nm along the vertical two–fold axis. These values match the real-space values along the horizontal and vertical axes in the FFT pattern. The ratio of these values is $\sim \tau$. This confirms the quasicrystalline structure of the molecular film.

To ensure that the autocorrelation maps reflect solely the ordering of the molecules, they are generated from molecular positions extracted from the STM images, rather than the STM images themselves. The centres of the molecules where marked with white circles, as shown in Figure 5.5(b). The autocorrelation map of Figure 5.5(b) is produced using the software Gwyddion and shown in Figure 5.5(c) The autocorrelation map was found to be similar to Figure 5.5(a). From this, we could conclude that the autocorrelation function in Figure 5.5(a) corresponds to the position of molecules. The orientation, as well as the positions of the molecules were investigated with pentacene as rods, and this method was used by K¨ahlitz *et al.* [104]. When this information was included in the autocorrelation, the image quality was found to be poor (not presented here).

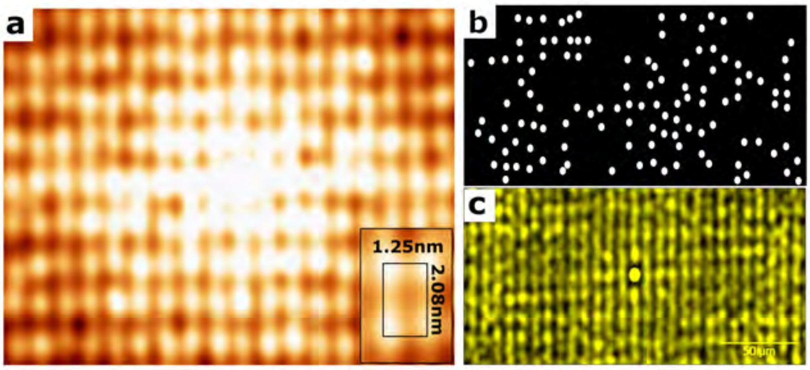

Figure 5.5: (a) 24 nm × 19 nm autocorrelation function of STM image from Figure 5.3(a), where the substrate contribution has been removed. (b) A binary map of molecular positions taken from the centre of molecules. (c) The autocorrelation function of the molecular positions extracted from (b).

The local alignment of molecules along the high symmetry directions results in common motifs. These motifs are highlighted and numbered in Figure 5.6(a), and they are enlarged in Figures 5.6(b) and (c). Motif 1 is highlighted by white squares and labelled with the number 1. It is formed by four molecules orientated along the five–fold axes, as indicated by the measured angles of $\alpha = 114 \pm 3°$ and $\beta = 67 \pm 1°$. These angles correspond to those between the two five–fold directions. The separations that were observed between the centre of the molecules in the horizontal and vertical directions were found to be 1.4 ± 0.06 nm, 1.90 ± 0.07 nm. These values are close to the edges of the length of the rectangular motif in the autocorrelation. Motif 2 is highlighted by white triangles and labelled with the number 2. It is formed by three molecules with orientations along the five–fold and two–fold axes, and appears either in an `"up"` or `"down"` configuration, as indicated by the direction of the triangle. The internal angle of the triangle where the two five–fold molecules meet is found to be 57 ± 5°. This result is expected as the molecules adopt high symmetry directions of the surface. The distance between the centres of the two molecules on the two five–fold axes is 1.18 ± 0.03 nm and the corresponding value of the molecules along the five–fold and two–fold axes is found to be 1.25 ± 0.07 nm. These distances are related to the model structure of the substrate, which will be discussed later in the chapter. A series of diamond-like structures were detected when more Pn was deposited. The total coverage of the deposition is about 0.6 ML. Figure 5.6(d) depicts these structures, which are highlighted by four solid black lines. Individual diamond diagonals are 3.09 ± 0.04 nm and 1.91 ± 0.05 nm, respectively. The ratio of these two lengths is found to be 1.62 ± 0.05.

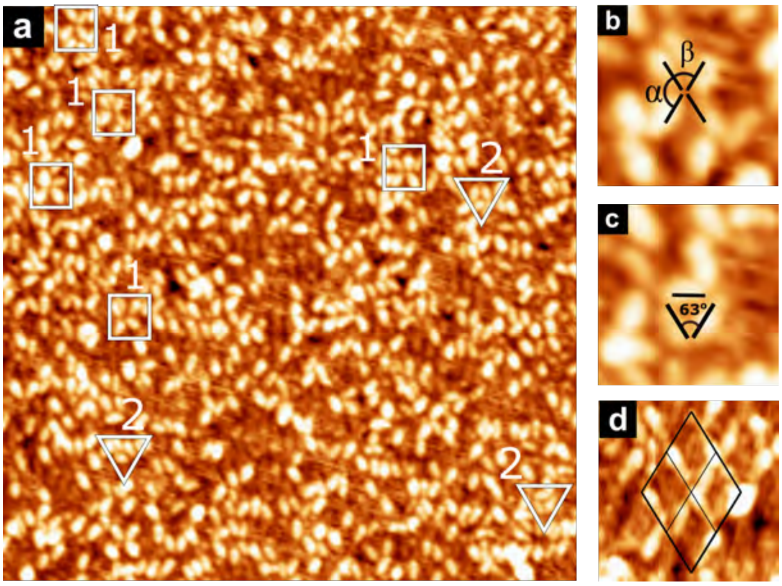

Figure 5.6: (a) An STM image (60 nm × 60 nm) taken at $V_b = 2$ V, $I_t = 0.11$ nA) contains repeating local motifs of Pn. The white boxes and triangle mark the positions of motifs 1 and 2. (b) and (c) both show enlarged views of the motifs highlighted in (a). (d) A high-coverage STM image (8.4 nm × 8.4 nm) of molecules, where a set of diamonds are highlighted in black.

The shape of the orbitals will affect the apparent shape of the molecules in STM. The STM colour map of Figure 5.7 reveals molecular orbitals at negative voltage (-0.3 V), as shown in Figure 5.7. Pn molecules characterised by four linear lobed features. This is consistent with the observations in the STM study of Pn growth on the five–fold *i*–Ag–In–Yb QC surface [7]. The lobed feature may be understood by the transfer of electrons from the lowest unoccupied molecular orbital (LUMO) of isolated molecules into the QC. This indicates that chemisorption has occurred. When a molecule is adsorbed on a metal surface, its orbitals are affected not only by a direct coupling to the substrate's electronic states but also by a mutual electronic coupling of different molecular states through the surface [105, 106]. This effect often leads to such a strong distortion of the molecular state such that it bears little resemblance to the natural orbitals of a free molecule. As a result, it is suggested that the lobed is the outcome of a hybrid state generated by strong interaction between the Pn LUMO and the substrate's d-electrons. The two-fold symmetry of the molecule suggests that this is due to disruption symmetrically or nearly symmetrically within the molecule; therefore, we can infer that the bond is formed at the centre of the molecule or at an equidistant position from the centre, with some characteristics of the substrate.

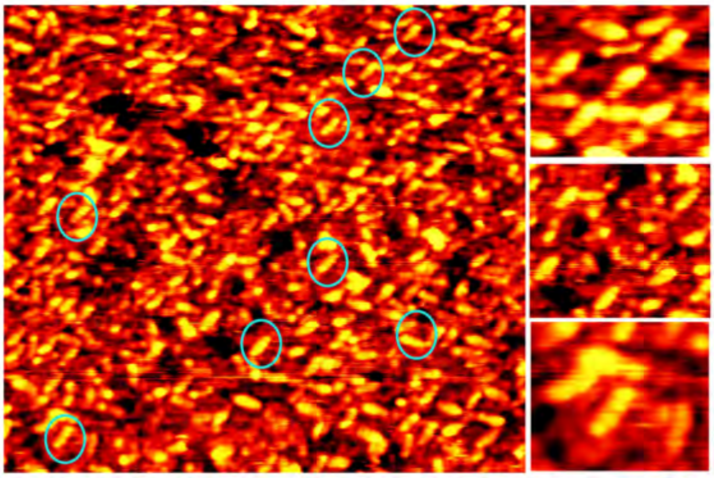

Figure 5.7: Colour map of the STM image of Pn on two-fold surface of the *i*–Ag–In–Yb quasicrystal for after 90 second deposition($V_b = +0.3$ V, $I_t = 0.19$ nA, 38 nm × 34.1 nm), four-lobed features highlighted by blue ovals.

5.3.2.3 Comparison with Model Structure

We now compare STM images with the model structure of the substrate and identify adsorption sites. A slab of the two-fold surface is shown in Figure 5.8(a). Red and green circles depict the 5^{th} shell Ag/ In and 3^{rd} shell Yb atoms, respectively. The 2^{nd}, and 4^{th} shell Ag/In atoms, as well as cluster centres are not presented for simplicity.

First, potential adsorption sites are considered in terms of geometry: to grow a quasicrystal layer, the adsorption sites must have distinct arrangements. To achieve this, the Yb atoms are generally more sparsely distributed in the surface plane than Ag/In. Notably, the Yb-Yb separation resembles the distance between the internal benzene rings, as well as the overall length of the Pn molecule $\sim$ 1.4 nm. From a chemical point of view, Pn is an electron donor [107], and it has been shown that the unoccupied states of the two–fold surface are dominated by Yb atoms [55]. Therefore, at the Yb site, there may be a strong interaction between the molecule and the substrate. This has been shown on a five–fold surface of the same quasicrystal [7].

Pn molecules can be used to decorate Yb atom pairs, as shown in Figure 5.8(b), Yb atom pairs can be decorated with Pn molecules. Pn molecules are highlighted by different colours representing their directions: black molecules are oriented along the five–fold axes, and dark blue molecules are oriented along the two–fold axes. This decoration could explain the observed Pn structure.

Along the five–fold symmetry axis marked in Figure 5.8(a), the black molecular motif shows the Yb-Yb separation that best matches the Pn molecular length. The spacing between these two atoms is 1.27 nm; the outer ring of the Pn molecule can sit directly on top of each atom, with a slight offset. Likewise, the Yb pair separation along the vertical two–fold direction is 0.97 nm, and the vertical black molecular motif provides a similar adsorption site, albeit with a slightly larger offset from the centre of the rings. Finally, the Yb-Yb horizontal spacing of 0.6 nm closely matches the distance between the next two adjacent benzene rings ($\sim$ 0.4 nm), so the centre of the Pn molecule can be located between the Yb pair.

The three 5^{th} Ag/In shell atoms are located between two Yb atoms along five-fold direction, forming a chain. This is less complex than some of the arrangements of Ag/In between two Yb sites along the two–fold axes. This may be the reason why the frequency of adsorption sites along the five–fold symmetry is higher than that of the two–fold symmetry. The allowed distance between the two molecules aligned side-by-side along two five–fold symmetry is 0.83 nm. It is above 0.6 nm along the two–fold axis. Therefore, the density of molecules adsorbed on the surface increases.

The motifs highlighted in Figure 5.6 can be explained by the model. Figure 5.8 (b) are the groups of molecules that form motifs 1 and 2. The angles between the pairs of Pn molecules forming motif 1 are α and β, giving 116.5°, and 63.3° matching the experimental measurements.

Similarly, the distance between the molecular centres is 2.05 nm and 1.26 nm along the vertical and horizontal directions, respectively, as highlighted by the black rectangles in Figure 5.8(a), which are in good agreement with the experimental values. These also match the real-space separation of horizontal and vertical lines obtained from the FFT in Figure 5.4(a). The same results were observed for motifs 2 and 3.

Figure 5.8(c) shows how the selection of Yb pairs as adsorption sites results in the formation of rows along the five–fold direction. The vertical spacing (perpendicular distance) between these rows is either S = 0.83 nm or L = 1.33 nm. These line separations follow a section of the Fibonacci sequence. This is consistent with the experimental observation that five–fold oriented Pn molecules form rows separated according to the Fibonacci sequences, as shown in Figure 5.4(c, d).

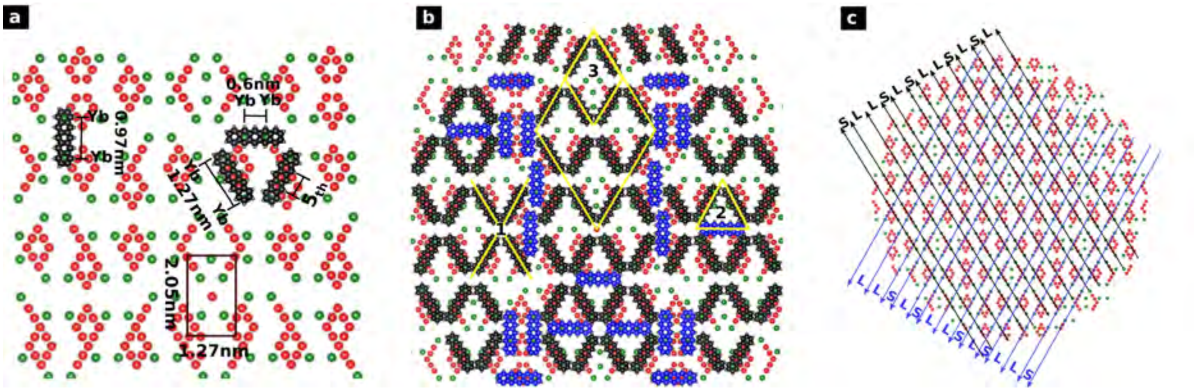

Figure 5.8: (a) Atomic structure of a plane intersecting the cluster centres in the *i*–Cd–Yb structure mode, green: 3^{rd} shell Yb and red: 5^{th} shell Ag/In.(b) Pentacene adsorption sites superimposed on the *i*–Cd–Yb model. (c) Fibonacci separation of rows along the five-fold axis, L = 1.34 nm, S = 0.83 nm.

5.3.2.4 Pentacene Adsorbed on the Yb Glue Atoms

In the STM images, some molecules were observed that could not be identified in the model of Pn adsorbed on Yb atoms. In this section, four interesting observations in the STM image are investigated in this section. First, Figure 5.9(a) reveals molecules appearing in pairs, highlighted with black rectangles and labelled with numbers 1 and 2. The pairs of adsorbed molecules are aligned side by side along five–fold axes. Examples of the pair molecules are magnified in Figure 5.9(d) and marked with number 1 and 2. The average distance between the centres of molecules along both five-fold axes was found to be 0.82 ± 0.05 nm, 0.83 ± 0.06 nm, and 1.5 ± 0.07 nm. The frequency of this pair of molecules is higher than the number of Yb sites. Nevertheless, in some of the adsorbed pairs, one of the molecules is slightly more shifted up than the other along the five-fold axis. Secondly, Pn adoption a head-to-head orientation nearly along the five–fold axis is observed. The separation between the centre-to-centre along the five–fold axis is 1.58 ± 0.05 nm, highlighted with a black rectangle and labelled with number 3 in Figure 5.9(a), and (d). This motif could not be identified in Pn adsorbed on Yb atoms in the model. The final observation is of single molecules observed in Figure 5.4(c), and (d) that are not located at the rows along five–fold axis and do not follow the Fibonacci sequence. That implies these molecules not adsorbed on suggested Yb sites.

The Yb glue sites can explain the observation of the configuration of pairs of molecules. The two–fold surface has the highest atomic density, which includes Yb glue atoms [53]. Figure 5.9(c) shows the model plane of the clean surface including the Yb glue shell, highlighted with dark blue circles, and molecules adsorbed on

3^{rd} Yb shells are represented in a black. The distance between two Yb glue shells along the five–fold is 5.7 nm, which fits the distance between the centres of the second and fourth benzene rings in Pn molecules. These are marked with blue Pn motifs in Figure 5.9(b). The vertical separation between the adsorption sites of Yb glue atoms along five–fold axes is 0.83 nm and 1.33 nm, similar to the separation of Yb sites. Molecular adsorption on Yb glue atoms contributes to increasing the frequency of the formation of adsorbed pair molecules. Moreover, the position of adsorbed sites on Yb glue atoms relative to 3^{rd} shells Yb is consistent with the morphological geometry of pair molecules adsorbed along the five–fold axis (motif 3).

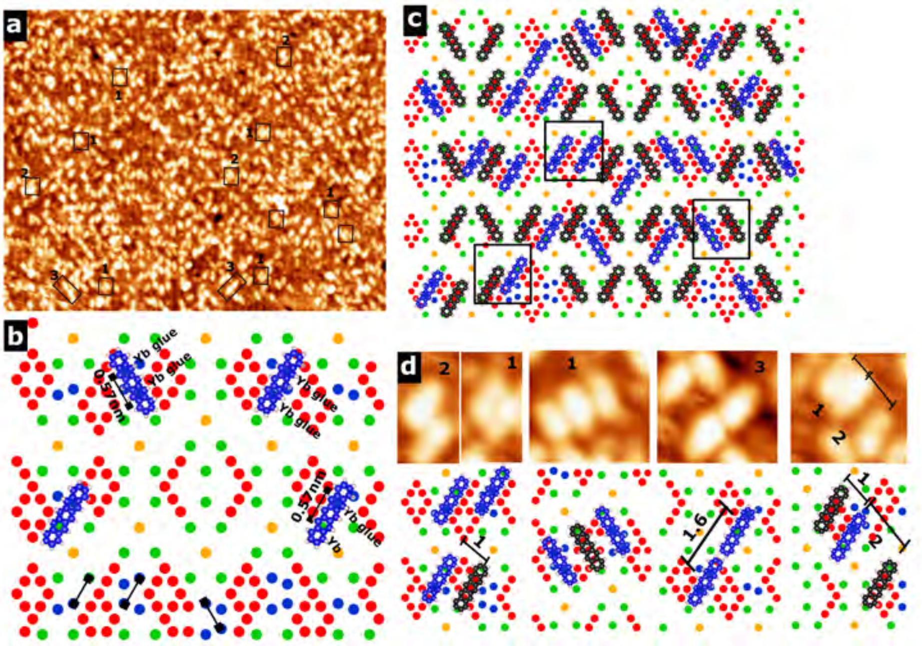

Figure 5.9: (a) 37.5 nm × 37.5 nm STM image showing a Pn pair, highlighted with a black rectangle. (b) In-plane atomic structure of a bulk plane, light green: 3^{rd} shell Yb, dark blue: glue Yb atoms and red: 5^{th} shell Ag/In showing the adsorption positions on Yb glue atoms. The molecules adsorbed on 3^{rd} shell Yb and Yb glue atoms are marked with black and blue Pn motifs. (c) Model showing positions of adsorption sites of Pn pairs relative to each other. (d) Enlarged STM images from (a).

5.4 Pentacene Growth on the Three-fold Surface

5.4.1 Substrate Structure

A STM image is employed to understand the absorption of pentacene on the three-fold surface. Figures 5.10(a) and (b) display near atomic resolution images of the three-fold surface taken at both positive and negative voltages (V = +1.5 V, -1.6

V, respectively). The high-symmetry directions are labelled with black arrows. The atomic structure of the surface is independent of voltage. However, the STM images showed a higher resolution at a negative bias than at positive bias. Atoms have not been resolved at negative bias in previous research [28].

Figure 5.10(a) depicts an STM image of 25 nm × 25 nm taken at positive bias (+1.5 V). The surface is decorated with different types of motifs and a single protrusion. Figure 5.10(b) shows the same section at negative bias. The atomic structure is unaffected by the type of voltage. However, it has a higher resolution than at positive bias. The autocorrelation function taken from Figure 5.10(a) is shown in Figure 5.10(d). It shows six-fold symmetry, and the average distance between spots determined from the autocorrelation pattern from the image is R = 2.14 ± 0.08 nm.

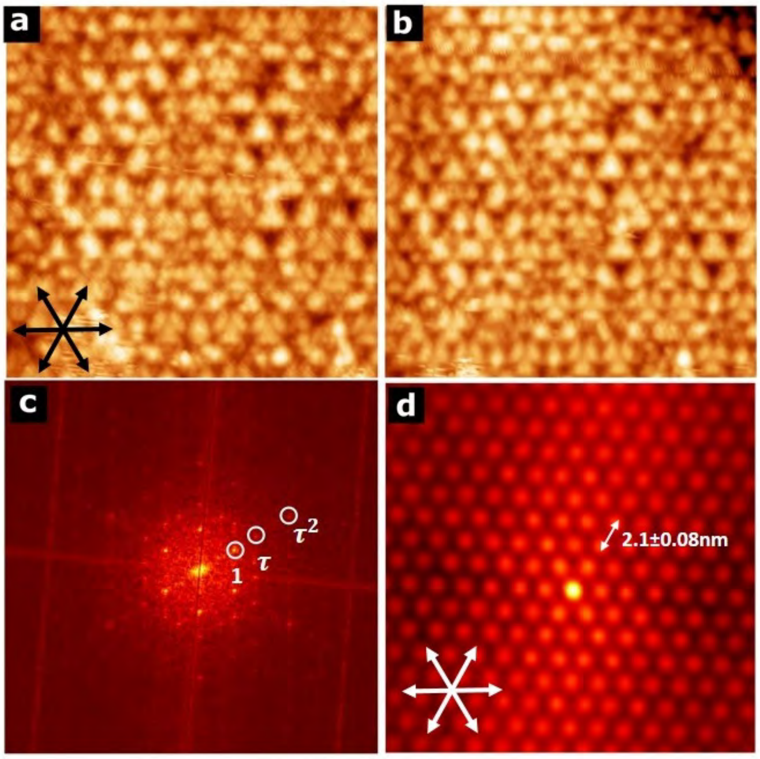

Figure 5.10: (a) and (b) 25 nm × 25 nm STM images of the three–fold surface at V_b = +1.5 V, I_t = 0.32 nA and V_b = -1.6 V, I_t = 0.22 nA, respectively. (c) The fast Fourier transforms (FFT) of (a) showing six-fold symmetry. (d) Autocorrelation function of (a).

The FFT pattern taken from Figure 5.10(a) is shown in Figure 5.10(c). The FFT pattern shows the six-fold pattern with maxima located at τ-scaling distances confirming the quasicrystalline long-range order of the surface, in agreement with the previous report [28].

Figure 5.11(a) shows an enlargement of a small area of Figure 5.10(a). The interesting motifs have been identified on the surface. Here, each motif will be referred to as motif 1, etc. The first motif is a small distorted hexagonal motif, marked with a black small hexagon, and labelled 1. The average short and long edge-lengths of a small distorted hexagon are 0.71 ± 0.06 nm and 1.03 ± 0.07 nm, respectively. It is consistent with previous reports [54, 108]. All small distorted hexagonal motifs have the same orientation. The small distorted hexagonal motif is aligned along the high symmetry axes, with two separations: the long L = 4.12 ± 0.08 nm and the short S = 2.5 ± 0.08 nm. As shown in inset of the bottom of Figure 5.11(a).

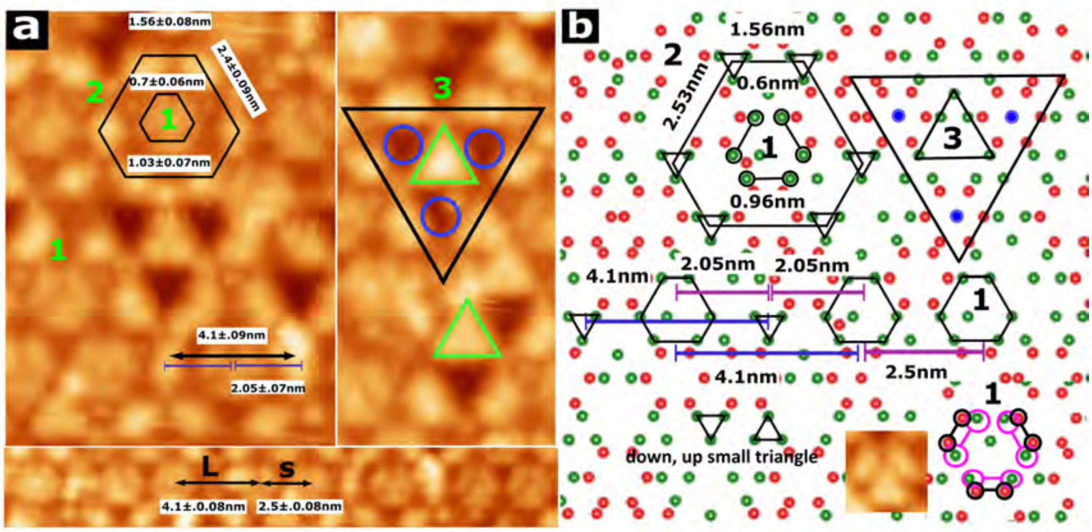

Figure 5.11: (a) STM image enlargement of the area taken from Figure 5.10 which includes interesting motifs such as a small and a large distorted hexagonal motif and an up triangle. Motifs have been highlighted with a variety of shapes to make identification with the model structure shown in (b) easier. (b) An atomic plane intersecting the cluster centres (green: 3^{rd} Yb, and red: 4^{th} Ag/In) which can explain observed motifs on the clean surface at positive bias. Marked are the same motifs as in (a).

The second motif is a large distorted hexagonal motif (motif 2). It consists of six single protrusions surrounding motif 1. This is marked with a large black hexagon and labelled with the number 2. The average short and long edge-lengths of the large distorted hexagonal motif are 1.59 ± 0.08 nm and 2.4 ± 0.09 nm, respectively. The diagonal of the motif 2 is 4.1 ± 0.09 nm. However, the separation between the single protrusion and the small hexagonal motif is 2.05 ± 0.07 nm, as marked with a dark blue line. This value is similar to the distance between the spots along the high symmetry in the autocorrelation function. The last motif observation is a large down triangular motif, which is marked with a black triangle. The three holes (cluster centre) are the vertices of this triangle, with a separation between the centre of the holes along high symmetry is 2.48 ± 0.07 nm. This is highlighted with blue circles. In the middle of this triangle is a large up triangle, named as motif 3. The edge-length of the triangle is 1.51 ± 0.09 nm, is marked and numbered with a green up triangle and number 3.

Comparison with the Bulk Structure

Features observed in the STM images can be compared to the section of the atomic structure of the bulk plane which intersects the RTH cluster centre, deduced from the bulk structure model of the binary *i*–Ag–In–Yb quasicrystal [12]. The atomic structure of the surface terminating bulk plane is illustrated in Figure 5.11(b). The 3^{rd} shell Yb and the 4^{th} shell Cd, are marked with green and red circles, respectively. In the Ag-In-Yb quasicrystal, Cd atoms are occupied by Ag and In atoms.

The previous report on the five-fold surface of *i*–Ag–In–Yb QC demonstrated that only the Yb sites can be detected by the STM at positive bias [28]. The distribution of Yb atoms in the model can explain the motifs observed in the STM image. The model of structure is decorated with up and down small triangles of Yb [56]. Moreover, the distribution of the Yb is inhomogeneous in the model. The model structure illustrates that the small distorted hexagonal motif is formed from two up and one down triangles, highlighted with a black small hexagon and labelled with number 1. The edge-length of the up and down triangle of Yb atoms is 0.6 nm. Moreover, the distance between the vertices of the two triangles of the 3^{rd} shell Yb is 0.96 nm. The lengths of triangles and the distance between vertices of triangles of Yb atoms are close to the short and long edge-lengths of the small distorted hexagonal motif in the STM image shown in Figure 5.11(a). It confirms the previous report [28]. Six down triangles of Yb atoms surround the small distorted hexagonal motif. This results in the formation of the large distorted hexagonal motif, with the two measured separations of 1.56 nm, and 2.53 nm. This is marked with a large black shied tile and labelled with number 2. The down Yb triangles correspond to a single protrusion in the STM image, and their two separations are close to the average of the long and short edge lengths of the large distorted hexagonal feature in the STM image. Furthermore, the separation between the down triangle and motif 1 along the horizontal axis is 2.05 nm. The distance between the two down triangles is the diagonal of motif 2, which is 4.1 nm. These distances are marked with a dark blue and pink line. These dimensions are consistent with the separation between the single protrusion and motif 1, and the diameter of a large hexagonal motif (motif 2) in STM. Also, the value of separation between the down triangle and motif 1 corresponds to the distance between spots in the autocorrelation pattern R = 2.14 ± 0.08 nm. The two separations between motif 1 are L = 4.1 nm and S = 2.5 nm, again matching the STM observation. The three cluster centres form a down large triangle, and the distance between the centres of clusters is 2.5 nm, as highlighted by a large black triangle in Figure 5.11(b). There are three Yb up triangles in the middle of this down triangle, which are highlighted with a small up triangle and labelled number 3. The separation between triangle vertices is 1.5 nm. The orientation and dimension of these two motifs match up to motif 3 in the STM image.

At negative bias, the STM image shows that the decoration of the surface remains unchanged. This observation can be explained by the presence of the six 4^{th} shells Ag/In sites, which surround the small, distorted hexagon of the 3^{rd} shell Yb. These two motifs are distinguished by pink and black, small, distorted hexagonal shapes. Therefore, the six 4^{th} shells Ag/In atoms form the small, distorted hexagonal motif in the same position as the Yb shell's small, distorted hexagonal motif, but with a slightly larger size. Additionally, the tunnelling current contribution from Ag/In and Yb becomes comparable at negative bias [109, 110]. As a result, the surface maintains the same atomic configuration at both voltages.

5.4.2 Pentacene Growth

Following the observation of the quasicrystalline order of Pn on the two-fold surface of the *i*–Ag–In–Yb, Pn was gradually deposited on the three-fold surface of the *i*–Ag–In–Yb QC.

STM images were taken at both positive and negative bias after depositing the pentacene for 2 minutes and 30 seconds. The resolution of the STM image was poor at positive bias (not presented here). The large protrusions were observed on the surface, and their size was larger than that of Pn molecule, indicating that this feature could not be a Pn molecule.

In the STM image, individual of pentacene molecules are observed on the surface as a bright rod-shape, which is highlighted by a blue and green oval in Figure 5.12(a). The average size of the rod shape is 1.4 ± 0.07 nm as measured using the line profile. This is equal to the position of the outer carbon rings in a single pentacene molecule. The molecules are adsorbed near to the sides of the small distorted hexagonal motifs (motif 1) of the clean surface. The three individual orientations of molecules are 0°, 53.5 ± 0.9°, and 123.6 ± 0.8° with respect to horizontal direction. These orientations indicate the molecules are aligned along the high symmetries (0°, 60°, and 120°) with respect to the horizontal axis of figure, are highlighted with a blue oval. A few molecules are found to be located at 145°

with respect to the horizontal, one is marked with a green oval and numbered as 4 in Figure 5.12(a). A line profile was used to measure the height of molecules from the surface. It is found that the average height of protrusions is 0.57 ± 0.04 nm. This suggests that Pn is adsorbed within the carbon ring parallel to the surface.

To understand the Pn adsorption sites, Pn motifs will be considered with reference to the model substrate. The small distorted hexagons (motif 1) that forms from the 3^{rd} shell Yb is highlighted by the pink distorted hexagon in Figure 5.12(b). The positions and orientations of molecules suggest that adsorbed sites could be between two 3^{rd} shells Yb triangles, and are highlighted by blue and green ovals. The separation between two 3^{rd} shell Yb hexagons is 0.97 nm along the high symmetry axes of the substrate. It fits with the distance between the first and fifth benzene rings in Pn. In addition, this indicates that molecules are aligned along the high symmetry axes (three-fold axes). Furthermore, the adsorption sites are located close to the distorted small hexagon (motif 1). This agrees with the STM images.

Feature number 4 in the STM image can be explained if Pn is adsorbed at Yb atoms, which are marked with a green oval in Figure 5.12(b). The distance between Yb atoms is 0.85 nm, and they are rotated 146° with respect to the horizontal axis. This value agrees well with STM observations.

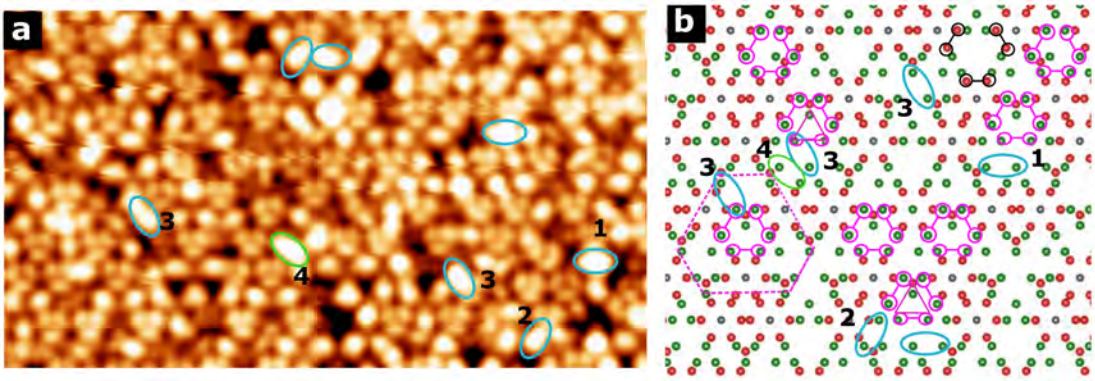

Figure 5.12: (a) 47 nm × 26 nm STM image after deposition of Pn for 2 minutes and 30 seconds (V_b = -1.4 V, I_t = 0.12 nA) showing individual Pn molecules adsorbed on three-fold surface. The molecules are highlighted with blue and green ellipses. (b) Atomic structure of a bulk plane showing motif 1. The 3^{rd} shell Yb forms motif 1, marked with small and large pink hexagons. The adsorption sites of molecules are highlighted with blue and green ellipses.

Resolved the 4^{th} shell Ag/In

Figure 5.13(a) is the same Figure 5.12(a). It is clearly seen this STM image shown the atomic structure of the clean surface at negative voltage (-0.7 to -2)V. It was found that the six small distorted hexagonal motifs (motif 1) form a large distorted hexagon, which is motif 3, with two edge-lengths of L = 4.1 ± 0.15 nm and S = 2.49 ± 0.15 nm. The length measured from the centre of motif 1, Highlighted with a large blue distorted hexagon and numbered 3. The edge-lengths of each distorted hexagon motif are related to τ-scaling. The inside of this feature is dimmer. Also, single protrusion is located at the middle in long length, which marked with a black oval in inset of the Figure 5.13(a). The separation between bright protrusion and motif 1 is 2.1 ± 0.04 nm. This hexagon has not been clearly observed in three-fold clean surface.

This feature was identified in the model, as shown in Figure 5.13(b). It is the same model as in Figure 5.12(b), but with the addition of the 4^{th} shell substrate, Ag/In. To explain Feature 3, the hypothesis that the 4^{th} shell Ag/In is surrounding a small, distorted hexagon of the 3^{rd} shell Yb will be investigated. A small distorted hexagon of Ag/In marked with a black, distorted hexagonal. The two distances between the centres of these motifs are 4.1 nm and 2.5 nm, marked with a blue distorted hexagon. In addition, the cluster of the 4^{th} shell, which is located in the middle of the long-length, is marked with a red triangular shape. Furthermore, in the middle of motif 3 is a high density of Yb atoms, which could not be resolved, and it is present in the dimmer area. The size of motif 3 is close to STM data. The six 4^{th} shells form a small triangle, which marked with a red triangle. The distance between this motif and motif 1 is 2.05 nm, which matches the STM observation. It's possible that the 4^{th} shell is revealed by a single Pn molecule. The value separation 2.05 nm is correspond to the distances between spots in autocorrelation function (Figure 5.10)

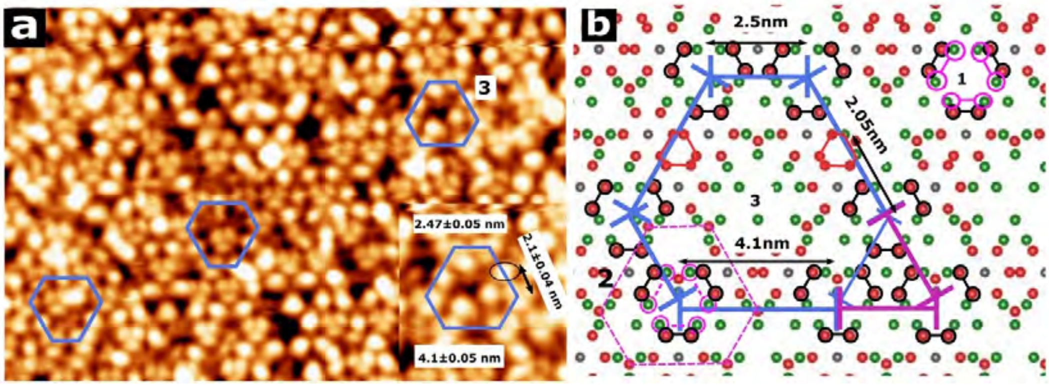

Figure 5.13: (a) 48 nm × 32 nm STM image is the same as Figure 5.12(a). It depicts motif 3, marked with a blue hexagon. An inset, enlarged view of motif 3. (b) The same model shown in Figure 5.12(a). It is taken from a different section that has rich Yb atoms, and it shows motif 3.

After dosing pentacene for 3 minutes and 13 seconds on the surface, STM images reveal an increased surface area covered by pentacene molecules. This gives a coverage of about 0.40 ML. When there is more than 0.40 ML of pentacene present, the substrate resolution is greatly reduced. STM images were taken at negative bias(- 1.4 to -2.2)V at a coverage 0.4 ML. STM data still shows a few of the small distorted hexagonal features (motif 1) that characterise the clean surface, highlighted with a blue rectangle and labelled M in Figure 5.14(a).

Two different features formed by Pn are observed: a rod feature representing a single molecule and a small triangular feature. The single molecules are observed as rod-shaped, their orientations are aligned along three high-symmetry directions, and they are highlighted with a black oval. Other molecules are highlighted with a green oval and are aligned 30° from the horizontal axis between the high symmetry directions. Small triangular protrusions are observed in two different orientations; the `"up"` and `"down"` triangular protrusions are marked with a green circle and labelled M_1 and M_2 in Figure 5.14(a). The up triangle shows as a bright protrusion inside, whereas the down triangle contains a hole inside. The edge-length of the down triangle is 0.98 ± 0.04 nm to 1.25 ± 0.03 nm, and for up triangle 1.04 ± 0.03 nm to 1.22 ± 0.03 nm. Examples of motif 1 (M) of the substrate, and the triangular features of molecules (M_1, M_2) are shown in Figure 5.14(d). The three up triangles result in the formation of a large triangle, which is marked with a green circle and labelled as M_3 in Figure 5.14(a). The separation between the centres of the up triangles in motif 2 (M_3) along three high symmetry axes is 2.49 ± 0.03 nm. Figure 5.14(c) is an STM image that is taken from a different area under the same condition, which shows similar triangles as in Figure 5.14(a). Figure 5.14(b) is the FFT pattern of Figure 5.14(a), which shows τ-scaled spots along a set of three high-symmetry directions.

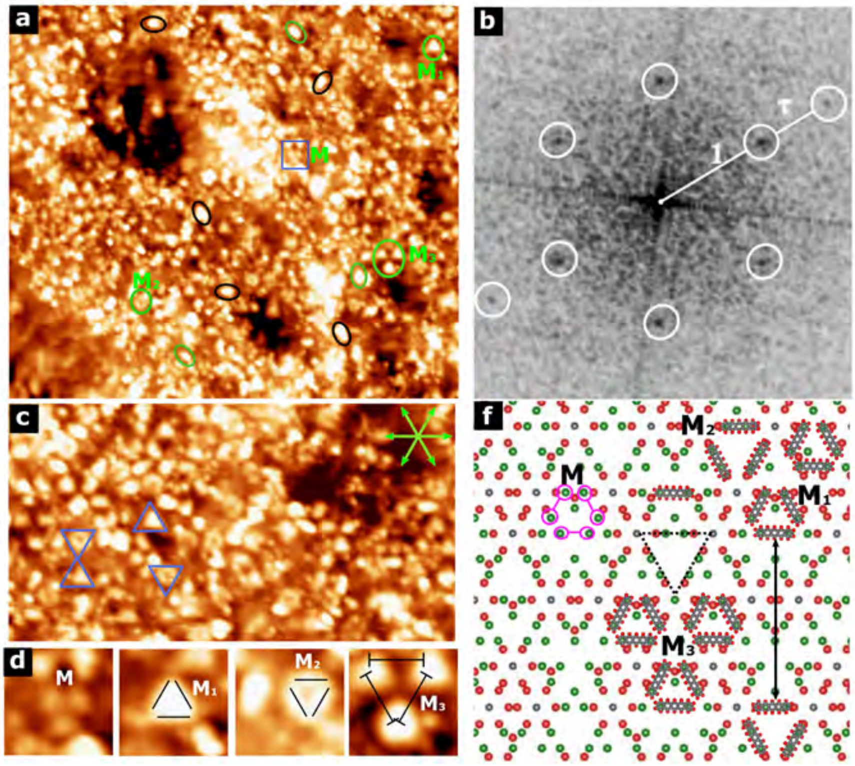

Figure 5.14: (a) 76.6 nm × 70 nm STM image after depositing Pn for 3 minutes and 13 seconds (V_b = -1.7 V, I_t = 0.14 nA) showing two types of Pn triangles: small triangular motif M_1, M_2, and large triangular motif M_3. (b) The FFT pattern of Pn on *i*–Ag–In–Yb of (a). (c) 45 nm × 24 nm STM image from different terraces (V_b = -1.4 V, I_t = 0.14 nA), showing same triangles observed in (a). (d) Enlarged examples of a triangular motif of molecules and a distorted hexagon motif of a clean surface. (f) Potential adsorption sites of Pn in the *i*–Ag-In–Yb model. Green and red atoms are the 3^{rd} shell of Yb and 4^{th} shell of Ag/In, respectively.

The observed features in the STM image are compared with the model structure of three-fold surface in Figure 5.14(f). The suggestion above, that the Yb small triangular motifs that form a small distorted hexagons may be adsorption sites, is investigated. The distance between Yb atoms between two small triangles along the high symmetry direction is 0.97 nm, and is marked with pink circles and labelled M. This separation is close to the distance outer benzene rings of Pn. Thus, outer rings of Pn locate on vertices of two small up and down triangles, and this leads to the formation of up triangular feature M_1 in the STM image, marked with up triangle and labelled M_1. The three small distorted hexagons form three of small up triangular motifs. The three stacked triangular molecules form motif 3 which labelled as M_3. The distance between centres of M_1 features along the two-fold high symmetry is 2.5 nm. The size and geometry of three small distorted hexagons of Yb atoms correspond to motifs M_1 and M_3 in the STM image. The formation of the down triangle motif M_2 could be explained by the three up triangle Yb atoms in the model, highlighted with a dashed triangle. The distance between the Yb atoms in the small up triangle is 0.6 nm. This distance is slightly larger than the distance between the first and third outer ring of Pn (distance is 0.5 nm). However, it could be the adsorption site. The molecules adsorb on these sites, forming the down triangular motifs. The down triangle motif M_2 is marked with the down triangle of Pn motif and labelled M_2. The position of the up and down triangular motifs in the model corresponds to their position in the STM data in Figure 5.14(c), which is highlighted with a black arrow in Figure 5.14(f). This matches with the STM observation. It can be clearly seen that inside of M_2 has no Yb atom, which may explain why the inside appears dim.

Figure 5.15(a) shows an STM image taken after depositing Pn for 3 minutes and 30 seconds on the clean surface [6]. By subtracting the area representing the substrate from the image, the coverage was estimated. The three high symmetry directions of the substrate are marked with the white arrows in Figure 5.15(a).

The previous two types of features are mainly observed: triangles and rods. The length of the rods is $\sim$ 1.0-1.4 nm and the size is close to the size of the Pn molecule (H-H distance along the long axis of the pair of molecule, 1.38 nm), suggesting that the rod corresponds to a single Pn molecule. Most of the single Pn molecules are aligned along the three high symmetry directions of the substrate, is marked with blue rectangle in Figure 5.15(a). It is found the perpendicular distance between molecules in a molecular pair that are oriented along high symmetry is 0.96 ± 0.04 nm, marked with a black circle in Figure 5.16(a). This image is a magnified small area in Figure 5.15(a). A few molecules are oriented between the high symmetry directions, 30° away from the substrate, which is marked with a green rectangle in Figure 5.15(a).

We conclude that the triangular features are formed by Pn molecules for the following reasons: the triangular features have the same size and orientation; the orientation of the triangles is the same as that of the isolated Pn molecules; the edge-lengths of the up triangles are 1.2–1.3 nm, 1.34 nm, and the triangles are observed at a height of about 0.35 nm from the substrate (darker region of the STM image).

Again, the triangular motifs were stared forming coverage at 0.40 ML and are observed in high coverage. The up and down small triangular motifs are labelled M_1 and M_2. All bright triangles have the same orientations and are arranged along the high symmetry. The two separations between the centre of triangles either short, S = 2.47 ± 0.03 nm or long, L = 4.11 ± 0.1 nm, are marked and labelled with blue line and L, and S. The frequency of down triangles is lower than with low coverage, and only a few down triangles are identified. The three up triangles form a large up triangle motif, with the distance between the centre of triangles of 2.46 ± 0.05 nm, is labelled with M_3.

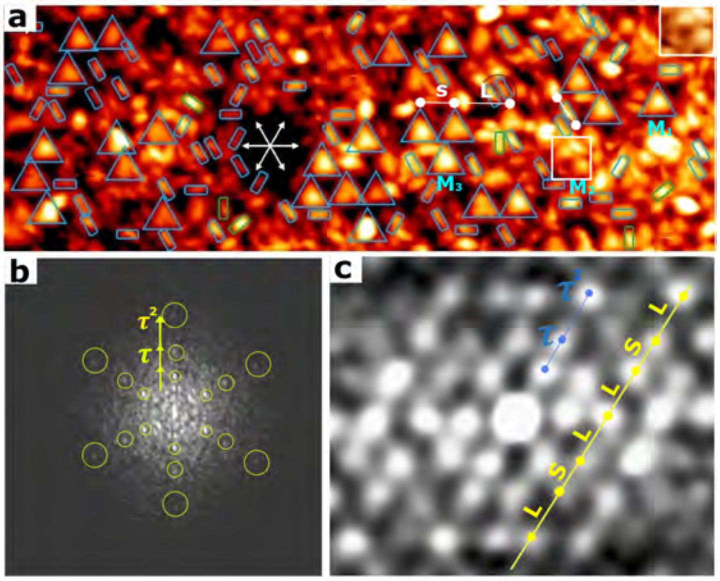

Figure 5.15: (a) 17 nm × 50 nm STM image after depositing of Pn for 3 minutes and 30 seconds at (V_b = -1.8 V, I_t = 0.12 nA). High symmetry directions of the substrate are indicated by white arrows. (b) The FFT of Figure (a), showing three-fold symmetry. (c) Autocorrelation function of STM image after removal of the substrate contribution, showing hexagonal symmetry and confirming the long-range quasicrystalline order of the molecular layer.

The long–range order of the molecular layer in real space can also be characterised by taking the FFT pattern of the STM data. The FFT pattern of Figure 5.15(a) is shown in Figure 5.16(b). The FFT pattern reveals spots distributed along six–fold symmetry, with different separations, exhibiting τ–scaling relationships.

The quasiperiodic distribution of the adsorbed molecules on the clean surface can equally be ascertained from the autocorrelation of STM images of the molecular layer. Again, the contribution from the substrate has been removed, so that only the Pn molecules are considered. The autocorrelation function of Figure 5.15(a) is presented in Figure 5.15(c). It shows six–fold symmetry, and the τ–scaling confirms the long–range quasicrystalline order of the molecular layer. The bright spots are arranged along high symmetry according to six directions, indicated by yellow arrows, each rotated 60° from each other. The yellow line is parallel to one of these directions. The two separations between the spots arranged along high symmetry direction are either at long, L = 2.4 ± 0.07 nm or short, S = 1.55 ± 0.12 nm, spacing with ratio L/S = 1.54 slightly less than τ. The spacing sequence follows (LSLLSL), which is marked with L and S along the high symmetry direction. The two spacing corresponds to the separation between the up triangle in STM image.

5.4.2.1 Comparison with Model Structure

We now compare STM images with the model structure in order to identify adsorption sites. The triangular and rod-like features can be explained by attaching the two terminal benzene rings of Pn to the Yb atoms, as shown by the Pn motifs in Figure 5.16(b). The distance between the two Yb atoms is 0.97 nm, which is close to the centre-to-centre distance of the two terminal benzene rings, 0.98 nm. This model produces triangular features of the same size and orientation as in the STM. The distance between the triangles in the model is 2.53 nm, which is also consistent with the value observed in the STM. Furthermore, the two closest parallel molecules in the model are 0.84 nm, which is close to the value observed in the STM, 1 nm which is highlighted by a black circle. Considering the different adsorption sites, it is possible to simulate Pn molecules dissociated between the high symmetry directions of the substrate. In this case, the Pn molecule is anchored (pinned) to the Yb triangle, the terminal benzene ring is attached to one atom of the Yb triangle, and two hydrogen atoms are attached to the other two Yb atoms of the triangle. As shown in an enlarged image of Figure 5.16(b) which

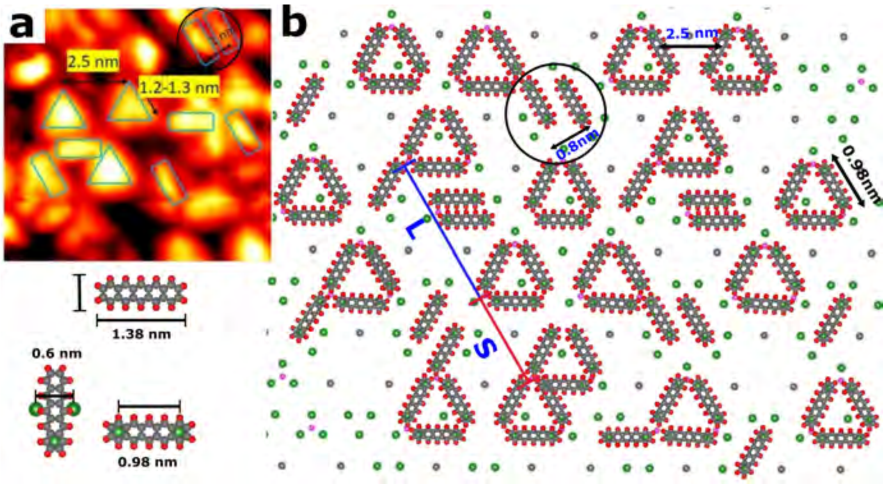

Figure 5.16: (a) Enlarged view of STM image highlighting pentagonal and rod features. (b) A three-fold *i*–Ag–In–Yb surface model for adsorbed Pn molecules. For simplicity, only Yb atoms (green) are shown, and 4^{th} shell Ag/In is omitted. The left panel shows the model of a pentacene molecule on Yb adsorption site. (Red H atom, gray C atom, and green Yb atom.

is shown in the inset of the bottom in Figure 5.16(a). The Yb-Yb distance is 0.60 nm, which is similar to the H-H distance of 0.6 nm.

5.4.2.2 High Coverage of Pentacene Growth

Figure 5.17(a) shows the surface with more than ∼ 1 ML of pentacene present. The STM image obtained after depositing Pn for 3 minutes and 30 seconds on the clean surface. No convincing evidence of surface ordering was observed in either FFT or autocorrelations. However, we can still clearly observe the individual molecules with higher density than the triangular motifs. The single molecules was oriented in six directions, 21°, 41°, 60°, 120°, 141°, 0° will be respect to the horizontal axis of Figure 5.16. The separations between single Pn on three-fold axes with oriented 30 from axes are as follows: 0.68 ± 0.98, 0.95 ± 0.74, 1.26 ± 0.03 nm, 1.53 ± 0.1, and 2.5 ± 0.09 nm.

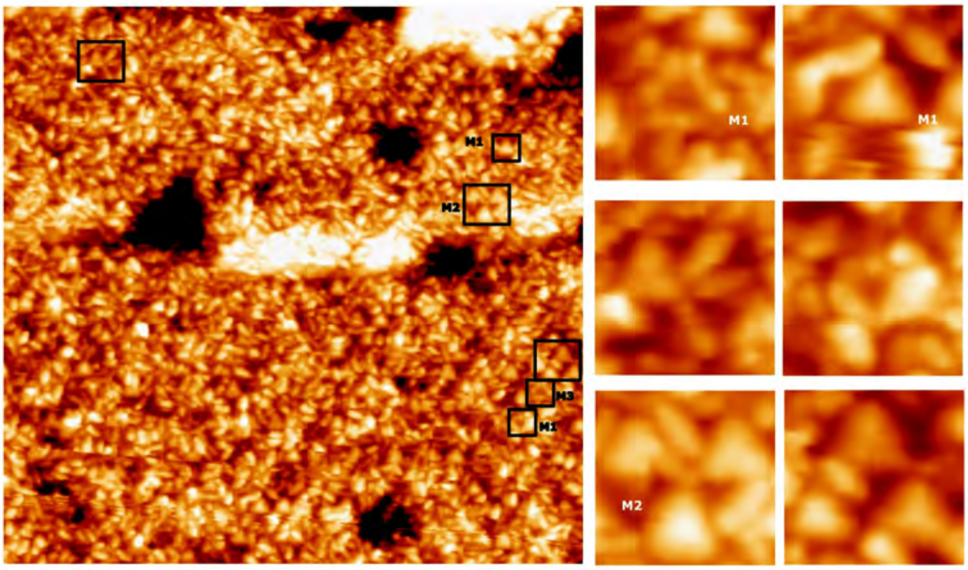

Figure 5.17: 27 nm × 26 nm STM image at a coverage of more than 1 monlayer, taken after depositing Pn for 3 minutes and 30 seconds). The triangle motifs are marked and labelled. An inset shows an enlarged view of these motifs.

To identify the adsorption sites of single molecules in the bulk model, compare STM data to the Yb site in the bulk model. Figure 5.18 depicts a comparison of the orientation and distances between the 3^{rd} shell Yb in the bulk model and the spacing between Pn and their orientations. One end of the Pn chain is found to be adsorbed between the Yb triangle base and the other end of Pn is found to be on one of the Yb triangle's vertices, is marked with a black arrow. The distance between the two locations is 1.37 nm. The middle of a Pn is adsorbed on a Yb atom. It can be seen that one end of the molecule is attached to a complete triangle, while the second side is only adsorbed on one Yb site. This adsorption site is analogous to the Tb site on (111) Au-Al-Tb 1/1 [73]. Molecular direction is determined by the position of the end of Pn adsorbed on one Yb. That could be the reason for the variety of molecular orientations. It was found that the orientation of the position adsorption corresponds to the orientation of a single molecule in the STM. In addition, the separation between adsorption sites is 1.26 nm, 2.5 nm which is close to the distance between molecules in the STM. The second adsorption is Pn adsorb between two triangle Yb with separation of 0.97 nm, which marked with a blue arrow. These adsorption can explain the separation between molecules 0.6 nm, and 0.96 nm in STM image.

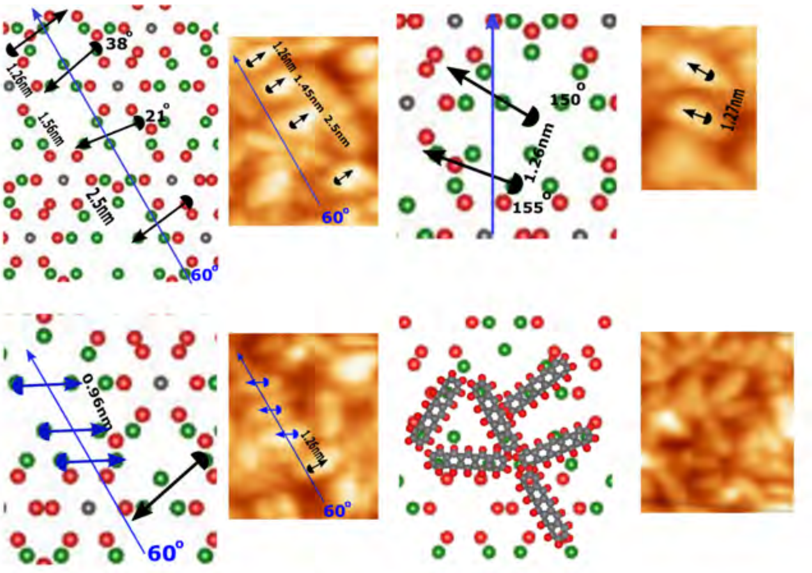

Figure 5.18: Enlarged view of individual molecules arranged along the three-fold axes with different orientations, side-to-side model representation of the adsorption sites. The blue and black arrows correspond to the positions of the molecules with respect to the Yb triangles. The Yb is marked with a green circle.

The STM image obtained from terraces near the area shown in Figure 5.17(a) is shown in Figure 5.19(a) after 12 hours. The pressure in STM does not change, confirming that there is no contamination on the surface. The FFT pattern of Figure 5.19(a) is shown in Figure 5.19(b). The FFT pattren confirm the quasicrstllaine film. Figure 5.19(a) shows the same observations (M_1)- (M_3). The high symmetry axes of the surface, labelled in black arrows. The up small triangles (M_1) are aligned in the three-fold axes, which is marked with a blue box in the STM image. The three separations between M_1 are S = 1.58 nm, L = 2.48 ± 0.07 nm, and S+L = 3.87 ± 0.1 nm. The L and S is shown in Figure 5.19(c).

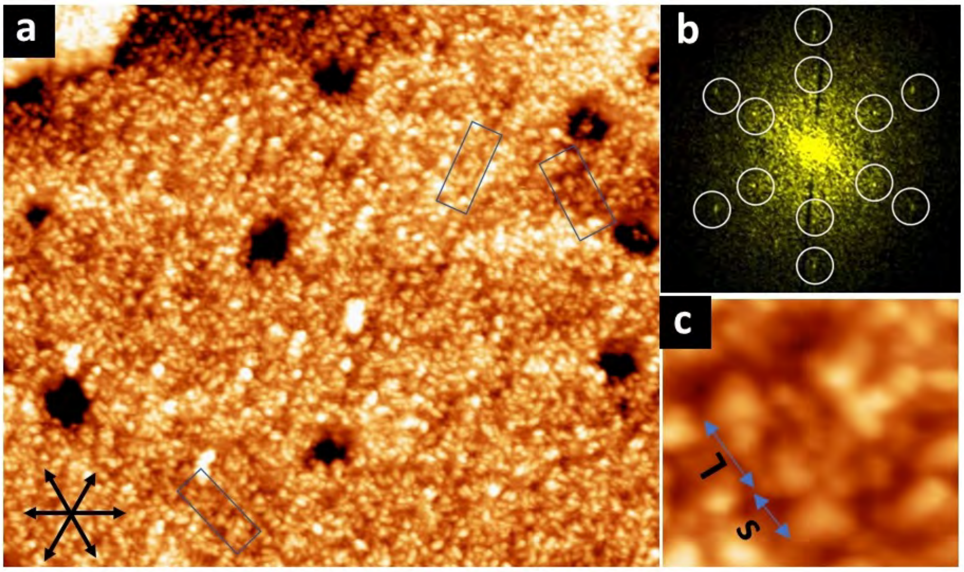

Figure 5.19: (a) 90 nm × 70 nm STM image after depositing of Pn for 3 minutes and 20 seconds at -1.3 V. (b) The FFT pattern of STM image in (a). (c) magnified views of the sections marked by a blue rectangle in(a).

The STM shows the individual molecules are arranged in the same orientation and distance as those observed in Figure 5.17. The orientations of molecules are 31.2 ± 0.3°, 59.1 ± 0.5°, 37.8 ± 2.5°, and 141 ± 3.9°. In addition, these single molecules were arranged to form different sizes of triangles, as shown in Figure 5.20.

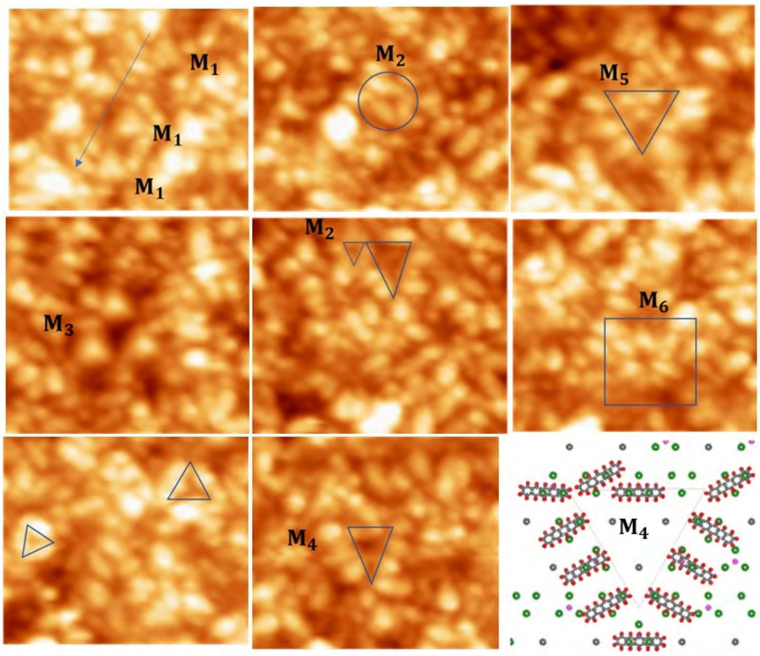

Figure 5.20: An enlarged view of the observed features in the STM image shown in Figure 5.19(a), showing different sizes of triangle.

These triangles have not been observed before. M_4 has an edge-length of 3.8 ± 0.3 nm, while M_5 has an edge-length of 2.45 ± 0.2 nm, and 4.15 nm. The triangle formation can be explained by the adsorption site, which suggests molecules that are not oriented parallel to three-folds.

5.5 Conclusions

STM images demonstrating the two-dimensional quasicrystalline growth of Pn molecules on two high symmetry surfaces of *i*-Ag-In-Yb QC were presented in this work. The Pn molecules adopt positions on a quasiperiodic lattice atop the two- and three-fold surfaces of the *i*–Ag–In–Yb sites. By comparing the STM images to the model substrate structure, it was possible to identify the adsorption site in both specimens.

The quasiperiodicty of the Pn film on the two-fold surface *i*–Ag–In–Yb QC was confirmed with the FFT pattern, and autocorrelation of the STM images. The molecules are oriented along two-fold and five-fold axes, which are high symmetry directions of the substrate. The molecules adsorbed along five-fold direction have higher frequency than those adsorbed on two-fold directions. The Pn molecules are adsorbed on the Yb sites.

Pn molecules on the three-fold surface also grow quasiperiodically. The FFT pattern and autocorrelation of the STM images are shown in the six-fold orientation order with τ scaling. The growth of Pn on the three-fold surface was characterised by formation of triangles with two sizes. The ratio between the edge-of the triangles of different sizes is τ. The adsorption site was identified, the molecules adsorbed on Yb sites as on the two-fold surface.

In conclusion, the separation of two Yb sites is similar to distances between the internal benzene rings. From a chemical point of view, Pn is an electron donor [107], and it has been shown that the unoccupied states of the two-fold and three-fold surface are dominated by Yb atoms [55]. Therefore, electrons may transfer from Pn to Yb sites and thus there may be strong interaction both molecules and Yb.

Chapter 6

The Surface Structure of Au-Al-Gd 1/1 Approximant

6.1 Introduction

Since the approximants have the same building blocks (RTH clusters), a comparison of their surface structure to their parent quasicrystal surfaces in bulk termination will be significant to understanding the surface of quasicrystals. Another reason for the study is to understand the clean surface of approximants so that they can be used as templates to grow new metallic and molecular thin films.

The sample is the Ag-In-Gd 1/1 approximant (110) surface. The sample surface has been characterised using STM and LEED. The STM data revealed different facets of approximants such as (111), (130), (402) and (603).

6.2 Experimental Details

An Au-Al-Gd 1/1 approximant sample was used for this study. It was synthesised using the self-flux method, which is the same procedure used to synthesise the Au-Al-Tb approximant [35, 11]. High-purity raw materials of a nominal composition $Au_{71}Al_{19}Gd_{10}$ are melted at 1273 K for 3 hours inside an alumina crucible under vacuum. Single grains are prepared using the self-flux method, and the specimen is slowly cooled to 1003 K at a rate of 3 K/min [11].

A centrifuge is then used to separate single grains from molten flux. X-ray diffraction on crushed powder is used to characterise individual grains. The single grains produced are single 1/1 approximant phases with the structure of a bcc crystal and its lattice parameter of 1.47581 nm, according to the X-ray diffraction pattern [111]. The composition of the single grains is estimated to be $Au_{70}Al_{16}Gd_{14}$, which falls within the antiferromagnetic zone, based on the relationship between the lattice parameter and the composition determined for polygrain 1/1 Au-Al-Gd approximant.

The standard sample preparation for surface investigation involves cutting the sample along the desired crystallographic direction; however, due to the small size of the Ag-Al-Gd 1/1 approximant sample, this was not possible. In addition, the whole surface of the specimen was not flat but tapered in the middle. The specimen was hand-polished along the (110) facet with diamond paste of 6 μm, 1 μm, and 0.25 μm grades successively. After 20 minutes of polishing with each grade, the sample was placed in an ultrasonic bath to remove any remaining paste. The surface was then further cleaned with sputter-anneal cycles (30 min Ar^+ sputter and three-hours anneal at 448 °C) under ultrahigh-vacuum conditions. The temperature was measured using a pyrometer with an emissivity of 0.35, which is similar to that of the related quasicrystals [85]. Substrate cleanliness was monitored with room temperature scanning tunnelling microscopy (STM).

6.3 Detailed Structure of the (110) Surface

6.3.1 Step Morphology

Figure 6.1(a) depicts a 74 nm × 71 nm STM image of the (110) surface of Au-Al-Gd exhibiting a step/terrace morphology. The interior angle of the terraces, marked with α, is 72.6 ± 0.4°. This value is consistent with the expected unit cell angle of the bcc (110) surface, which is 70°. Figure 6.1(b) shows a histogram of the step heights of Figure 6.1(a). In this histogram, four different heights were measured: 0.42 nm, 0.65 nm, 1.01 nm, and 1.24 nm. The most common step height is shown in Figure 6.2(a), which displays consecutive terraces with a step height of 1.02 ± 0.07 nm.

As shown in Figures 6.3(a) and (c), the small width of terraces with step heights of 1.44 ± 0.2 nm, 0.59 ± 0.07 nm, and 0.23 nm indicates that these terraces are less stable. The line profiles drawn over the terraces of Figures 6.3(a) and (c) are shown in Figures 6.3(b) and (d).

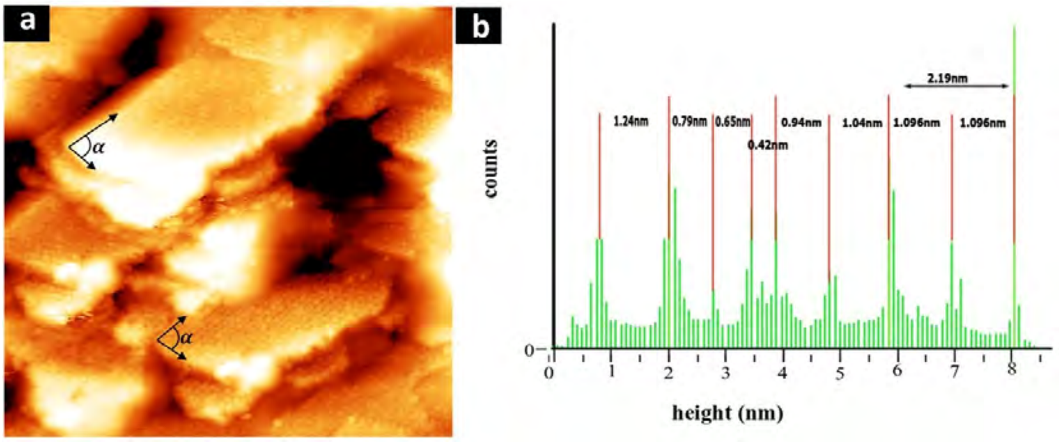

Figure 6.1: (a) 74 nm × 71 nm STM image (V_b = 0.9 V, I_t = 0.124 nA) showing the morphology of terraces. (b) histogram of step height for (110) surface, taken from figure (a) showing the four different values of step height. (c) 47 nm × 37 nm STM image showing.

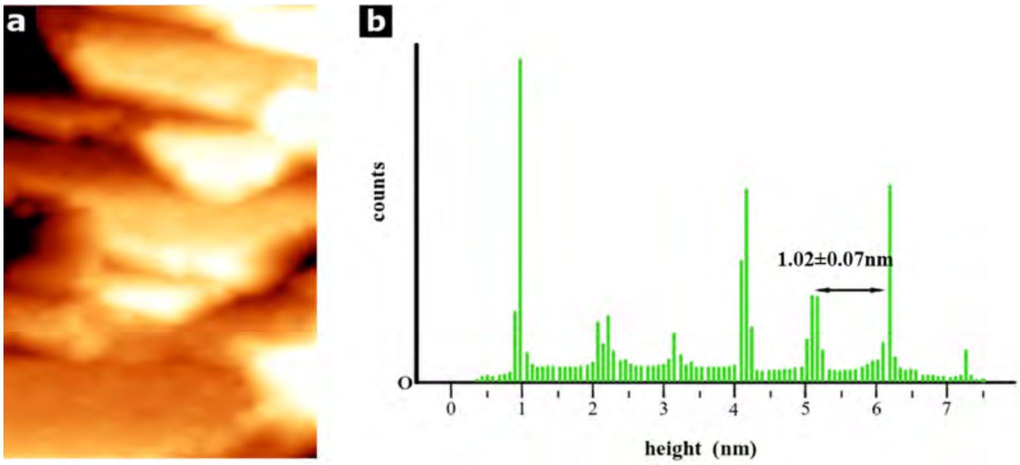

Figure 6.2: (a) 32 nm × 46 nm STM image (V_b = -0.82 V, I_t = 0.124 nA).(b) A histogram taken from (a), showing the step height distribution. The average step height is labeled.

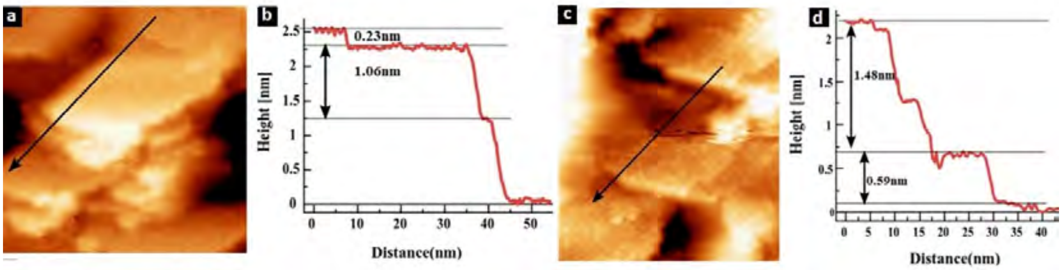

Figure 6.3: (a) 57 nm × 57 nm STM image. (b) A line profile across the terraces of (a) showing the step height is 0.23 nm. (c) 33 nm × 38 nm STM image, both (a) and (c) taken from Figure 6.1(a). (d) A line profile across the terraces of (c) showing step height is 1.48 nm and 0.59 nm.

Discussion

Research conducted through (STM) has consistently indicated that the surfaces of Tsai-type quasicrystals are terminated by rare-earth atoms. Specifically, the planes of these surfaces are densely populated with rare-earth atoms, as evidenced by multiple research papers [28, 52]. This phenomenon can be attributed to the low surface free energy and low-lying unoccupied 3d states of rare-earth (RE) atoms, which contribute to surface stabilisation [53, 109, 112]. Although there is no atomic-level resolution available for the Ag-In-R(100) approximant surfaces (where R = Yb, Tb, and Gd), it is highly probable that this phenomenon also applies to these cases [113]. Therefore, the analysis of step heights for the (110)Au-Al-Gd surface is conducted in relation to Gd dense planes.

In order to explain the step heights, the bulk structure of the Au-Al-Gd 1/1 approximant is presented. Figure 6.4(a) shows only the Gd icosahedron shells, with the top and bottom pentagons representing the two faces of the icosahedron shell highlighted in blue and red shapes, respectively, at the bottom of Figure 6.4(a). The bulk model consists of two types of layers: flat and puckered layers. The puckered layers corresponding to the top and bottom pentagons are marked with blue and red boxes, while the flat layer is marked with a green line. The flat layer contains one Gd layer, and the puckered layer can be considered to consist of three layers of Ga atoms. This puckered layer is referred to as a Gd surface slab, and it can be seen that the puckered layer is the diagonal of a pentagon.

Figure 6.4(a) shows the four main values of separation between the two puckered slabs. The separation between the two tops of the diagonal of the top pentagonals of the puckered slabs is 1.02 nm, which is marked with a blue dashed line. This separation is similar to the most frequent step height in the STM image. This measured step height (1.04 ± 0.08 nm) corresponds to the distance between adjacent lattice planes in the bulk.

$$d_{(hkl)} = \frac{a}{\sqrt{h^2+k^2+l^2}} \tag{6.1}$$

$d_{(110)} = 1.04$ nm, where $a = 1.48$ nm [11]. The two distances between the top puckered slab of the top and bottom pentagons are 0.42 nm and 0.6 nm, and they are marked with dashed blue and red lines. Additionally, the separation between the top of the puckered slab of the bottom pentagons and the bottom puckered layers of the top pentagons is 0.24 nm. All these values of separation are similar to two of the step heights observed in the STM image.

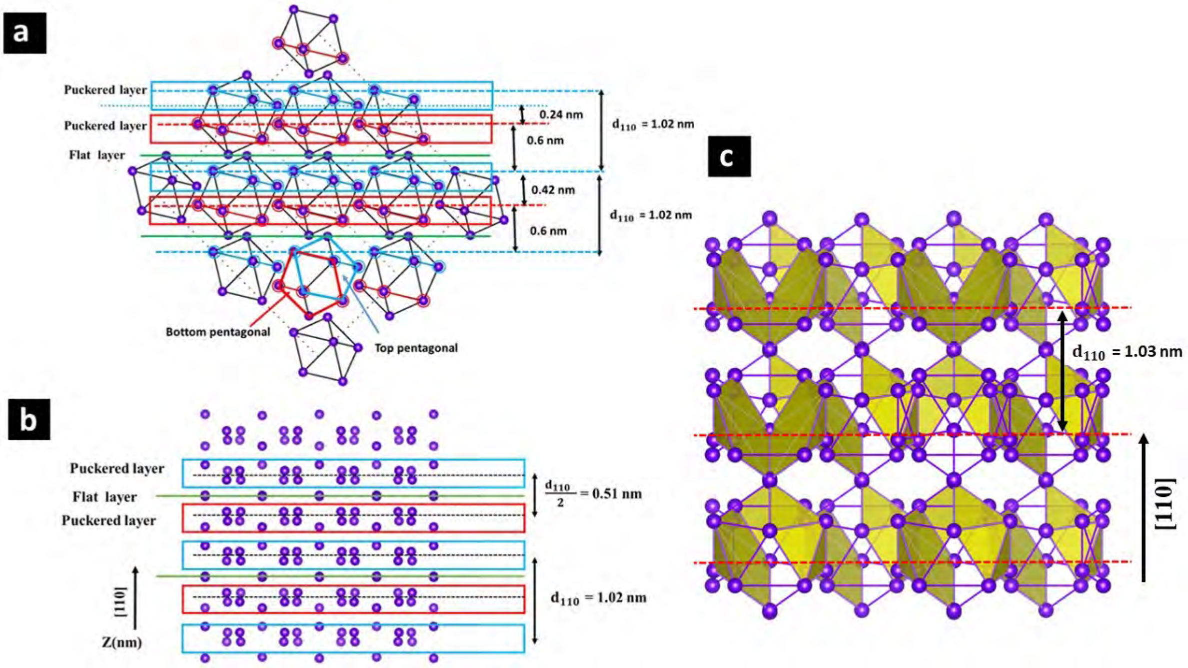

Figure 6.4: (a) Bulk model of Gd atoms showing the perpendicular arrangement of (110) planes from the side. The flat (green line) and puckered layers (blue and red lines) are shown. (b) Bulk model of Gd planes arranged along the [110] direction, showing the puckered layer consisting of groups of three planes. The distance between centres of the puckered layers is 1.02 nm, as labelled. Groups of planes which correspond to the measured step height are highlighted with a red box. (c) A bulk model of Gd atoms illustrating where surface terminations would truncate the Gd icosahedron along the [110] direction. It is the same model as in (b). It shows the positions that correspond to the measured step height.

Figure 6.4(b) shows a side view of the Gd planes in the bulk model; these Gd planes are arranged perpendicular to the [110] direction. The puckered layer of the top and bottom pentagons is bounded by blue and red boxes, respectively. The flat layer is marked with a green line. The atomic density of the puckered layers is much higher compared to the flat layers. The step height is formed at highest atomic density planes of the rare element on the plane. The separation of the layer of puckered slabs (i.e., centre to centre) is 0.51 nm, which is not observed in the STM image. The layer of the puckered slab of the top pentagons is a mirror plane of the layer of the puckered slab of the bottom pentagons. Therefore, the measured step height can be considered as the separation between one of the two types of slabs. We suggested that the distance between the two tops of the puckered layer of bottom pentagons can explain the step height in STM images, which is highlighted with a red box.

Figure 6.4(c) shows an enlarged version of Figure 6.4(b), where the icosahedral shells are used to build the model. The red lines are the same as the lines in

Figure 6.4(a), which are above the bottom puckered layer. The icosahedral shells are arranged on the same level in this model, and the figure also demonstrates prospective truncations at each level above the bottom of the icosahedral shell.

The flat Gd layer cannot be explain all observed step heights. The perpendicular spacing between flat layers is 1.04 nm. However, the other step heights of terraces, such as 0.4 nm, 0.6 nm, and 0.2 nm, cannot be explained by only the flat layers. It has been found that the separations between flat and puckered layers are 0.4 nm, 0.6 nm, and 0.25 nm. Additionally, the atomic structure of the flat layer does not match the observation of the atomic structure of the terrace in the STM image at negative bias.

It is suggested that the terraces form on top of puckered layers for three reasons. First, the puckered slab has the highest atomic density of Gd atoms. Second, it can explain the four values of measured step heights in the STM image. It can be assumed that the terraces are formed by cutting every icosahedron, which makes the step height of 1.04 nm the most common step height.

6.3.2 STM Images at Negative Bias

STM images taken at negative bias are shown in Figure 6.5. Two features of interest visible are atomic rows running along the [001] direction and bright protrusions located atop these rows. Rectangular vacancies are observed in some sections of the terraces, as shown in Figure 6.6(a). The dimensions of these rectangular defects are 1.39 nm × 1.97 nm, which are close to the lattice constant of the centred rectangle unit cell of the (110) surface.

The FFT of the atomically resolved STM image in Figure 6.6(a) is presented in Figure 6.6(b). The FFT pattern shows two-fold symmetry along the [110] and [001] directions. It shows a centred rectangle pattern, which is marked with white spots. The two lattice constants in real space are 2.05 ± 0.09 nm and 1.40 ± 0.06 nm, unit vectors in FFT are labelled with a_1^* and a_2^*. The distance in real space between the spots is 1.01 ± 0.05 nm along the [110] direction, which is highlighted with a green dotted circle. The FFT also shows the rhombohedral unit cell of the surface, marked with a white rombohedron. The lattice constants are 1.26 ± 0.05 nm, and 1.15 ± 0.01 nm, with the angle between these vectors being 107.5 ± 0.38°, confirming the surface is bcc.

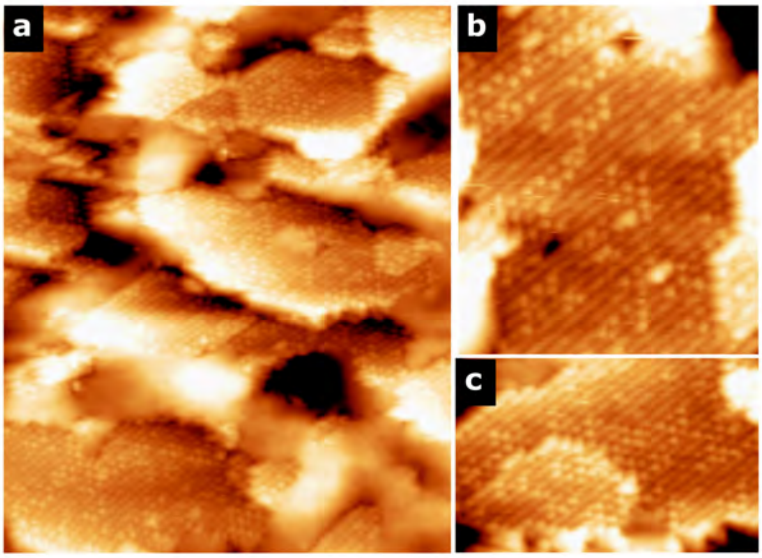

Figure 6.5: STM image taken from different terraces showing the structure at negative bias. (a) 63 nm × 77 nm STM image (V_b = -2.1 V, I_t = 0.183 nA). (b) 25 nm × 29 nm STM image (V_b = -1.6 V, I_t = 0.124 nA). (c) 31 nm × 20 nm STM image (V_b = -1.2 V, I_t = 0.21 nA).

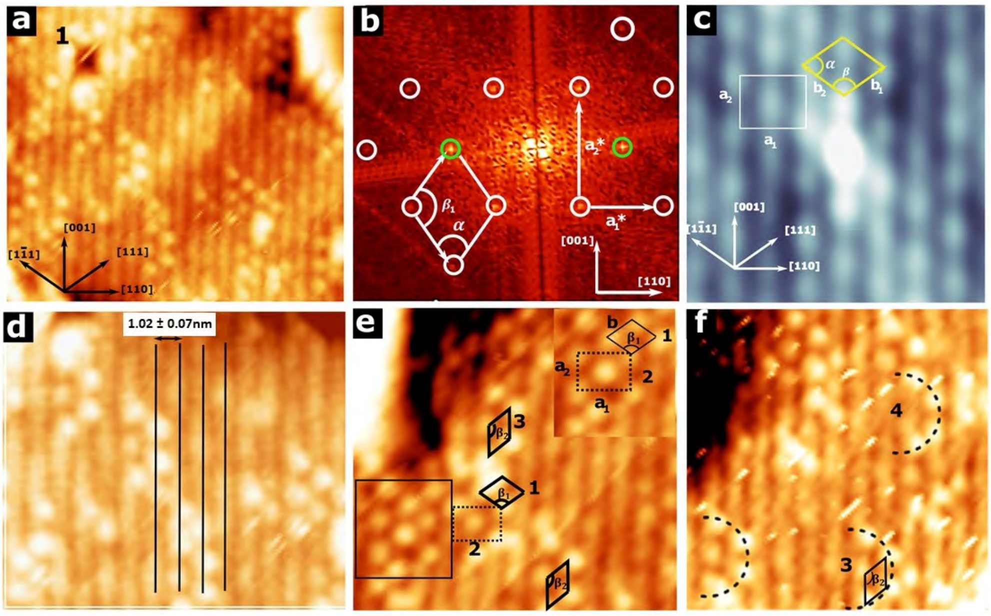

Figure 6.6: (a) An enlargement of the area depicted in Figure 6.5(b). (b) FFT of (a). The surface unit cell of the facet is marked. (c) Autocorrelation function of (a) (7 nm × 8 nm). (d) 14 nm × 13 nm STM image (V_b = -2.1 V, I_t = 0.138 nA) taken from (a). (e) and (f) 14 nm × 13 nm, and 14 nm × 14 nm STM images taken from different terraces, showing the two motifs, the half-circle and the centred rectangle, labelled 1 and 4.

In order to determine the unit cell, we analysed the autocorrelation function of the image taken from the high density bright protrusions, as shown in Figure

6.6(c). The atomic structure can be described by a rhombohedral unit cell which is marked with a yellow rhombohedral motif. The two edge lengths are 1.26 ± 0.03 nm, and 1.16 ± 0.05 nm along the [111] and $\left[1\bar{1}1\right]$ directions, respectively. The unit vectors are at an angle of 109.6 ± 0.3°, and 70 ± 0.3°, which are very close to the expected unit cell angles of the bcc (110) surface. Along the [110], the distance between the spots is 1.99 ± 0.06 nm. The separation between spots along the [001] direction is 1.38 ± 0.06 nm. These two distances correspond to the real-space distance between spots along two-fold symmetry in the FFT, which is highlighted with a white circle.

The area at the top of Figure 6.6(a) is magnified in Figure 6.6(d). The row alignment along [001] has a high density of atoms, with a separation between the rows along the [110] direction of 1.02 ± 0.07 nm, which is marked with a black line. This separation corresponds to the spot in the FFT which is highlighted with a green circle in the FFT pattern. In addition, bright protrusions distributed above the rows are observed to form two features, a centred rectangle and a rhombohedral motif, labelled number 1 and 2 in Figure 6.6(e). The two edge-lengths of the rhombohedral unit cell are 1.26 ± 0.05 nm and 1.26 ± 0.04 nm with an angle β = 110.4 ± 0.3°.

The centred rectangle motifs are identified near the end and beginning of the step height in the STM image. The edges of the centred rectangle are 1.41 ± 0.05 nm, and 2.05 ± 0.09 nm along the [001] and [110] directions, respectively. The bright protrusions form the incomplete centred rectangle motif, labelled with number 4 in Figure 6.6(f). Motif 4 appears to be a half-circle, with two separations is 1.42 ± 0.05 nm and 1.26 ± 0.04 nm along the [001] and [111] directions, respectively. The angles between these vectors are 125.3 ± 0.2°, and 55 ± 0.2°, respectively, marked with β_2 and number 3

6.3.3 Discussion

We now examine a potential explanation for the features observed by STM. Comparing STM results to a bulk model structure is necessary here. The motifs observed in the STM are magnified in Figure 6.7(a) and (b), while Figure 6.7(c) depicts the (110) plane in the model derived from the puckered layer, which is highlighted in Figure 6.4(a) with a red rectangle. The first and second sub-layers of the puckered layer are considered. Different coloured circles correspond to atoms belonging to different shells of the RTH cluster: purple: 3^{rd} shell Gd, red: 4^{th} shell Au/Al, light blue and light green: 2^{nd} shell Au/Al [114]. The atomic positions of the 1^{st} shell Au/Al have been omitted. It is expected that there is a tunnelling current contribution from Au/Al atoms at negative bias [8]. The 2^{nd} and 4^{th} shell can explain the observed features at negative bias. The 4^{th} shell is arranged in a row in the model along the [001] direction, which is denoted by a black vertical line. The distance between adjacent rows along the [110] direction is 1.02 nm. Furthermore, the row has a high density of 4^{th} shell Au/Al atoms. The separations and directions of 4^{th} shell Au/Al atoms match the observed rows in the STM image.

A circular feature has also been identified and marked with a black circle, labelled as A. This feature is formed by six atoms, four from the 4^{th} and two 2^{nd} shells Au/Al, all six shells surrounding a 3^{rd} shell Gd. This feature will be referred to as an `"motif A"`. Motif A represents the bright protrusions observed in the rows of the STM image and can explain the unit cell of the bcc surface. The vertices of the solid black rectangle tiles are located on the motif A, which is marked and labelled with a black rectangle and the number 2.

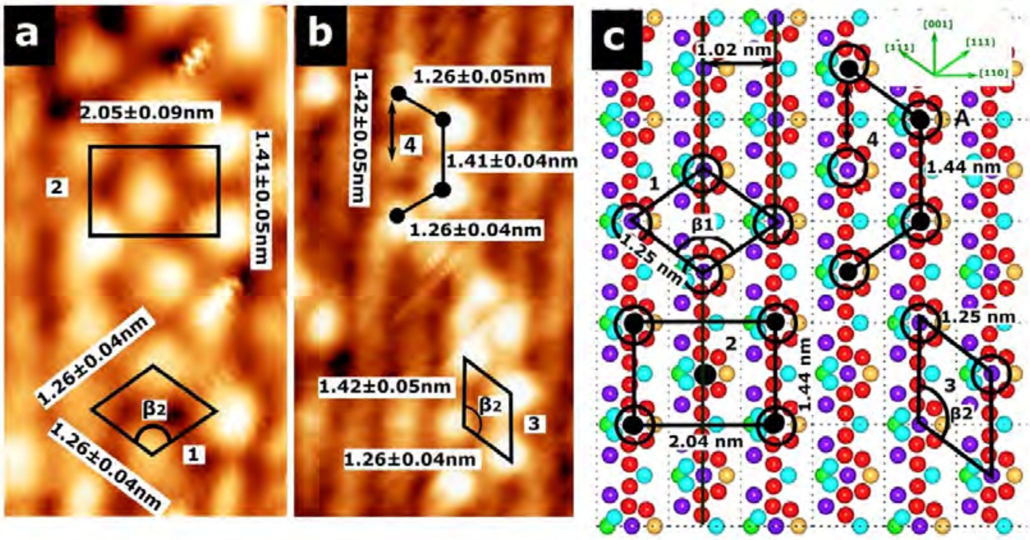

Figure 6.7: (a) 5 nm × 9 nm STM image showing the rhombohedral motif and the centred rectangle motif which are marked with 1 and 2. (b) 6 nm × 11 nm STM image showing the incomplete the centred rectangle motif and rhombohedral motif (3). (c) Model schematic of (a). Red: 4^{th} shell Au/Al, light blue and green: 2^{nd} shell Au/Al, and purple: 3^{rd} shell Gd. It shows the motifs observed in (a) and (b), which are marked as the same motifs as in (a) and (b).

The centers of motif A are separated by two distances: 2.04 nm along the [110] direction and 1.44 nm along the [001] direction. These arrangements of motif A form a centred rectangle shape, is labelled 2, which corresponds to motif 2 in the STM image. A Motifs are arranged along the [111] and $\left[1\bar{1}1\right]$ directions, with a separation of 1.25 nm and an angle of 110° and 70° between two vectors.

Four A motifs form a primitive unit cell (rhombohedral), labelled as 1. This unit cell matches the surface unit cell in the STM images, which corresponds to motif number 1. The third motif is the rhombohedral motif, which is marked with the number 3. The two edge lengths are 1.44 nm, and 1.26 nm, with an angle between the vectors of 124°. The two rhombohedral motifs with different orientations form an incompletely centred rectangle shape, which is labelled 4.The most commonly observed STM feature is the incomplete centred rectangle. The four motifs correspond to those observed in the STM image. In STM observations, the centers of bright protrusions are bright, confirming that Gd atoms in the center of motif A are resolved at a negative bias of $\geq$2 V. The negative bias becomes comparable due to contributions from both compounds [110].

6.3.4 STM Image at Positive Bias

A high-resolution STM image of a terrace is shown in Figure 6.8. The STM images were taken with a positive bias from three different areas, revealing two types of atomic structures. The first type is a zigzag row, which is indicated by a black arrow and aligned in the [001] direction, as shown in Figure 6.8(d). The second type is a row of bright dots, as shown in Figure 6.8(c). It was found that the contrast of the bright protrusions on the tops of the rows is lower than that at a negative bias.

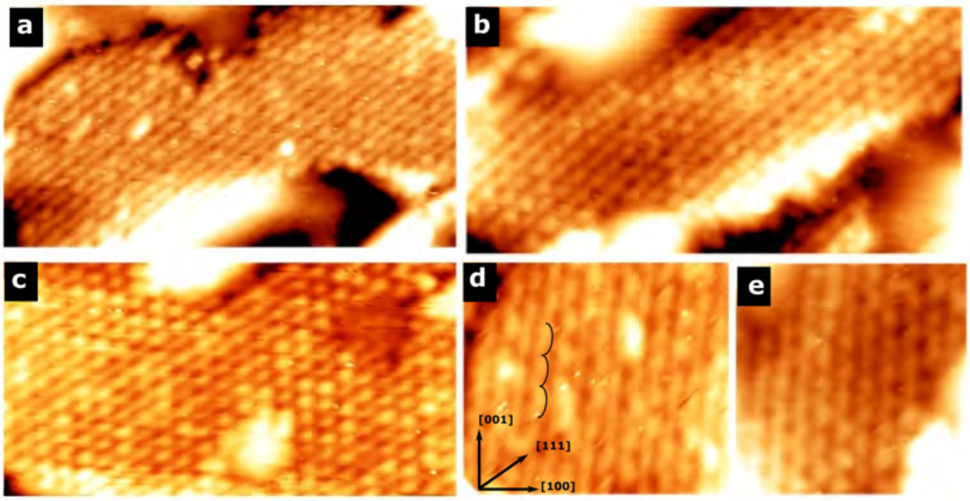

Figure 6.8: STM images taken from various terraces with different tip conditions showing the atomic structure of the surface at positive voltage. (a) 73 nm × 20 nm STM image (V_b = +1.1 V, I_t = 0.179 nA). (b) 32 nm × 16 nm STM image (V_b = +1.1 V, I_t = 0.124 nA). (c) 27 nm × 64 nm STM image (V_b = +1.1 V, I_t = 0.137 nA). (d) and (e) are magnified areas of (a) and (c), showing the zigzag rows.

Figure 6.9(a) shows two rough-edged terraces, labelled A and B. Figure 6.9(b) is a high-resolution enlargement of the area in terrace A. The structure is a zigzag row in the direction of [001]. The angle between the bonds of the zigzag structure is 108.9 ± 0.6°, which is labelled with a φ in the inset of Figure 6.10(a). However, the atomic structure obtained from the surface is not very clear. Figures 6.10(b) and (d) depict the FFT pattern and autocorrelation of Figure 6.10(a). The FFT pattern and the autocorrelation function of the STM image confirm the rhombohedral unit cell of the bcc surface. The lattice constant in real space is 1.19 ± 0.02 nm along the horizontal direction in the FFT pattern, which is highlighted with a white circle. This lattice constant represents the separation between the rows along the [110] direction in the STM image, which is marked with a black arrow in Figure 6.10(c). In the autocorrelation function, the separation between the spots along [001] and [110] directions is 1.35 ± 0.05 nm and 2.1 ± 0.07 nm. The length of the rhombohedral unit cell's side is 1.25 ± 0.05 nm and 1.14 ± 0.07 nm in the $\left[1\bar{1}1\right]$ and [111] directions, respectively. The angle between the two directions is 109.4 ± 0.3°.

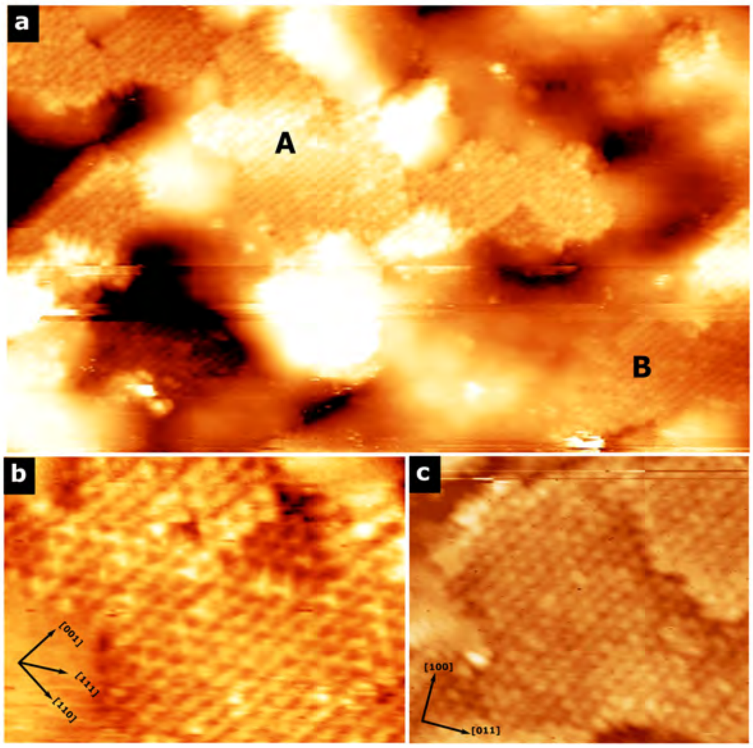

Figure 6.9: STM images taken at ($V_b = +1.5$ V, $I_t = 0.149$ nA). (a) 90 nm × 54 nm STM image showing two flat terraces, labelled with A, and B. (b) Enlargement area taken from terrace A, 22 nm × 16 nm. (c) 26 nm × 22 nm STM image taken from terrace B after a repeat scan to obtain high resolution.

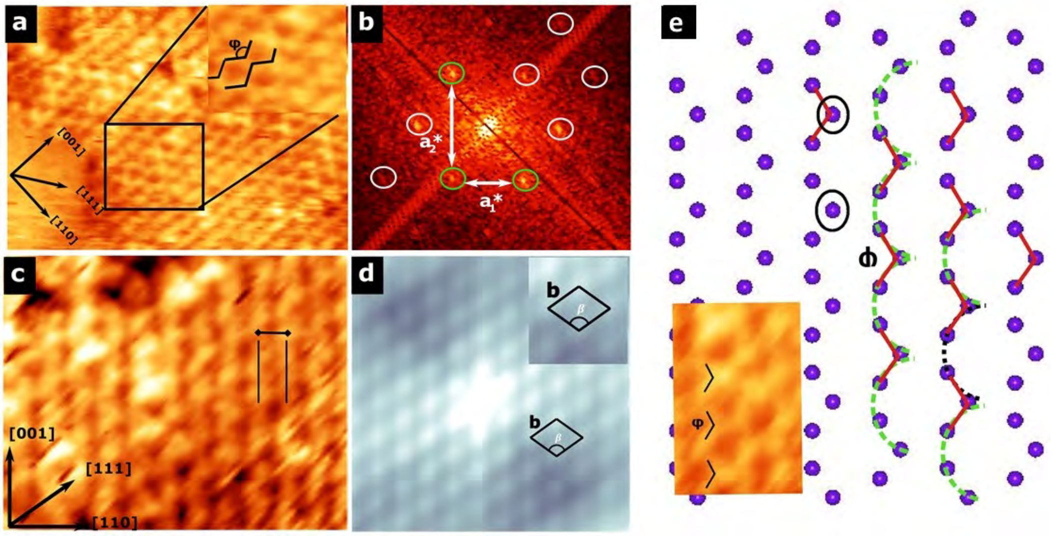

Figure 6.10: (a) 22 nm × 16 nm STM image taken from area A in Figure 6.9 (b), with magnification. The zigzag row is observed. (b) The FFT pattern of (a) confirms the unit cell of the (110) surface. (c) 11.8 nm × 9.4 nm STM image merged with the inverse of FFT taken from terrace A. The direction of the surface is labelled. (d) Autocorrelation function of the STM image in (a) showing the rhombohedral unit cell. (e) a bulk model of the (110) plane obtains two layers of Gd atoms. It shows the zigzag structure.

Figure 6.11(a) shows a high-resolution STM image taken from the terrace in surface B with different tip conditions. This image reveals bright rows running along the [001] and [100] directions. The FFT pattern of Figure 6.11(a) is illustrated in Figure 6.11(b). Using two lattice constants in real space, $a_1 = 2.01 \pm 0.07$ nm and $a_2 = 1.38 \pm 0.05$ nm, the centered rectangle unit cell of dimensions a_1 and a_2 is highlighted. The two dimensions of centred rectangle corresponds to a_2 and $a_2 \times \sqrt{2}$. In order to determine the unit cell, the autocorrelation function of Figure 6.11(a) is presented in Figure 6.11(c). The maxima in the autocorrelation function reflect the periodicity of the image. The unit cell is found to be rhombohedral with dimensions 1.24 ± 0.05 nm, 1.17 ± 0.05 nm, $\beta = 109.1 \pm 0.3°$, and 70.4 ± 0.4°, which is consistent with that of the (011) plane of the Au-Al-Gd 1/1 approximant lattice, (1.26 nm, $\beta = 110°$). An STM image merged with an inverse FFT, is shown in Figure 6.11(d). The protrusions are separated by a distance of 1.94 ± 0.06 nm and are arranged along the [001] direction. In addition, protrusions are arranged along the [110] direction with a separation of 1.39 ± 0.06 nm. The two separations correspond to lattice constants a_2 and a_1 in real space of the FFT pattern. The geometry and dimensions of STM data in positive bias are analogous to those of negative bias measurements. The results of analysing the atomic structure of the two terrace surfaces shown in Figure 6.9(b) and (c) confirm that the two surfaces have the same surface unit cell of (110).

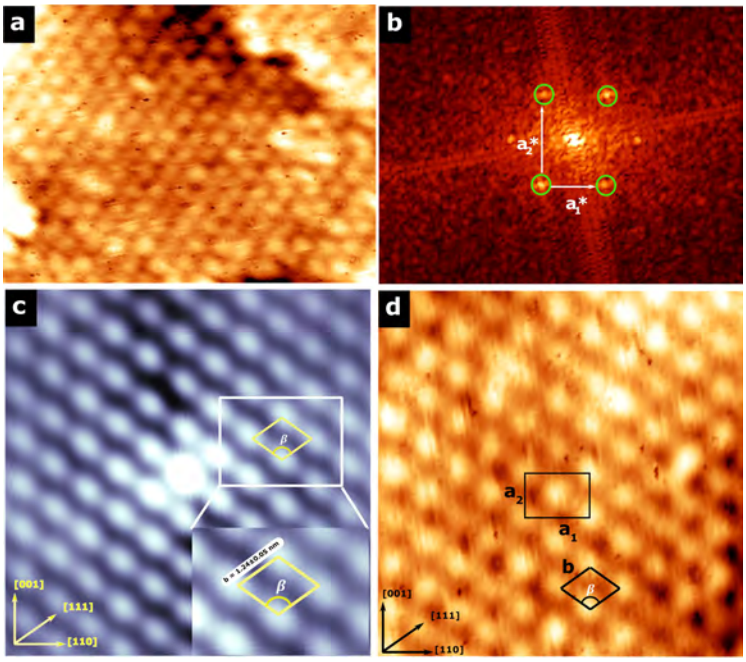

Figure 6.11: (a) 20 nm × 15 nm STM image taken from Figure 6.9(c). (b) The FFT of the image shown in (a). (c) Autocorrelation function of the STM image in (a), with size of image (11 nm × 11 nm). (d) Inverse FFT merged with (a), the rhombohedral and centre rectangle motifs are marked with the same black motifs.

6.3.5 Discussion

Since the position of the Gd atoms in a bulk model of the (110) plane can be resolved at positive bias, we will compare STM measurements at positive bias with the position of the Gd atoms in the bulk model. Figure 6.10(e) shows the Gd atom bulk model from Figure 6.7(c), omitting the 4^{th} and 2^{nd} shells. The Gd atoms obtained from two layers are arranged in a zigzag pattern along the [001] direction. The angle between the bonds of the zigzag structure is 110°, which corresponds to the angle in the STM image in Figure 6.10(a). Because the 3^{rd} shell Gd is in the centre of motif A, the separation and orientation of Gd atoms are unaffected by positive bias and are denoted by a black circle. Therefore, the geometry and dimension of Gd atoms match the STM observation, confirming that Gd atoms in the two layers are resolved in the STM image.

Figure 6.7(c) shows that the Gd atoms are located in the centre of motif A, providing an explanation for the single protrusions detected in the STM observations displayed in Figure 6.11. Furthermore, the shape of motif A and the unit cell is similar to the shape of the bright protrusions on the surface of the unit cell in STM. This finding leads to the observation that the protrusions observed in the STM at a positive bias of $\geq +1.5$ V display the 3^{rd} shell Gd positioned at the center of motif A, whereas the contribution from the 4^{th} shell Ag/In is minimal across the Fermi level and can not be resolved in voltage $\geq +1.5$ V [110]. These results indicate that the STM image resolves the single layer of Gd, which may provide an explanation for why the row structure is not as evidently observed as in the STM image.

6.3.6 Comparing STM Images at Different Bias Polarities

The STM images presented in Figures 6.12(a) and (b) were obtained by applying positive and negative bias voltages to the same area of the surface terrace. The data obtained from the STM images shows a clear dependency on the bias voltage, as shown in Figures 6.12(c) and (d). Specifically, when using a negative bias voltage, a row-structure can be observed with brighter protrusions lying on the rows. In contrast, when using a positive bias voltage, the row-structure is formed of dim protrusions, and the brightness of the bright protrusions located above the row is lower than that observed at negative bias. To enhance the resolution of the images, the STM data in Figures 6.12(c) and (d) was merged with the inverse of the FFT, as illustrated in Figures 6.12 (e) and (f). These figures depict STM

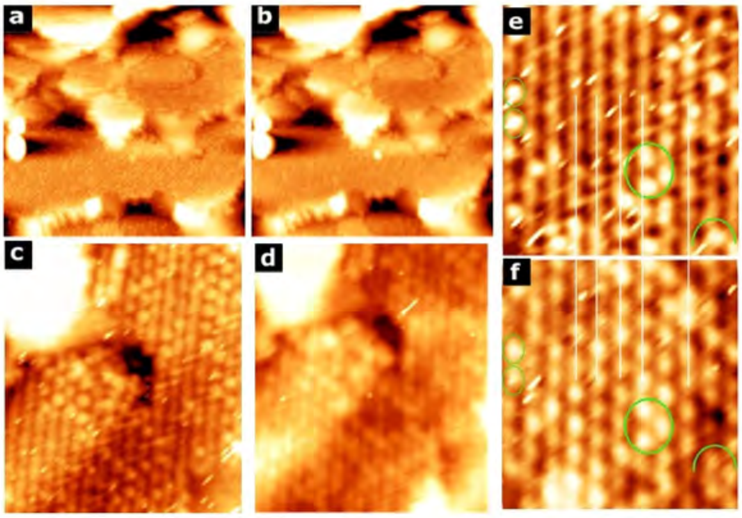

Figure 6.12: (a) 70 nm × 67 nm STM image at (V_b = -0.82 V, I_t = 0.158 nA) showing a flat terrace with bright protrusions. (b) 70 nm × 67 nm STM image at (V_b = +0.82 V, I_t = 0.158 nA) taken from the same area as (a), showing the protrusion brightness reduced and the rows formed along the [001] direction. (c) and (d) are 19 nm × 22 nm STM images, magnifications of areas from (a) and (b), showing the row structure in both biases. (e), (f) 13 nm × 12 nm STM images merge with an inverse FFT.

images taken from the same area with the same scale for both biases, with white lines highlighting the positions of the rows. The structure of the rows is unaffected by the inverse FFT at negative bias, whereas the intensity of the row-dim spot increases and becomes more visible at positive bias. There is no observed shift in the adjacent rows when changing the bias, and the positions of the bright protrusions remain unchanged with the application of both voltages, as marked with a green circle. This indicates that they belong to the same cluster in the bulk model.

6.4 Detailed Structure of the (111) Surface

6.4.1 Step Morphology

A large-scale STM image is displayed in Figure 6.13(a), showing the step/terrace morphology of (111). Figure 6.13(c) is a histogram obtained from Figure 6.13(b) that depicts the distribution of step heights, with the measured step height being 3.83 ± 0.07 nm.

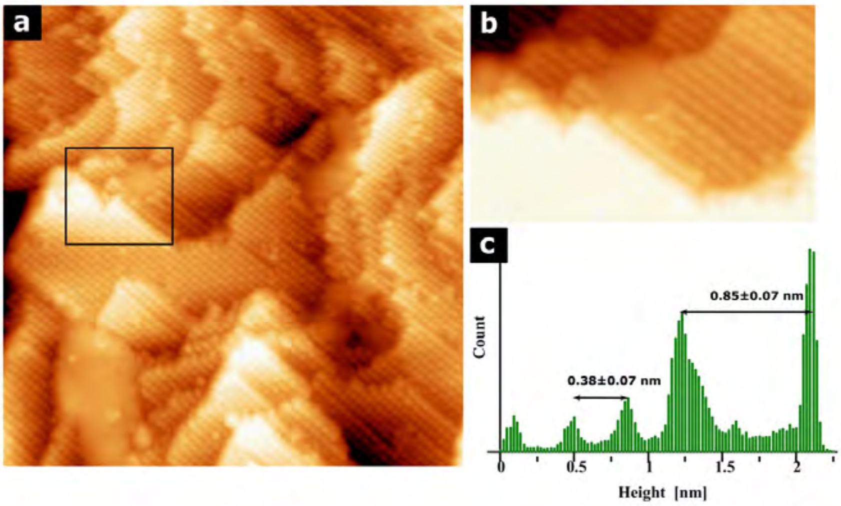

Figure 6.13: (a) 93 nm × 93 nm STM image of the (111) surface showing step/terrace morphology. (b) An enlarged area is highlighted with a black rectangle in (a), which is 38 nm × 24 nm STM image. (c) A histogram displaying the most frequently measured step height from (b).

In the bulk model, the step heights in the STM images correspond to adjacent atomic planes. The Gd planes in the bulk model are arranged perpendicularly to the [111] direction, as shown in Figure 6.14(a). A Gd surface slab is formed by three Gd planes and is marked with a black box, which we will refer to as the Gd surface slab. These slabs are separated by 0.43 nm, measured from center to center, and the distance between the low density of Gd atoms in the slab matches the measured step height in the STM. Therefore, each slab constitutes a step height in the STM images. It was found that the first layer has a low atomic density of Gd, and the second layer has a high atomic density in the slab bulk, marked with red and blue lines. We consider the first layer in the slab as the surface. The separation of adjacent lattice planes in the bulk is

$$d_{(111)} = \frac{a}{\sqrt{h^2 + k^2 + l^2}} = 0.852\ nm \tag{6.2}$$

The measured step height of terraces can be considered as (0.5 × $d_{(111)}$). However, the value of the interplanar the spacing ($d_{(111)}$ = 0.85 nm) is observed in a few of the measured step heights. The interplanar spacing ($d_{(111)}$ = 0.85 nm) refers to the distance between three slabs. The lattice points of the body-centred-cubic structure would be the only periodic interpretation of the cluster-centre planes for the Au/Al-Gd(111) system. Similar to the quasicrystal, the (111)-terminated plane can be found at every cluster centre plane. Therefore, the step heights will form every 0.43 nm (0.5 × $d_{(111)}$).

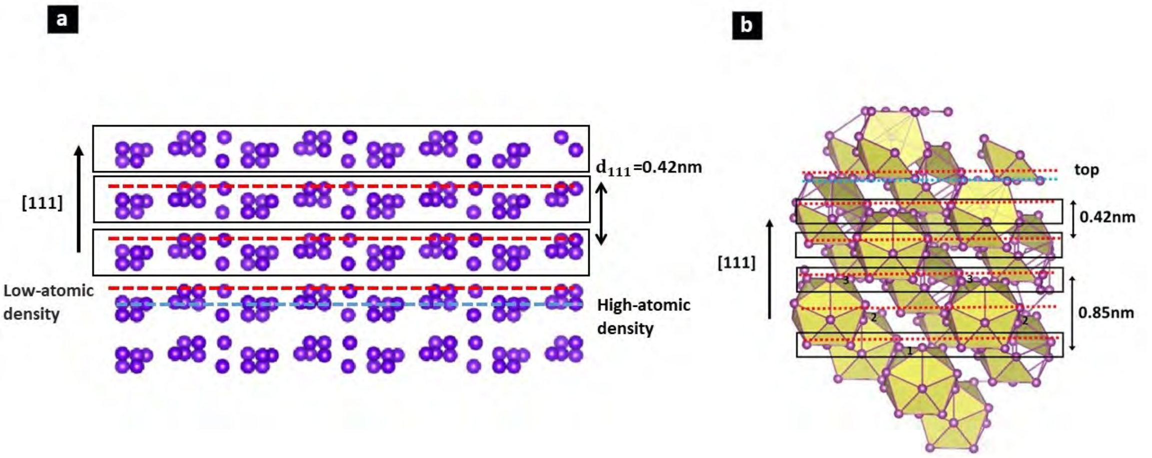

Figure 6.14: (a) Bulk model of Gd planes arranged along the [111] direction. Groups of three planes are separated by 0.42 nm, as labeled. (b) A bulk model of Gd atoms showing a side view of the (111) surface built from the Gd icosahedron The smallest step height for Gd atoms is represented by dashed red lines separated by 0.42 nm.

The atomic structure of Tsai-type quasicrystals has been a topic of extensive research, and understanding the formation of step heights on the terminated plane is crucial for advancing our knowledge of these materials.

The view side of the bulk model along the [111] direction is shown in Figure 6.14(b) to explain the presence of the step height formed in the (RE) terminated plane. Figure 6.14(b) is an enlarged section of Figure 6.14(a) that uses icosahedral shells to build the model. It is suggested that the truncations occur at the bottom of the icosahedron, marked with a dashed blue line below the top of each icosahedron, with step heights of 0.42 nm. The cut that forms the step height is located close to those previously reported by Coates *et al.* [8], which are highlighted with a dashed blue line. The difference in the value of the step height from that observed in [8] is because the cutting occurred for each icosahedron and the rare-earth (RE) atoms in the sample are Gd and not Tb.

6.4.2 STM Image

Figure 6.15(a) and (b) show a high-resolution images of the surface at both voltages (the zoomed area in Figure 6.13(a)). The location of the bright protrusions is not affected by the type of voltage. However, it was observed that the atomic density of rows along [101] increased at a negative bias.

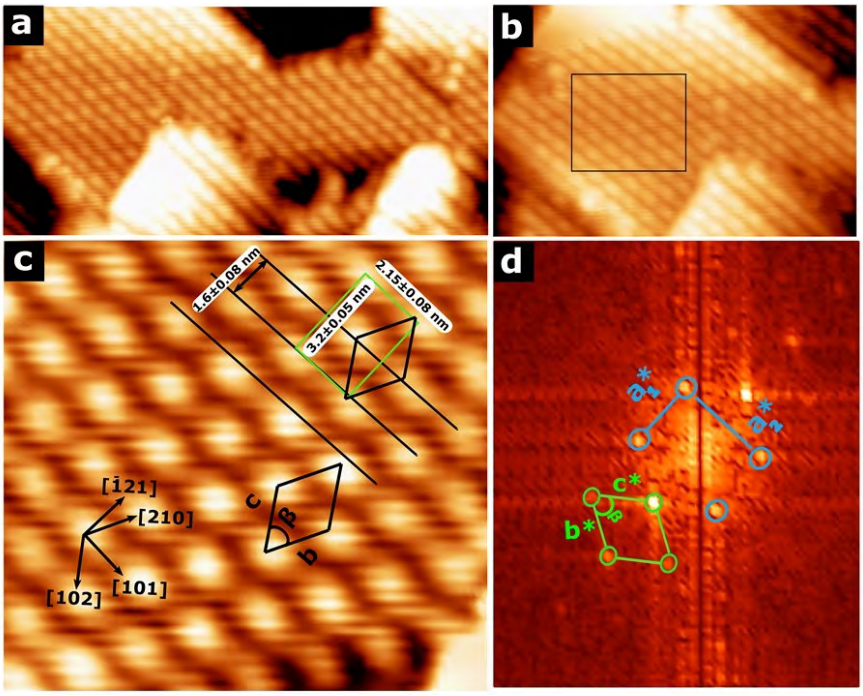

Figure 6.15: (a) Zoomed-in STM image in Figure 6.13(a) (V_b = - 0.69 V, 53 nm × 25 nm). (b) 36 nm × 23 nm STM image (V_b = + 0.68 V). (c) An enlarged section that is highlighted with a black rectangle in (b). It shows the 14 nm × 13 nm STM image merged with an inverse FFT, showing a rhombohedral cell marked with a black rhombohedral motif. (d) The FFT pattern of (a), where spots are highlighted by green circles, showing the rhombohedral cell.

Figure 6.15(c) is highlighted with a black rectangle in Figure 6.15(b) and merged with an inverse FFT. It shows large, bright protrusions aligned along the [101] direction, with a distance of 2.15 ± 0.08 nm, is marked with a black line. The rows are arranged along the $[\bar{1}21]$ direction, with a separation of 1.6 ± 0.08 nm. In addition, the distance between protrusions is 3.22 ± 0.05 nm. The surface is decorated with a rhombohedral cell, as marked by a black shape. The two edges-lengths are aligned along the [102] and [210] directions, with the lattice constants b = 2.0 ± 0.1 nm, c = 1.98 ± 0.08 nm and β = 62 ± 0.4°, respectively. These are the two lattice constants of a surface (111) rhombohedral cell.

The FFT of surface of the flat area in Figure 6.13(b) is shown in Figure 6.13(d). The unit cell is rhombohedral with two lattice constants: $|b|$ = 1.98 ± 0.09 nm, $|c|$ = 2.01 ± 0.08 nm, and β = 68.8 ± 0.4°, marked with a green rhombohedral cell. The FFT pattern confirms that the symmetry and dimension of the unit cells observed by STM are consistent with the (111) surface. The spots highlighted by a blue circle reflect the protrusions arranged along the two-fold direction. The two real spacings are a_1 = 3.3 ± 0.1 nm and a_2 = 2.1 ± 0.12 nm which are labelled a_1^* and a_2^*. These two values are close to the separation between protrusions along the $[\bar{1}21]$ and [101] directions in the STM image, which is is a central rectangle with dimensions of a_2 and $a_2\times\ \sqrt{3}$. The spacing between two spots, which is highlighted with a green circle, is 1.61 ± 0.06 nm, matching the distance between rows along the $[\bar{1}21]$ direction.

6.4.3 Discussion

We now suggest an explanation for the features observed in STM. Comparing the model of the (111) plane with STM observations, Figure 6.16(c) presents the model of the (111) plane. The 3^{rd} shell Gd, 4^{th} shell and 5^{th} shell Au/Al are marked with purple, red and blue circles, respectively. The set of 3^{rd} shell Gd, 4^{th} and 5^{th} shells Au/Al form the circular motif, which is highlighted with a black circle. The vertices of the rhombohedral cell reside on the centres of the cluster, marked with a green rhombohedral motif. The distance between two centre motifs along the [102] and [210] directions is 2.04 nm and the angle between them is 60°. The size of the rhombohedral motif is close to the rhombohedron observed in the STM image. This motif is arranged along $[\bar{1}21]$ and [101] directions with separation 3.5 nm and 2.04 nm respectively. This correspond to central rectangle observed in STM image.

At negative bias, the contributions from 4^{th} shell Au/Al, 5^{th} shell Au/Al, and 3^{rd} shell Gd become comparable [110]. The contribution of the tunnelling current from Au/Al atoms increases the atomic density of the row in the [101] direction, which corresponds to the STM data observed at negative bias.

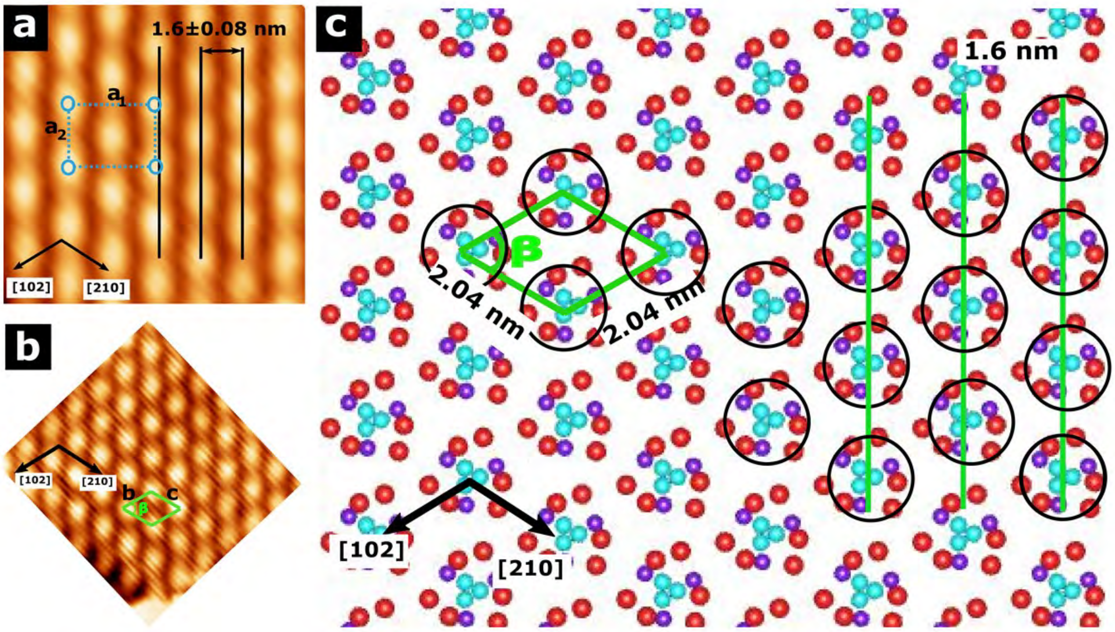

Figure 6.16: (a) 11 nm × 11 nm STM image showing close-packed features. (b) 15 nm × 14 nm STM image with an inverse FFT and a 50° rotation. (c) Atomic structure of the (111) plane. Purple, red and blue dots represent atoms of 3^{rd} shells Gd, the 4^{th} and 5^{th} shells Au/Al sites, respectively. A rhombohedral unit cell is marked.

Figures 6.17(a)-(c) depict an STM image taken from different areas, showing terrace morphology. A terrace kink angle α, with a value of 119 ± 2° is marked in Figure 6.17(b). A histogram of the area highlighted with a black dashed rectangle in Figure 6.17(a) is shown in Figure 6.17(d). It was found that the step height is 1.25 ± 0.07 nm. However, the step height of 0.81 ± 0.08 nm is observed in the small flat terraces, as shown in Figure 6.17(b). Hexagonal defects is observed on the surface, as shown in the inset of Figure 6.17(a). The step height is close to that observed in (111) Au-Al-Tb [8], and is 1.5 times larger than the separation of adjacent lattice planes in the bulk $d_{(111)}$.

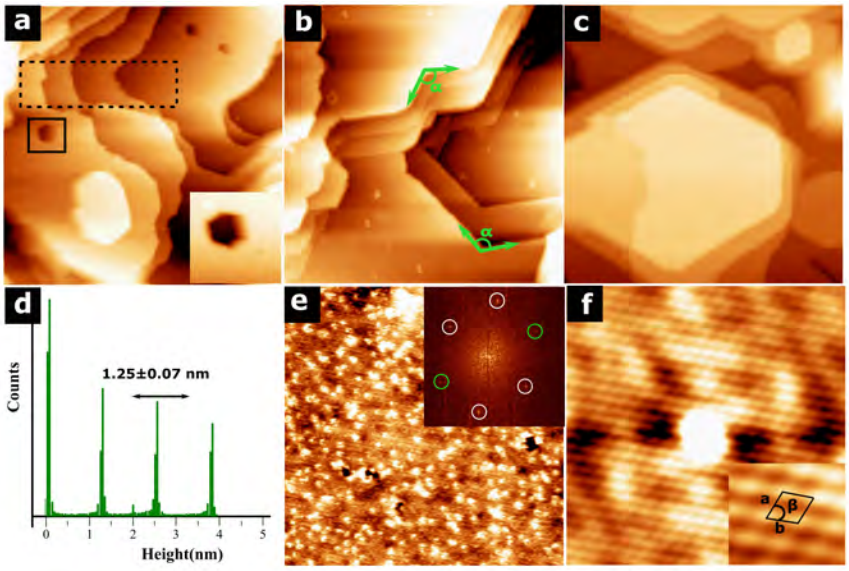

Figure 6.17: (a)-(c) STM image showing the step height and morphology of terraces. (a) 150 nm × 150 nm STM image taken at (V_b = -0.9 V and I_t = 0.108 nA), showing the hexagonal defect. (b) 100 nm × 100 nm STM image taken at V_b = +1.4 V, showing the Here α indicates the terrace kink angle. (c) 100 nm × 100 STM image taken at (V_b = +1.5 V). (d) A histogram of step height of (a); the average step height is marked. (e) 27 nm × 27 nm STM image taken at V_b = +1.2 V. An inset shows the FFT of (e). (f) 21 nm × 21 nm autocorrelation of (e) showing the six-fold symmetry of the surface.

It is difficult to observe the atomic surface because of the bright protrusion. However, the FFT and autocorrelation functions are obtained from the surface. The autocorrelation together with the FFT of Figure 6.17(e) is shown in the insets of Figures 6.17(e) and 6.17(f), respectively. The unit cell, which is determined from the autocorrelation function, is marked with a black rhombohedral. It is found that a rhombohedral unit cell with lattice parameters of 0.45 ± 0.05 nm, 0.55 ± 0.08 nm, and $\beta = 61.14 \pm 0.18°$. The lattice parameters are not the same as those in the (111) plane of the bee model structure (2.0 nm, 2.02 and $\beta = 60°$). The FFT pattern shows six-fold symmetry, which is expected from a (111).

6.5 Detailed Structure of the (130) Surface

6.5.1 Step Morphology

Three large-scale STM images taken from different areas are shown in Figures 6.18(a), (b), and (c), showing the step/terrace morphology of the (130) surface. The bulk model structure's predicted two-fold symmetry is consistent with the terrace kink angle, which is indicated and has a value of β = 104.2 ±0.5°. The distribution of step heights is depicted in Figures 6.19(c) and (d) by a histogram taken from Figures 6.19(a) and (b), with 0.42 ± 0.05 nm and 0.85 ± 0.07 nm being the two most typical step heights.

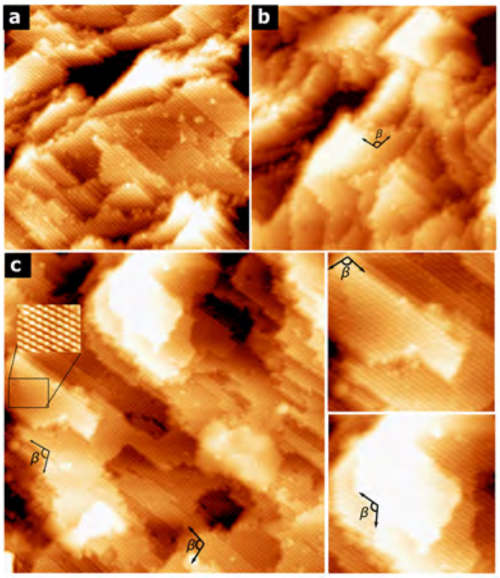

Figure 6.18: (a)-(c) Large-scale STM images obtained from different areas, showing the (130) surface: (a) 100 nm × 100 nm STM image. (b) 100 nm × 100 nm STM image at $V_b = +1.5$ V. (c) 125 nm × 125 nm at ($V_b = +01.28$ V, $I_t = 0.194$ nA). Right of (c) shows the terrace kink angle, marked with β.

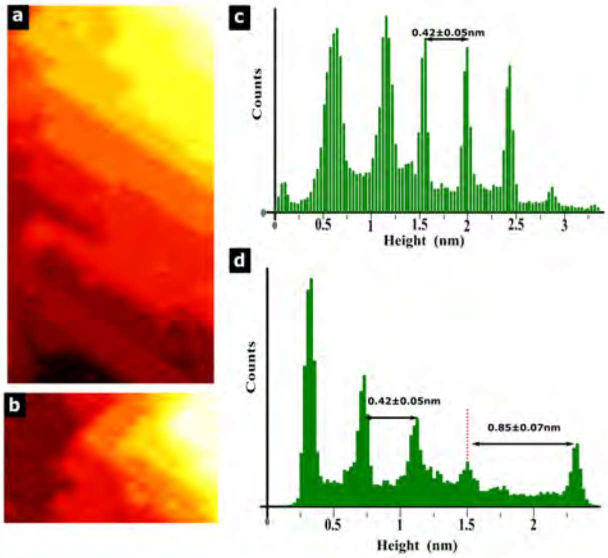

Figure 6.19: (a), and (b) 29 nm × 53 nm, and 28 nm × 17 nm STM images of the step terrace structure of the (130) surface taken from different areas with the same tip condition. (c) and (d) Histogram taken from (a) and (b), showing the step height distribution. The observed step heights are marked.

In the bulk model, we take the step heights into consideration in terms of atomic planes. The Gd planes in the bulk are arranged perpendicular to the

[130] direction, as shown in Figure 6.20(a). For example, Gd surface slabs are highlighted with a black box and formed by six Gd planes, which we will refer to as Gd surface slabs. These slabs are 0.47 nm apart, measured from centre to centre, and marked with a dashed red line. The separation between the centres of the slab of Gd atoms matches the measured step height in the STM. As a result, in the STM image, each slab in the bulk model represents a step height. It was found that the three layers at the top of the slab, marked with a green box, constitute the step height in the bulk model. In order to determine the atomic structure of the surface, we consider the three layers on top of a slab. In the bulk, adjacent lattice planes are separated by

$$d_{(130)} = \frac{a}{\sqrt{h^2 + k^2 + l^2}} = 0.468\ nm \tag{6.3}$$

The measured step height of terraces can be described as $\mathrm{d}_{(130)}$. In the Au-Al-Gd (130) system, the lattice points of the body-centred-cubic structure are the only periodic interpretation of the cluster-centre planes. Similarly to the quasicrystal, the (130)-terminated plane can be found at every cluster centre plane, resulting in step heights being formed every 0.47 nm ($\mathrm{d}_{(130)}$). As shown in Figure 6.20(b), the surface of the steps is formed at the top of the diagonal of the top pentagonal face of the icosahedron.

The termination plane in the Tsai-type quasicrystal surface has a high density of rare-earth atoms. This has been related to the rare-earth (RE) atoms' low surface free energy and low-lying unoccupied 3d states [53, 112, 109]. Although the Ag-In-R(100) approximant surfaces (R = Yb, Tb, and Gd) lack atomic resolution, it is thought likely that this is also true for these instances [113]. The (130) Au/Al-Gd surface's step heights are explicable in terms of Gd dense planes.

The view side of the bulk model along the [130] direction is shown in Figure 6.20(c) to explain how the step heights. It is an enlarged section of Figure 6.20(a). The icosahedral shells are used to construct the model. It is suggested that the truncations occur in the top icosahedron. The possible truncations are shown as solid red lines at the top of each icosahedron, with step heights of 0.47 nm. The section that is highlighted with a dashed black box is magnified in the inset of the right Figure 6.20(c).

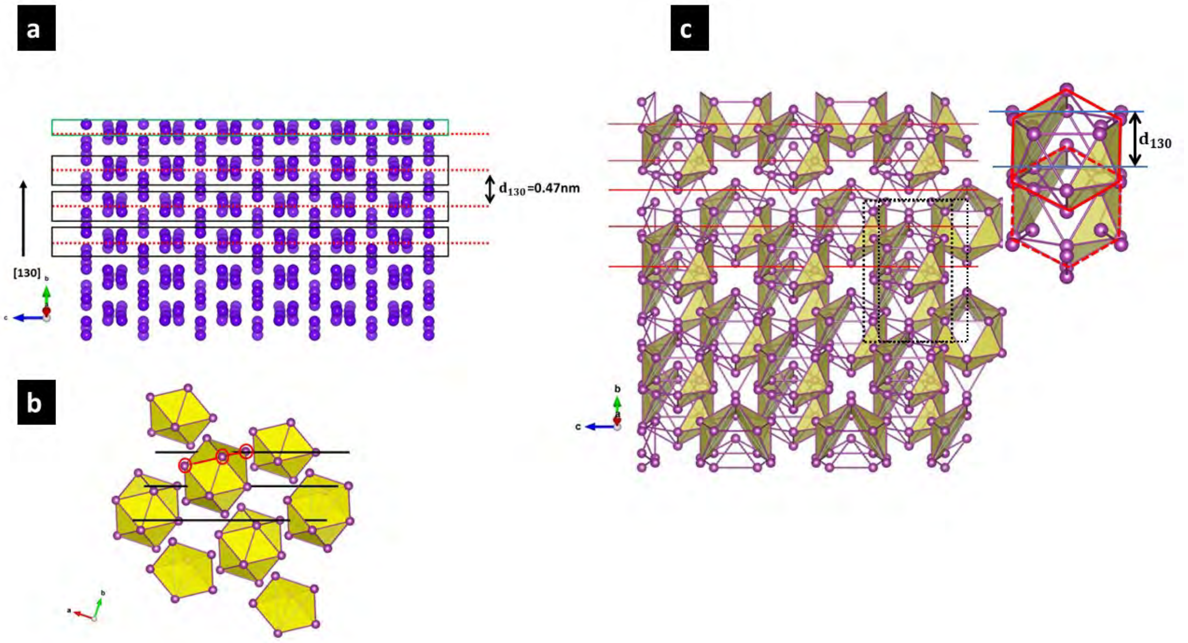

Figure 6.20: (a) A bulk model of Gd planes arranged along the [130] direction. A group of six planes forms a slab, marked with a black box. The distance between the centres of slabs is 0.47 nm, as labeled. (b) A Gd atom bulk model with the (130) planes arranged perpendicularly. The (130) plane is indicated by a black line. It shows the top and bottom pentagonal faces of the Gd icosahedron. It shows the truncations that occur on the top point of the diameter of the bottom pentagonal face. (c) A bulk model of Gd atoms showing a side view of the (130) surface built from the Gd icosahedron. The step height for Gd atoms is represented by dashed lines and separated by 0.47 nm.

6.5.2 Bias-Voltage Dependence

STM data was obtained from the clean (130) surface at various bias voltages, ranging from +1.5 V to -1.5 V. The data was taken from the same area on the surface with the same tip conditions. Atomic structures of the surface at voltage biases of +1.5 V and -1.5 V are displayed in Figures 6.21 (a) and 6.21(b), respectively. Figure 6.21(b) depicts bright protrusions distributed along the$[13\bar{1}]$ and [100] directions at a positive bias. The FFT pattern of the STM image in Figure 6.21(b) is presented in Figure 6.21(c). It was found that the angle between $\left[3\bar{3}1\right]$ and $[13\bar{1}]$ directions is 73.4 ± 0.3°, labelled as β. This value is consistent with the bulk model in (130). Additionally, Figure 6.21(d) illustrates the rows along the $[13\bar{1}]$ direction, which have a high density of atoms. Furthermore, these rows are formed by bright protrusions arranged in the $\left[3\bar{3}1\right]$ direction. The FFT pattern of the STM image in Figure 6.21(e) is shown in Figure 6.21(f), with β labelled again.

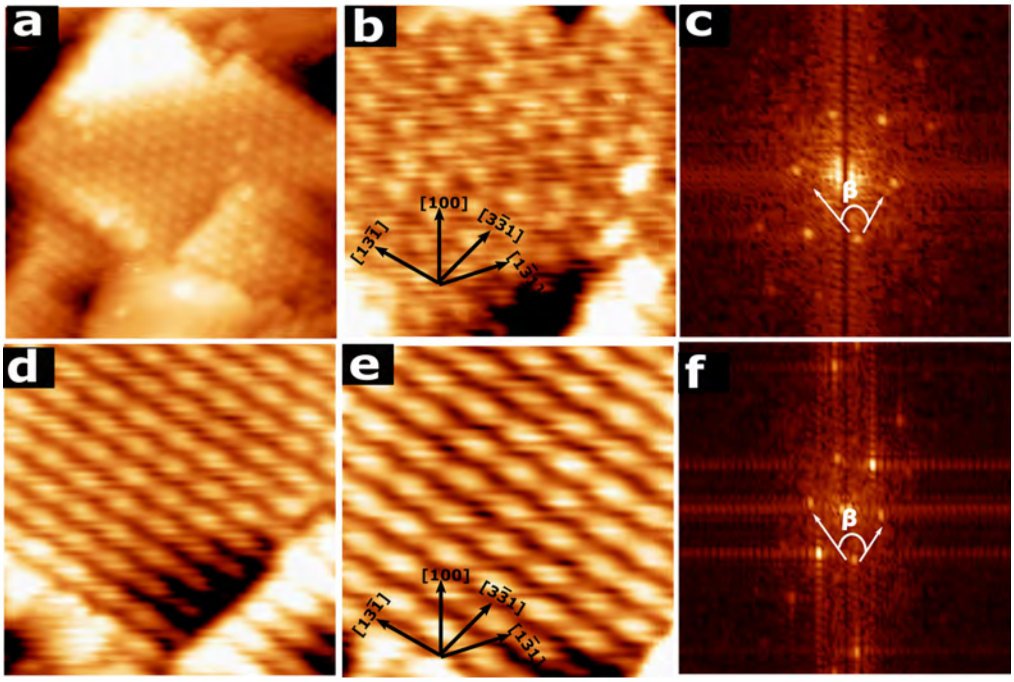

Figure 6.21: Voltage-dependent changes in cluster corrugation on the (130) plane. (a) 34 nm × 34 nm STM image show the surface at $V_b = +1.5$ V. (b) 15 nm × 15 nm STM image showing clusters on the surface. (c) FFT of the STM image in (b), showing $\beta = 73.4 \pm 0.3°$. (d) 15 nm × 15 nm STM image from same area in Figure (a) with sam tip condition at $V_b =$ - 1.5 V. (e) 12 nm × 12 nm STM image showing an enlarged view of (d). It shows a high atomic density along the [131] direction. (e) 15 nm × 15 nm STM image showing an enlarged view of (d). (f) FFT of flat area of (d) confirming the same value of β at positive bias.

6.5.3 STM Image at Positive Bias

Figure 6.22(a) depicts an STM image of the (130) facet, revealing the step/terrace structure. The terraces of the (130) facet are found to be separated by a step of 0.45 ± 0.04 nm height, measured using a histogram, as shown in the inset Figure 6.22(a). The measured step heights correspond to the expected periodicity along [130] which is $\frac{a}{\sqrt{10}}$. Figure 6.22(b) is a zoom of the flat area in Figure 6.22(a). It shows the high resolution of the surface at $V_b = +1.5$ V. It exhibits rows of bright dots arranged along the [100] and [$13\bar{1}$] directions, and the angle between these directions is 72 ± 0.9°. The separation between the protrusions is 2.8 ± 0.08 nm and 1.96 ± 0.1 nm along $\left[3\bar{3}1\right]$ and [$13\bar{1}$] directions, with the angle between vectors of 73.4 ± 0.6° which is labelled with θ. The surface is characterised by a centred oblique motif, which is highlighted with a green oblique.

Figure 6.22(c) depicts the FFT of the STM image shown in Figure 6.22(a). By analysing the position of the spots on the FFT pattern, the geometry of the surface can be determined. The real-space lattice parameters are calculated from the FFT using the following relation:

$$|b_i| = \frac{\pi}{|b_i^*| \sin \theta} \tag{6.4}$$

where $i = 1, 2$, b_1^* and b_2^* are the unit vectors in the FFT pattern, and θ is the angle between the unit vectors. When measuring angles in radians, the value π is used, whereas when measuring the angle in degrees, the value 1 is used. The FFT confirms the oblique unit cell of the surface, which is highlighted with a yellow oblique shape. The two lengths of the oblique unit cell in real space are a* = 1.46 ± 0.05 nm and b* = 2 ± 0.1 nm, and the angle between these two vectors is β = 66.3 ± 0.5°. These dimensions and symmetry are close to the (1.48 nm, 2.3 nm, β = 70°) plane of the (130) model structure.

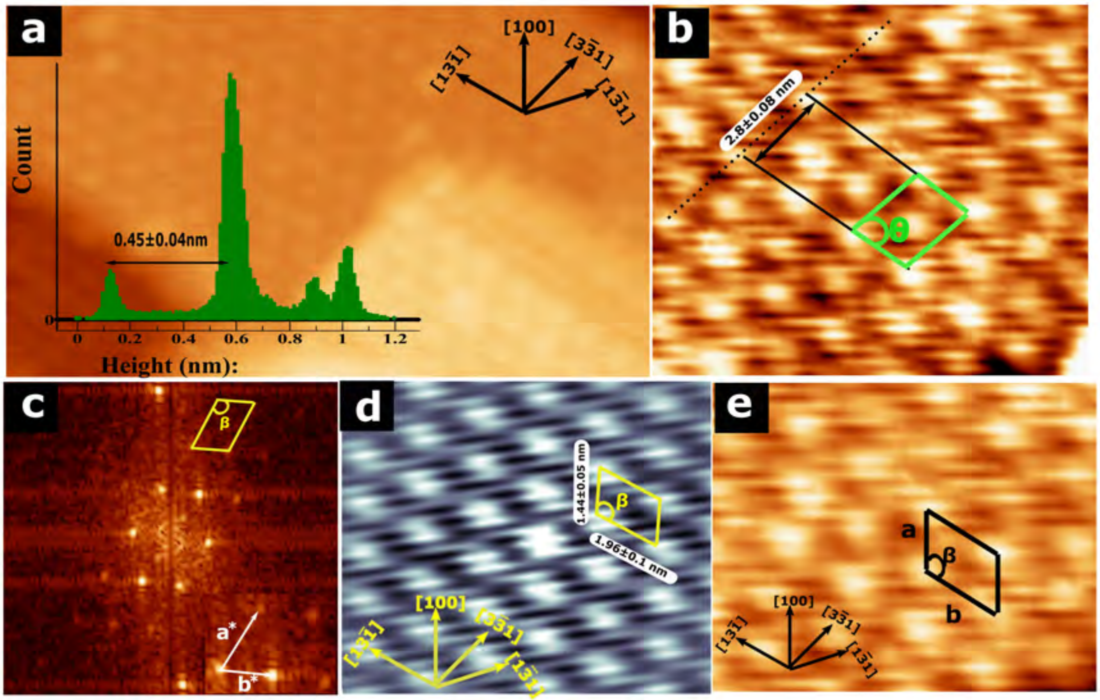

Figure 6.22: (a) 31 nm × 18 nm STM image at V_b = +1.5 V, the inset shows histogram of step height. The step height is labelled. (b) A zoomed in STM image of (a), showing close-packed features. (11 nm × 10 nm). (c) The FFT of (a) showing the oblique unit cell. (d) Autocorrelation function of the STM image in (b) (12 nm × 10 nm). (e) 10 nm × 8 nm STM image showing an enlarged view of the oblique feature in (b).

The autocorrelation function of Figure 6.22(b) is shown in Figure 6.22(d). It confirms the oblique unit cell of the surface, marked with a yellow oblique. The edge-lengths are: a = 1.44 ± 0.05 nm, b = 1.95 ± 0.11 nm along the [100] and [13$\bar{1}$] directions, respectively, and angle between these directions is 109.3 ± 0.5°.

Figure 6.22(e) is an enlargement of the oblique feature in Figure 6.22(b). Due to the size of protrusions ($\geq$ 1 nm) the structure of the surface can be resolved with clusters but not atomic resolution. The surface is characterised by a oblique unit cell arrangement of bright protrusions and is marked with a black oblique shape. The lattice of oblique protrusions on the surface has dimensions a_1 = 1.45 nm ± 0.08 nm and b = 2.01 ± 0.1 nm along the [100] and $[13\bar{1}]$ directions, respectively. These dimensions are consistent with a (1×1) structure, indicating that the surface is organized according to an oblique unit cell arrangement. The Au-Al-Gd's (130) surface has an oblique (1×1) unit cell with two lengths of 2.3 nm and 1.48 nm.

6.5.4 STM Image at Negative Bias

Figure 6.23(a) shows an enlarged view of the flat area in Figure 6.21(d). It shows that the atomic density of rows running along the $[13\bar{1}]$ direction is increasing at a negative bias. The STM image is merged with an inverse FFT, as shown in Figure 6.15(b), resulting in an image that shows large, bright protrusions aligned along the $[13\bar{1}]$ direction, which is marked with a black line. The distance between these protrusions is measured to be $a_1 = 2.01 \pm 0.09$ nm. Moreover, these rows are arranged along the $\left[1\bar{3}1\right]$ direction and are separated by a distance of 1.35 ± 0.1 nm, marked with a black arrow. Additionally, the distance between successive protrusions along the $\left[3\bar{3}1\right]$ direction is a_2 = 2.7 ± 0.09 nm. Both a_1 and a_2 are highlighted by a green-centred oblique.

The protrusions are arranged along the [100] and $[13\bar{1}]$ directions, with separations of a = 1.4 ± 0.08 nm, b = 2.04 ± 0.1 nm and $\beta = 109.6 \pm 0.4°$, respectively. These two lattice constants form the oblique cell. As a result, this oblique cell is regarded as the surface's unit cell. It is denoted by a black oblique cell in Figure 6.23(b). The two lattice constants match a (130) surface unit cell. At both voltages, the surface's two unit cells are the same.

The FFT of the STM is shown in Figure 6.23(c). It confirms that the unit cell is oblique. The two lattice constants of the centre oblique cell which are labelled with a_1^* and a_2^* were measured. It was found that the two lattice constants are $a_1 = 1.96 \pm 0.14$ nm, and $a_2 = 2.77 \pm 0.1$ nm, respectively. The angle formed by these two vectors is equal to $\beta = 68.7 \pm 0.4°$. The FFT pattern confirms the symmetry and dimension of the centre oblique that is marked with a green centre oblique in Figure 6.23(b).

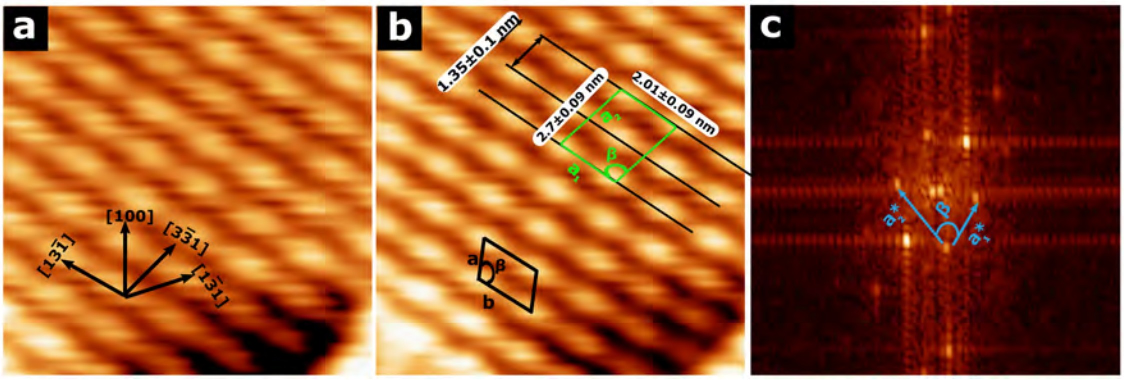

Figure 6.23: (a) An enlarged STM image of Figure 6.21 (d) (V_b = -1.5 V, 11 nm × 11 nm). (b) Same image as (a) emerged with Inverse FFT, showing the oblique cell, marked with a black oblique shape, (12 nm × 12 nm). (c) The FFT pattern of (a), where spots are highlighted by circles, shows the two-fold symmetry of the distribution of protrusions.

6.5.5 Discussion

We now suggest a potential explanation for the features that have been observed in STM images. This explanation involves comparing STM observations to model bulk. On Tsai-type quasicrystal and approximant surfaces, rare-earth atoms can be resolved at a positive bias, as has been shown in previous studies [28, 52, 53, 55]. As a result, Gd atoms can explain the STM data at positive bias. The atomic structure that is visible at positive bias in Figure 6.22(b) can be explained by the two layers located on top of the slab, which are highlighted with a green box in Figure 6.20(a). Figure 6.24(b) depicts a model (130) plane, which consists of two layers of Gd atoms and is marked with purple dots. The Gd atoms form a circular cluster, which is highlighted with a black circle. The Gd clusters are arranged along the [100] and [$13\bar{1}$] directions, with an angle of 107° between the two vectors, labelled β. The distance between the centres of cluster along the [001] and [$13\bar{1}$] directions is 1.48 nm and 2.3 nm, respectively. The unit cell is marked with a red oblique. The dimension and geometry of the unit cell match the STM observation in positive bias, as shown in Figure 6.24(a).

Figure 6.24(d) depicts the same plane with 4^{th} and 5^{th} shells Au/Al sites indicated by red and orange dots, respectively. One cluster of 4^{th} and 5^{th} shells Au/Al represents one bright protrusion in the STM image, which is marked with a black oval. The 4^{th} and 5^{th} shells Au/Al are high density along the [$13\bar{1}$] direction. The separation between the centres of motifs is 2.3 nm. The motifs direction and separation correspond to high density of atomic rows along the [$13\bar{1}$] direction in the STM image. The separation between the centre motifs is 3.1 nm along the

$\left[3\bar{3}1\right]$ direction, and the angle between the $\left[3\bar{3}1\right]$ and $[13\bar{1}]$ directions is 118°. The dimension and angle of the observed center oblique motif in STM image ($a_1 = 2.7 \pm 0.1$ nm, $a_2 = 2 \pm 0.1$ nm, $\beta = 109.6 \pm 0.4°$, as shown in Figure 6.24(c)) are closely related to the center cluster of Au/Al shell in model. It is evident that the vertices of the center oblique motif reside on the center cluster of Au/Al, which is marked with a green center oblique motif.

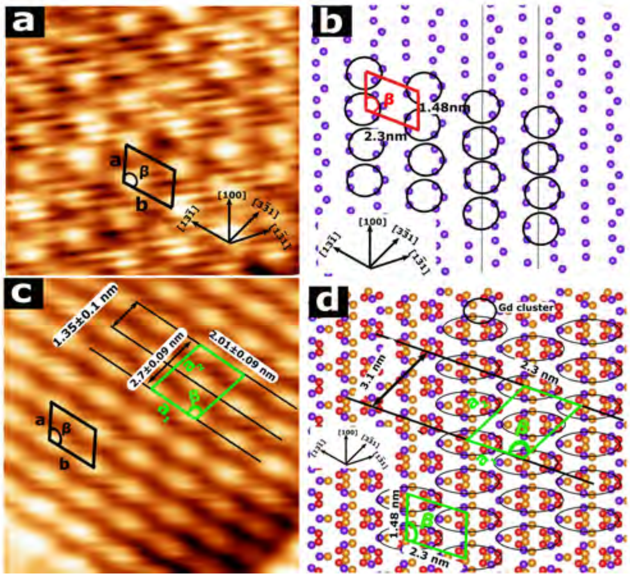

Figure 6.24: (a) The same STM image as in Figure 6.22(b), showing close-packed features. (11 nm × 10 nm). (b) A bulk model of the (130) plane, showing the structure of the two layers of Gd atoms, which is highlighted with a blue box in Figure 6.20(b). (c) 14.5 nm × 13.5 nm STM image showing the unit cell of surface at negative bias (-0.69V). (d) Model of the atomic structure of the (130) terminated plane, showing the 4^{th} shell Au/Al, 5^{th} shell Au/Al and 3^{rd} shell Gd marked with red, green, and purple dots. The rhombohedral unit cell is marked.

6.6 Detailed Structure of the (603) Surface

6.6.1 Step Morphology

Figures 6.25(a) and (b) show a step/terrace morphology at negative bias. Figure 6.25(c) shows the histogram of step heights observed in Figure 6.25(b), revealing a distribution with an average of 0.25 ± 0.04 nm. Figure 6.25(d) illustrates the (603) planes arranged perpendicularly in bulk structure; 3^{rd} shell Gd and 4^{th} shell Au/Al are marked with purple and red dots, respectively. This figure shows a flat and puckered layer similar to those observed in the (110) and (130) planes. Once again, the puckered layer is considered in explaining the STM observation, which is marked with a black line. Figure 6.25(e) depicts a sectional view of the bulk structure 3^{rd} shell Gd atoms along the [603] direction, providing a useful model for understanding the step heights observed in STM images in terms of bulk separated planes. The red lines indicate that the (603) planes cut each icosahedron shell, which is the same as the black lines indicating the puckered layer in Figure 6.25(d). The expected periodicity $\frac{a}{\sqrt{h^2+k^2+l^2}}$ along the [603] direction is $\frac{a_2}{\sqrt{45}}$, which corresponds to the distance between these planes. The step height in STM data is similar to expected periodicity $d_{(603)}$.

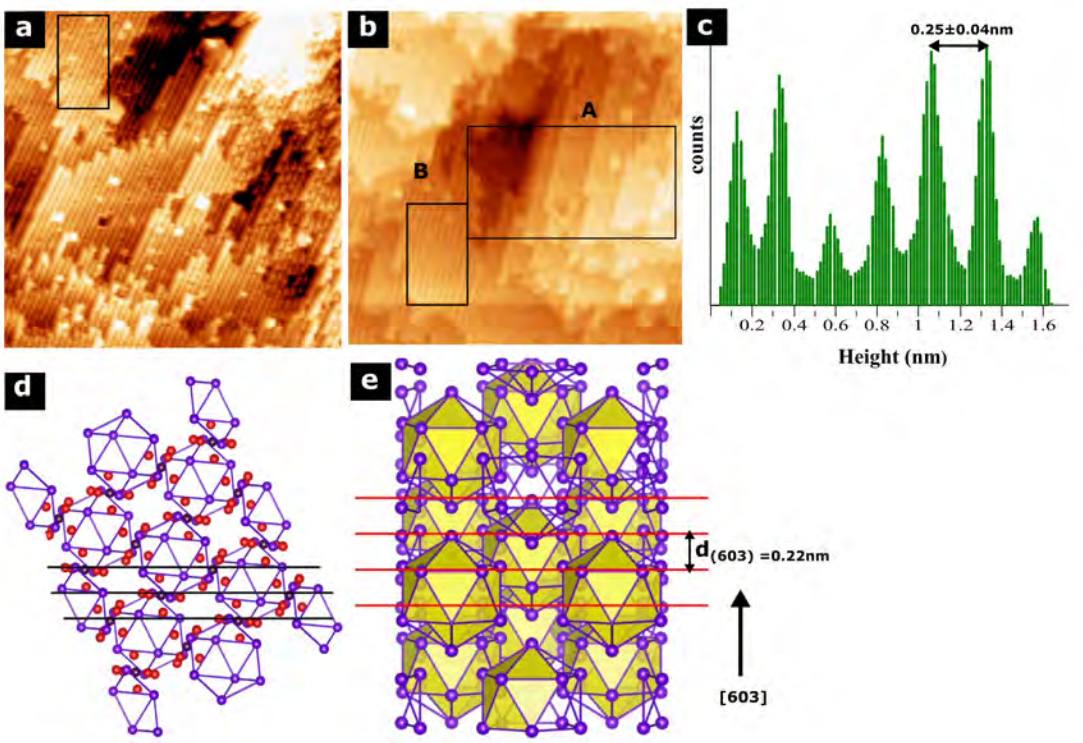

Figure 6.25: (a) 89 nm × 89 nm STM image of (603) surface (V_b = -1.1 V, I_t = 0.19 nA). (b) 80 nm × 80 nm STM image of (603) surface (V_b = -1.6 V, I_t = 0.198 nA), both STM images showing the morphology of terraces. (c) Histograms taken from (b), showing the step height distribution. (d) A Gd atom bulk model with the (603) planes arranged perpendicularly. (e) A bcc bulk unit cell of Au-Al-Gd 1/1 approximant projected normal to [603].

6.6.2 STM Image

Figures 6.26(a) and (b) show enlarged areas that are highlighted by a black rectangle in Figures 6.25(a) and (b). Because the protrusion is larger than 1 nm, it represents a cluster of atoms. These rows are aligned in the [100] direction. The rows are arranged along the [021] direction, with a separation of 1.6 ± 0.03 nm. The rows have two different types of atomic structure. One row consists of protrusions, and the second type of row has the high-density atoms, marked with black and dark blue rectangles in Figure 6.26(a). The unit cell parameters of the protrusion rows are $a_1 = 3.2 \pm$ nm, and $a_2 = 1.48 \pm 0.07$ nm, marked with a black rectangle. The rectangular unit cell is measured from the visible protrusions in straight rows.

Figure 6.26(c) shows more resolved protrusions in straight rows. The separation between the protrusions is $b_2 = 0.8 \pm 0.07$ nm along the [100] direction. Thus, the lattice constant a_2 reduced to a half, where there is no change, which is $b_1 = 3.4 \pm 0.08$ nm. In addition, this figure shows a high-resolution image, which reveals that the row structure of the high-density atoms is zigzag. It also reveals that the unit cell of the surface is rectangular. Although the zigzag rows do not resolve the atoms, the cluster observations confirm that the unit cell is rectangular, with two lattice constants, $a_1 = 3.16 \pm 0.07$ nm, $a_2 = 1.48 \pm 0.07$ nm, marked with a black rectangle. That confirms that both row structures have the same unit cell.

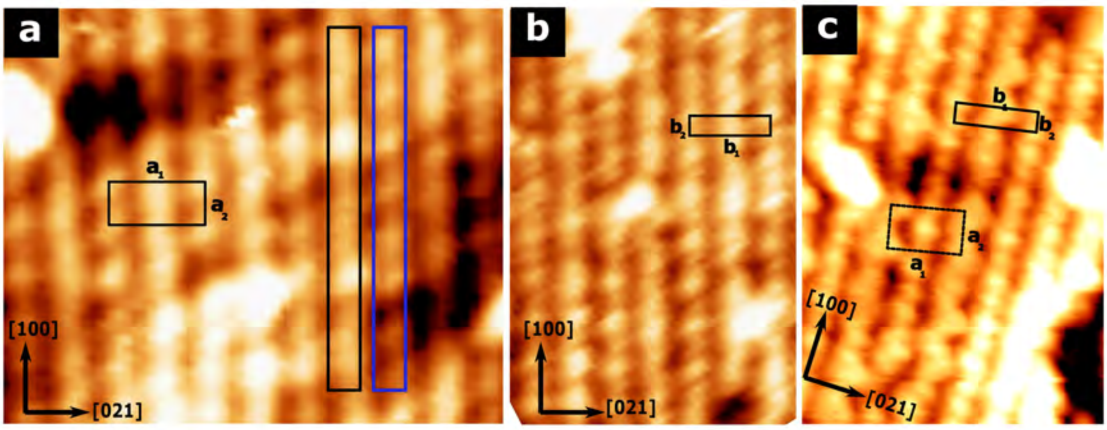

Figure 6.26: (a) 17 nm × 14 nm STM image the (603) facet of the Au-Al-Gd, it is taken from area that highlighted by a black rectangle in Figure 6.25(a). (b) 13 nm × 15 nm STM image showing taken from area highlighted by a black rectangle and labelled B in Figure 6.25 (b). (c) 13 nm × 18 nm STM image showing high resolution zigzag row structure.

The FFT of Figure 6.26(a) is shown in Figure 6.27 (a). It confirms the two-fold symmetry of the surface. The unit cell is rectangular, with the two lattice constants being $a_1 = 3.13 \pm 0.04$ nm and $a_2 = 1.52 \pm 0.04$ nm, marked with white circles. The FFT of Figure 6.26 (b) is shown in Figure 6.27(b). This FFT pattern reveals the impact of increasing atomic density of the row on the FFT pattern. It reveals the unit cell, which is highlighted with a green rectangular shape. The two lattice constants are $a_1 = 3.4 \pm 0.1$ nm and $a_2 = 1.68 \pm 0.06$ nm, and angle between them is $70 \pm 0.6°$, marked with β. These two lattice constants are close to those observed in the FFT shown in Figure 6.27(a), but with a different angle. The separation between the spots, which is highlighted by a green arrow, is 1.62 ±

0.09 nm. This is consistent with the separation between the rows along the [021] direction in the STM image. Figure 6.27(c) shows the FFT pattern taken from a location near the terrace in Figure 6.26(c). It shows the unit cell is a rectangular, with two lattice constants of $b_1 = 3.35 \pm 0.09$ nm, and $b_2 = 0.87 \pm 0.05$ nm. These lattice values are similar to b_1 and b_2 in the STM image in Figure 6.26(c). The FFT demonstrates the effect of an increasing density of protrusions on the unit cell, particularly if they are resolved from two layers.

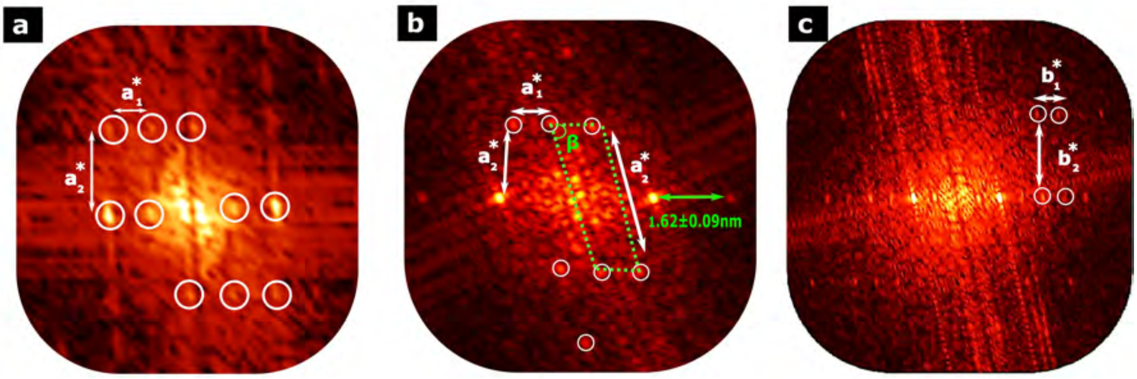

Figure 6.27: (a) The FFT of the STM image taken from Figure 6.26(a), showing two-fold symmetry. The unit cell of surface is outlined. (b) The FFT of the STM image of Figure 6.26(b), showing the effect resolved more protrusion on the surface unit cell. (c) The FFT of the STM image taken from surface near to area shown in Figure 6.26(c). It shows that the surface unit has the same lattice constants in (b).

6.6.3 Discussion

Figure 6.28 shows the structure of the (603) plane extracted from two layers in the bulk model. The STM images detect the presence of Au/Al atoms at negative bias [8]. The 4^{th} and the 5^{th} shells Au/Al are highlighted with red and green dots, respectively. The analysis of the STM data reveals that the observations can be explained by two types of motifs formed from the 4^{th} shell of Au/Al in the (603) plane model.

The first motif, the square of four 4^{th} shells Au/Al sites, is marked with a small blue square. The square motifs possess two opposite orientations due to the fact that the schematic plane extracted from it consists of two converging planes. Both square motifs are aligned along the [100] direction, with a separation of 0.72 nm. The second motif, consisting of the 4^{th} shell arranged in a zigzag line, is marked with a blue zigzag line. The separation between the centers of the two vertical row types, namely square and zigzag, is 1.6 nm along the [021] direction. These two vertical rows are marked with black and dark blue rectangles. The structure of both vertical row types, as well as the separation between them, is consistent with STM observations.

The unit cell of the row consisting of the first motif is marked with a dark blue rectangle and labelled 1 at the bottom of Figure 6.28. It is located on a square of four Au/Al atoms of the 4^{th} shell with the same orientation. The distance between the square motifs that have the same orientation is 1.48 nm and 3.2 nm along the [100] and [021] directions, respectively. Similarly, the 4^{th} shell constitutes a triangle motifs in the zigzag row, marked with a dashed black triangle. The separation between their centre is 1.48 nm and 3.2 nm along the [001] and [021] directions, is marked with a black rectangular unit cell. The structure of the zigzag rows is represented by the triangle motifs that are observed in Figure 6.26(c). Both the structure of the vertical rows and their unit cells correspond to the unit cell observed in the STM data in Figures 6.26(a) and (c).

The distance between the 4^{th} shell that has a different orientation along [100] is 0.72 nm, marked with a small dashed rectangle. The separation between the 4^{th} shell is 3.2 along the [021]. These two lattices are slightly smaller than the distance between protrusions in the first type of vertical row, which are: b_2= 3.4 ± 0.08 nm, b_2 = 0.8 ± 0.07 nm in Figure 6.26(b) and (c). We found that the unit cell identified in Figure 6.27(b) by FFT was close to a parallelepiped, which was marked and labelled with a blue motif, and 3. The STM observations confirm the two layers are resolved and that can explain the complicated unit cell in STM images. The additional 4^{th} shell is surrounded by the 5^{th} shell, which may explain why the other 4^{th} shell has not been resolved.

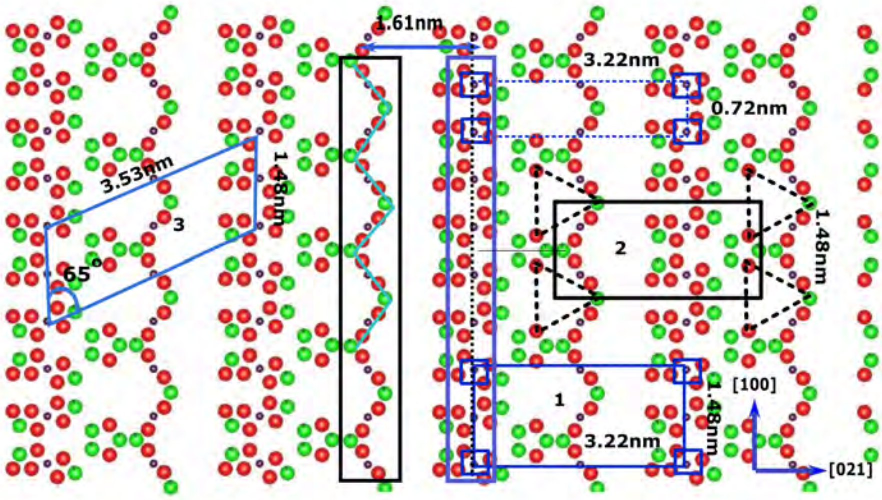

Figure 6.28: Atomic structure of the (603) plane is cut close to the centre of the RTH clusters. The Au/Al atoms marked by a square belong to the 4^{th} shell of the RTH cluster. The red and green dots are represented the 4^{th} and 5^{th} shell.

6.7 Detailed Structure of the (402) Surface

6.7.1 Step Morphology

Figure 6.29(a) depicts an STM image of the step/terrace structure of a different sort of facet. The step height is shown in Figure 6.29(c), as measured by the histogram presented in Figure 6.29(b). The measured step height of 0.32 ± 0.08 nm is consistent with the predicted value for the (402) facet, which is $d_{(402)} = 0.33$ nm, with a periodicity of $\frac{a_2}{\sqrt{20}}$. In the bulk, adjacent lattice planes are separated by:

$$d_{(402)} = \frac{a}{\sqrt{h^2 + k^2 + l^2}} = 0.33\, nm \tag{6.5}$$

However, the terraces consists of small step height 0.48 ± 0.05 nm, marked with a black arrow. These terraces are small and flat; as a result, we did not consider them.

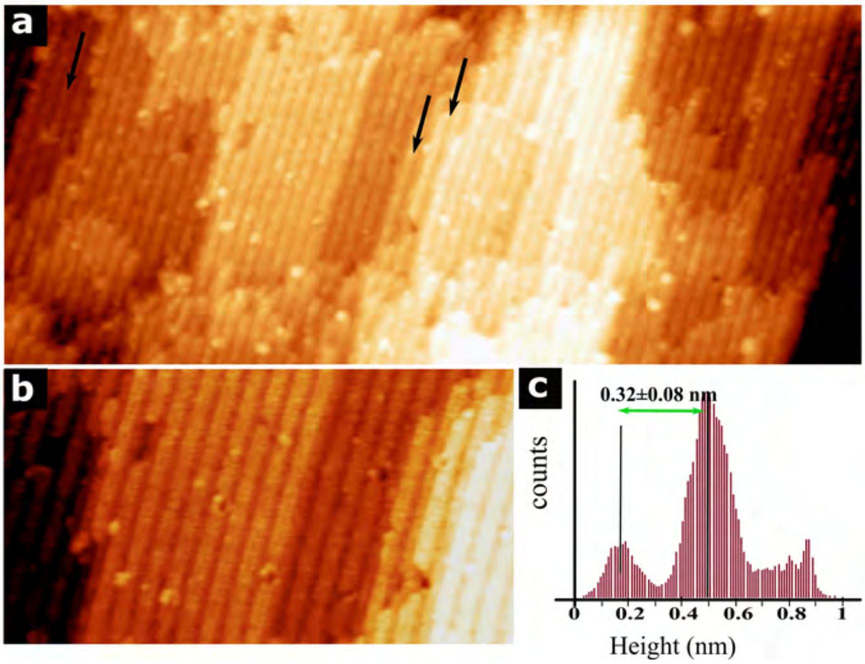

Figure 6.29: (a) 171 nm × 72 nm STM image ($V_b = +1$ V, $I_t = 0.21$ nA). (b) 63 nm × 34 nm STM image taken at ($V_b = +0.8$ V, $I_t = 0.19$ nA) displaying the magnified step height terraces depicted in (a). (c) A histogram taken from (b), showing the step height distribution. The average step height is labelled.

A zoomed-in view area of Figure 6.29(b) is shown in Figures 6.30(a), (d), and (f). The STM images are obtained at both bias voltages. A rows are running along the [100] direction, as shown in Figure 6.30(a). The separation between the adjacent rows is 2.8 ± 0.08 nm along the [021] direction. The row atomic structure has a more visible positive bias than a negative. The width of the row is 1.46 ± 0.06 nm.

A FFT of the STM image shown in Figure 6.30(a) is shown in Figure 6.30(b). The lattice constants in real space are $a_1 = 0.83 \pm 0.12$ nm, and $a_2 = 2.84 \pm 0.2$ nm, with an angle of 100° between the two vectors.

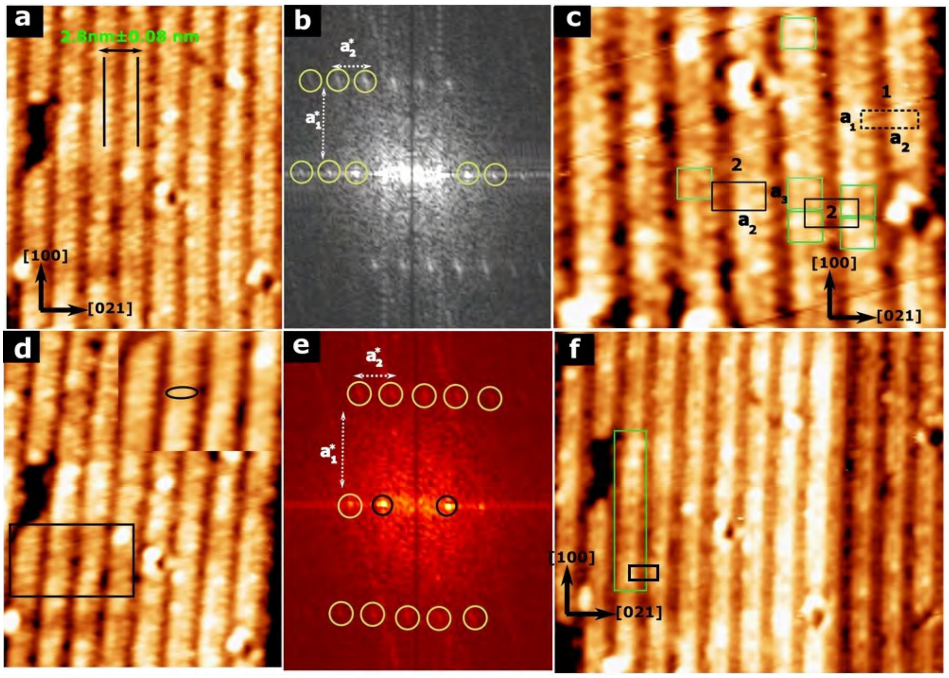

Figure 6.30: (a) 23 nm × 27 nm STM image ($V_b = +0.8$ V, $I_t = 0.154$ nA), showing the rows arranged along the [100] direction. (b) FFT of (a), showing the rectangle pattern, with two lattices are labelled. (c) 19 nm × 18 nm STM image showing the magnified vertical rows taken from (a). The surface unit cell is marked by a black rectangle. (d) 24 nm × 29 nm STM image ($V_b = +0.8$ V, $I_t = 0.19$ nA) showing the same area in (a). The protrusion is large and and become elliptical. (e) FFT of (d) showing the rectangle unit cell and the angle between two lattices is 90°. (f) 35 nm × 31 nm STM image ($V_b =$ -0.6 V, $I_t = 0.198$ nA). It shows the vertical rows without resolution in cluster centre.

The structure of rows is resolved in a positive bias, as shown in Figure 6.30(c). The vertical row consists of bright protrusions with a separation of a_1 0.79 ± 0.05 nm and $a_2 = 2.81 \pm 0.08$ nm along the [100] and [021] directions, respectively. As a result, the unit cell is a rectangle, as indicated by a black rectangle and number 1. The orientation of protrusions is initially unclear in STM images, but further analysis revealed the presence of individual protrusions with opposite orientations, as highlighted by a green rectangle. These two protrusions represented one motif. It was found that the distance between the centres of these motifs is $a_1 = 1.57 \pm 0.053$ nm, and $a_2 = 2.81 \pm 0.08$ nm along the [100] and [021], respectively. This is marked with a black rectangle and the number 2, and may represent the surface unit. Additionally, the middle of a few protrusions is dim.

Figure 6.30(d) exhibits the same STM image as 6.30(a) at the same voltage. Notably, the protrusion in Figure 6.30(d) has assumed an oval shape, which is discernible. Moreover, the shape of the protrusion can be clearly observed as oval in Figure 6.30(d). The FFT pattern of Figure 6.30(d) is shown in Figure 6.30(e), demonstrating that the angle between the two lattices measures 90°, and the surface unit cell is a rectangle. The distance between two spots, which is marked with a black circle, is 2.8 ± 0.16 nm. This corresponds to the separation between the centre of vertical rows along the [021] direction in STM image.

Figure 6.30(f) illustrates the STM image at a negative bias, revealing the same bright rows as observed in the positive bias case. However, the width of the dim rows is found to be greater than that observed in the positive bias. Notably, the distance between the protrusions along the [100] direction has increased and is marked with a green rectangle, measuring 1.64 ± 0.6 nm. As a result, the unit cell of the surface can be deduced to be rectangular with lattice constants of 1.64 ± 0.6 nm and 2.84 ± 0.2 nm, marked with a black rectangle.

6.7.2 Discussion

To understand the step height of terraces (402), the model of the side view of the Gd planes in the bulk, arranged perpendicular to the [402] direction, is presented in Figure 6.31(a). we can consider as a slab, and each slab consists of five layers of Gd atoms, which are highlighted by a blue rectangle in the bottom of the figure. These slabs are symmetrical on the horizontal axis because each plane appears to be a mirror image of the other. The distance between the centres of the mirror slab is 0.33 nm, which is close to the step heights observed in STM. The surface structure could be the first two layers of slab, which are highlighted by a red box.

Figure 6.31(b) shows the side view of the Gd planes. Again, the two layers of Gd are at the bottom point of the up pentagon's diameter, which is marked with a red rectangle. The distance between the first and second layers is less than 0.05 nm.

Figure 6.31(c) shows the same Figure 6.31 (a) with the icosahedral shells used to describe the model. The top of the icosahedron and truncations are marked with a red circle and line. Prospective terminated planes are truncated at the icosahedron's top.

Now we compare the surface structure of Au-Al-Gd with the same surface of the Au-Al-Tb 1/1 approximants [11]. Figure 6.32(a) shows the atomic structure of the (402) plane, which is taken from two layers, which are highlighted with a red box in Figure 6.31(b). Different colours correspond to atoms belonging to different shells of the Tsai-type cluster; the red: 4^{th} shell Au/Al, and the purple: 3^{rd} shell Gd. The 1^{st} shell Au/Al atomic positions have been omitted.

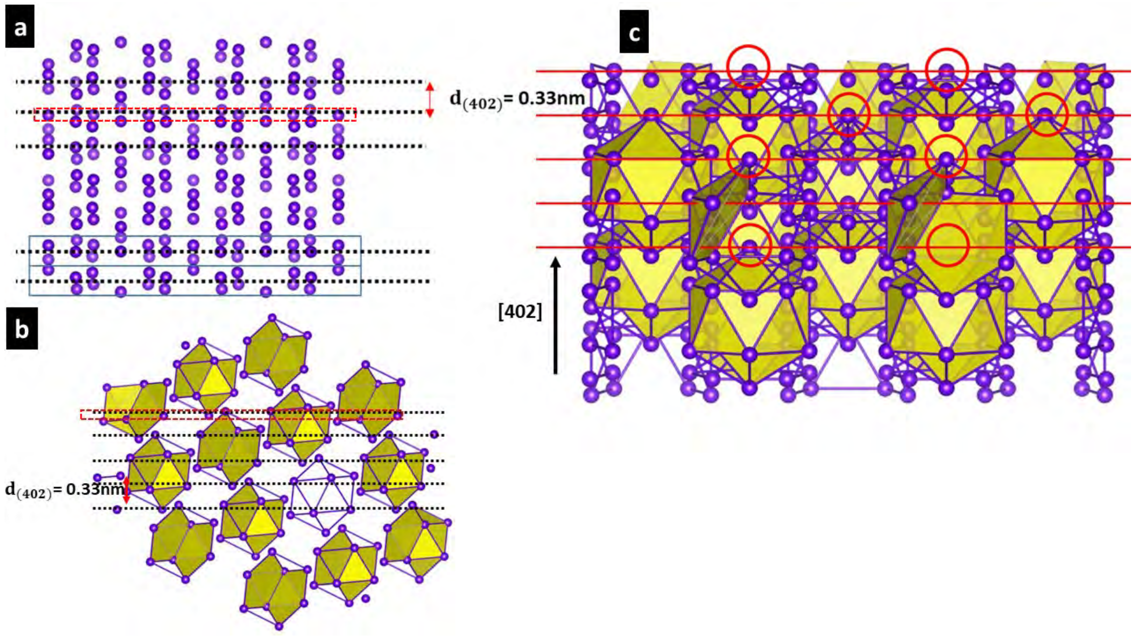

Figure 6.31: (a) Gd planes in bulk, aligned in the [402] direction. A group of five planes is indicated by a slab and marked with a blue box. The distance between the slab's centres is 0.33 nm. (b) The (402) surface-terminated plane is located at the bottom of the up-pentagon's diameter, as indicated by a black dashed line in the side view of the icosahedron shell. (c) same (a) with the icosahedron shell. Surface terminations showing truncate at the top of each Gd icosahedron. The red circle and lines represent the icosahedron's top and the planes that cut it.

The four Gd atoms surrounding the square of the 4^{th} shell Au/Al and the two atoms of the 2^{nd} shell Au/Al atoms, marked with a black dashed oval. This motif represented one protrusion in the STM image. The oval motif is aligned along the [100] direction with a separation of 0.74 nm along [100] direction. These motifs form the vertical rows with a separation of 3.2 nm between the centres along the [021] direction. The oval motif and the distance between the centres of the vertical rows corresponded to the STM observations shown in Figures 6.30(a) and (c).

The unit cell of one layer of the (402) plane is located on the four oval motifs with the same orientation, forming a rectangular cell. A black rectangle highlights the two lattice constants of this rectangle, with $a_1 = 3.2$ nm, $a_2 = 1.44$ nm. whereas the presented model consists of two layers separated by 0.05 nm. When the scan resolves two layers, the number of oval motifs doubles, and the value of the lattice constant a_2 reduced by half. The distance between the centres of the oval motif

(Gd clusters) is 0.74 nm and a_1 remains constant at 3.2 nm. The unit cell is highlighted with a blue rectangle and number 1. This unit cell corresponds to the small rectangle, with two lattice constants, $a_1 = 0.79 \pm 0.05$ nm and $a_2 = 2.81 \pm 0.08$ nm in STM image shown in Figure 6.30(c).

We will investigate the assumption that each pair of oval protrusions represents a motif. A pair of oval shapes is marked with a small black square; the separation between the centres of these motifs along the [100] and [021] is 1.48 nm and 3.2 nm, respectively. This represents the surface unit cell, which is marked with a black rectangle and number 2 in Figure 6.32(a). The rectangular unit corresponds to the surface unit cell in the STM image, and it is highlighted with a black rectangle and 2 in Figure 6.32(b).

At a negative bias, Au/Al atoms may be resolved [8]. The square of 4^{th} shells positioned in the middle of the oval motif, which could explain the continued observation of the row in the STM image at negative bias, and the width of the rows slightly decreases compared to positive bias. Furthermore, the separation between the oval motifs along [100] direction is increasing to 1.66 nm, as shown in the STM image in Figure 6.30(f). This could support the unit cell of (402) (3.2 nm × 1.48 nm).

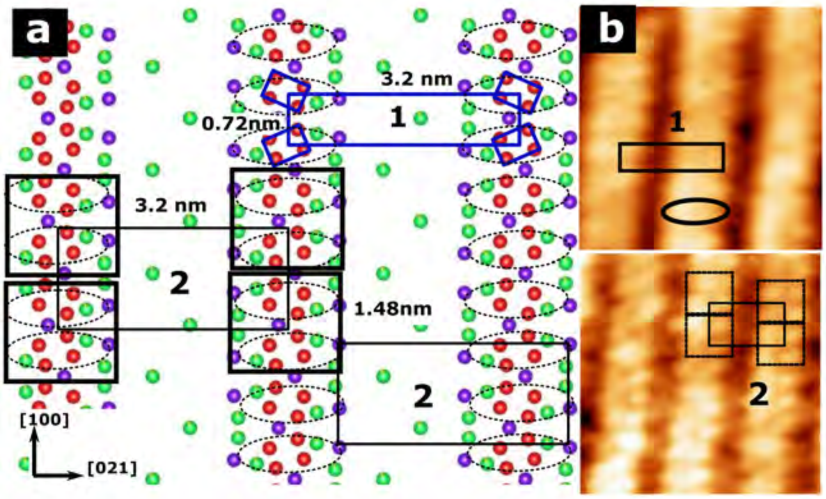

Figure 6.32: A model atomic (402) plane, red: 1^{st} shell Au/Al, light green: 2^{nd} shell Au/Al, purple: 3^{rd} shell Gd. (b) The STM image as in Figure 6.30(d).

6.8 Detailed Structure of the (701) Surface

100 nm × 100 nm STM image shown in Figure 6.33(a) reveals a step-terrace structure. The terraces were found to be separated by 0.24 ± 0.05 nm steps. The measured step heights correspond to the expected $d_{(701)}$ periodicity along [701] which is $\frac{a}{\sqrt{50}} = 0.21$ nm. Figure 6.33(b) shows the STM image that emerged with

FFT inverts. It shows the parallel rows, and the structure of the row is nearly square. The spacing between the centres of the rows is 4.5 ± 0.1 nm, as indicated by a green arrow. The unit cell is a centred rectangle with dimensions of a and a × $\sqrt{50}$, which is close to the unit cell observed in STM (1.6 ± 0.07 nm and 4.5 ± 0.1 nm) which is marked with a large black rectangle. This structure is similar to that observed in [113].

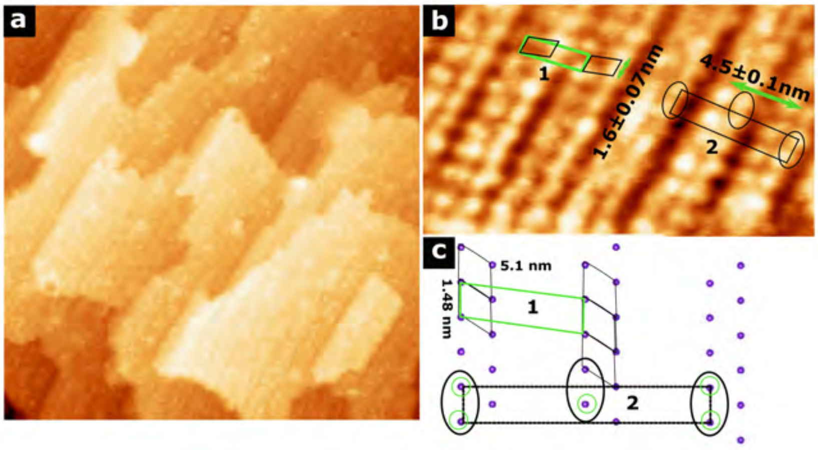

Figure 6.33: (a) 100 nm × 100 nm STM image at $V_b = +1.4$ V, displaying the step/terrace structure of the surface of (701) Au-Al-Gd. (b) a 27 nm × 16 nm STM image shows an enlarged area of (a) showing the unit cell of (701). (c) schematic model showing the space lattice of the (701) plane.

6.9 LEED Pattern

Figure 6.34 shows the LEED pattern of the (110) surface of the Au-Al-Gd 1/1 approximant which was recorded at 20 eV and 25.3 eV. The LEED pattern exhibits a few spots arranged in a centered rectangle unit cell. It was found that two lattice constants in real space are: $|a_1| = 2.16 \pm 0.08$ nm and $|a_2| = 1.55 \pm 0.06$ nm. This value is consistent with the lattice constant derived from the (110) bulk.

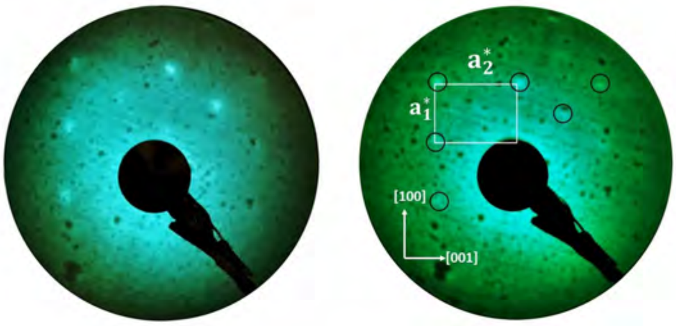

Figure 6.34: LEED patterns obtained from the Au-Al-Gd (110) surface at 20 eV and 25.3 eV.

The surface of the Au-Al-Gd sample after sputtering and annealing produces different structures in different areas distributed on sample surface. STM images obtained from various areas are shown in Figure 6.35(a)-(c). The largest area obtained is 100 × 110 nm; it shows the morphology of terraces. However, the size of the flat terraces is too small to obtain the LEED pattern for these facets. No co-existing facets along different crystallographic directions were observed located the same area. So, it is difficult to identify the Miller indices (hkl) of the facet planes using the angle between two facets in STM images. The Miller indices of the planes in the STM images are identified by determining the step height and comparing the STM images with the bulk structure.

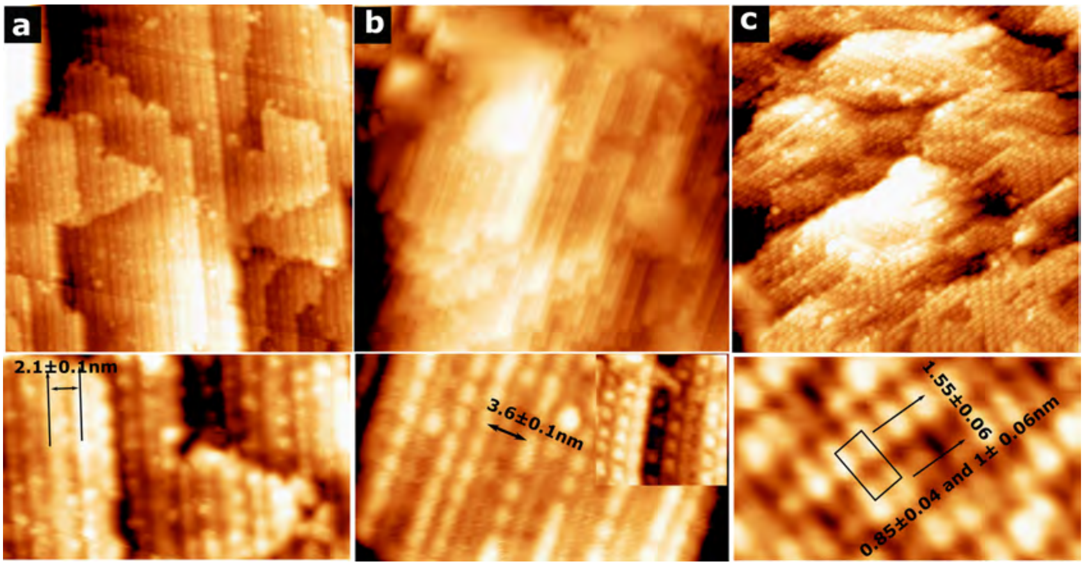

Figure 6.35: STM images taken from different terraces showing different structure and small flat terraces (a) 80 nm × 80 nm STM image at $V_b = +1.2$ V. An inset of bottom (a), 32 nm × 19 nm STM image is shown in a magnified area of (a). (b) 80 nm × 74 nm STM image at $V_b = +1$ V. An inset of the bottom (b) shows an enlarged area of (b), displaying a 27 nm × 15 nm STM image. (c) 100 nm × 100 nm STM image at $V_b = +1$ V. An inset of the bottom (c) shows an enlarged area of (c), displaying a 10 nm × 6 nm STM image.

6.10 Conclusions

STM results from the Au-Al-Gd 1/1 approximate surface are presented and show a predominant orientation of (110). However, additional structures are also identified.

The (110) facet has been investigated, finding the step height and unit cell of the surface. Terraces are formed at the puckered layers that break each icosahedron in the bulk. The surface structure is bias-dependent. At positive bias, Gd atoms are resolved and arranged in rhombohedral patterns. At negative bias, the 4^{th}

shell of Au/Al atom is resolved as rows.

The facets (111), (130), (603), (701), and (402) were characterised. The observed step heights in different structures were consistent with the expected periodicity of the facets; for example, the observed step (0.25 ± 0.04) nm for the (603) facet is consistent with $\frac{a}{\sqrt{45}}$ which is the expected periodicity along [603]. Furthermore, terraces are formed at Gd-containing planes, which break each icosahedron in bulk. This conclusion was reached by comparing the step height and terrace structure with the model structure.

The Gd cluster were resolved at positive biases. In addition, the Gd atom clearly defines the surface unit. The STM images confirm the resolving of multiple Gd layers because the two layers are close to each other and separated by less than 0.1 nm. The 4^{th} Au/Al shell, on the other hand, was found to be resolved at negative biases. This is consistent with the calculated results for the electronic structure and surface stability of the intermetallic Ag-In-Ca [115].

Chapter 7

Characterisation of the Surface Structure of an Intermetallic Compound Catalyst-Ga_3Ni_2

7.1 Introduction

This chapter describes the characterisation of the surface atomic structure of Ga_3Ni_2 (010) using STM and LEED. This is the first study of this surface using ultra-high vacuum techniques. To provide a greater understanding of the role of the crystal surface in catalytic reactions, it attempts to characterise the structure of the clean surface. To perform these experiments, obtaining a chemically clean and atomically ordered Ga_3Ni_2 surface requires the employment of cycles of sputtering and annealing.

Because of their higher selectivity for specific reactions and greater long-term stability, intermetallic compounds have proven to be attractive alternatives to pure and alloy metal catalysts in heterogeneous catalytic reactions [13]. Intermetallic compounds can be created in a regulated and repeatable way, and their ordered crystal structures indicate that the number of catalytically active sites and the spacing between them are well-defined and repeated evenly throughout the crystal. The active sites can be adjusted to the needs of a specific chemical reaction by selecting intermetallic compounds with acceptable crystal structures and chemical components [116]. Fixed crystal structures prevent the clustering of catalytically active atoms during catalyst activity, which is a significant distinction from alloys.

Large facilities use a $Cu/ZnO/Al_2O_3$ catalyst to generate methanol under high pressure (50–100 bar) from CO, CO_2 and H_2 (supplied from fossil fuels) [117]. Recently, an Ni-Ga catalyst was discovered by Studt *et al.* [118] to convert CO_2 to methanol at room temperature. This catalyst generates methanol and water, which is an excellent fuel for a fuel cell and would be useful in connection with the decentralised usage of hydrogen produced by solar or wind power[119]. They discovered that Ni_5Ga_3 is a particularly active and selective catalyst. The same or greater methanol synthesis activity was found when it was compared to that of conventional Cu/ZnO/Al_2O_3 catalysts, with significantly less CO production.

Using less expensive alternatives to precious metals in industrial heterogeneous catalysis processes is desirable. In the Ga–Ni system (GaNi, $GaNi_3$, Ga_3Ni_5), several intermetallic catalysts free of precious metals (including noble metals) have been identified that reduce CO_2 to methanol at ambient pressure [118, 120].

This project describes an investigation of the surface structure of the crystal using (STM) and (LEED). Comparing the structure of the surface that is obtained at different temperatures to the atomic structure of the bulk phase of the Ga_3Ni_2(010) single crystal, four types of surface reconstruction are observed at a low annealing temperature of 366–420°C. The formation of an atomic structure Ga_3Ni_2(010)-(1×1) layer termination is observed at annealing temperatures greater than 430°C.

7.1.1 Phase Diagram of Ga-Ni Crystal

As shown in Figure 7.1, Ga_3Ni_2 is a stoichiometric compound that disintegrates peritectically at 950 °C and can be primarily crystallised from a Ga-rich solution in the temperature range between 369 °C and 950 °C, according to the binary Ga–Ni phase diagram published by Okamoto [121] based on a thorough study by Schmetterer *et al.* [122]. The most significant challenge during crystal formation from a high-temperature solution is the material transfer of the excess component (Ga). The crystal formation of Ga_3Ni_2 should begin at the greatest temperature possible, because the liquidus temperature will steadily decline throughout the experiment as Ga accumulates in the liquid phase. The results recommend Ga_3Ni_5 as a particularly active and selective catalyst among the binary phases in the Ni–Ga system. Ga_3Ni_5 cannot be generated from a binary liquid phase, according to the Ga–Ni phase diagram [121]. Only one compound with a constant stoichiometry that is in equilibrium with a binary Ga–Ni melt, namely Ga_3Ni_2 [118].

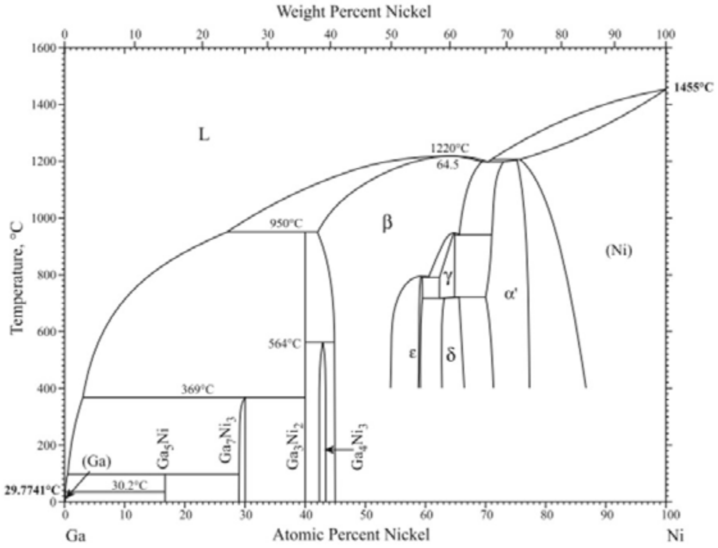

Figure 7.1: Ga-Ni phase diagram [121].

7.1.2 Bulk Structure

Ga_3Ni_2 crystallises in the Al_3Ni_2-type structure [123], which has a tetragonal arrangement, with space group $P\bar{3}m1$ and a unit cell dimension of $|a| = 0.41$ nm and $|c| = 0.49$ nm [124, 123]. The trigonal unit cell is depicted in Figure 7.2(a). The lattice parameters were determined by X-ray diffraction (XRD). The unit cell is formed by two Ni atoms and three Ga atoms. As shown in Figure 7.2(a), site isolation is obvious since all Ni atoms have only Ga near-neighbour environments. The (010) plane, which was studied in this thesis, is highlighted with a green rectangle. The atomic structure of the (010) plane for four layers is depicted in Figure 7.2(b). The top layer showing the surface unit is a rectangular cell with side lengths of $|a_1| = 0.41$ nm and $|a_2| = 0.48$ nm, and the angle between two vectors is 90°, as shown in the inset of Figure 7.2(b) [124]. Figure 7.2(c) is the side view of the (010), showing the order of the (010) along the [120] direction. The inter-layer spacing ($d_{(hkl)}$) for the hexagonal unit cell can be calculated using the equation:

$$\frac{1}{d^2_{(hkl)}} = \frac{4(h^2+hk+k^2)}{3a^2} + \frac{l}{c}^2 \tag{7.1}$$

For plan (010)

$$d_{(010)} = (\frac{\sqrt{3}}{2})a = 0.35\ nm \tag{7.2}$$

Figure 7.2(d) shows the first and last planes in the unit cell, with inter-layer spacing $d_{(hkl)} = 0.35$ nm. The rows of atoms aligned along the [001] axis in the first plane shift by a half lattice constant ($|a_1|$) with respect to the second plane along the [100] axis.

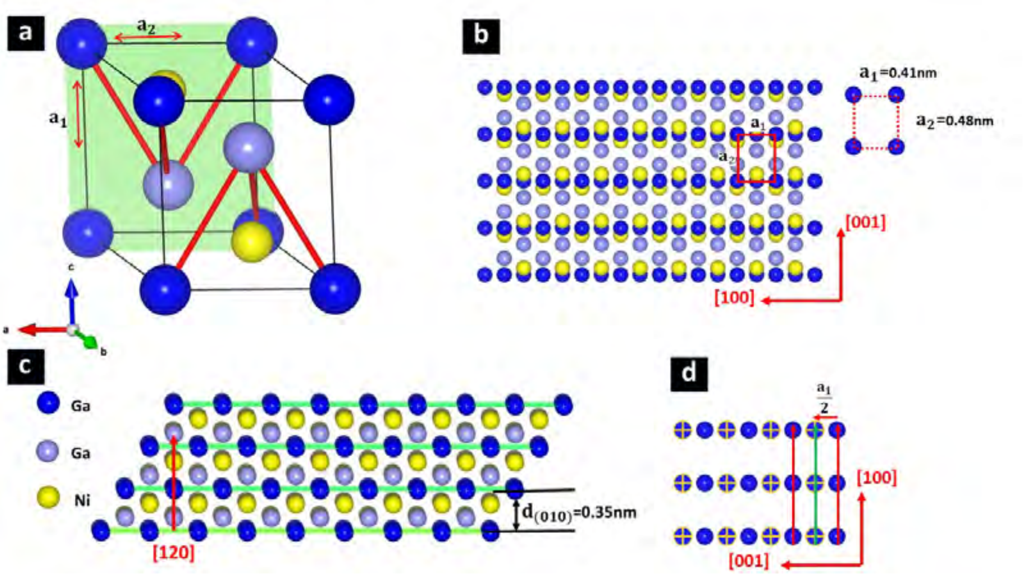

Figure 7.2: (a) Diagram showing the structural model of the unit cell of Ga_3Ni_2 [124, 123]. The dark and light blue dots represent Ga atoms at the top and middle of the unit cell, and the yellow dots represent Ni atoms. (b) Ball model of the Ga_3Ni_2 (010) surface. The unit cell is highlighted with a red rectangle. (c) A side view of planes arranged along the [120] direction. The separation between successive (010) planes $d_{(010)}$ is labelled. (d) Diagram of the (010) top and bottom Ga rich-planes with $d_{(hkl)} = 0.35$ nm. The two planes are marked with yellow and blue circles. It demonstrates that the position of the Ga atom in the bottom plane is shifted by a half lattice $|a_1|$ from the top plane.

7.1.3 Oxidation Properties

Wencka *et al.* investigated the catalyst characterisation and effect of surface oxidation on the catalytic properties of a Ga_3Ni_2 intermetallic compound for carbon dioxide reduction. The analysis was conducted using temperature-programmed desorption (TPD) and X-ray photoelectron spectroscopy (XPS) [125].

At temperatures of 300 °C and 600 °C, TPD was used to examine the dispersion of active sites available for the chemisorption of H_2 and CO on the Ga_3Ni_2 catalyst surface. In the TPD experiment, the sample was exposed to a catalyst composed of a mixture of H_2 and CO_2 gases (4.9 mol% H_2 in Ar for H_2–TPD and 10 mol%CO in He for CO–TPD) at a flow rate of 30 mL min^{-1}. The temperature was gradually increased from 80 °C to 650 °C using a ramp rate of 10 K min^{-1} while helium was flowing, and the adsorption data of H_2 and CO were recorded.

Compared to the catalyst reduced at a lower temperature of 300 °C, the surface coverage of hydrogen on the catalyst reduced at a higher temperature of 600 °C was higher by a factor of 1.8. Higher reduction temperatures increase CO adsorption by roughly the same factor (1.7).

Before the activity tests, the catalyst was reduced for two hours at 300 °C or 600 °C, respectively, in the presence of hydrogen. The CO_2 conversion procedure was performed between room temperature and 500 °C. Figure 7.3(a) depicts the CO_2 conversion data over the Ga_3Ni_2 catalyst reduced at 300 or 600 °C, respectively. The conversion over the catalyst reduced at 600 °C was significantly higher than the conversion over the catalyst reduced at 300 °C, which corresponds to the larger metal dispersion of the former catalyst, which chemisorbs more CO_2 at the surface. After the reaction, the nickel oxide, NiO was evaluated. The result did not indicate any activity within the tested temperature range.

Figure 7.3(b) depicts the increase in CO selectivity with increasing annealing temperature. It reveals that 100% CO selectivity was obtained at temperatures below 200 °C, where CO_2 conversion is low, reaching a maximum of 5%. whereas at annealing temperatures higher than 300 °C the selectivity towards CO decreases until reaching 50% at the highest temperature of 500 °C. This indicates that Co and CH_4 were produced at low temperatures.

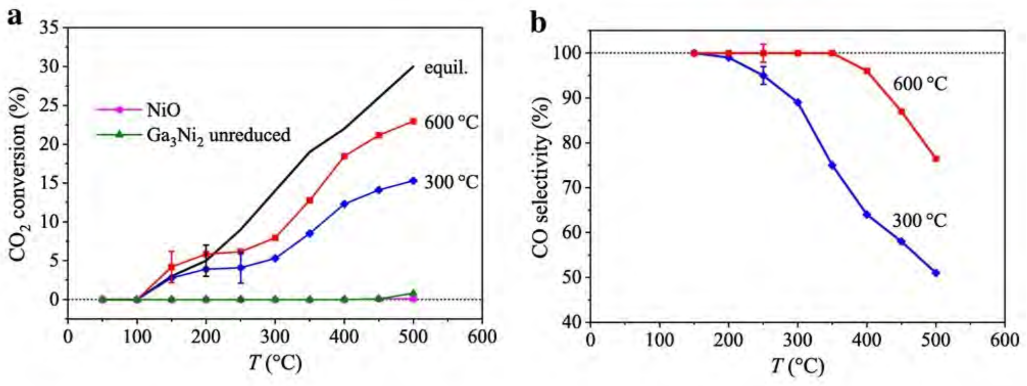

Figure 7.3: (a) CO_2 converter data over the Ga_3Ni_2 catalyst lowered at 300 °C or 600 °C (CO_2:H_2 ratio of 1:1, GHSV = 60,000 h1). The equilibrium conversion of the RWGS reaction is demonstrated by the solid black curve [126, 127]. In the investigated temperature range, converting over nickel oxide (NiO) and unreduced Ga_3Ni_2 exhibited no activity. (b) curve shows the CO selectivity data over the Ga_3Ni_2 catalyst has decreased at 300 °C or 600 °C, respectively.

XPS was used to study the elemental composition and chemical bonding of the elements (oxide, metal) within a thin surface layer of the material (3–5 nm in our case). The XPS analysis of an initial sample at 25 °C reveals that the concentrations of Ga and Ni increased with increasing depth until 10 nm, then did not change significantly at depths greater than 10 nm, as depicted in Figure

7.4(a). Conversely, the concentrations of oxygen decreased with increasing depth.

The concentrations of O, Ga, and Ni were measured in the uppermost surface layer (3–5 nm depth) at the annealing temperature of 300 °C for four hours. The surface Ni/Ga concentration ratio remained constant at $R_{Ni}^{surfc} = 0.12 \pm 0.02$ and the oxygen concentration remained constant, as shown in Figure 7.4(b)

The concentrations of O, Ga, and Ni in the surface layer were then measured as a function of time for 2.5 hours after the 600 °C treatment, as shown in Figure 7.4(c). Ga and Ni concentrations increased after 12 minutes of annealing, then remained constant, whereas the oxygen concentration dropped by a factor of 10 during the next 12 minutes. This indicates that the oxides were removed from the surface in UHV in about 12 minutes at 600 °C.

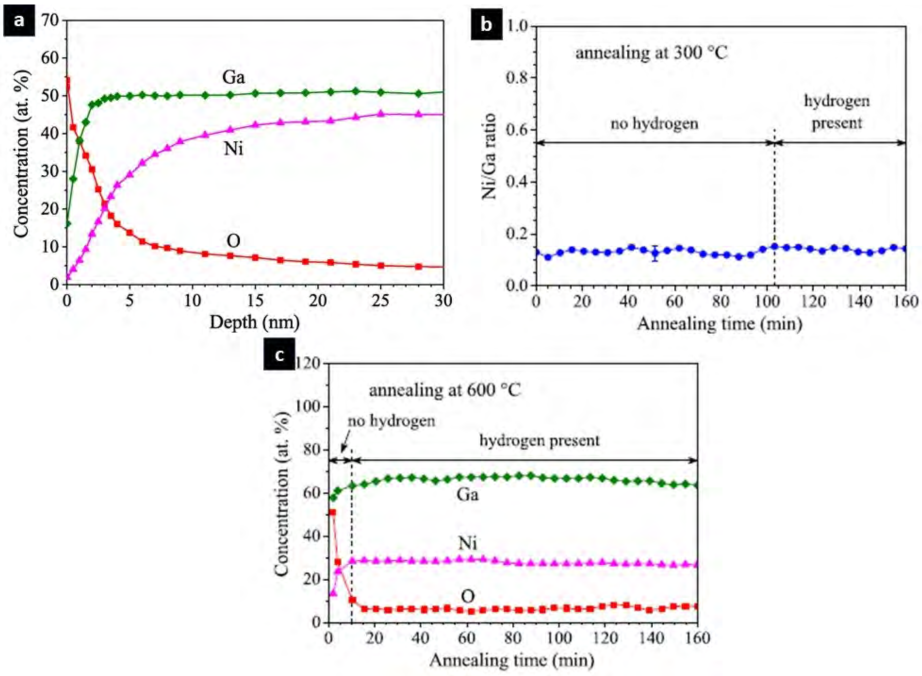

Figure 7.4: (a) XPS curve depicting the elemental concentration with depth profile (in at.%) of a Ga_3Ni_2 single crystal oxidised by air at 25 °C. (b) Curve showing the time dependence of the Ni/Ga concentration ratio in the surface layer (3–5 nm depth) during annealing temperature at 300 °C. (c) Time dependence of the O, Ga and Ni concentrations in the surface layer during annealing at 600 °C [125].

7.2 Experimental Details

The single crystal had a rectangular shape. The sample was grown from a Ga-rich solution using the Czochralski method [128]. It was hand-polished using diamond paste with a 0.25 μm grade. The sample was put into an ultrasonic bath to remove the residual paste after polishing with each grade for 20 minutes. A mirror-like surface was observed while polishing. An image of the crystal attached to the tantalum plate is shown in Figure 7.5. Then, the sample was cleaned in UHV by cycles of 30 minutes with an operating voltage of 1 kV sputtering and two hours of annealing from a low to high temperature at a range of (340-450) °C at P= 1.6 $\times 10^{-9}$. The temperature was monitored by a pyrometer set to an emissivity of 0.35. This procedure was repeated until carbon and other impurities are reduced to near the background level and atomic resolution of a flat terraced surface morphology was obtained in STM.

Figure 7.5: An optical image of the crystal Ga$_3$Ni$_2$(010) mounted on a tantalum plate.

7.3 Results and Discussion

The structural quality of the crystal surface was monitored using LEED. LEED is primarily used to demonstrate the crystal's purity; it also provides information on the surface geometry. The appearance of LEED with bright, sharp spots can be considered evidence of a clean and orderly surface. By analysing the position of the spots on the LEED pattern, the geometry of the surface can be determined.

The effect of temperature on the surface structure of Ga$_3$Ni$_2$(010) crystal was investigated using LEED. LEED patterns were taken after annealing the surface at five different temperatures: 360, 390, 410, 420, and 430 °C. A sharp LEED pattern was observed following the sputtering of the surface and annealing of the sample for two hours at all five different temperatures. A representative pattern at electron energies of 37-43 eV and 63 eV for each temperature is shown in Figure 7.6. It was found that the density of spots reduces with increasing temperature at the same beam energy. The LEED patterns reveal the two-fold symmetry of the surface. Three different types of LEED patterns (4×2), (2×1) and (1×1) were observed depending on annealing temperature. At low temperature, (4×2) and c(2×2) pattern were observed. At intermediate temperature a (2×1) pattern was observed. At high temperature a (1×1) pattern was observed. These patterns are described in detail below.

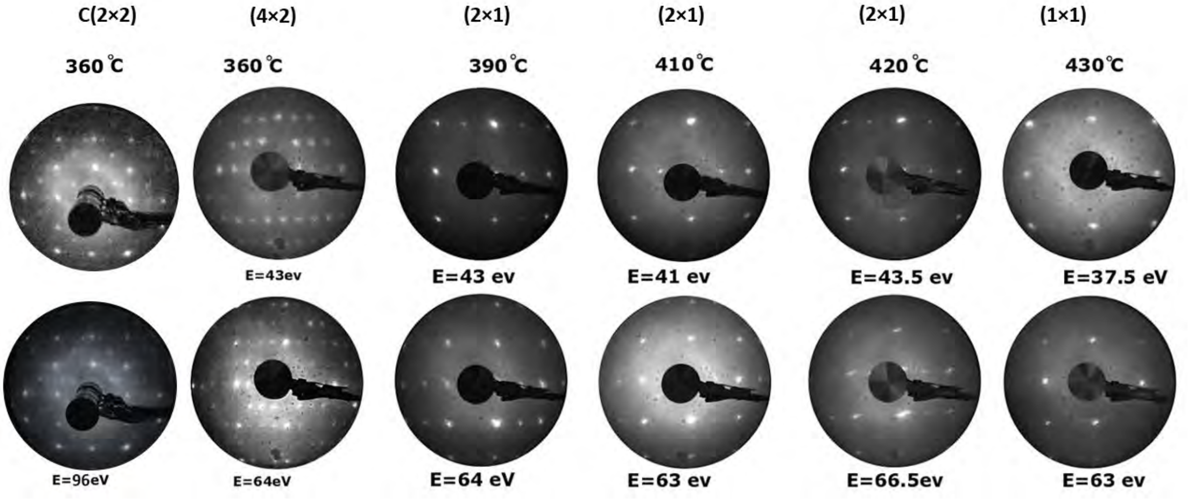

Figure 7.6: LEED patters from the $Ga_3Ni_2(010)$ surface at five different temperatures at identical energy of 37-43 eV and 63 eV, respectively.

7.4 STM of the Surface at Different Annealing Temperatures

To gain insight into the effect of the annealing temperature on surface properties at the atomic structural level, the sample topography was studied using STM. The (010) surface of crystal was annealed at different temperatures, and then the STM images were obtained and compared with the atomic structure of the (010) plane in the bulk model. The temperatures used for annealing the surface were 360 °C, 390 °C, 410 °C, 420 °C, and 430 °C for 2 hours. The Figure 7.7 displays STM images of the surface taken at each temperature, showing the transition of surface reconstruction forms with increasing annealing temperature until it reaches structural composition (1×1). The STM images reveal four types of surface structures that occur on the surface with increasing annealing temperatures. The STM images are consistent with the LEED patterns taken at the same temperature.

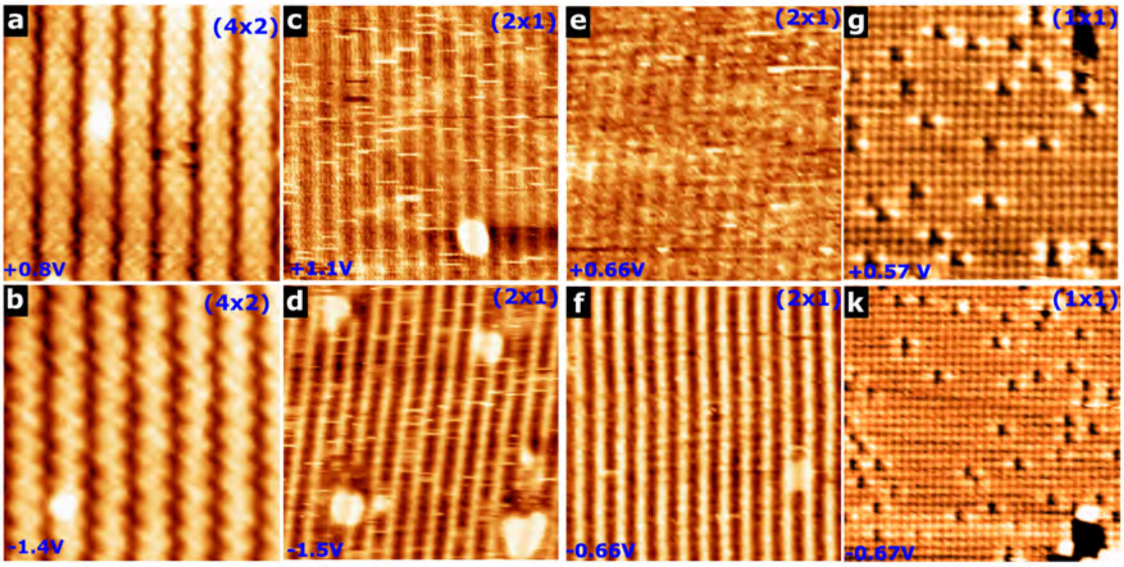

Figure 7.7: 11 nm × 11 nm STM images from Ga$_3$Ni$_2$(010) surface after annealing at different temperatures at positive and negative voltage, (a) and (b) at T = 380 °C. (c) and (d) at T=390 °C. (e) and (f) at T = 410 °C (g) and (k) at T = 430 °C.

7.5 (1×1) Structure

7.5.1 LEED Pattern

A sharp LEED pattern was observed following cycles of sputtering for 30 minutes and annealing the surface at 425 °C-430 °C for two hours. Figure 7.8(a)-(c) depicts LEED diffraction patterns taken at beam energies of 42 eV to 63 eV. The LEED spots are sharp, with a background low intensity indicating good crystalline quality.

The LEED pattern shows rectangular symmetry. A white rectangle represents the rectangle surface unit cell, and the two reciprocal lattice constants are labelled $|b_1^*|$ and $|b_2^*|$. The reciprocal lattice $|b_1^*|$ to $|b_2^*|$ ratio is 1.14, which corresponds to the unit cell's lattice $|a_2|$ to $|a_1|$ ratio in the model. The dimension of the unit cell in the LEED pattern was determined by comparing it to the LEED pattern of Ag(111) at the same energy using the k-vectors of Ag. The LEED pattern from Ag(111) becomes observable around 63 eV and 100 eV. This does not leave many coinciding energies where both Ag(111) and Ga$_3$Ni$_2$(010) patterns are observed, and precludes the use of the sharper LEED pattern, observed at an energy of 145 eV energy from Ga$_3$Ni$_2$. Therefore, the energies of Ga$_3$Ni$_2$ were calibrated to the 63 and 100 eV energies of Ag(111). It is found that the two lattice constants in real space are $|b_1| = 0.39 \pm 0.18$ nm, and $|b_2| = 0.46 \pm 0.3$ nm. This value is consistent with the lattice constant derived from the bulk value. The surface

LEED pattern is thus interpreted as (1×1). We conclude from this that the atomic structure of the (1×1) surface begins to appear after an annealing temperature of 425 °C. Despite the increase in annealing temperature, the surface unit cell remains constant.

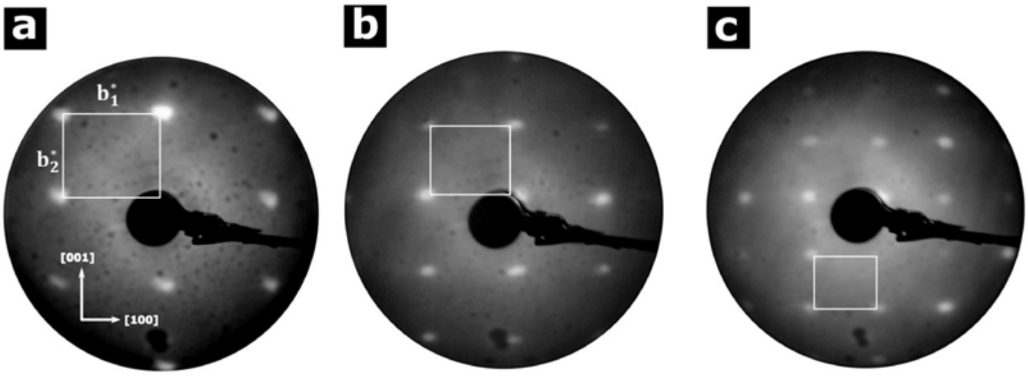

Figure 7.8: LEED pattern for the surface at annealing temperatures = 430 °C, The reciprocal surface unit cell is outlined. (a)-(c) beam energy of(40, 63, and 145) eV.

7.5.2 STM Result

The structure was deduced from atomic resolution STM images of typical areas 14 nm × 14 nm and 11 nm × 11 nm taken at both voltages V_b = -1.2 to + 1.2 V. Figures 7.9(a) and (b) show high-resolution STM images of the structure. Two lattice constants were determined from line profiles. The two separations along the [001] and [100] directions are $|b_2| = 0.46 \pm 0.2$ nm and $|b_1| = 0.39 \pm 0.2$ nm. It was found that the two lattice constants of STM are consistent with the inter-atomic spacing of $Ga_3Ni_2(010)$, which is 0.41 nm and 0.48 nm [124]. It is concluded that the surface unit cell is (1×1).

The FFT of Figure 7.9(b) is depicted in Figure 7.9(c), which confirms the periodic two-fold symmetry. The real-space unit cell parameters were determined from the FFT pattern; $|b_1| = 0.4 \pm 0.04$ nm and $|b_2| = 0.45 \pm 0.04$ nm. The unit cell of the surface is marked with a yellow rectangle. There is a remarkable degree of similarity between the FFT pattern of the STM image and the LEED patterns at same temperature in Figure 7.8, as has been noted for previous systems. The autocorrelation function calculated from the STM image in Figure 7.9(b) is shown in Figure 7.9(d). Along the [100] and [001] directions, the periodicity lattices are separated by $|b_1| = 0.4 \pm 0.03$ nm, and $|b_2| = 0.46 \pm 0.05$ nm. The STM observations, and FFT confirm the structure of surface is (1×1).

Dim defects with bright protrusions that decorate the edges of defects characterise the surface. It could refer to a group of atoms or a high density of atoms. The locations of protrusions on the surface were independent of the bias voltage. However, the protrusions are brighter at positive bias than at negative bias. This suggested that atoms resolved on the surface consisted of one type of atom. The surface unit cell is a rectangle that corresponds to Ga atomic positions in the (010) plane and is represented by a black rectangle and labelled (1) in Figure 7.10(d). The unit cell and its lattice parameters $|b_1|$, and $|b_2|$ are consistent. Overall, the resultant structure is a non-reconstructed (1×1) surface unit cell.

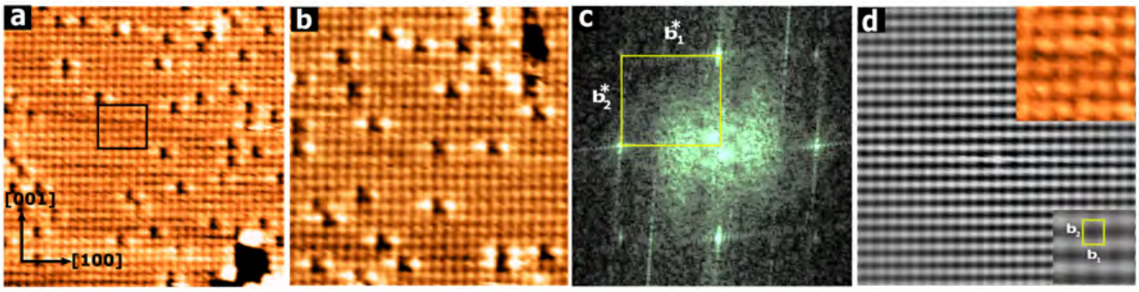

Figure 7.9: (a) and (b) STM images showing atomic-resolution of (1×1) at both bias voltages at 430 °C. (a) 14 nm × 14 nm STM image of the surface (V_b = -0.53 V, I_t = 0.137 nA). (b) 11 nm × 11 nm (V_b = 0.57 V, and I_t = 0.137 nA). (c) FFT pattern of the STM image in (a), showing two-fold symmetry. (d) autocorrelation function calculated from STM image in(a), showing two-fold symmetry (8.8 nm × 8.8 nm).

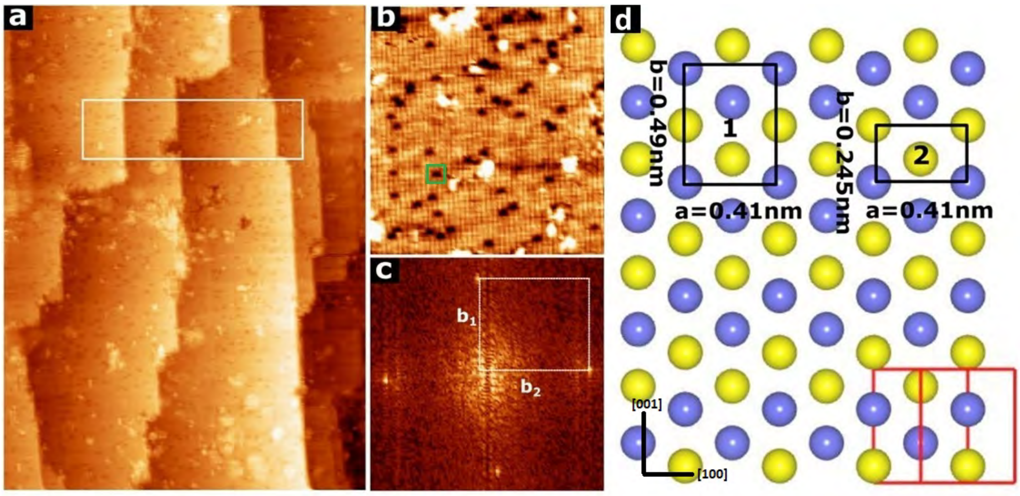

Figure 7.10: (a) 67 nm × 19 nm STM image of the surface showing terraces with step height 0.37 ± 0.06 nm. (b) An enlarged area obtained from (a) showing the defects on the surface in an 18 nm × 19 nm STM image at V_b = + 0.53 V. (c) FFT of the STM image in (b), showing the unit cell of the surface is (1×1). (d) A (010) plane showing the unit cell of surface (1×1). The Ga and Ni atoms are coloured with blue and yellow dots, respectively. The surface unit cell of (1×1) is marked with a black rectangle and labelled with number 1.

Figure 7.10(a) shows an STM image obtained after the preparation cycle at the same annealing temperature, T = 425-430 °C. It depicts a terrace arrangement with a step height of 0.37 ± 0.06 nm. Figure 7.10(b) shows an atomic-resolution STM image of the terraces, with defects distributed on the surface. The defect appears in the image as a dim rectangle highlighted by a green rectangle and may correspond to missing atoms. Although it is difficult to measure the two lattice constants from the STM image, the FFT of Figure 7.10(b) is shown in Figure 7.10(c). The two lattice constants measured from the FFT are $|b_1| = 0.41 \pm 0.01$ nm and $|b_2| = 0.43 \pm 0.03$ nm, confirming the unit cell of the surface as (1×1).

7.6 (2×1) Structure

7.6.1 LEED Pattern

The LEED pattern of the surface was taken after several cycles of cleaning, sputtering for 30 minutes, and annealing the surface at 390 °C, 410 °C, and 420 °C for 2 hours each cycle, in separate experiments. The LEED patterns of the surface are shown in Figure 7.11 (a-c) at beam energy of 41-44 eV. The observed LEED patterns reveal additional superstructure spots. In addition, it was found that the diffraction spots are more intense and sharp with a lower background at an annealing temperature of 420 °C compared to 390 °C.

Figure 7.12 depicts the LEED obtained at an annealing temperature of 420 °C and taken from the same area on the surface within a range of electron energies from 45 eV to 150 eV. The surface unit cell is marked with a white rectangular shape.

To find the surface unit cell at these temperatures, we compare the LEED patterns in similar beam energy at 390 °C, 410 °C, and 420 °C to LEED pattern of (1×1) at 430 °C (Figure 7.8(a)). The primitive unit cell (1×1) is found to match for the white rectangle marked in Figure 7.11(a), and the primitive unit cell's lattice constants are labelled $|b_1^*|$, and $|b_2^*|$. The new unit cell and two lattice constants are marked and labelled with a small white rectangular shape and $\frac{b_1^*}{2}$, and $|b_2^*|$ in Figure 7.11 (b). The density of spots in the LEED pattern increases with the number of spots in a rectangular unit in the reciprocal lattice doubling along the [100] direction. The new spots are observed to be located half-way between the two substrate spots that are arranged along the [100] direction. It can be seen that the size of the unit cell along the [001] direction is the same for both structures, while the size along the [100] direction is half the distance. In the real space, this distance is then doubled, revealing that surface undergoes (2×1) reconstruction. The ratio of reciprocal lattice vectors $\frac{b_1^*}{2}$ to b_2^* is 1.66, which is consistent with the ratio of $\frac{2|a_1|}{|a_2|}$ of the Ga_3Ni_2 (010) in the model. The two parameter constants of the surface are identified by calibrating to the LEED pattern of Ag(111), as mentioned for the LEED (1×1) pattern. It is found that the two lattice constants $|2b_1| = 0.83$ nm and $|b_2| = 0.51$ nm.

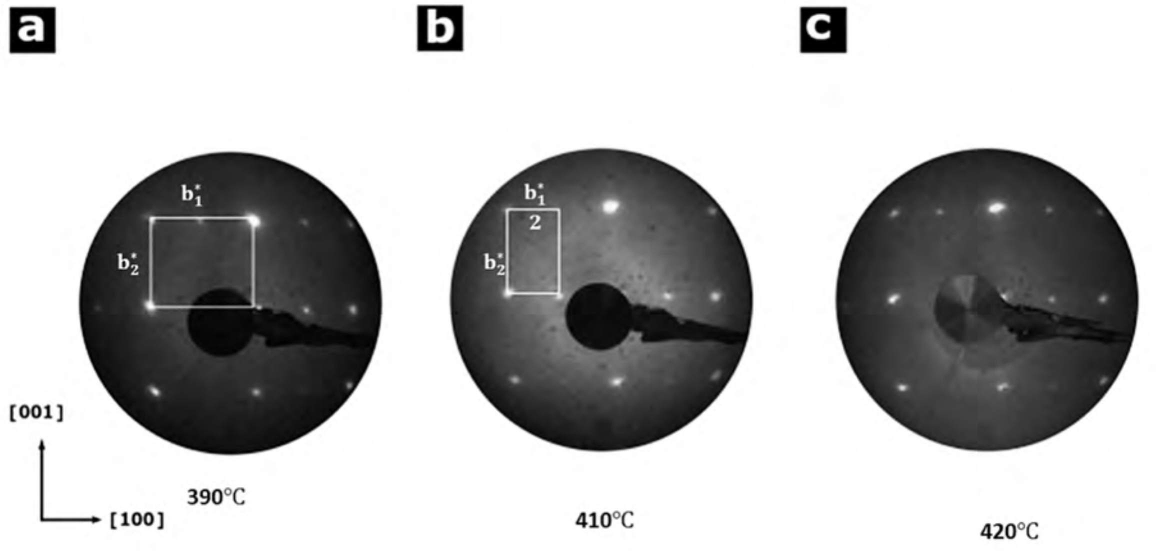

Figure 7.11: LEED patterns of the reconstructed (2×1) surface. (a) After annealing temperature at 390 °C and beam energy 44 eV. (b) After annealing at 410 °C and beam energy 41 eV. (c) After annealing at 420 °C and beam energy 44 eV.

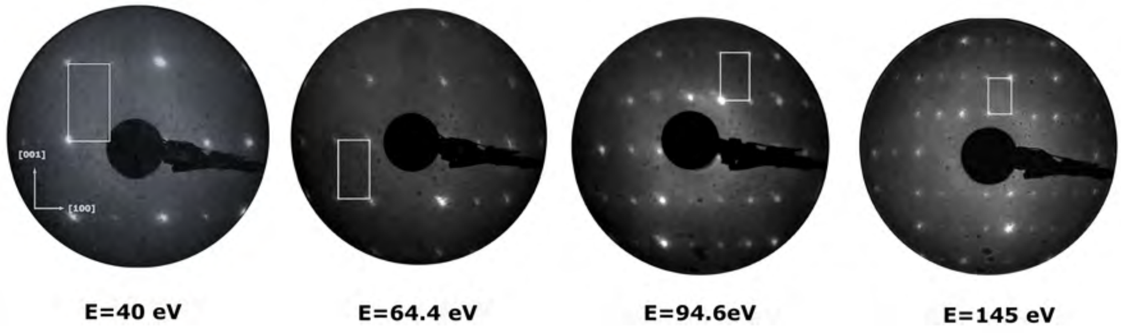

Figure 7.12: LEED pattern of the reconstructed (2 × 1) surface recorded at T = 420 °C, obtained at different electron energies.

7.6.2 STM Result

Three treatment cycles were carried out, with each cycle consisting of 30 minutes of sputtering and 2 hours annealing at 390 °C, 410 °C and 420 °C for 2 hours. Following that, LEED and STM images of the surface were recorded. Firstly, the STM observations at 390 °C will be presented. An atomically resolved STM image of clean surface was taken at both bias voltages.

Figure 7.13 shows the STM images taken from the same area with voltages ranging between - 1.7 V and + 1.7 V and at an annealing temperature of 390 °C. It is observed that the atomic structure of the terrace depends on the type of voltage. At both bias voltages, the flat terrace is distinguished by bright protrusions aligned in rows along the [001] direction. At a negative bias in the range of -0.5 V to -1.7 V and a high positive bias, the rows of atoms are aligned along the [001] direction with a separation of 0.82 ± 0.04 nm. A magnified area is highlighted by a white rectangle in the inset of the first STM image in Figure 7.13. It displays the atomic arrangement along the [001] direction with a separation of 0.46 nm at V_b = -0.8 V.

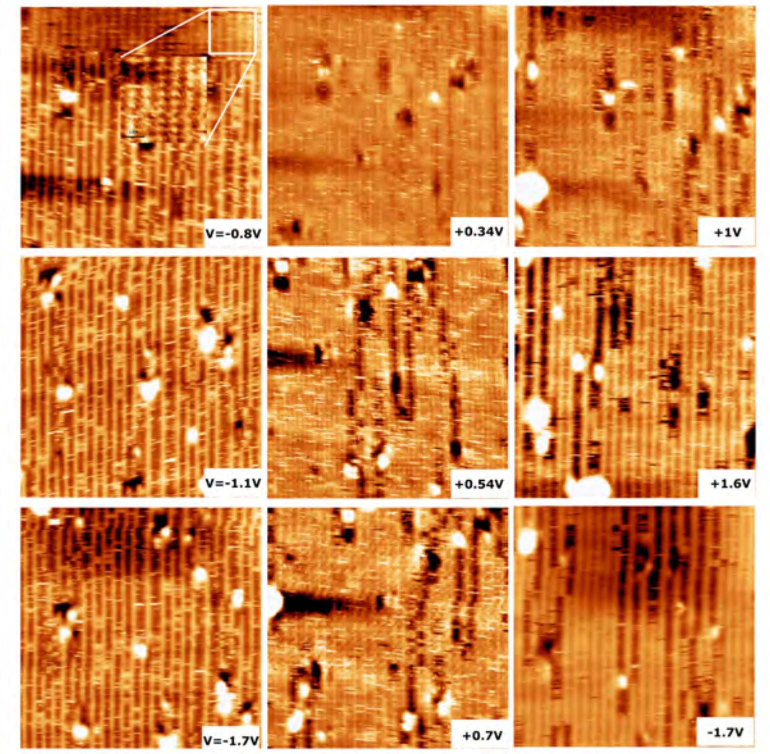

Figure 7.13: A series of voltage-dependent STM images of surface. Bias voltages from V_b = -1.7 V to V_b = +1.7 V. The STM images 20 nm × 20 nm show the (2×1) reconstruction at 390 °C.

Figure 7.14(a) depicts an image taken from a different part of the surface at negative bias. Figure 7.14(b), and (c) show a magnification of the area which is highlighted by a black rectangle in Figure 7.14(a). The row structure is visible in these images, and the visible protrusions are arranged along the [001] and [100] directions. The periodicity was determined using line profiles, and it was found that the row spacing is $|2b_1| = 0.82 \pm 0.04$ nm along the [100] direction, which agrees with twice the constant lattice of $|a_1|$ in the bulk model. The periodicity of the protrusion alignments along [001] direction is $|b_2| = 0.47 \pm 0.04$ nm, which agrees with the $|a_2|$ lattice in the bulk model. Overall, the results indicate that the surface unit cell is (2×1), as highlighted with a black rectangle in Figure 7.14(c).

The FFT function of the STM image in Figure 7.14(c) is depicted in Figure 7.15(a), which shows it shows rectangular symmetry. In real space, the two lattice constants are $|2b_1| = 0.81 \pm 0.04$ nm and $|b_2| = 0.47 \pm 0.04$ nm. The periodicity can be better resolved in the two-dimensional image of the autocorrelation functions calculated from the STM image. Figure 7.15(b) shows the autocorrelation functions of Figure 7.14(c), with a separation between spots is $|2b_1| = 0.81 \pm 0.03$ nm and $|b_2| = 0.48 \pm 0.04$ nm, along the [100] and [001] directions, respectively. The STM images exhibited the same aspect as the LEED pattern at these temperature, as shown in Figure 7.12.

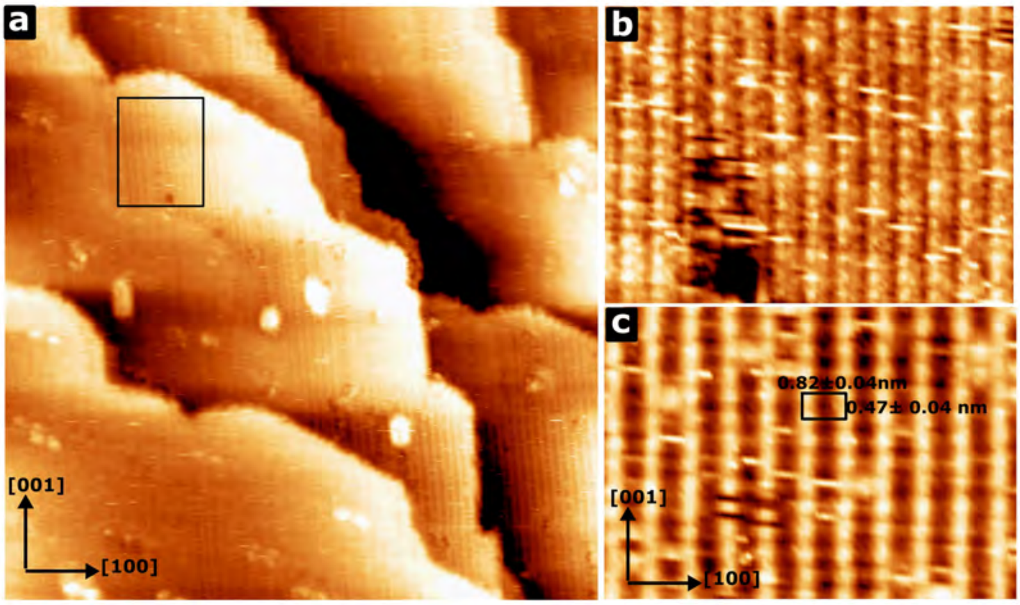

Figure 7.14: (a) STM image of a large scale area (60 nm × 60 nm, V_b = -0.543 V, I_t = 0.137 nA). (b) and (c) The zoomed section that is highlighted with a black rectangle in (a), showing an atomically resolved image of the (2×1) reconstruction. (b) 11 nm × 8 nm STM image at V_b = -0.34 V. (c) 0.88 nm × 0.63 nm STM image.

Figure 7.15(c) shows the proposed structural model for a (2×1) reconstruction. The blue and yellow dots, as well as the dashed black circles, represent Ga and Ni atoms, as well as omitted Ga atoms in the rich Ni-plane. This model is only used as an illustrative example, as the DFT calculation is typically used to determine the type of reconstruction mechanism for this model. The Ga atoms were selected to explain the (2×1) reconstitution, with a distance of $|2b_1| = 0.81$ nm between the first and third Ga atoms along the [100] direction, highlighted with blue dots. The second Ga atom is missing and highlighted with a dashed circle. The distance between Ga atoms along the [001] direction is 0.49 nm. The (2×1) unit cell is highlighted with a black rectangle, corresponding to the (2×1) reconstruction observed in the STM.

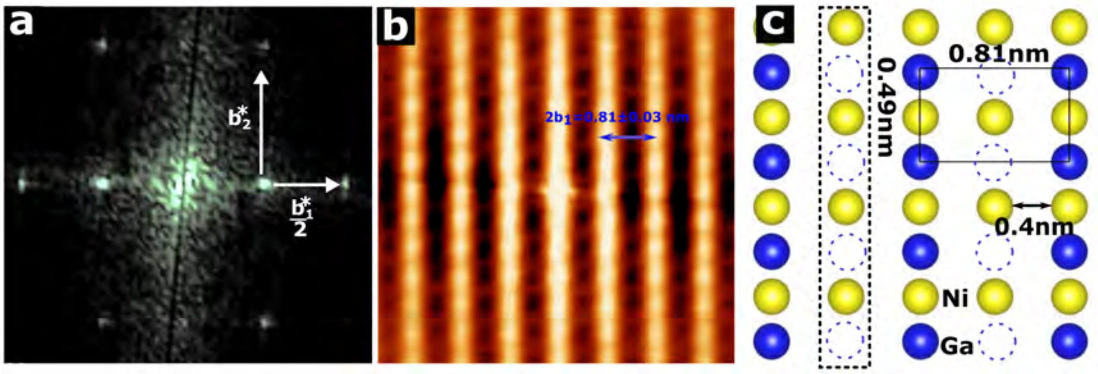

Figure 7.15: (a) The FFT function of Figure 7.14(c) showing the two lattice constants in real space labelled $\frac{b_1^*}{2}$, b_2^*. (b) Autocorrelation function of Figure 7.14(c). (c) The structural model built from the STM image of the (2×1) reconstructed surface sample. The Ga and Ni atoms are marked with dark blue and yellow dots. The omitted Ga atoms are marked with dashed black circles.

The rows observed in Figure 7.13 will be presented here. Figure 7.16 shows an enlarged STM image obtained from the same terrace as shown in Figure 7.13, at V_b= + 0.34 V. Due to the rows appearing between previous rows and aligned along the [001] direction, these rows are not discovered in the terrace shown in Figure 7.15 which is obtained from different terraces. It was found that the new rows are located at the centre between the previous rows, with the separation of close to $|b_1|$ = 0.4 ± 0.03 nm along the [100] direction, as shown in the inset of Figure 7.16(a). Figure 7.16(c) shows the autocorrelation function obtained from Figure 7.16(a), where the periodicity of the rows can be clearly seen. The two lattice constants $|b_1|$, and $|b_2|$ have values of 0.402 ± 0.04 nm, and 0.46 ± 0.041 nm, respectively. The FFT pattern taken from Figure 7.16(a) is depicted in Figure 7.16(d), showing a rectangular lattice. The values of the two lattice parameters, $|b_1|$ and $|b_2|$, are 0.41 ± 0.04 and 0.48 ± 0.05 nm, respectively, therefore the values of two lattice parameters in the STM image corresponded to two lattice parameters of the unit cell in the bulk model. The colour contrast between the rows indicates that the inner rows are not on the same surface level.

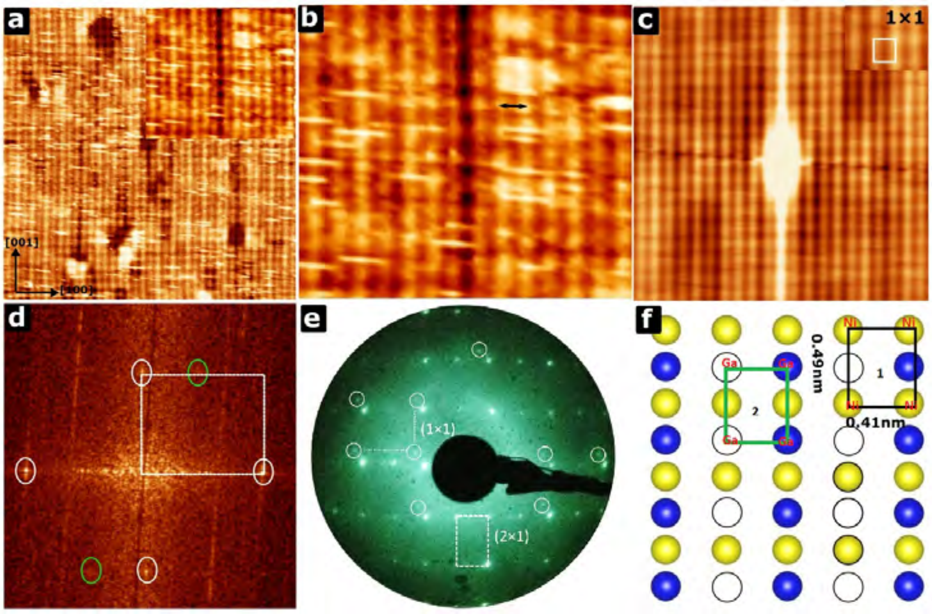

Figure 7.16: (a) 16 nm × 16 nm STM image of the surface at (V_b = +0.343 V, I_t = 0.137 nA). (b) 5.7 nm × 5 nm STM image shows the enlarged area of (a). (c) (c) The autocorrelation function of an area of (a). Size: (9 nm × 9 nm). (d) The FFT pattern of (a) shows (1×1) structure. (e) LEED pattern taken at E = 118 eV shows two unit cells of surface, (2×1) and (1×1). The unit cells are marked with large and small white rectangles. (f) A schematic diagram showing a ball model of (1×1) surface unit cell. The blue and yellow dots represent Ga and Ni atoms, respectively. The unit cell is marked with a black rectangle.

Figure 7.16(f) depicts the (010) plane model, with blue and yellow circles highlighting the Ga and Ni atoms, respectively. According to the STM data, there are two possible explanations: (i) the surface has two types of atoms, Ga and Ni. In this case, the surface depends on the bias voltage, and it is possible that one of the two types does not undergo reconstruction, resulting in the (1×1) unit cell highlighted by a black rectangle and number(1). Alternatively, (ii) the surface has only one type of atom, such as Ga, indicating that the missing row of Ga atoms is transferred from the under-layer to the surface as a row along the [001] axis with increasing annealing temperature. The black circles and blue dots mark the Ga atoms at the under-layer and surface, respectively. In this case, the (1×1) unit cell produced by the approaching of the missing Ga atoms to the surface is highlighted with a green rectangle and number(2).

The surface was investigated after annealing at 420 °C for 2 hours using STM. The STM images were taken from different areas at both voltages, as shown in Figure 7.17. Figures 7.17(a) and (b) show a large flat terrace composed of well-reconstructed (2×1), the rows running along the [001] direction at both biases. It was found that the structure of some surface terraces is independent of voltage.

On the other hand, the atomic structure of a few terraces was discovered to be dependent on type of voltage. Large flat terraces, as shown in Figure 7.17(c) and (e), are composed of well-reconstructed (2×1) rows running along the [001] surface direction at a negative bias. Figures 7.17(d) and (f) show that atomic rows could not be resolved on the surface when a small positive bias (= 0.57 to +0.743) V was applied.

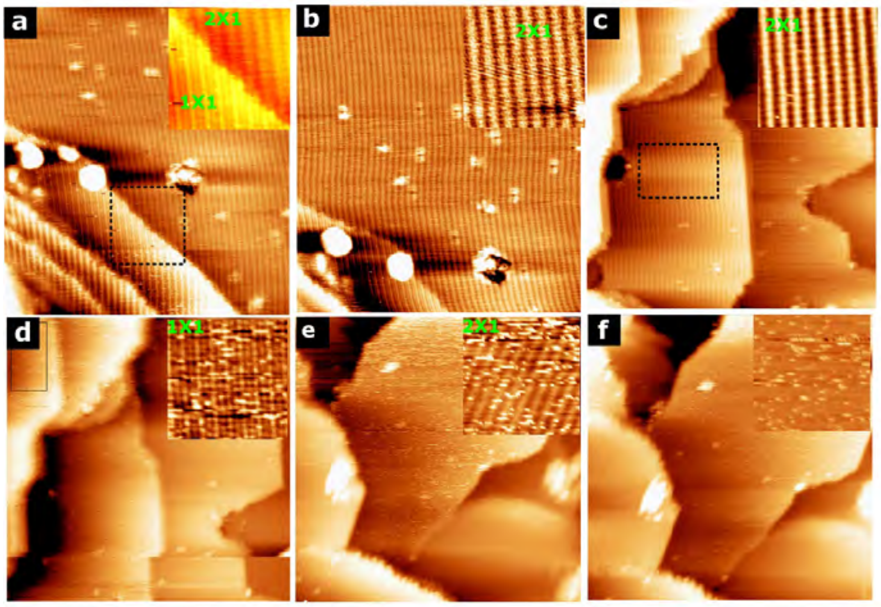

Figure 7.17: (a)-(f) A series of STM images shows bias dependence. (a) and (b) (37 nm × 40 nm) STM image at V_b = -0.71 V and V_b = +0.61 V, respectively, with I_t = 0.137 nA. Both show that the structure of surface is (2×1). (c) and (d) (47 nm × 49 nm) and (49 nm × 49 nm) STM images at V_b = -1 V, and V_b = +1 V, respectively, with I_t =0.146 nA. (c) The atomic structure of the surface is illustrated (2×1) at a negative voltage. (d) Exhibiting the surface's atomic structure is (1×1) at positive bias. (e) and (f) (58 nm × 58 nm) STM images show that the structure is (2×1) at V_b = -0.74 V and distorted at (V_b = +0.74 V). All enlarged view of the inset area are 7 nm × 7 nm.

Figure 7.18(a) presents the area marked with a black rectangle in Figure 7.17(d). It reveals new rows are appearing between the main (2×1) rows at positive bias. Therefore, the new rows (inner rows) could be very close to the surface, leading to the noise in the STM image. Figure 7.18(c) depicts the FFT of Figure 7.18(a). Bright spots in the FFT pattern, which are indicated by the yellow circles that show (1×1) structure. The two real space distances between two-high contrasting intensity spots are $|b_1|$ = 0.41 nm and $|b_2|$ = 0.45 nm. The dim spots refer to $|b_1|$ = 0.81 nm, which is marked with a blue circle. The autocorrelation function of Figure 7.18(a) is shown in Figure 7.18(b). It was found that the two separations between the new rows along [100] and [001] directions are $|b_1|$ = 0.41

± 0.03 nm and $|b_2|$ = 0.48 ± 0.06 nm or 0.42 ± 0.05 nm. The lattice constants obtained from the FFT pattern and autocorrelation match the two lattices in the bulk model and confirm the structure as (1× 1). These results in the voltage range +0.5 and +0.7 confirm the same previous observation (1×1) in the STM image at 390 °C.

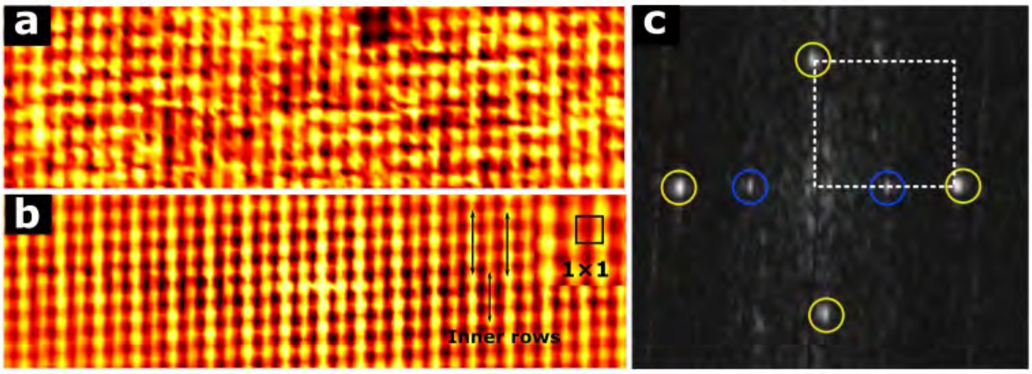

Figure 7.18: (a) 12.5 nm × 4 nm STM image at V_b = +1 V. It shows the inner rows between the rows of the (2×1) along the [100] direction. (b) Autocorrelation function of (a). (c) The FFT pattern taken from (a), showing the two lattices constants in real space match (1×1).

We propose two possible explanations. The first is that two types of surface termination planes are observed. The first type, is not affected by the type of applied voltage, and its structure is (2×1). The second type of terrace depends on the bias of the applied voltage. Thus, its atomic structure may consist of two elements, Ga and Ni. The second explanation is that Ga rows could move from bulk to surface.

The LEED pattern was taken from different areas on the sample surface after annealing at 425 °C, as shown in Figure 7.19. It shows two types of structure (2×1) and (1×1) that may support the types of surface structure of a terrace that were observed at 388 °C. In addition, the unit cell of surface (1×1) that was forming on step height is 0.36 ± 0.03 nm is still being observed at higher temperatures.

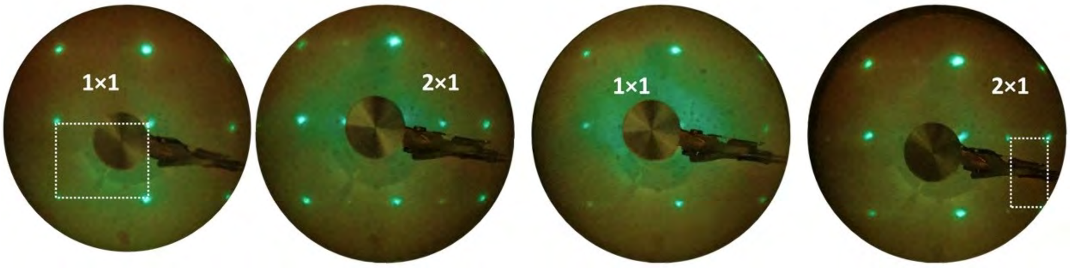

Figure 7.19: LEED pattern taken from different parts of sample at annealing temperature 425 °C for three hours and E= 40 eV.

7.7 (4×2) Structure

7.7.1 LEED Pattern

Figure 7.20 (a) shows the LEED pattern taken after sputtering for 30 minutes and at the annealing temperature of 360 °C for 2 hours. The observed LEED image shows the density of additional superstructure spots increasing with decreasing annealing temperatures. The unit cell of the superstructure and the two lattice parameters are marked and labelled with a small white rectangle and $\frac{b_1^*}{4}$ and $\frac{b_2^*}{2}$ in Figure 7.20(a). To find the primitive unit cell, we compare the LEED patterns at 368 °C and 430 °C with the same energy. The primitive and new unit cells are highlighted with a large white rectangular shape in Figure 7.20(a). The unit cell (1×1) represents the brightest spots. Three dim spots are found between the two bright spots along the [100] direction, and one dim spot is found between the bright spots along the [001] direction. The superstructure spots on the row appeared at the position of $(1/4) \times |b_1^*|$ and $(1/2)\times |b_2^*|$. In real space, the periodicity is 4 times the $|a_1|$ and twice $|a_2|$ along the [100] and [001] directions, respectively. These findings suggest that the structure of the surface is (4×2).

The LEED patterns reveal that the structure of the surface transfers from reconstruction to (1×1) with increasing temperature, as shown in Figure 7.20. The transfer occurs at three specific temperatures: 366-380 °C, 380-420 °C, and above 425 °C. The surface structure remains the same with increasing annealing temperatures above 430 °C, forming the (1×1) surface. This indicates that the surface atoms have the lowest potential energy.

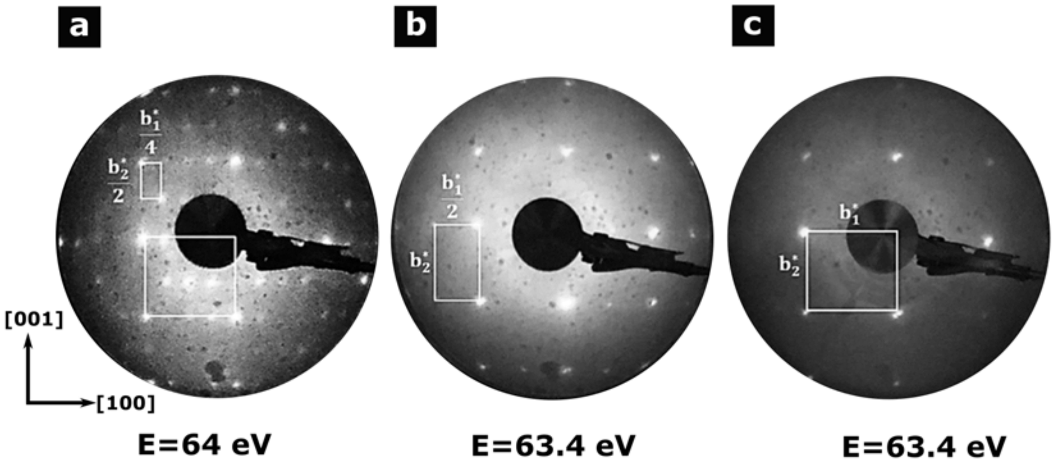

Figure 7.20: (a) LEED pattern displaying the reconstructed (4×2) surface at T = 366 °C. (b) LEED pattern showing the reconstructed (2×1) surface at annealing temperature = 410 °C. (c) LEED pattern showing the (1×1) surface unit corresponding to the bulk termination at annealing temperature = (425-435) °C.

7.7.2 STM Result

STM images were taken after the LEED patterns at specific temperatures indicated that the surface was suitable for STM investigations. STM images that are consistent with the LEED results were obtained. The sample was cleaned with two separate cleaning cycles, annealing for 2 hours at 366 °C, and 388 °C. STM images with higher resolution are presented in Figures 7.21(a) and (b). The atoms are nearly resolved at both bias voltages in the range of -0.5 V to +1.5 V, and thus we can say that T = 388 °C is the temperature where the surface becomes ordered. Further analysis of the surface in these two images is presented below. Large flat terraces are formed as a result of annealing for a longer time. The atomic structure of the surface at both annealing temperatures, 366 °C and 388 °C, consists of rows along the [001] direction, and the distance between two consecutive rows along the [100] direction is 1.62 ± 0.06 nm and 1.63 ± 0.05 nm, respectively. That suggests the structure of the surface is the same for both.

We will now discuss the STM observations taken at an annealing temperature of 388 °C. The STM images of the surface annealed at T = 388 °C show step terrace structures, as shown in Figure 7.22(a) and (b). In some areas, the step edges form rectangles. The step edges of the terraces are parallel to the [001] direction, while the depressions are parallel to the [100] direction. The terraces show no atomic resolution.

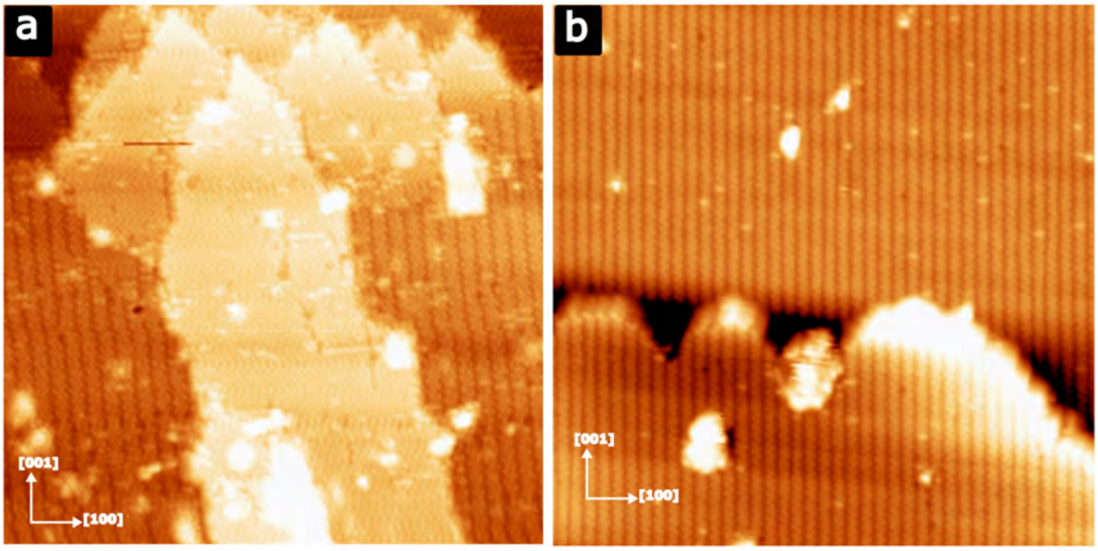

Figure 7.21: (a) 53 nm × 53 nm STM image of a surface after annealing at 366 °C for 2hours (V_b = -0.8 V, I_t = 0.175 nA). (b) 63 nm × 63 nm STM image of the same surface obtained after annealing at 388 °C for 2 hours (V_b = -1.548 V, I_t = 0.149 nA).

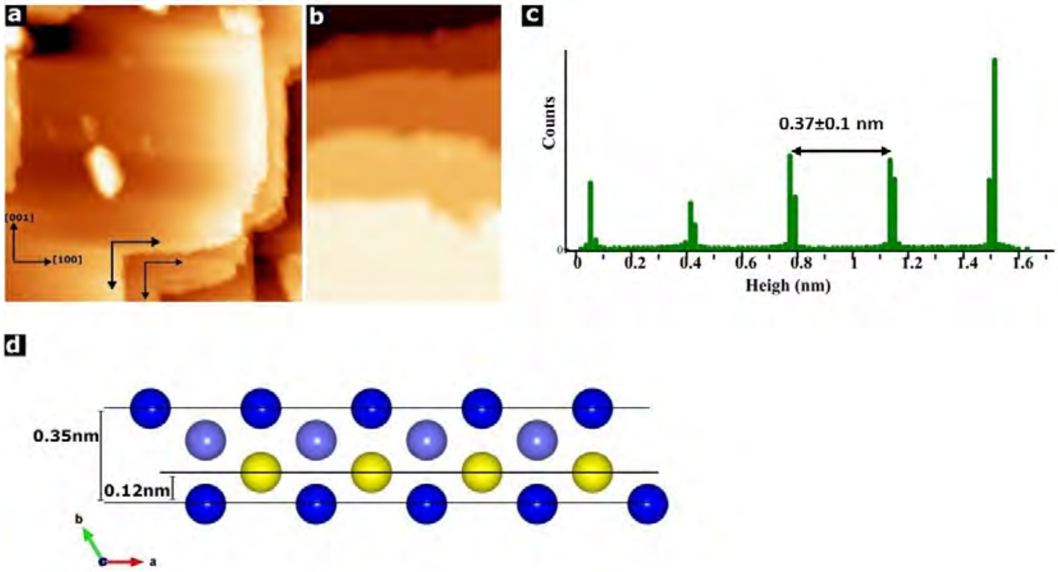

Figure 7.22: (a) 65 nm × 65 nm STM images of the surface at (V_b = 0.59 V, I_t = 0.145 nA), showing step-terrace structure. The sample was annealed at T = 380 °C for 2 hours. (b) 25 nm × 38 nm STM image showing the step/terrace morphology of surface V_b = -1.7 V, I_t= 0.145 nA. (c)A histogram of step heights in (b), showing flat terraces are separated by steps of 0.37 ± 0.11 nm. (d) A side view of planes along the [120] direction, showing that the (010) planes are separated by $d_{(010)}$= 0.35 nm. .

The step heights and stacking relations of adjacent terraces were determined in order to identify the surface atomic structure. The step height of terraces between two consecutive terraces in the [100] direction is determined using a histogram, as shown in Figure 7.22(c). The average step height is found to be 0.37 ± 0.11 nm, in agreement with the spacing $d_{(010)}$ = 0.35 nm between adjacent isostructural (010) lattice planes in Ga_3Ni_2 in the [010] direction, as shown in Figure 7.22(d).

Two types of terraces observed are illustrated in Figure 7.23(a), labelled as A and B in Figure 7.23(b). The A terrace is characterised by atomic rows, while the B terrace is characterised by the absence of atomic rows. The step height of A terraces is 0.47 ± 0.05 nm, while for B terraces this is 0.36 ± 0.03 nm. The histogram of the distributed step height of Figure 7.23(a) is shown in Figure 7.23(c). The histogram shows a step height difference of 0.62 nm between terraces A and B. The two types of terraces are observed again at various step heights, as shown in Figure 7.24(a). The terraces are labelled A and B. The inset of right Figure 7.24(a) displays a zoomed area highlighted with a black dashed rectangle in Figure 7.24(a).

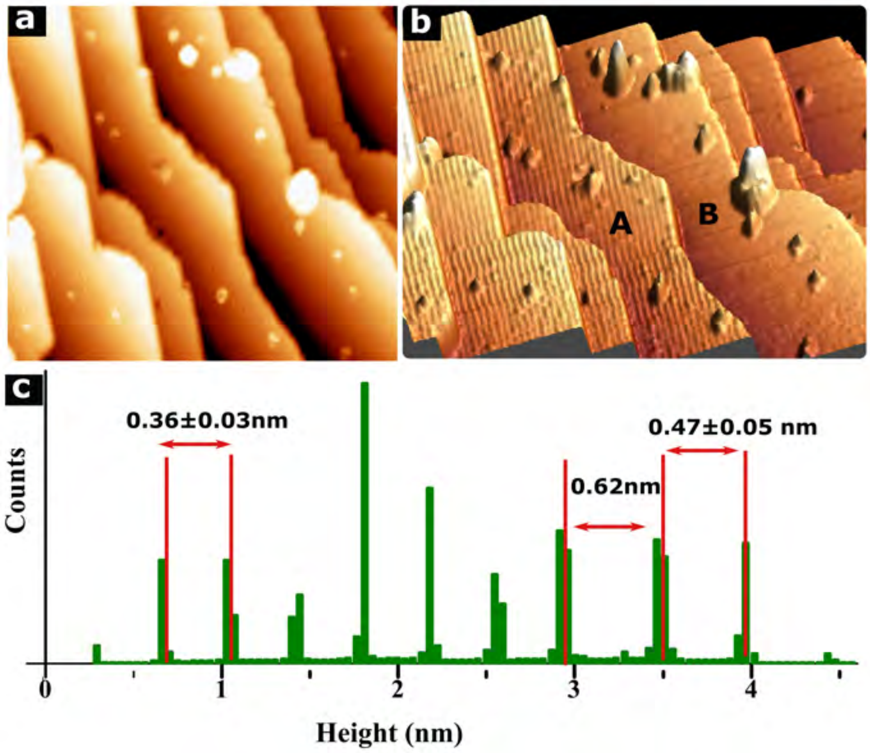

Figure 7.23: (a) 113 nm × 103 nm STM images of surface at (V_b = 0.8 V, I_t = 0.145 nA), showing the step/terrace of surface. (b) Derivative of STM image in (a) showing two types of terraces, labelled with A, and B. (c) A histogram used to calculate the height of the terraces in (a).

The atomic structure of terrace type A has been resolved, whereas that of terrace type B has not. The step height between these two terraces is $d_{(010)} = 0.12 \pm 0.04$ nm, as shown in Figure 7.24(b), which presents the step heights measured using the line profile. This step height is consistent with the lattice constant of ($d_{(010)}/3$) in the [120] direction. Both types of terraces discussed here.

The atomic structure of terrace A was obtained for voltage bias ranges of V_b = (-0.4 V, +1.5 V). Figures 7.25(a), and (b) show STM images at a negative bias of -0.714 V and a positive bias of +0.8 V, respectively. The STM images taken at different voltages revealed the periodic row structures running along the [001] direction. Figures 7.25(c), and (d) show an enlarged area of Figures 7.25(a), and (b). The average separation between the centres of rows is 1.62 ± 0.06 nm along the [100] direction. This spacing between rows is four times that of the bulk model's lattice constant ($|a_1|$ = 0.41 nm). In positive bias, the row atomic structure is a column, whereas it is a zigzag structure in negative bias.

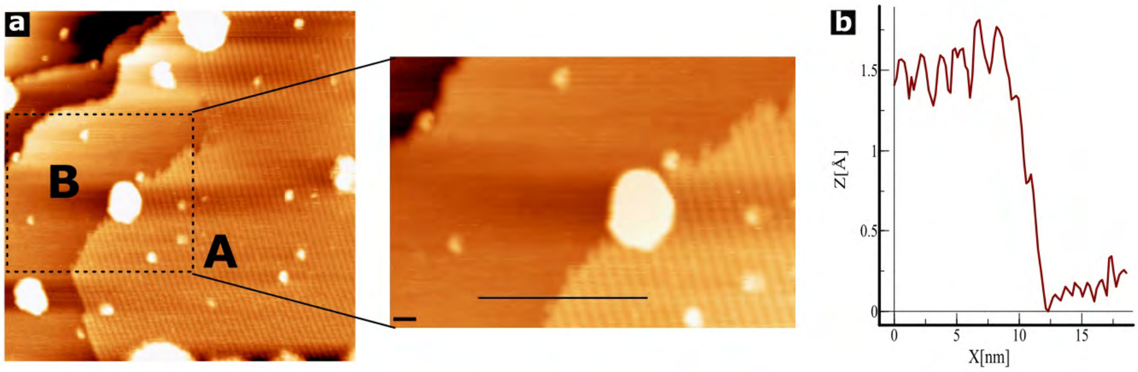

Figure 7.24: (a) A large scale STM image of a clean surface prepared after annealing temperature T = 380 °C at (V_b = +1 V, I_t = 0.149 nA, 90 nm × 90 nm). Magnification of the area indicated by the black rectangle inset in right figure (a). (b) The line from inset right Figure (a) indicates the origin of the line profile.

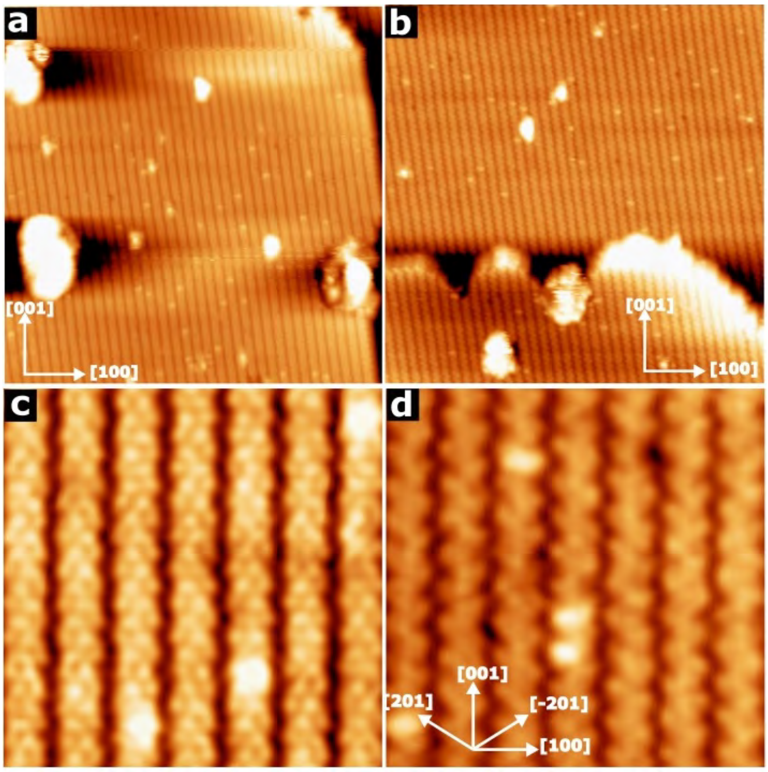

Figure 7.25: (a) 60 nm × 60 nm STM image (V_b = 0.8 V, I_t = 0.12 5nA). (b) 60 nm × 60 nm STM image of surface (V_b = -1.4 V, I_t = 0.149 nA). (a) and (b) show that the bright rows form the (4×2) reconstruction. (c) and (d) 11 × 11 nm STM image showing the enlarged area from (a) and (b). They show near atomic resolution of the rows.

An enlarged view of the row structure at a negative voltage is shown in Figure 7.26(a). The structural details of the row are shown in Figure 7.26(b). Meanwhile, adjacent zigzag structures had an antiphase arrangement, so that the zigzag structure had a head-to-head orientation along the [100] direction. The average distance between the zigzags in the [100] direction is $|4b_1| = 1.62\pm$ 0.07 nm, which is four times as large as the $|a_1|$ distance in model. In addition, the bright spots of zigzag structure are oriented along the [$\bar{2}$01] and [201] directions, with an average length of 0.98 ± 0.06 nm and 0.95 ± 0.04 nm, respectively. The distance between the head-to-head of the zigzag structure rows along the [001] direction is $|2b_2| = 1.01$ ± 0.1 nm, which is twice the lattice constant $|a_2|$ (0.48 nm). As a result, the rectangle cell, which is highlighted in Figure 7.30(b) with a green rectangle shape, is the surface unit cell, corresponding to a (4×2) superstructure.

Figure 7.26(c) shows the FFT pattern of Figure 7.26(a), which confirms two-fold symmetry and reveals that the unit cell of the surface is a rectangle. The two lattice parameters in the FFT pattern are labelled with $\frac{b_1^*}{4}$ and $\frac{b_2^*}{2}$. The two real space lattices in the FFT pattern are $|4b_1| = 1.62 \pm 0.06$ nm and $|2b_2| = 0.99 \pm 0.09$ nm. It was found that the lattice parameter $|4b_1|$ is 4 times larger than the lattice $|a_1|$, and that $|2b_2|$ is twice the lattice $|a_2|$ of bulk. The surface unit cell is correspond to the unit that is highlighted with a green rectangle in Figure 7.26(b).

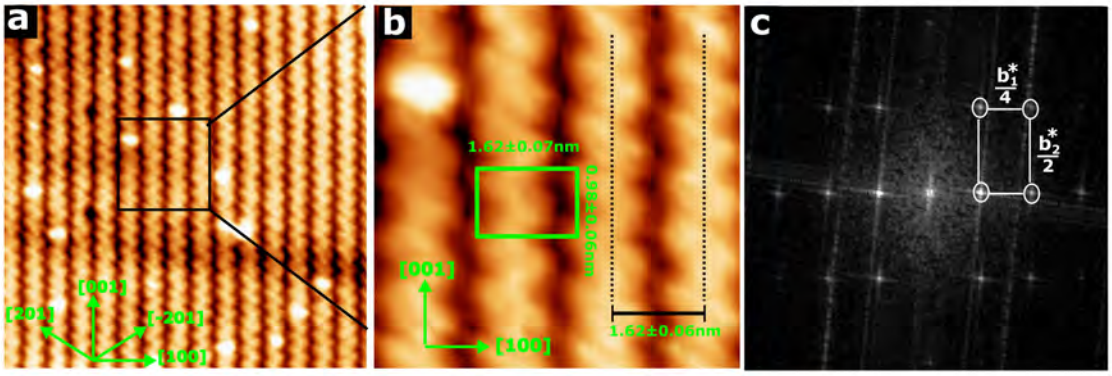

Figure 7.26: ((a) Atomically resolved STM image (25 nm × 25 nm, V_b = -0.714 V, I_t = 0.149 nA). (b) Enlarged area from Figure (a), showing the bright rows in the [001] direction, and the structure of the rows is zigzag. The unit cell is indicated. (c) The FFT function of (a) showing the rectangular unit cell. The two parameters $\frac{b_1^*}{4}$ and $\frac{b_2^*}{2}$ are labelled.

As shown in Figure 7.27(a), the width of the row appears wider at positive bias than at negative bias. The results suggest one type of atom is resolved at both voltages. The FFT function indicates that the unit cell is a rectangle with real space parameters of $|4b_1| = 1.62 \pm 0.03$ nm and $|2b_2| = 1.01 \pm 0.03$ nm, which are labelled with $\frac{b_1^*}{4}$ and $\frac{b_2^*}{2}$ in Figure 7.27(b). The FFT function at positive bias is similar to that at negative bias. The inverse FFT, shown in Figure 7.27(c), reveals that the structure of a row is composed of small dots separated by four times the lattice constant $|a_1|$ and twice the lattice constant $|a_2|$ along the [100] and [001] directions, respectively. The positions of the bright spots coincided with the locations of one type of atom in the (010) plane, which is compatible with a (4×2) reconstruction highlighted with a blue rectangle in Figure 7.27(c). Figure 7.27(e) shows the autocorrelation function of Figure 7.27(a), confirming that the surface unit cell is a rectangle with two lattice constants of 1.01 ± 0.07 nm and 1.63 ± 0.05 nm. Figure 7.27(f) depicts the LEED pattern at low energy, which corresponds to the FFT pattern, and in both patterns, the lattice constants match

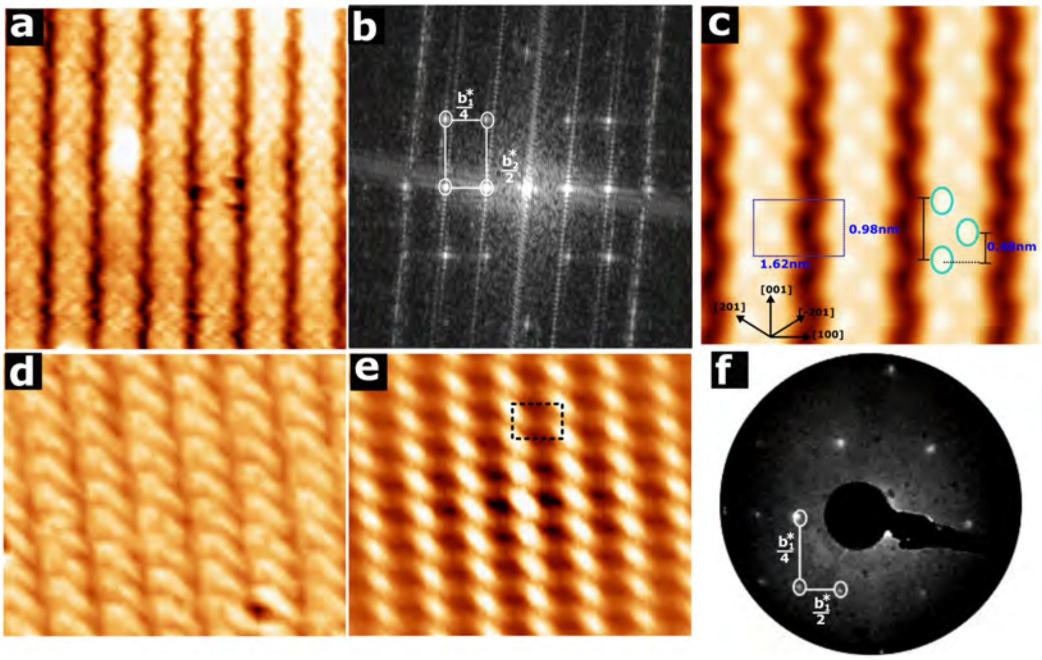

Figure 7.27: (a) 11 nm × 11 nm STM image enlargement of Figure 7.24(a) at positive voltage, showing row alignment along the [001] direction. (b) The FFT function of(a). (c) 12 nm × 12 nm inverse FFT of (a), showing the surface unit cell, labelled with a white rectangle. (d) 11 nm × 9 nm STM image at $V_b = +0.8$ V. (e) An autocorrelation function of the STM image in (d) showing showing the surface unit cell is (4×2). (f) LEED pattern recorded for E = 18.6 eV, corresponding to the FFT pattern in (b).

The terrace B, as shown in Figure 7.23(b) is also, present in Figure 7.28(a). The step height was measured using a histogram is 0.36 ± 0.03 nm. Although the atoms were not resolved, the FFT pattern of the area marked with a black rectangle in Figure 7.28(a) is shown in Figure 7.28(b). The lattice constants a and b are 0.41 ± 0.01 nm and 0.43 ± 0.04 nm, respectively, with an angle of 90° between the two vectors being which confirms the structure as (1×1). The inverse FFT, which reveals the rectangular unit cell of (010), is shown in Figure 7.28(c).

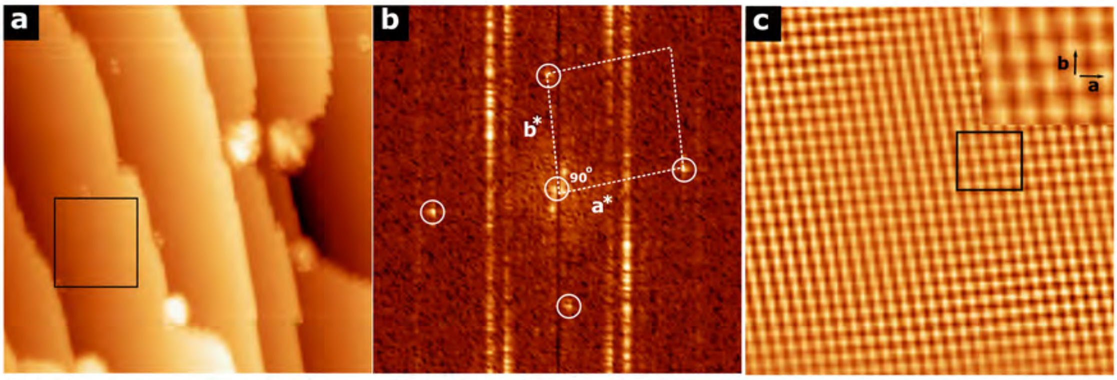

Figure 7.28: (a) 70 nm × 70 nm STM image shows flat terraces of type B, with step height of 3.74 ± 0.05 nm. (b) FFT function of (a) showing the (1×1) unit cell. (c) 11.2 nm × 11.2 nm inverse FFT of (b), showing the surface unit cell.

Discussion

We now discuss a possible explanation for the features observed in the STM image. We will not determine the mechanism of surface reconstruction, but will instead try to find a relationship between the atomic positions of the (010) surface and STM features. The results of XPS were used to understand and support the interpretation of (4×2) structure. Shedwick *et al.* [129] studied the XPS of (100) Ga$_3$Ni$_2$, revealing a Ga to Ni ratio of 50% to 50% after sputtering, which is different from the bulk composition of 60% Ga and 40% Ni. At a low annealing temperature of 310 °C, the concentration of Ga atoms increases by 60%, and is the same as the bulk composition. The amount of Ga increased from 60% to 80% as the annealing temperature increased from 350 °C to 400 °C, with the surface composition being higher than the bulk. After annealing at 400 °C the concentration of Ga increased to 83%.

First, an explanation of the step heights will be presented. Figure 7.29 shows the side view of the arrangement of the (010) planes along the orthogonal [120] direction. The distances between two terminated planes, Ga-rich and Ga-Ni are 0.12 nm and 0.59 nm, respectively. These two separations corresponded to the step heights $d_{(010)} = 0.12 \pm 0.04$ nm and 0.62 nm that were observed in STM images. In addition, these two planes are different in chemical composition, which could be consistent with the STM observations that show the two surfaces differ in atomic composition. The Ga-Ni terminated plane is separated by two distances: 0.47 nm and 0.59 nm. These two separations are close to the step height of (4×2) in A terraces in STM image.

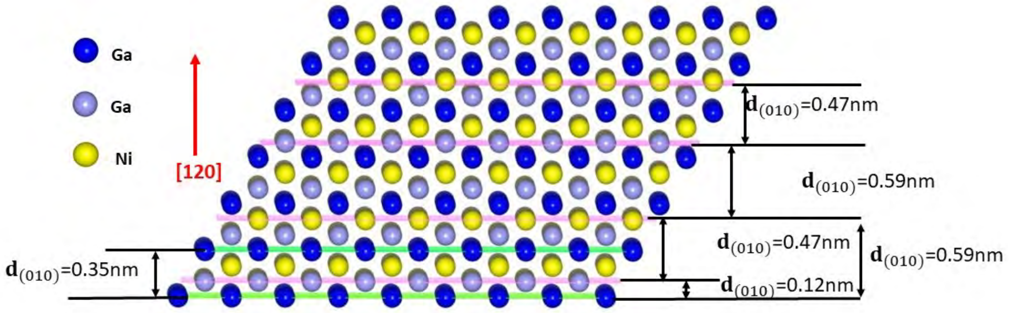

Figure 7.29: The side view of the perpendicular arrangement of the (010) planes along the [120] direction.

In cleaning cycles after sputtering, the surface will be rough, and some Ga atoms will leave the surface. After annealing at 360 °C, the Ga atoms on the surface rearrange to lower the surface energy. Figure 7.30(a) depicts a hypothetical reconstruction-structure model of (010)-(4×2) constructed based on the observed STM features. The Ga, Ni, and omitted Ga in Ga-Ni plane are marked with blue, yellow, and black dots, respectively. The terminated plane contains Ga and Ni atoms. The Ga atom positions are used to construct the (4×2) reconstruction, while the Ni atom positions are ignored. It is found that the spacing between the fifth and the first Ga atoms along the [100] direction is 0.8 nm, which corresponds to the width of the bright rows in the STM data. Meanwhile, the dark rows in the STM image are consistent with missing one row of Ga extending in the [001] direction, highlighted by a column of black circles. Therefore, it is suggested that three rows of Ga atoms form one of the bright columns depicted in the STM image, marked with a black dashed box. The missing row corresponds to the faint column in the STM image. Additionally, the width of a faint column is smaller than that of a bright column, as shown in Figure 7.30(c). It is clear that the centre of the bright protrusions forming the columns in the STM image does not lack an atom. By comparing with the model, it can be observed that the center of the bright protrusion column in the STM image corresponds to the second atom column of the wide column marked with a black dashed box in the model. This suggests that the Ga sites in the second atomic column might not have been removed from their [001] sites. The distance between the centers of the columns is 1.6 nm, which corresponds to the STM observation marked with a black arrow in Figures 7.30(a) and (b). In addition, half of the Ga atoms on both sides of the row are alternately removed. As a result of alternately removing the Ga atoms, two Ga sites are arranged in a zigzag structure along the [201] direction, as indicated by a green arrow in Figure 7.30(a). Figure 7.30(b) shows the omitted Ga atoms in the column, which are marked with a black circle and are removed from Figure 7.30(a) for clarity. The four Ga atoms form an oblique shape, marked with a black oblique in the model. The geometry and orientation of oblique feature corresponds to the bright protrusion shape in the zigzag column in the STM image. The surface unit cell (4×2) is identified in the bulk model and is highlighted with a black rectangle. The separation between the first and fifth Ga atoms along the [100] direction is 1.62 nm. Moreover, the separation between the first and third Ga atoms along [001] direction is 0.98 nm. The separations between bright and dim protrusions and their orientations correspond to the morphology of the row structure in the STM image.

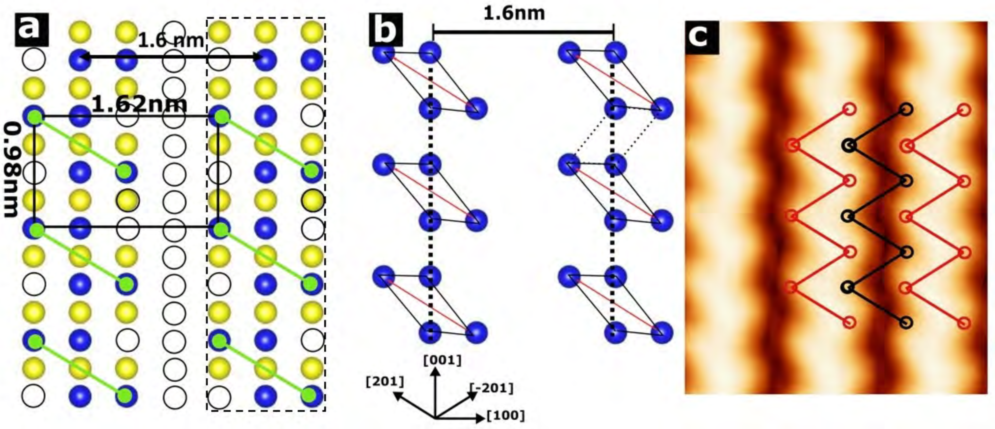

Figure 7.30: (a) Schematic diagrams of the (4×2) model reconstruction. The Ga, Ni, and omitted Ga atoms are marked with blue, yellow, and black dashed circles in the bulk model. (b) same model in(a) after removing the Ni and black circled Ga which do not contribute to the model (4×2). (c) Inverse FFT of(b), with black and red zigzag lines overlaid on bright rows.

7.8 c(2×2) Structure

7.8.1 LEED Pattern and STM Result

STM images are shown in Figures 7.31(a) and (b), which were obtained after sputtering for 20 minutes and annealing at 340 °C for 1:30 hours. The two types of structures revealed are as follows: The first is (4×2), which was previously discussed. The second type of structure is c (2×2), as shown in Figure 7.31(c). The FFT and autocorrelation functions of Figure 7.31(c) are shown in Figures 7.31(d) and (e). The FFT and autocorrelation functions confirm the surface unit cell is c(2×2). The two lattice constants a and b are measured from the autocorrelation function: 1.036 ± 0.04 nm and 0.8 ± 0.03 nm, respectively. Figure 7.32 shows the

LEED pattern taken at an annealing temperature of 360 °C. It confirms the two types of structures that were shown in STM images.

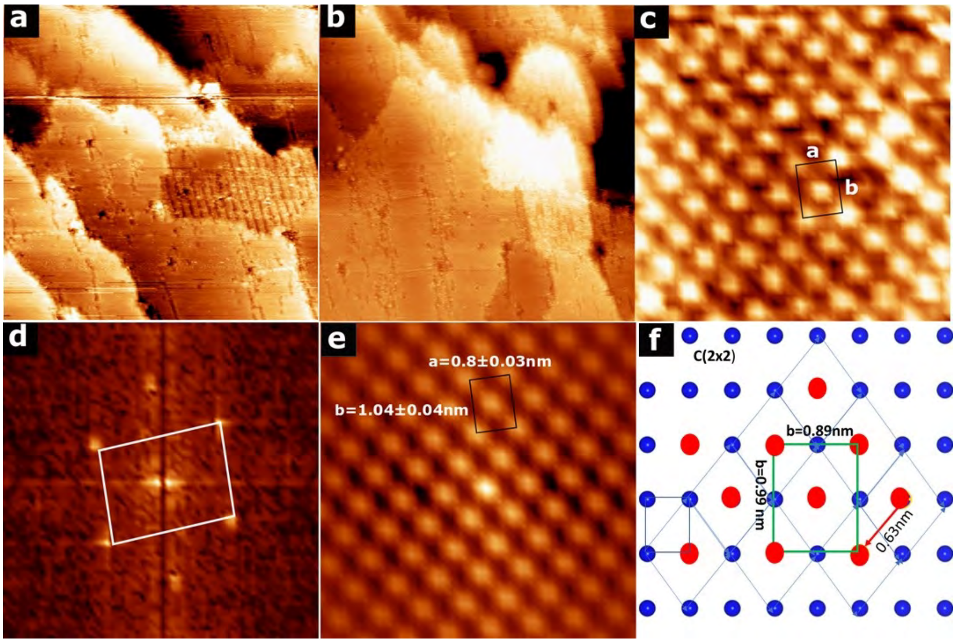

Figure 7.31: (a) 80 nm × 80 nm the STM image at V_b = -1.4 V, displaying both types of structure (4×2) and c(2×2). (b) 80 nm × 80 nm STM image at V_b = 1.2 V. (c) An enlarged area of (b) showing the surface unit cell is the centred rectangle. (d) The FFT pattern of the STM image is shown in (c). (e) The autocorrelation function shows centred rectangle unit cell. Two lattice constants are labelled. (f) A schematic model of atom sites, indicated by red dots. Ga atoms are indicated by dark blue dots.

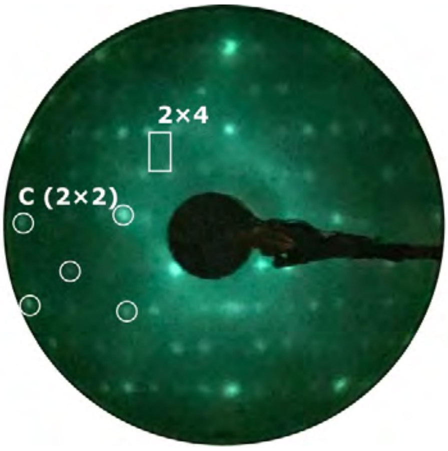

Figure 7.32: LEED pattern taken at annealing temperature = 360 °C and E = 107 eV, showing (4×2) and c(2×2), are labelled.

In order to determine the relationship between the STM image and the (010) plane model, the two have been compared. It was found that the position of the protrusion in the STM corresponds to a position located in the centre of a rhombus. The rhombus and the protrusion site are marked with a blue rhombus and a red dot in Figure 7.31(f). The surface unit cell is a centered rectangle, marked with a green rectangle. The distance between the sites along the [100] and [001] directions is 0.8 nm and 0.99 nm, respectively.

7.9 Dependence of Surface Quality on Annealing Time

The surface was investigated using LEED to study the effect of annealing time on structural transformation. LEED was obtained after sputtering in Ar^+ for 30 minutes and annealing the surface for 90 minutes at T = 360 °C. Annealing was employed to reconstruct the surface of the sample with the aim of obtaining a good crystalline structure. To improve the LEED pattern, we further annealed the sample in 5 cycles using increasing higher temperatures of 380 °C, 400 °C, 420 °C, and 440 °C for 20 minutes. The LEED patterns were obtained for a variety of energies at a range 40-60 eV after each annealing cycle. Figure 7.33 (a-f) depicts the most important LEED patterns.

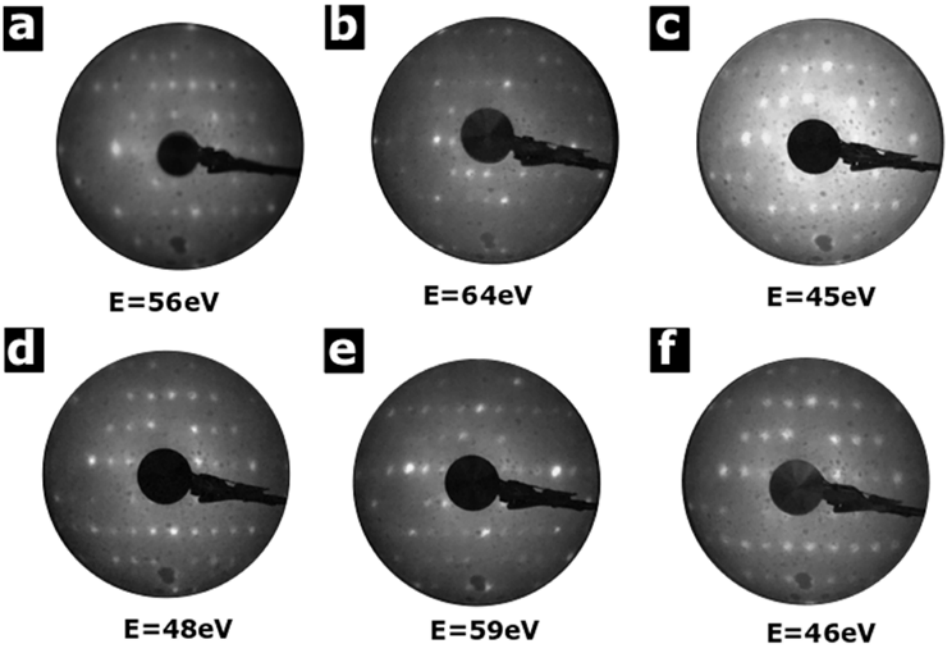

Figure 7.33: LEED patterns of the surface after sputtering for 30 minutes and annealing at (a) annealing temperature = 380 °C for 2 hours. (b) annealing temperature = 400 °C for 20 minutes. (c) and (d) annealing temperature = 420 °C for 20 minutes. (e) and (f) annealing temperature = 440 °C for 20 minutes, LEED pattern, showing the reciprocal space is constant with annealing time after 20 minutes. The surface unit cell is (4×2).

Figure 7.33(a) represents the LEED pattern of the sample annealed at 360 °C. It can be seen that the surface has a (4×2) structure. Figure 7.33(b) to (f) represent the LEED pattern obtained after annealing the sample at 380°C-440 °C for 20 minutes. It was found that the (4×2) pattern of the surface has not changed, and therefore the reconstruction of the surface is preserved. Thus, we conclude that after 5 annealing cycles for 20 minutes, the quality of the surface has not improved and that we have to anneal more than 20 minutes at higher temperature to obtain a visible change of the surface.

The experiment was repeated with a long annealing time at a higher temperature. The sample was sputtered in Ar$^+$ for 40 minutes, then annealed for 2 hours at 400 °C. The LEED pattern was observed at two electron energies, 44 eV and 60 eV. The surface has the structure of (2×1) as expected at this annealing temperature, as shown in Figure 7.34(a). A second annealing at 430 °C for 40 minutes further changes the structure of the surface. The superstructure spots become weaker in the LEED pattern and the structure (1×1) in the reciprocal space appears, as shown in Figure 7.34(b). However, dim spots are observed at a high electron energy, which indicates the surface is (2×1), as shown in Figure 7.34(c). As a result, we suggest that annealing for 40 minutes may partially change the structure of the surface, but it is not enough to create a complete (1×1) structure.

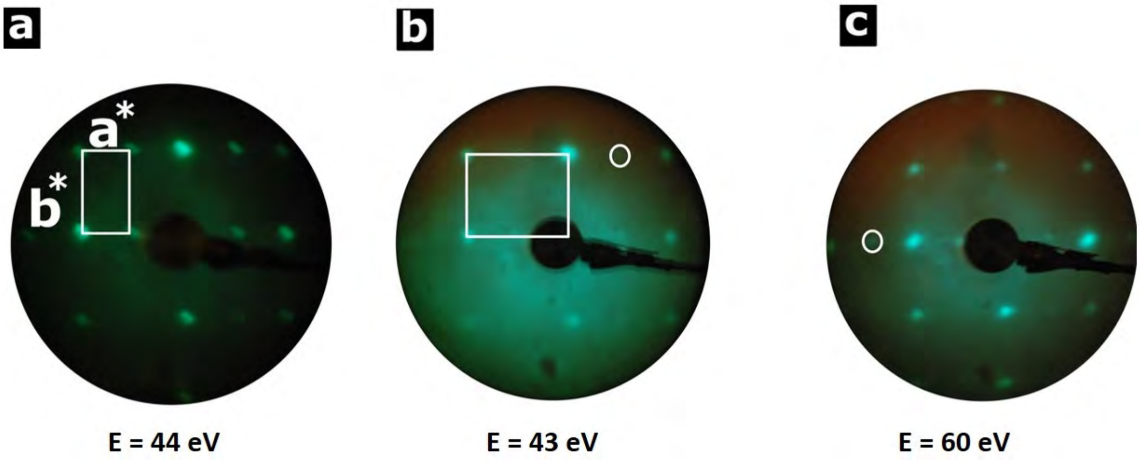

Figure 7.34: LEED pattern of the surface showing (2×1) in the reciprocal space after sputtering for 40 minutes and annealing at (a) T = 400 °C for 2 hours. (b) and (c) The LEED pattern taken after annealing temperature at T = 430 °C for 40 minutes at two beam energies. They show the additional spots are dimmer with a long annealing time.

The LEED pattern shown in Figure 7.35(a) is obtained after annealing temperature at 420 °C for 2 hours. It illustrates the (2×1) structure. Figure 7.35(b) is taken after annealing for 1 hour and 20 minutes. The LEED pattern shows

(1×1). This experience confirm that the annealing time for the surface transfer from (2×1) superstructure to (1×1) is 1 hour and 20 minutes .

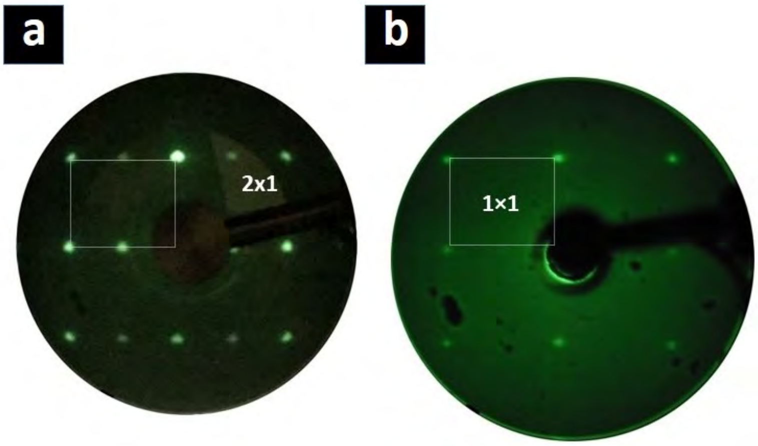

Figure 7.35: (a) and (b) LEED pattern showing after annealing temperature = 460 °C for 1hour and 20 minutes the structure is transfer from (2×1) to (1×1), both LEED pattern at 38 eV.

7.10 Effect of High Annealing Temperature

The effects of annealing time on surface structure were investigated. Figures 7.36(a)-(d) show STM images taken after annealing for 2 hours at 410 °C and 425-430 °C, respectively. The STM image in Figure 7.36(b) shows the clean surface with an atomic structure of (1×1). STM images obtained at the same annealing temperature of 425-430 °C but for a longer annealing time of 3 hours are shown in Figures 7.36(c) and (d). These STM images reveal the appearance of metal clusters growing on the surface, and their size increases with each repetition of the same treatment cycles at the same annealing temperature. However, these clusters were observed only at annealing temperatures higher than 430 °C. The STM images of these clusters are not present here. Therefore, both the annealing time and temperature have an effect on the surface form, structure, and appearance of the metal clusters. However, the LEED patterns taken at annealing temperatures higher than 430°C confirm that the (1×1) surface structure remains constant with increasing annealing temperatures.

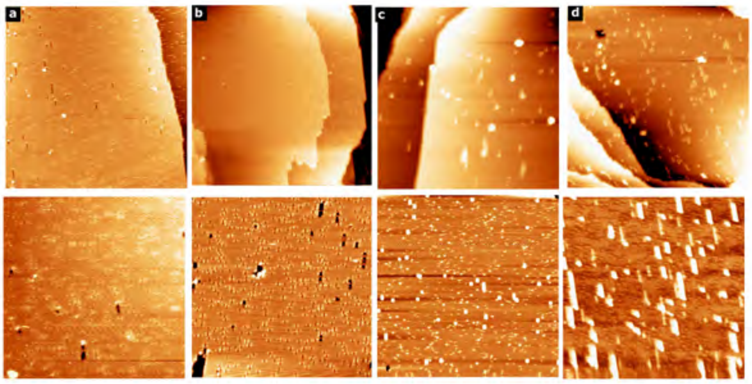

Figure 7.36: STM images taken after increasing annealing time on several treatment cycles. (a) Top: 100 nm × 100 nm STM image taken after annealing temperature 410 °C for 2 hours. Bottom 46 nm × 46 nm STM image no atoms resolve on surface. (b) Top: 80 nm × 80 nm STM image taken after annealing temperature 425-230 °C for 2 hours. Bottom: 50 nm × 50 nm STM image showing the structure (1×1). (c) Top: 80 nm × 80 nm STM image after annealing 3 hours. Bottom: shows no atoms resolved and little material on the surface, 130 nm × 130 nm. (d) Top: 100 nm × 100 nm STM image taken after annealing for 3 hours showing this material increasing with increasing annealing time. Bottom: 50 nm × 50 nm image.

7.11 Conclusions

For the first time, the (010) surface of Ga$_3$Ni$_2$ sample was investigated using STM and LEED. Three surface reconstructions were found, and corresponding models were proposed. The type of surface structure depends on annealing temperature and time. The surface structure changes from (4×2) to (1×1) as the annealing temperature rises. The three types of surface reconstructions were identified at specific annealing temperatures. The initial surface reconstructions (4×2) c(2×2) are formed between annealing temperatures of (366 and 390)°C. The surface with structure (2×1) forms at 390 °C to 420 °C. When the annealing temperature exceeds 430 °C, the final surface structure is (1×1) formed and remains constant with increasing annealing temperature.

High resolution STM images of the three types of structures was obtained. The non-reconstructed (1×1) structure was observed at a voltage range of +0.5 to +1 V after annealing above 420 °C. At annealing temperatures higher than 440 °C, metal clusters grew on the surface.

We demonstrated that for a well-formed (4×2) and c(2×2) structure, annealing at 366 °C for at least 60 minutes is required. The lowest annealing temperature at which the superstructure appeared was 340 °C. Additionally, the three surface structures (4×2), (2×1), and (1×1) were observed on Ga$_3$Ni$_2$(100) using LEED patterns, as shown in Appendix C.

Chapter 8

Summary

The aim of this thesis was to expand the understanding of pentacene (Pn) adsorption on two high-symmetry (two- and three-fold) surfaces of the *i*–Ag–In–Yb quasicrystal, using scanning tunnelling microscopy (STM). The two projects were successful in producing quasicrystalline Pn films. Pn molecules were adsorbed on Yb sites. This is in agreement with the adsorption Pn on the five-fold *i*–Ag–In–Yb quasicrystal [7]. This is attributed to electron transfer from Pn to Yb site, as well as the comparability of the size of Pn molecules with the distance between Yb atoms.

Pn adsorption on a two-fold surface created the diamond features, which are characteristic of substrate symmetry. Triangular motifs, on the other hand, were observed in the Pn film deposited on a three-fold surface. The Fast Fourier Transforms (FFT) and autocorrelation functions of the distribution of Pn molecules showed a two- and six-fold pattern that were located at τ-scaling distances (where τ is the golden mean), indicating the molecules' quasicrystalline order.

The surface of the Au-Al-Gd 1/1 approximant was also investigated in this thesis. The surfaces revealed step/terrace morphology after sputter-annealing cycles. A approximant bulk structures were formed by the same (RTH) clusters that form their parent icosahedral Ag-In-Yb quasicrystals. It was found that the surface is bulk-terminated, and it forms at the bulk planes that cut each icosahedron, an atomic shell of the RTH cluster. Surface of *i*–Ag–In–Yb quasicrystal is also found to bulk terminated. STM images of the surface revealed the structures of various crystallographic orientations, whereas the Ag-In-Yb surface revealed only one surface orientation. The unit cell and step heights in STM images were used to identify various structures in the 1/1 approximant model.

The final project presented in this thesis was the study of $Ga_3Ni_2(010)$ surface. The objective was to determine the surface preparation condition and investigate the effect of annealing temperature on surface structure. The surface was investigated using low-energy electron diffraction (LEED) and scanning tunnelling microscopy (STM). The STM and LEED images confirm four structures occur at specific annealing temperatures. These structures were c(2×2), (4×2), (2×1), and (1×1). The three superstructures were observed at low temperatures, annealing at less than 410 °C. In the temperature range 360-390 °C, c(2×2) and (4×2) structure were obtained. The (2×1) structure was found at the 400-420 °C annealing range. Finally, the (1×1) structure was obtained after annealing at a temperature higher than 430 °C.

Future Studies

The work on the Ga_3Ni_2 crystal project will be expanded to include STM and LEED studies of the interaction of oxygen with the surface. An XPS study of the Ga_3Ni_2 surface under different annealing conditions revealed that the concentration of Ga at the oxidised surface is significantly greater than that of Ni relative to the values of the bulk. STM and LEED studies on the oxidised surface would be helpful to further understand the oxidation behaviour. Furthermore, density of states calculations and STM simulations from Ga_3Ni_2 would be beneficial in confirming whether the surface is Ga-terminated or Ga/Ni-terminated.

Appendix A

List of Publications

- Alofi, A., Burnie, D., Coates, S., McGrath, R. and Sharma, H. R. 2021. Adsorption of Pentacene on the 2–Fold Surface of the Icosahedral Ag–In–Yb Quasicrystal. Materials transactions, 62(3), pp.312-316.
- Sharma, H. R. Coates, S., Alofi, A. and McGrath, R., 2022. Growth of pentacene molecules on Tsai-type quasicrystals and related crystal surfaces. Journal of Vacuum Science & Technology A: Vacuum, Surfaces, and Films, 40(1), p.013211.

Appendix B

Presentations

- Pentacene thin film growth on twofold surface of icosahedral Ag-In-Yb quasicrystal, Surface Science Conference (ISSC-23) 2021, 19th–215th April 2021, Online conference
- Growth Pentacene films on surfaces of icosahedral Ag-In-Yb, Nanoscience@Surfaces Summer School, 25th–85th July 2022, Liverpool, UK.
- Adsorption of pentacene on the 2–fold surface of the icosahedral Ag–In–Yb quasicrystal, ECMetAC Days 2020. 7th–9th December 2020, Online conference.

Appendix C

LEED Observation of Ga_3Ni_2(100)

LEED Pattern

The experiment was repeated on a new sample (100)Ga_3Ni_2 in order to investigate the existence of different types of surface reconstructions that had been previously observed in the sample (010)Ga_3Ni_2. The three LEED patterns that were observed in the sample (010) have been observed in (100)Ga_3Ni_2. The three LEED patterns obtained were: (4×2), (2×1), and (1×1).

A (2×1) LEED pattern was observed after annealing temperature of 460 °C for 2 hours, as shown in Figure C.2. Following this, the surface was annealed at a temperature of 500 °C for 1 hour and 20 minutes at pressure 8 $\times 10^{-9}$ mbar. The LEED pattern shown in Figure C.3 reveals the LEED pattern (1×1). The pressure in the RT-UHV equipment was higher than in the VT-UHV, which may have caused the annealing temperature to rise. However, after annealing at 450 °C and 460 °C the under reduced pressure, (2×1) and (1×1) LEED patterns were obtained, respectively. It is clear that as pressure is reduced, the annealing temperature required for surface reconstruction decreases.

The sample was sputtered for 30 minutes before being annealed for 1 hour and 15 minutes at 388 °C. The LEED pattern a (4×2) surface reconstruction was obtained, as shown in Figure C.1. This annealing temperature for the appearance of the (4×2) surface is the same as that observed for the previous (010) sample. As a result, the LEED confirms the (4×2) reconstruction, which appears at 390 °C .

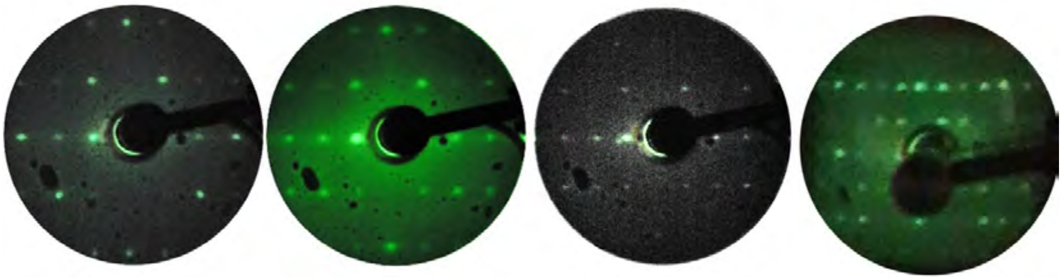

Figure C.1: LEED patterns of the reconstructed (4 × 2) surface after annealing temperature at 388 °C and beam energy (12, 14, 15, 35) eV.

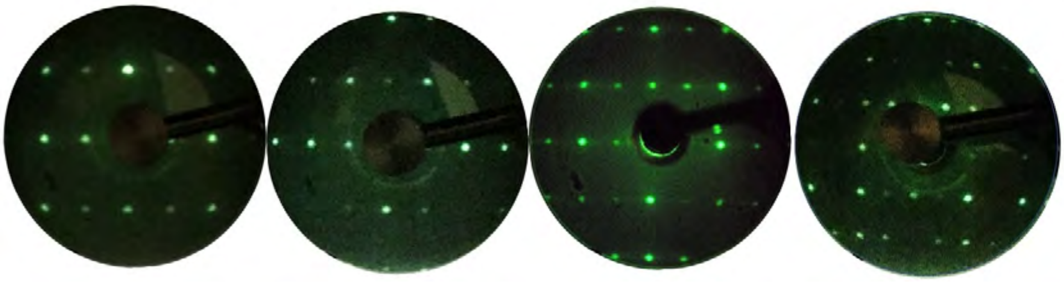

Figure C.2: LEED patterns of the reconstructed (2 × 1) surface after annealing temperature at 460 °C and beam energy (38, 44, 59, 85) eV.

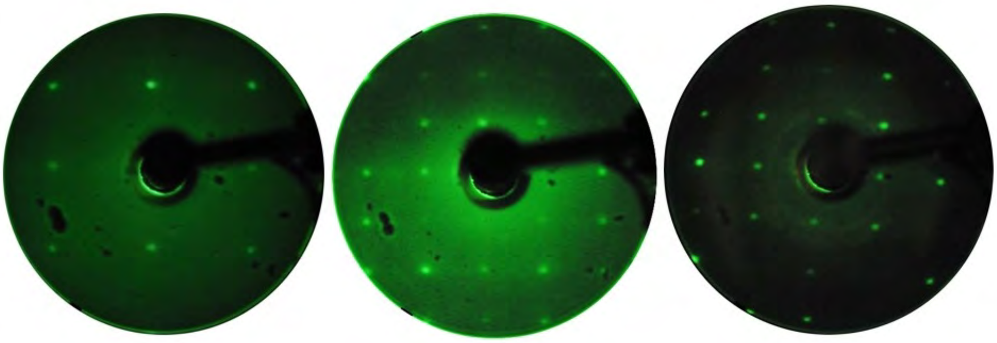

Figure C.3: LEED patterns of the (1 × 1) surface after annealing temperature at 500 °C and beam energy (34, 100, 121) eV.

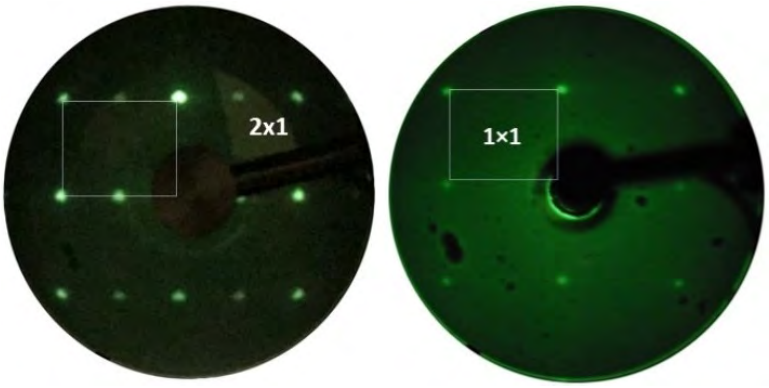

Figure C.4: Left LEED pattern showing after annealing temperature = 460 °C for 2 hour and right LEED pattern after annealing temperature = 500 °C for 1 hour and 20 minutes. The structure is transfer from (2 × 1) to (1 × 1), both LEED pattern at 38 eV .

Bibliography

[1] D. Shechtman, I. Blech, D. Gratias, and J. W. Cahn, "Metallic phase with long-range orientational order and no translational symmetry," *Physical Review Letters*, vol. 53, no. 20, p. 1951, 1984.

[2] D. Levine and P. J. Steinhardt, "Quasicrystals: a new class of ordered structures," *Physical Review Letters*, vol. 53, no. 26, p. 2477, 1984.

[3] S. Förster, K. Meinel, R. Hammer, M. Trautmann, and W. Widdra, "Quasicrystalline structure formation in a classical crystalline thin-film system," *Nature*, vol. 502, no. 7470, p. 215, 2013.

[4] H. Sharma, M. Shimoda, and A. Tsai, "Quasicrystal surfaces: structure and growth of atomic overlayers," *Advances in Physics*, vol. 56, no. 3, pp. 403–464, 2007.

[5] R. McGrath, J. Ledieu, E. J. Cox, and R. D. Diehl, "Quasicrystal surfaces: structure and potential as templates," *Journal of Physics: Condensed Matter*, vol. 14, no. 4, p. R119, 2002.

[6] H. Sharma, S. Coates, A. Alofi, and R. McGrath, "Growth of pentacene molecules on Tsai-type quasicrystals and related crystal surfaces," *Journal of Vacuum Science & Technology A: Vacuum, Surfaces, and Films*, vol. 40, no. 1, p. 013211, 2022.

[7] J. Smerdon, K. Young, M. Lowe, S. Hars, T. Yadav, D. Hesp, V. Dhanak, A. Tsai, H. Sharma, and R. McGrath, "Templated quasicrystalline molecular ordering," *Nano Letters*, vol. 14, no. 3, pp. 1184–1189, 2014.

[8] S. Coates, K. Nozawa, M. Fukami, K. Inagaki, M. Shimoda, R. McGrath, H. R. Sharma, and R. Tamura, "Atomic structure of the (111) surface of the antiferromagnetic 1/1 Au-Al-Tb approximant," *Physical Review B*, vol. 102, no. 23, p. 235419, 2020.

[9] S. Yoshida, S. Suzuki, T. Yamada, T. Fujii, A. Ishikawa, and R. Tamura, "Antiferromagnetic order survives in the higher-order quasicrystal approximant," *Physical Review B*, vol. 100, no. 18, p. 180409, 2019.

[10] A. Ishikawa, T. Hiroto, K. Tokiwa, T. Fujii, and R. Tamura, "Composition-driven spin glass to ferromagnetic transition in the quasicrystal approximant Au-Al-Gd," *Physical Review B*, vol. 93, no. 2, p. 024416, 2016.

[11] A. Ishikawa, T. Fujii, T. Takeuchi, T. Yamada, Y. Matsushita, and R. Tamura, "Antiferromagnetic order is possible in ternary quasicrystal approximants," *Physical Review B*, vol. 98, no. 22, p. 220403, 2018.

[12] H. Takakura, C. P. Gómez, A. Yamamoto, M. de Boissieu, and A. P. Tsai, "Atomic structure of the binary icosahedral Yb–Cd quasicrystal," *Nature materials*, vol. 6, no. 1, p. 58, 2007.

[13] M. Armbrüster, R. Schlögl, and Y. Grin, "Intermetallic compounds in heterogeneous catalysis—a quickly developing field," *Science and Technology of Advanced Materials*, 2014.

[14] V. Fournée, A. Ross, T. A. Lograsso, J. W. Anderegg, C. Dong, M. Kramer, I. Fisher, P. C. Canfield, and P. A. Thiel, "Surface structures of approximant phases in the Al-Pd-Mn system," *Physical Review B*, vol. 66, no. 16, p. 165423, 2002.

[15] S. Burkov, "Structure model of the Al-Cu-Co decagonal quasicrystal," in *Physics and Chemistry of Finite Systems: From Clusters to Crystals*, pp. 77–83, Springer, 1992.

[16] L. Bendersky, "Quasicrystal with one-dimensional translational symmetry and a tenfold rotation axis," *Physical Review Letters*, vol. 55, no. 14, p. 1461, 1985.

[17] Z. Mai, L. Xu, N. Wang, K. Kuo, Z. Jin, and G. Cheng, "Effect of phason strain on the transition of an octagonal quasicrystal to a β-mn-type structure," *Physical Review B*, vol. 40, no. 18, p. 12183, 1989.

[18] J. Jiang, K. Fung, and K. Kuo, "Discommensurate microstructures in phason-strained octagonal quasicrystal phases of Mo-Cr-Ni," *Physical Review Letters*, vol. 68, no. 5, p. 616, 1992.

[19] Q. Yang and W. Wei, "Description of the dodecagonal quasicrystal by a projection method," *Physical Review Letters*, vol. 58, no. 10, p. 1020, 1987.

[20] H. Chen, D. Li, and K. Kuo, “New type of two-dimensional quasicrystal with twelvefold rotational symmetry,” *Physical Review Letters*, vol. 60, no. 16, p. 1645, 1988.

[21] A. Thiel, P, “Progress in Surface Science,” no. 75, pp. 69–89, 2004.

[22] A. P. Tsai, “Discovery of stable icosahedral quasicrystals: progress in understanding structure and properties,” *Chemical Society Reviews*, vol. 42, no. 12, pp. 5352–5365, 2013.

[23] B. Grfinbaum and G. Shephard, “Tilings and patterns,” 1987.

[24] H. R. Sharma, *thesis*. Freie Universit (Berlin), 2011.

[25] A. Yamamoto and K. Ishihara, “Penrose patterns and related structures. ii. decagonal quasicrystals,” *Acta Crystallographica Section A: Foundations of Crystallography*, vol. 44, no. 5, pp. 707–714, 1988.

[26] P. J. Nugent, *Surfaces of the icosahedral Ag-In-Yb quasicrystal: structure, reactivity and thin film growth*. The University of Liverpool (United Kingdom), 2011.

[27] R. Li, Z. Li, Z. Dong, and K. A. Khor, “A review of transmission electron microscopy of quasicrystals-how are atoms arranged?,” *Crystals*, vol. 6, no. 9, p. 105, 2016.

[28] C. Cui, P. Nugent, M. Shimoda, J. Ledieu, V. Fournée, A. Tsai, R. McGrath, and H. Sharma, “The atomic structure of the threefold surface of the icosahedral Ag–In–Yb quasicrystal,” *Journal of Physics: Condensed Matter*, vol. 24, no. 44, p. 445011, 2012.

[29] A. Tsai, A. Inoues, Y. Yokoyama, and T. Masumoto, “New icosahedral alloys with superlattice order in the Al–Pd–Mn system prepared by rapid solidification,” *Philosophical Magazine Letters*, vol. 61, no. 1, pp. 9–14, 1990.

[30] U. Mizutani, “Hume-rothery rules for structurally complex alloy phases,” *MRS Bulletin*, vol. 37, no. 2, p. 169, 2012.

[31] T. Ishimasa, “New group of icosahedral quasicrystals,” in *Handbook of Metal Physics*, vol. 3, pp. 49–74, Elsevier, 2008.

[32] T. Fujiwara and Y. Ishii, *Quasicrystals*, vol. 3. Elsevier, 2007.

[33] J. Guo, E. Abe, and A., “Tsai,Phys. Rev,” vol. 62, pp. 605–608, 2000.

[34] J. Guo and A. Tsai, “Stable icosahedral quasicrystals in the Ag-In-Ca, Ag-In-Yb, Ag-In-Ca-Mg and Ag-In-Yb-Mg systems,” *Philosophical Magazine Letters*, vol. 82, no. 6, pp. 349–352, 2002.

[35] C. Cui and A. P. Tsai, “Growth of large-grain Ag–In–Yb icosahedral quasicrystals and approximant crystals,” *Journal of Alloys and Compounds*, vol. 536, pp. 91–93, 2012.

[36] A. P. Tsai, J. Guo, E. Abe, H. Takakura, and T. J. Sato, “A stable binary quasicrystal,” *Nature*, vol. 408, no. 6812, pp. 537–538, 2000.

[37] J. Guo, E. Abe, and A. Tsai, “Stable icosahedral quasicrystals in binary Cd-Ca and Cd-Yb systems,” *Physical Review B*, vol. 62, no. 22, p. R14605, 2000.

[38] C. P. Gómez and S. Lidin, “Comparative structural study of the disordered MCd_6 quasicrystal approximants,” *Physical Review B*, vol. 68, no. 2, p. 024203, 2003.

[39] A. Goldman and R. Kelton, “Quasicrystals and crystalline approximants,” *Reviews of Modern Physics*, vol. 65, no. 1, p. 213, 1993.

[40] K. Franke, H. Sharma, W. Theis, P. Gille, P. Ebert, and K. Rieder, “Quasicrystalline epitaxial single element monolayers on icosahedral Al-Pd-Mn and decagonal Al-Ni-Co quasicrystal surfaces,” *Physical Review Letters*, vol. 89, no. 15, p. 156104, 2002.

[41] C. Janot, *Quasicrystals.* (Grenbole-France), 2nd ed., 1944.

[42] T. Ishimasa, Y. Tanaka, and S. Kashimoto, “Icosahedral quasicrystal and 1/1 cubic approximant in Au–Al–Yb alloys,” *Philosophical Magazine*, vol. 91, no. 33, pp. 4218–4229, 2011.

[43] Y. G. So, K. Kimoto, and K. Edagawa, “Formation of an icosahedral quasicrystal and its approximant in Au-Al-Sc system,” *Materials Transactions*, vol. 56, no. 4, pp. 495–499, 2015.

[44] S. Matsukawa, K. Tanaka, M. Nakayama, K. Deguchi, K. Imura, H. Takakura, S. Kashimoto, T. Ishimasa, and N. K. Sato, “Valence change driven by constituent element substitution in the mixed-valence quasicrystal and approximant Au–Al–Yb,” *Journal of the Physical Society of Japan*, vol. 83, no. 3, p. 034705, 2014.

[45] J. Ruan, K. Kuo, J. Guo, and A. P. Tsai, “Crystalline phases displaying pseudo-icosahedral symmetry in $Ag_{42}In_{42}RE_{16}$(RE=Gd, Tb, Dy, Ho, ER, Tm, Yb, and Lu),” *Journal of Alloys and Compounds*, vol. 370, no. 1-2, pp. L23–L27, 2004.

[46] G. H. Gebresenbut, R. Tamura, D. Eklöf, and C. P. Gómez, “Syntheses optimization, structural and thermoelectric properties of 1/1 tsai-type quasicrystal approximants in RE–Au–SM systems (RE=Yb, Gd and SM=Si, Ge),” *Journal of Physics: Condensed Matter*, vol. 25, no. 13, p. 135402, 2013.

[47] G. H. Gebresenbut, M. S. Andersson, P. Nordblad, M. Sahlberg, and C. Pay Gomez, “Tailoring magnetic behavior in the Tb-Au-Si quasicrystal approximant system,” *Inorganic Chemistry*, vol. 55, no. 5, pp. 2001–2008, 2016.

[48] Q. Lin and J. D. Corbett, “M3 (Au, Ge) 19 and M3. 25 (Au, Ge) 18 (M=Ca, Yb): Distinctive phase separations driven by configurational disorder in cubic YCd_6-type derivatives,” *Inorganic Chemistry*, vol. 49, no. 10, pp. 4570–4577, 2010.

[49] Y. Morita and A. P. Tsai, “Approximants in the Ag–In–M and Au–Sn–M (M=Ca or rare earth metals) systems,” *Japanese Journal of Applied Physics*, vol. 47, no. 10R, p. 7975, 2008.

[50] P. Boulet, D. Mazzone, H. Noel, P. Rogl, and R. Ferro, “Phase equilibria and magnetic studies in the ternary system Ce–Au–Sn,” *Journal of Alloys and Compounds*, vol. 317, pp. 350–356, 2001.

[51] Q. Lin and J. D. Corbett, “Approximant phases and an icosahedral quasicrystal in the Ca-Au-Ga system: The influence of size of gallium versus indium,” *Inorganic Chemistry*, vol. 47, no. 17, pp. 7651–7659, 2008.

[52] H. R. Sharma, M. Shimoda, K. Sagisaka, H. Takakura, J. Smerdon, P. Nugent, R. McGrath, D. Fujita, S. Ohhashi, and A. Tsai, “Structure of the fivefold surface of the Ag-In-Yb icosahedral quasicrystal,” *Physical Review B*, vol. 80, no. 12, p. 121401, 2009.

[53] C. Cui, P. Nugent, M. Shimoda, J. Ledieu, V. Fournée, A. Tsai, R. McGrath, and H. Sharma, “Structure of the twofold surface of the icosahedral Ag–In–Yb quasicrystal,” *Journal of Physics: Condensed Matter*, vol. 26, no. 1, p. 015001, 2013.

[54] C. Cui, M. Shimoda, and A. P. Tsai, “Studies on icosahedral Ag–In–Yb: a prototype for Tsai-type quasicrystals,” *RSC Advances*, vol. 4, no. 87, pp. 46907–46921, 2014.

[55] D. Burnie, S. Coates, R. McGrath, and H. R. Sharma, “Bias-voltage dependent stm images from the 2–fold surface of the icosahedral Ag-In-Yb quasicrystal,” in *Journal of Physics: Conference Series*, vol. 1458, p. 012017, IOP Publishing, 2020.

[56] S. Coates, S. Thorn, R. McGrath, H. R. Sharma, and A. P. Tsai, “Unique growth mode observed in a Pb thin film on the threefold surface of an i-Ag-In-Yb quasicrystal,” *Physical Review Materials*, vol. 4, no. 2, p. 026003, 2020.

[57] J. Ledieu, C. Muryn, G. Thornton, R. Diehl, T. Lograsso, D. Delaney, and R. McGrath, “C_{60} adsorption on the quasicrystalline surface of $Al_{70}Pd_{21}Mn_9$,” *Surface Science*, vol. 472, no. 1-2, pp. 89–96, 2001.

[58] V. Fournée, É. Gaudry, J. Ledieu, M.-C. De Weerd, D. Wu, and T. Lograsso, “Self-organized molecular films with long-range quasiperiodic order,” *ACS Nano*, vol. 8, no. 4, pp. 3646–3653, 2014.

[59] J. A. Smerdon, L. H. Wearing, J. Parle, L. Leung, H. R. Sharma, J. Ledieu, and R. Mcgrath, “Ordering of adsorbed species on quasicrystal surfaces,” *Philosophical Magazine*, vol. 88, no. 13-15, pp. 2073–2082, 2008.

[60] S. Coates, R. McGrath, and H. R. Sharma, “4-fold quasicrystalline molecular overlayer,” 2018. Submitted for Publication.

[61] H. R. Sharma, J. Smerdon, P. Nugent, A. Ribeiro, I. McLeod, V. Dhanak, M. Shimoda, A. Tsai, and R. McGrath, “Crystalline and quasicrystalline allotropes of Pb formed on the fivefold surface of icosahedral Ag-In-Yb,” *The Journal of Chemical Physics*, vol. 140, no. 17, p. 174710, 2014.

[62] P. J. Nugent, J. Smerdon, R. Mcgrath, M. Shimoda, C. Cui, A. P. Tsai, and H. R. Sharma, “Step-terrace morphology and reactivity to C_{60} of the five-fold icosahedral Ag–In–Yb quasicrystal,” *Philosophical Magazine*, vol. 91, no. 19-21, pp. 2862–2869, 2011.

[63] N. Kalashnyk, J. Ledieu, É. Gaudry, C. Cui, A. P. Tsai, and V. Fournée, “Building 2d quasicrystals from 5-fold symmetric corannulene molecules,” *Nano Research*, pp. 2129–2138, 2018.

[64] J. Smerdon, J. Parle, L. Wearing, L. Leung, T. A. Lograsso, A. R. Ross, and R. McGrath, “C60 adsorption on an aperiodically modulated Cu surface,” in *Journal of Physics: Conference Series*, vol. 226, p. 012006, IOP Publishing, 2010.

[65] J. Y. Park, D. Ogletree, M. Salmeron, R. Ribeiro, P. C. Canfield, C. J. Jenks, and P. A. Thiel, “Elastic and inelastic deformations of ethylene-passivated tenfold decagonal Al-Ni-Co quasicrystal surfaces,” *Physical Review B*, vol. 71, no. 14, p. 144203, 2005.

[66] J. Hoeft, J. Ledieu, S. Haq, T. Lograsso, A. Ross, and R. Mcgrath, “A dsorption of benzene on the five-fold surface of the quasicrystal,” *Philosophical Magazine*, vol. 86, no. 6-8, pp. 869–874, 2006.

[67] H. Kroto, “C60B buckminsterfullerene, other fullerenes and the icospiral shell,” *Computers & Mathematics with Applications*, vol. 17, no. 1-3, pp. 417–423, 1989.

[68] G. Portella, J. Poater, J. M. Bofill, P. Alemany, and M. Sola, “Local aromaticity of [n] acenes,[n] phenacenes, and [n] helicenes (n= 1- 9),” *The Journal of Organic Chemistry*, vol. 70, no. 7, pp. 2509–2521, 2005.

[69] P. Puschnig, E.-M. Reinisch, T. Ules, G. Koller, S. Soubatch, M. Ostler, L. Romaner, F. S. Tautz, C. Ambrosch-Draxl, and M. G. Ramsey, “Orbital tomography: Deconvoluting photoemission spectra of organic molecules,” *Physical Review B*, vol. 84, no. 23, p. 235427, 2011.

[70] J. Smerdon, M. Bode, N. Guisinger, and J. Guest, “Monolayer and bilayer pentacene on cu (111),” *Physical Review B*, vol. 84, no. 16, p. 165436, 2011.

[71] F. J. M. Zu Heringdorf, M. Reuter, and R. Tromp, “The nucleation of pentacene thin films,” *Applied Physics A*, vol. 78, no. 6, pp. 787–791, 2004.

[72] K. Müller, A. Kara, T. K. Kim, R. Bertschinger, A. Scheybal, J. Osterwalder, and T. A. Jung, “Multimorphism in molecular monolayers: Pentacene on cu (110),” *Physical Review B*, vol. 79, no. 24, p. 245421, 2009.

[73] S. Coates, R. McGrath, H. R. Sharma, and R. Tamura, “Pentacene growth on the (111) surface of the 1/1 Au-Al-Tb approximant: Influence of surface geometry on adsorption,” *Physical Review Materials*, vol. 5, no. 7, p. 076002, 2021.

[74] Y. W. Chung, *Practical guide to surface science and spectroscopy.* Academic Press, 2001.

[75] J. Venables, *Introduction to surface and thin film processes.* Cambridge University Press, 2000.

[76] A. Chambers, *Basic Vacuum Technology.* CRC Press, 1998.

[77] K. Oura, V. Lifshits, A. Saranin, A. Zotov, and M. Katayama, *Surface Science: an introduction.* Springer Science & Business Media, 2013.

[78] S. Hars, *Surface structure and epitaxy on Ag-In-Rare earth quasicrystals and related approximants.* The University of Liverpool (United Kingdom), 2015.

[79] A. P. Tsai and C. Cui, "Crystal growth of quasicrystals," in *Handbook of Crystal Growth*, pp. 1113–1156, Elsevier, 2015.

[80] J. Repp, G. Meyer, S. M. Stojković, A. Gourdon, and C. Joachim, "Molecules on insulating films: scanning-tunneling microscopy imaging of individual molecular orbitals," *Physical Review Letters*, vol. 94, no. 2, p. 026803, 2005.

[81] J. Czochralski, "Ein neues verfahren zur messung der kristallisationsgeschwindigkeit der metalle," *Zeitschrift für Physikalische Chemie*, vol. 92, no. 1, pp. 219–221, 1918.

[82] P. W. Bridgman, "Certain physical properties of single crystals of tungsten, antimony, bismuth, tellurium, cadmium, zinc, and tin," in *Collected Experimental Papers, Volume III*, pp. 1851–1932, Harvard University Press, 2013.

[83] H. R. Trebin, *Quasicrystals: Structure and Physical Properties.* John Wiley & Sons, 2003.

[84] L. Michael, *Surface Studies of Model Intermetallic Catalysts.* The University of Liverpool (United Kingdom), 2015.

[85] H. R. Sharma, M. Shimoda, S. Ohhashi, and A. P. Tsai, "First UHV surface studies of single-grain icosahedral Ag–In–Yb quasicrystal," *Philosophical Magazine*, vol. 87, no. 18-21, pp. 2989–2994, 2007.

[86] S. Günther, B. Kaulich, L. Gregoratti, and M. Kiskinova, "Photoelectron microscopy and applications in surface and materials science," *Progress in Surface Science*, vol. 70, no. 4-8, pp. 187–260, 2002.

[87] R. J. Tilley, *Crystals and Crystal Structures.* John Wiley & Sons, 2020.

[88] P. M. Chaikin, T. C. Lubensky, and T. A. Witten, *Principles of condensed matter physics*, vol. 10. Cambridge University Press, 1995.

[89] D. C. Grinter, *Surface studies of metal oxide catalysts and ultrathin films.* PhD thesis, UCL (University College London), 2011.

[90] G. Binnig, H. Rohrer, C. Gerber, and E. Weibel, "Tunneling through a controllable vacuum gap," *Applied Physics Letters*, vol. 40, no. 2, pp. 178–180, 1982.

[91] R. H. Fowler and L. Nordheim, "Electron emission in intense electric fields," *Proceedings of the Royal Society of London. Series A, Containing Papers of a Mathematical and Physical Character*, vol. 119, no. 781, pp. 173–181, 1928.

[92] J. A. Stroscio and W. J. Kaiser, *Scanning tunneling microscopy*, vol. 27. Academic press, 1993.

[93] B. Voigtländer, *Atomic force microscopy.* Springer, 2019.

[94] N. Koch, N. Ueno, and A. T. Wee, *The molecule-metal interface.* Wiley Online Library, 2013.

[95] T. A. Pham, *Constructing low-dimensional molecular networks on metal surfaces.* PhD thesis, University of Groningen, 2016.

[96] I. Horcas, R. Fernández, J. Gomez-Rodriguez, J. Colchero, J. Gómez-Herrero, and A. Baro, "Wsxm: A software for scanning probe microscopy and a tool for nanotechnology," *Review of scientific instruments*, vol. 78, no. 1, p. 013705, 2007.

[97] D. Nečas and P. Klapetek, "Gwyddion: an open-source software for spm data analysis," *Open Physics*, vol. 10, no. 1, pp. 181–188, 2012.

[98] NVIDIA Corporation, "Nvidia VPI FFT algorithm documentation." `https://docs.nvidia.com/vpi/algo_fft.html`, 2021.

[99] T. A. Ell, N. Le Bihan, and S. J. Sangwine, *Quaternion Fourier transforms for signal and image processing.* John Wiley & Sons, 2014.

[100] R. Heilbronner and S. Barrett, *Image analysis in earth sciences: microstructures and textures of earth materials*, vol. 129. Springer Science & Business Media, 2013.

[101] S. Ohhashi, J. Hasegawa, S. Takeuchi, and A. Tsai, "Crystal growth of quasicrystal and partial phase diagram involving quasicrystal in the Ag–In–Yb system," *Philosophical Magazine*, vol. 87, no. 18-21, pp. 3089–3094, 2007.

[102] S. Coates, K. Nozawa, K. Sagisaka, T. Kusawake, R. McGrath, H. R. Sharma, and R. Tamura, "Statistical approach to chemical identification in stm from complex alloy materials," pp. 1–9.

[103] C. P. Gomez *(private communication).*

[104] P. Kählitz, M. Schoen, and H. Stark, "Clustering and mobility of hard rods in a quasicrystalline substrate potential," *The Journal of Chemical Physics*, vol. 137, no. 22, p. 224705, 2012.

[105] J. Lagoute, K. Kanisawa, and S. Fölsch, "Manipulation and adsorption-site mapping of single pentacene molecules on Cu (111)," *Physical Review B*, vol. 70, no. 24, p. 245415, 2004.

[106] C. Chavy, C. Joachim, and A. Altibelli, "Chem. Phys. Lett," *Chemical. Physics. Letters*, vol. 214, p. 569, 1993.

[107] J. E. Anthony, "The larger acenes: versatile organic semiconductors," *Angewandte Chemie International Edition*, vol. 47, no. 3, pp. 452–483, 2008.

[108] S. Coates, *Quasicrystal systems with simple symmetries.* PhD thesis, University of Liverpool, 2019.

[109] Y. Ishii and T. Fujiwara, "Hybridization mechanism for cohesion of Cd-based quasicrystals," *Physical Review Letters*, vol. 87, no. 20, p. 206408, 2001.

[110] H. Sharma, G. Simutis, V. Dhanak, P. Nugent, C. Cui, M. Shimoda, R. McGrath, A. Tsai, and Y. Ishii, "Valence band structure of the icosahedral Ag-In-Yb quasicrystal," *Physical Review B*, vol. 81, no. 10, p. 104205, 2010.

[111] "See supplemental material at http://link.aps.org/supplemental/10.1103/physrevb.98.220403 for the powder x-ray diffraction patterns for the $Au_{73}Al_{13}Gd_{14}$ and $Au_{73}Al_{14}Tb_{14}$ compounds. in addition, we have listed the detailed structural information on both compounds obtained from the structural refinements.,"

[112] K. Nozawa and Y. Ishii, "Electronic structures and stability of Ag-In-Ca surfaces," in *Journal of Physics: Conference Series*, vol. 226, p. 012030, IOP Publishing, 2010.

[113] S. Hars, H. Sharma, J. Smerdon, T. Yadav, A. Al-Mahboob, J. Ledieu, V. Fournée, R. Tamura, and R. McGrath, "Surface structure of the Ag-In-(rare earth) complex intermetallics," *Physical Review B*, vol. 93, no. 20, p. 205428, 2016.

[114] K. Deguchi, M. Nakayama, S. Matsukawa, K. Imura, K. Tanaka, T. Ishimasa, and N. K. Sato, "Crystal structure of superconducting 1/1 cubic Au–Ge–Yb approximant with Tsai-type Cluster," *Journal of the Physical Society of Japan*, vol. 84, no. 1, p. 015002, 2015.

[115] S. Hars, *Surface structure and epitaxy on Ag-In-Rare earth quasicrystals and related approximants.* The University of Liverpool (United Kingdom), 2015.

[116] M. Armbrüster, K. Kovnir, Y. Grin, and R. Schlögl, "Complex metallic phases in catalysis," in *Complex Metallic Alloys-Fundamentals and Applications*, pp. 385–400, Wiley-VCH, 2010.

[117] H. Arnold, F. Dobert, J. Gaube, G. Ertl, H. Knozinger, and J. Weitkempl, "Handbook of Heterogeneous Catalysis," *Ertl, G., Knoezinger, H., Weitkamp, J., Eds*, pp. 2165–2186, 2008.

[118] F. Studt, I. Sharafutdinov, F. Abild-Pedersen, C. F. Elkjær, J. S. Hummelshøj, S. Dahl, I. Chorkendorff, and J. K. Nørskov, "Discovery of a Ni-Ga catalyst for carbon dioxide reduction to methanol," *Nature Chemistry*, vol. 6, no. 4, pp. 320–324, 2014.

[119] A. Arico, S. Srinivasan, and V. Antonucci, "Dmfcs: from fundamental aspects to technology development," *Fuel Cells*, vol. 1, no. 2, pp. 133–161, 2001.

[120] I. Sharafutdinov, C. F. Elkjær, H. W. P. de Carvalho, D. Gardini, G. L. Chiarello, C. D. Damsgaard, J. B. Wagner, J. D. Grunwaldt, S. Dahl, and I. Chorkendorff, "Intermetallic compounds of Ni and Ga as catalysts for the synthesis of methanol," *Journal of Catalysis*, vol. 320, pp. 77–88, 2014.

[121] H. Okamoto, "Ga-Ni (gallium-nickel)," *Journal of Phase Equilibria and Diffusion*, vol. 31, no. 6, pp. 575–576, 2010.

[122] C. Schmetterer, H. Flandorfer, C. L. Lengauer, J.-P. Bros, and H. Ipser, "The system Ga–Ni: A new investigation of the Ga-rich part," *Intermetallics*, vol. 18, no. 2, pp. 277–285, 2010.

[123] E. Hellner and F. Laves, “Kristallchemie des In und Ga in legierungen mit einigen übergangselementen (NI, PD, PT, CU, AG und AU),” *Zeitschrift für Naturforschung A*, vol. 2, no. 3, pp. 177–184, 1947.

[124] M. Wencka, M. Pillaca, and P. Gille, “Single crystal growth of Ga_3Ni_2 by the Czochralski method,” *Journal of Crystal Growth*, vol. 449, pp. 114–118, 2016.

[125] M. Wencka, J. Kovač, V. D. Dasireddy, B. Likozar, A. Jelen, S. Vrtnik, P. Gille, H. J. Kim, and J. Dolinšek, “The effect of surface oxidation on the catalytic properties of Ga_3Ni_2intermetallic compound for carbon dioxide reduction,” *Journal of Analytical Science and Technology*, vol. 9, no. 1, pp. 1–10, 2018.

[126] S. S. Kim, H. H. Lee, and S. C. Hong, “The effect of the morphological characteristics of TiO_2 supports on the reverse water–gas shift reaction over $PtTiO_2$ catalysts,” *Applied Catalysis B: Environmental*, vol. 119, pp. 100–108, 2012.

[127] S. S. Kim, K. H. Park, and S. C. Hong, “A study of the selectivity of the reverse water–gas-shift reaction over Pt/TiO_2 catalysts,” *Fuel processing technology*, vol. 108, pp. 47–54, 2013.

[128] P. Gille and B. Bauer, “Single crystal growth of $Al_{13}Co_4$ and $Al_{13}Fe_4$ from Al-rich solutions by the czochralski method,” *Crystal Research and Technology: Journal of Experimental and Industrial Crystallography*, vol. 43, no. 11, pp. 1161–1167, 2008.

[129] O. Shedwick, R. McGrath, and H. R. Sharma, “Analysis of surface Ga_3Ni_2 crystal by XPS,” *unpublished.*

ProQuest LLC
789 East Eisenhower Parkway
P.O. Box 1346
Ann Arbor, MI 48106 - 1346 USA